

Topics in Current Chemistry Collections

Minhua Shao *Editor*

Electrocatalysis

Topics in Current Chemistry Collections

Journal Editors

Massimo Olivucci, Siena, Italy and Bowling Green, USA
Wai-Yeung Wong, Hong Kong, China

Series Editors

Hagan Bayley, Oxford, UK
Greg Hughes, Codexis Inc, USA
Christopher A. Hunter, Cambridge, UK
Seong-Ju Hwang, Seoul, South Korea
Kazuaki Ishihara, Nagoya, Japan
Barbara Kirchner, Bonn, Germany
Michael J. Krische, Austin, USA
Delmar Larsen, Davis, USA
Jean-Marie Lehn, Strasbourg, France
Rafael Luque, Córdoba, Spain
Jay S. Siegel, Tianjin, China
Joachim Thiem, Hamburg, Germany
Margherita Venturi, Bologna, Italy
Chi-Huey Wong, Taipei, Taiwan
Henry N.C. Wong, Hong Kong, China
Vivian Wing-Wah Yam, Hong Kong, China
Chunhua Yan, Beijing, China
Shu-Li You, Shanghai, China

Aims and Scope

The series *Topics in Current Chemistry Collections* presents critical reviews from the journal *Topics in Current Chemistry* organized in topical volumes. The scope of coverage is all areas of chemical science including the interfaces with related disciplines such as biology, medicine and materials science.

The goal of each thematic volume is to give the non-specialist reader, whether in academia or industry, a comprehensive insight into an area where new research is emerging which is of interest to a larger scientific audience.

Each review within the volume critically surveys one aspect of that topic and places it within the context of the volume as a whole. The most significant developments of the last 5 to 10 years are presented using selected examples to illustrate the principles discussed. The coverage is not intended to be an exhaustive summary of the field or include large quantities of data, but should rather be conceptual, concentrating on the methodological thinking that will allow the non-specialist reader to understand the information presented.

Contributions also offer an outlook on potential future developments in the field.

More information about this series at <http://www.springer.com/series/14181>

Minhua Shao

Editor

Electrocatalysis

With contributions from

Radoslav R. Adzic • Dianxue Cao • Jingguang G. Chen • Dan Du
Manuel J. S. Farias • Juan M. Feliu • Erin M. Gaffney
David P. Hickey • Feng Jiao • Jin-Cheng Li • Meng Li • Yuehe Lin
Dong Liu • Nebojsa S. Marinkovic • Shelley D. Minteer
Minhua Shao • Brian M. Tackett • Gang Wang • Guoxiong Wang
Zidong Wei • Ke Ye • Wenlei Zhu



Springer

Editor

Minhua Shao

Department of Chemical and Biological Engineering
Hong Kong University of Science and Technology
Hong Kong, China

Partly previously published in Topics in Current Chemistry Volume 376 (2018); Topics in Current Chemistry Volume 377 (2019).

ISSN 2367-4067

Topics in Current Chemistry Collections

ISBN 978-3-030-43293-5

© Springer Nature Switzerland AG 2020

This work is subject to copyright. All rights are reserved by the Publisher, whether the whole or part of the material is concerned, specifically the rights of translation, reprinting, reuse of illustrations, recitation, broadcasting, reproduction on microfilms or in any other physical way, and transmission or information storage and retrieval, electronic adaptation, computer software, or by similar or dissimilar methodology now known or hereafter developed.

The use of general descriptive names, registered names, trademarks, service marks, etc. in this publication does not imply, even in the absence of a specific statement, that such names are exempt from the relevant protective laws and regulations and therefore free for general use.

The publisher, the authors, and the editors are safe to assume that the advice and information in this book are believed to be true and accurate at the date of publication. Neither the publisher nor the authors or the editors give a warranty, expressed or implied, with respect to the material contained herein or for any errors or omissions that may have been made. The publisher remains neutral with regard to jurisdictional claims in published maps and institutional affiliations.

This Springer imprint is published by the registered company Springer Nature Switzerland AG
The registered company address is: Gewerbestrasse 11, 6330 Cham, Switzerland

Contents

| | |
|---|-----|
| Preface | vii |
| Pt-Based Catalysts for Electrochemical Oxidation of Ethanol | 1 |
| Nebojsa S. Marinkovic, Meng Li and Radoslav R. Adzic: | |
| Topics in Current Chemistry 2019, 2020:11 (4, April 2019) | |
| https://doi.org/10.1007/s41061-019-0236-5 | |
| Recent Advances in the Electro-Oxidation of Urea for Direct Urea Fuel Cell and Urea Electrolysis | 41 |
| Ke Ye, Gang Wang, Dianxue Cao and Guoxiong Wang: | |
| Topics in Current Chemistry 2018, 2020:42 (26, October 2018) | |
| https://doi.org/10.1007/s41061-018-0219-y | |
| Determination of Specific Electrocatalytic Sites in the Oxidation of Small Molecules on Crystalline Metal Surfaces..... | 79 |
| Manuel J. S. Farias and Juan M. Feliu: Topics in Current Chemistry 2019, | |
| 2020:5 (10, January 2019) https://doi.org/10.1007/s41061-018-0228-x | |
| Bimetallic Electrocatalysts for CO₂ Reduction | 105 |
| Wenlei Zhu, Brian M. Tackett, Jingguang G. Chen and Feng Jiao: | |
| Topics in Current Chemistry 2018, 2020:41 (26, October 2018) | |
| https://doi.org/10.1007/s41061-018-0220-5 | |
| Dispersive Single-Atom Metals Anchored on Functionalized Nanocarbons for Electrochemical Reactions..... | 127 |
| Jin-Cheng Li, Zidong Wei, Dong Liu, Dan Du, Yuehe Lin and Minhua Shao: Topics in Current Chemistry 2019, 2020:4 (8, January 2019) https://doi.org/10.1007/s41061-018-0229-9 | |
| Electrometabolic Pathways: Recent Developments in Bioelectrocatalytic Cascades | 149 |
| David P. Hickey, Erin M. Gaffney and Shelley D. Minteer: | |
| Topics in Current Chemistry 2018, 2020:43 (3, November 2018) | |
| https://doi.org/10.1007/s41061-018-0221-4 | |

Preface

Electrocatalysis plays a central role in electrochemical energy conversion. This Topical Collection aims to cover recent progress and trends in advanced electrocatalysts for various electrocatalytic reactions. It includes 6 contributions covering electrooxidation of ethanol (Marinkovic & Adzic et al.), urea (Ye & Wang et al.), and other small molecules (Farias & Feliu), CO₂ electrochemical reduction (Chen & Jiao et al.), single atom-based electrocatalysts (Li & Shao et al.), and bioelectrocatalysis (Hickey & Minteer et al.).

In their contribution, **Marinkovic & Adzic et al.** presented recent achievements towards developing Pt-based electrocatalysts for ethanol oxidation reaction and understanding the rationale behind the low selectivity towards CO₂ production. **Ye & Wang et al.** overviewed the reaction mechanisms of urea oxidation in different electrolytes and the recent advances in the development of electrocatalysts for this reaction. **Farias & Feliu** summarized recent works on identification of real active sites in electrocatalytic reactions such as electro-oxidation of CO, methanol, and ammonia on Pt surfaces. Electrochemical reduction of CO₂ has attracted much attention. **Chen & Jiao et al.** summarized recent literature on the topic of bimetallic electrocatalysts for CO₂ reduction in their contribution. Tuning the properties of a bimetallic catalyst could result in a wide range of products, including carbon monoxide, hydrocarbons, carboxylate and liquid oxygenates. Dispersive metal single-atoms in carbon nanomaterials are promising electrocatalysts for electrochemical energy conversion reactions. **Li and Shao et al.** highlighted the advanced synthetic methods, characterization techniques and electrochemical applications of carbon-based single-atom metal catalysts for O₂ reduction, water splitting, and other emerging reactions including CO₂ reduction, H₂O₂ production, and N₂ reduction. **Hickey & Minteer et al.** introduced the lessons that can be learned from *in vivo* enzymatic pathways and novel enzymatic pathways that have been developed for synthetic biology of electrochemical energy production and conversion. They also discuss the recent bio-inspired developments to utilize catalytic cascades for non-biological applications ranging from energy conversion to biosensing and the electrochemical production of important chemicals.

I would like to thank all the authors for their great contributions and referees for their time reviewing the manuscripts. I believe these excellent contributions collected in this Topical Collection will make significant contributions to the electrocatalysis community. I also want to take this opportunity to acknowledge editorial staff of *Topics in Current Chemistry*. The successful publication of this Topical Collection has not been possible without their strong support.



Minhua Shao

Department of Chemical and Biological Engineering, Energy Institute,
Hong Kong University of Science and Technology



REVIEW

Pt-Based Catalysts for Electrochemical Oxidation of Ethanol

Nebojsa S. Marinkovic¹ · Meng Li² · Radoslav R. Adzic²

Received: 16 October 2018 / Accepted: 18 March 2019 / Published online: 4 April 2019
© Springer Nature Switzerland AG 2019

Abstract

Despite its attractive features as a power source for direct alcohol fuel cells, utilization of ethanol is still hampered by both fundamental and technical challenges. The rationale behind the slow and incomplete ethanol oxidation reaction (EOR) with low selectivity towards CO₂ on most Pt-based catalysts is still far from being understood, and a number of practical problems need to be addressed before an efficient and low-cost catalyst is designed. Some recent achievements towards solving these problems are presented. Pt film electrodes and Pt monolayer (Pt_{ML}) electrodes on various single crystal substrates showed that EOR follows the partial oxidation pathway without C–C bond cleavage, with acetic acid and acetaldehyde as the final products. The role of the substrate lattice on the catalytic properties of Pt_{ML} was proven by the choice of appropriate M(111) structure (M = Pd, Ir, Rh, Ru and Au) showing enhanced kinetics when Pt_{ML} is under tensile strain on Au(111) electrode. Nanostructured electrocatalysts containing Pt–Rh solid solution on SnO₂ and Pt monolayer on non-noble metals are shown, optimized, and characterized by in situ methods. Electrochemical, in situ Fourier transform infrared (FTIR) and X-ray absorption spectroscopy (XAS) techniques highlighted the effect of Rh in facilitating C–C bond splitting in the ternary PtRh/SnO₂ catalyst. In situ FTIR proved quantitatively the enhancement in the total oxidation pathway to CO₂, and in situ XAS confirmed that Pt and Rh form a solid solution that remains in metallic form through a wide range of potentials due to the presence of SnO₂. Combination of these findings with density functional theory calculations revealed the EOR reaction pathway and the role of each constituent of the ternary PtRh/SnO₂ catalyst. The optimal Pt:Rh:Sn atomic ratio was found by the two in situ techniques. Attempts to replace Rh with cost-effective alternatives for commercially viable catalysts has shown that Ir can also split the C–C bond in ethanol, but the performance of optimized Pt–Rh–SnO₂ is still higher than that of the Pt–Ir–SnO₂ catalyst.

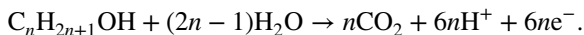
Keywords Platinum-based catalysts · Ethanol oxidation · In situ FTIR · In situ EXAFS

Chapter 1 was originally published as Marinkovic, N. S., Li, M. & Adzic, R. R. Topics in Current Chemistry (2019) 377: 11. <https://doi.org/10.1007/s41061-019-0236-5>.

Extended author information available on the last page of the article

1 Introduction

Easy storage and handling, high energy density, and wide availability are features that make alcohols attractive fuel cell liquid combustibles and the most promising alternative power sources for transportation, portable electronics, and stationary applications. However, many obstacles have restrained the more rapid development of direct alcohol fuel cells. The major problem in oxidation of any alcohol other than methanol is particularly difficult breaking of the C–C bond, which is a necessary step for a complete oxidation to CO₂. The complete oxidation of any primary monohydroxy alcohol can be written as:



Due to the complex oxidation and sets of parallel reactions, the predominant pathway of any alcohol leads to incomplete oxidation products with the transfer of less than $6n$ electrons [1–4].

The mechanism of the simplest alcohol (methanol) oxidation on Pt has been studied for several decades as the only alcohol that does not need the C–C bond cleavage for the oxidation to CO₂. However, ethanol has the intrinsic advantage in terms of doubling the number of electrons exchanged. Furthermore, its low toxicity, comparable electrochemical activity, high theoretical mass/energy density (8.0 kWh/kg), and easy production by fermentation from sugar-containing materials makes it an attractive power source. Unlike methanol, ethanol is a renewable fuel requiring simple logistics for its applications. These features make it an attractive fuel for fuel cells and favorable alternative power source. Unfortunately, the slow and incomplete ethanol oxidation reaction (EOR) occurring at the anode even on the best available catalysts known to-date is the main impediment to practical application and commercialization of direct ethanol fuel cells (DEFCs). Additional factors hindering development of DEFCs include low activity, complex reaction mechanism, ethanol crossover from the anode to the cathode and CO poisoning, as well as the high costs of precious metals of Pt-based catalysts [1–7]. Although details of the reaction mechanism are still debated, good agreement exists about reaction pathways that form acetaldehyde (CH₃CHO) and acetic acid (CH₃COOH) as the main products of the oxidation of ethanol at a Pt electrode in acidic solution (Fig. 1). Thus, at moderately positive potentials of interest for fuel cell applications (up to 0.6 V), the main oxidation products have the C–C bond intact and the reaction yields two or four electrons [1–4]. Further oxidation involving cleavage of the C–C bond on

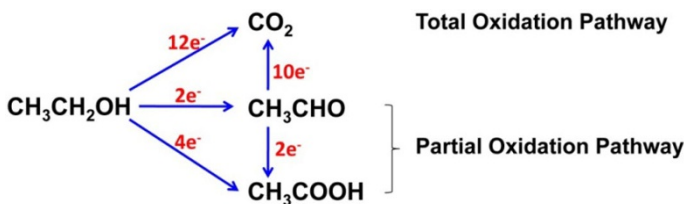


Fig. 1 Schematic representations of the parallel pathways during EOR [2]

Pt proceeds mostly through re-adsorption of acetaldehyde, yielding adsorbed carbon monoxide CO_{ads} as an intermediate [2]. Carbon-containing species as CO_{ads} are especially strongly adsorbed on Pt surface, thus blocking Pt sites for further adsorption of reactants until they are removed by further oxidation. CO_{ads} is oxidized above 0.6 V, when the Pt surface becomes covered by Pt–OH or Pt–O species produced by oxidation of water, which further react with CO_{ads} yielding CO_2 as the final product. Thus, on pure Pt, carbon dioxide appears only at very high positive potentials [8].

Products and adsorbed intermediates of EOR in acidic solution have been verified using several techniques [3, 7, 8]. A recent study showed that the ethanol oxidation on Pt/C yields primarily acetic acid and acetaldehyde as the products, with carbon dioxide occurring in the range of only 0.7–7.5% depending on the initial concentration of the alcohol [9]. Such a low selectivity of Pt toward CO_2 is a practical problem to be addressed in designing DEFCs. In addition, it contrasts with the consensus in chemistry stating that kinetics of any catalytic reaction is expected to be faster if it leads to a more stable product. Since CO_2 is significantly more stable than acetic acid and acetaldehyde, the low selectivity of the EOR to CO_2 is also a fundamental question.

Consequently, pure Pt is not capable of catalyzing oxidation of ethanol through the total oxidation pathway. However, Pt is a necessary catalyst constituent to provide efficient adsorption of ethanol, the first reaction step in its oxidation. Modifications of pure Pt have been developed to improve activity of Pt by the addition of co-catalysts, in various structures and compositions, including adatoms, adlayers and intermetallic Pt–M assemblies, bimetallic alloys, metal oxides, and core–shell nanostructures [10–18]. The co-catalyst promotional effect is explained in terms of bifunctional effect (promoted mechanism) [19] and electronic effect (ligand effect or intrinsic mechanism) [20]. According to the bifunctional effect, the oxidative removal of the strongly adsorbed poisoning species (i.e., species that cannot be further oxidized at that anode potential) is facilitated in the presence of an oxyphilic co-catalyst (e.g., Ru, Sn, Ir, Re, Os, Pb, etc.) by supplying oxygen atoms at an adjacent site at a lower potential than that accomplished by pure Pt. The electronic effect postulates that the presence of the co-catalyst modifies the electronic structure of Pt, and therefore the bonding strength of poisoning species and oxygen-containing species. Moreover, the addition of the co-catalysts decreases Pt content in the electrocatalysts, therefore reducing the noble metal content. Pt–Sn and Pt–Ru are found to be the most active binary catalysts [12]. Despite the increase in overall activity, the addition of Sn or Ru decreases platinum selectivity towards CO_2 formation [10, 21]. Therefore, the addition of the co-catalyst facilitates the products of partial oxidation pathway.

Because existing Pt-based binary catalysts could not achieve total oxidation of ethanol to CO_2 at moderate positive potentials, the prospects were focused on addition of a third component. Pt–Ru–W, Pt–Sn–Ni and Pt–Sn–Rh further enhanced activity, but the yield of carbon dioxide was still low [12, 22]. The first multi-functional ternary electrocatalyst effective in splitting the C–C bond in ethanol at room temperature and capable of carrying out the reaction to CO_2 was designed by Adzic et al. [23]. Combining the attributes of Pt for ethanol dehydrogenative adsorption, SnO_2 for the supply of oxygen-containing species and Rh that is known to be capable of splitting C–C bond as observed in metal/gas interface studies [24, 25], an active ternary Pt/Rh/ SnO_2 catalyst was obtained. Reports from other groups have

since proven that Pt-Rh can be highly active catalyst for ethanol oxidation in various form, but the activity strongly depends on the substrate and synthesis [26–30].

In this review we describe the synthesis, characterization, electrochemical activity, and optimization of ternary PtRh/SnO₂ catalysts. Attempts to reduce the cost of the catalyst by replacing Rh with alternative co-catalysts are illustrated, in which it was shown that Ir in ternary catalysts could also be used to split the C–C bond in ethanol [31]. We also underline particularly exciting results with ethanol oxidation to CO₂ on a Pt monolayer under tensile strain, as reported by Li et al. [32]. The emphasis is given to *in situ* characterization of the electrocatalysts by IR spectroscopy and X-ray absorption spectroscopy in an attempt to show how the combination of these spectroscopies, electrochemical techniques, and theoretical studies can enhance the understanding of the ethanol electrooxidation. The examples shown here hold great promise that impediments to practical direct alcohol fuel cells can be overcome.

2 In Situ Characterization of New Catalysts for Ethanol Oxidation

2.1 In Situ FTIR Experimental Details

Infrared (IR) spectroscopy has proven to be one of the most useful techniques for studying electrode/electrolyte interface at a molecular level. It provides information on the species involved in adsorption/desorption, surface bonding, orientation, coordination, etc., and has substantially advanced our knowledge on various electrochemical systems, including both organic and inorganic chemical reactions [33–38].

In many absorption spectroscopy techniques, the intensity I of the transmitted signal through an absorbing medium is compared to the intensity of the incident radiation I_0 [33, 34]. In IR spectroscopy, the two intensities are related to the extinction coefficient ϵ , thickness of the absorption layer b , and the concentration c by Beer's law, as $I=I_0 \exp(-\epsilon bc)$. The spectrum is usually presented as the variation of absorbance $A=-\ln(I/I_0)$ on the wavelength of the radiation λ , or wave-number $\bar{\nu}=1/\lambda$, which is related to frequency ν , as $\bar{\nu}=1/\lambda=\nu/c$. In infrared reflection-absorption spectroscopic (IRRAS) experiments described below, instead of absorbance, one usually presents subtractively normalized change in reflectivity, $-\Delta R/R=-(R_s-R_0)/R_0$, where the reflection signals R_0 and R_s are taken at the reference and sample potential E_r and E_s , respectively [34–43]. For small differences in R_s and R_0 , $-\Delta R/R$ is proportional to the absorbance [39]. However, unlike the regular transmission experiment in which absorbance peaks are always positive-going, the bands in the *in situ* IR spectroelectrochemical experiment can be both positive- and negative-going, representing the gain and the loss of a species at the sample potential relative to that at the reference, respectively [44–54]. Because the change in the band intensities taken at two potentials is usually of the order of a fraction of a percent, a sufficient number of scans (usually over a hundred) must be coadded to overcome statistical noise. Furthermore, care must be taken to minimize the changes in the reflectivity induced by the factors other than potential, e.g., changes in the air

surrounding the cell that contains CO_2 and water vapor, which would otherwise render portions of the spectra unusable [55].

The setup for the IRRAS technique used in most studies presented below is based on the Otto's configuration in which the solution is squeezed between internal reflection element (IRE) and the working electrode, as shown in Fig. 2 [55, 56]. The IR light enters the IRE and strikes the IRE/solution interface at the angle θ . If the refractive index n_1 of the IRE element is higher than that of the solution (n_2), there exists a critical angle $\theta_c = \sin^{-1}(n_2/n_1)$ above which the IR beam totally reflects back into the IRE. Simultaneously, an evanescent wave is generated and propagates inside the rarer medium to a depth of a 1–3 μm , carrying information on the absorption of species in its path. This phenomenon is utilized in internal reflection spectroscopy [33]. In infrared electrochemistry, the electrode is placed within the penetration depth of the evanescent wave, so that the reflected IR radiation also carries the information on the species at the electrode surface. The incident angle of the IR light should be accurately adjusted to a few degrees above θ_c to obtain the greatest sensitivity [55–58].

The necessary accuracy in the incident angle can only be achieved if the light is collimated. However, common FTIR spectrometers have the IR beam focused into a spot in the middle of the internal chamber of the instrument. A hemisphere (or hemicylinder) of a high-refractive index material can be used to collimate the IR beam by keeping the focal point at the distance $d=r/(n_1-1)$ before the curvature of the IRE, where r and n_1 are the radius and index of refraction of the IRE, respectively [33, 55, 57]. The IR beam travels from the source of the IR spectrometer, reflects off of the first gold mirror so that the instrument's focal point F is moved to the point F' in front of

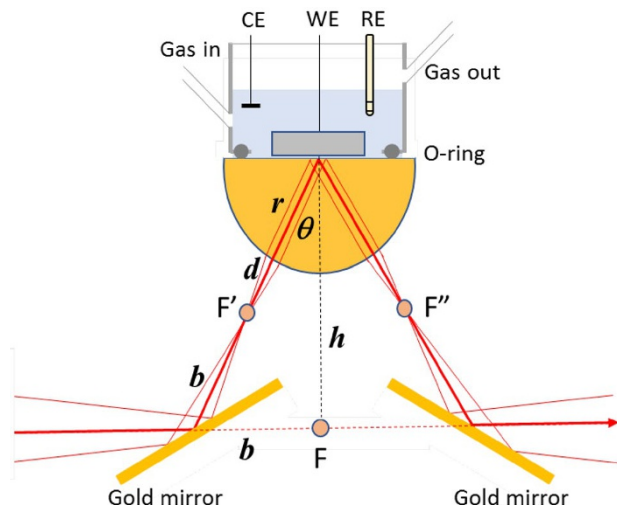


Fig. 2 Schematic representation of the setup for in situ FTIR spectroelectrochemical experiments. The electrochemical cell built on top of the flat surface of the ATR hemisphere is made of Teflon with bored holes for gas purging and a three-electrode system consisting of a working electrode (WE), Pt wire-gauze counter electrode (CE), and a leak-proof Ag/AgCl reference electrode (RE)

the IRE. In the setup shown in Fig. 1, the IRE is made of zinc selenide because of its wide transmittance permitting investigation in a broad range of spectral vibrations, and good chemical resistance. The collimated IR light reflects off the ZnSe-solution interface, refocuses at the point F'' , and travels to the IR detector inside the FTIR instrument upon reflection from the second gold mirror. Taking the average indices of refraction for ZnSe and solution (water) of 2.4 and 1.3, respectively, the incidence angle at the ZnSe/water interface can be set to 35° , i.e., just about 2° higher than θ_c [59]. This angle of incidence corresponds to the maximum of the electric field strength of ZnSe/water/Pt three-phase system for the incident radiation that matches the frequency of linearly bonded carbon monoxide (CO_L) at Pt surface, $\sim 2050 \text{ cm}^{-1}$ [58]. For the radius r of the IRE hemisphere of 1.27 cm, the distances between two mirrors and the height of the flat surface of ZnSe from the incident IR beam path can be calculated ($2b = 5.86 \text{ cm}$ and $h = 4.18 \text{ cm}$).

While Otto configuration has the advantage of being able to accept a variety of different surfaces including flat poly- and single-crystals as well as rough surfaces composed of a catalyst layer deposited onto a flat surface of an inactive material, another setup is used if the electrochemical experiment involves gas evolution. In Kretschmann configuration, the working electrode is deposited as a thin film (tens of nanometers) over the flat side of IRE, and the solution side is semi-infinite, thus allowing the volatile products to escape [60]. The presence of the thin metal film was shown to enhance the IR absorption bands by one or two orders of magnitude, although the nature of the enhancement is still being debated [61–63]. Indeed, the Fresnel equations for three-phase stratified medium show that the electric field strength, associated with dissipation of the electric energy within the phase, can be orders of magnitude higher in Kretschmann configuration as opposed to that in Otto configuration. However, the enhancement occurs in a very narrow range of incidence angles and for very thin metal films only [64, 65]. The setup depicted in Fig. 1 can be used for both configurations, but the optimization of the setup is critical, especially for the Kretschmann configuration where a slight misalignment of the accessory could result in many times lower absorption intensity [58, 66].

In a typical IR spectroelectrochemical experiment, one usually chooses the reference potential at which the considered reaction does not occur, whereas the sample potentials are selected to cover the potential range in which the reaction proceeds. For studies occurring at anodic potentials, the reference potential is held sufficiently negative. For instance, in sulfate/bisulfate adsorption at Pt electrodes the reference potential is usually kept in hydrogen adsorption region or just positive to it, whereas the sample potentials are chosen to extend over more positive potentials [67–69]. The sample and reference potentials in oxidation reactions described below are taken in a similar manner.

Nicolet Nexus 670 FT-IR spectrometer equipped with a liquid nitrogen-cooled MCT detector was used in the studies. One-hundred and twenty-eight interferograms with 8 cm^{-1} resolution were collected at each potential. The reference spectrum was collected at the potential before the onset of ethanol oxidation, i.e., at 0.05 V vs. RHE, and sample spectra were collected at increasingly higher potentials; the resulting spectra are given as absorbance. The working electrodes were pressed against the IRE to create a solution layer with the thickness of $\sim 1 \mu\text{m}$. Traces of oxygen in

the electrolyte were removed by bubbling argon above the electrode, while dry air was purging the IR optical path to remove CO₂ and water vapor in air.

2.2 In Situ XAS Experimental Details

X-ray absorption spectroscopy (XAS) is based on modulation of an atom's probability to absorb X-rays at energies near and above the binding energy of the atom's core-level electron. If the X-ray energy is higher than the core-level electron's binding energy, the atom absorbs X-rays and the electron (called photoelectron) is ejected. The eviction of an electron from the first shell corresponds to K-edge, whereas photoelectron ejection from the second, third, and higher shells are labeled L, M, etc. Due to the spin-orbital coupling, multiple distinct transitions are observed from higher shells [70–75]. The hole in core-electron level is filled by another electron from the higher energy level, and the energy difference between the two levels may be radiatively emitted by X-ray fluorescence.

The change in absorption coefficient (μ) around the edge is followed in X-ray absorption spectroscopy (XAS) as the function of X-ray energy, E . Graphically represented, the spectrum is, in principle, similar to the one shown in Fig. 3. The XAS spectrum is divided into two parts: the spectral part within ca. ± 50 eV around the edge (E_0 , Fig. 3a) is called X-ray absorption near-edge spectroscopy (XANES), whereas the part of the spectrum at higher energies is termed extended X-ray absorption fine structure (EXAFS). The two parts of the spectrum are treated in a different manner and offer related information on the analyzed system [71].

Because the XANES part of the XAS spectrum corresponds to the multielectron transitions that are difficult to express mathematically, this spectral region is modeled qualitatively. The important features are the edge shift arising as the consequence of the oxidation state of the photo-absorber and pre-edge features that can be used in fingerprinting. In addition, linear combination analysis (LCA) can be used to distinguish a mixture by matching its spectrum with a modeled one obtained by adding together fractions of spectra of various standards.

When a series of XANES spectra are taken “in-operando”, principle component analysis (PCA) can be used to identify a set of constituents of the XAS spectra [70–75]. For electrochemical measurements, delta mu ($\Delta\mu$) technique has been developed to identify subtle changes on the surface due to the adsorption or desorption of species from the electrolyte caused by the potential change [76, 77]. Dominating bulk metal–metal interactions are removed as constant by spectral subtraction of two XANES spectra of the same sample at two different potentials. For instance, in delta mu spectrum of carbon-supported Pt nanoparticles obtained as $\Delta\mu = \mu(V) - \mu(DL)$, where $\mu(V)$, and $\mu(DL)$ represent spectra at a potential V and that of the double layer where no adsorbate species are present, surface adsorbates (O and OH) and sub-surface O were identified and interpreted by the comparison with theoretical curves made based on crystallographic models [78].

Unlike XANES, the EXAFS region can be described mathematically. The X-ray absorption coefficient decreases with energy by the relation $\mu \sim 1/E^4$, except when the photon energy is sufficient to eject an electron, causing a sharp rise in the

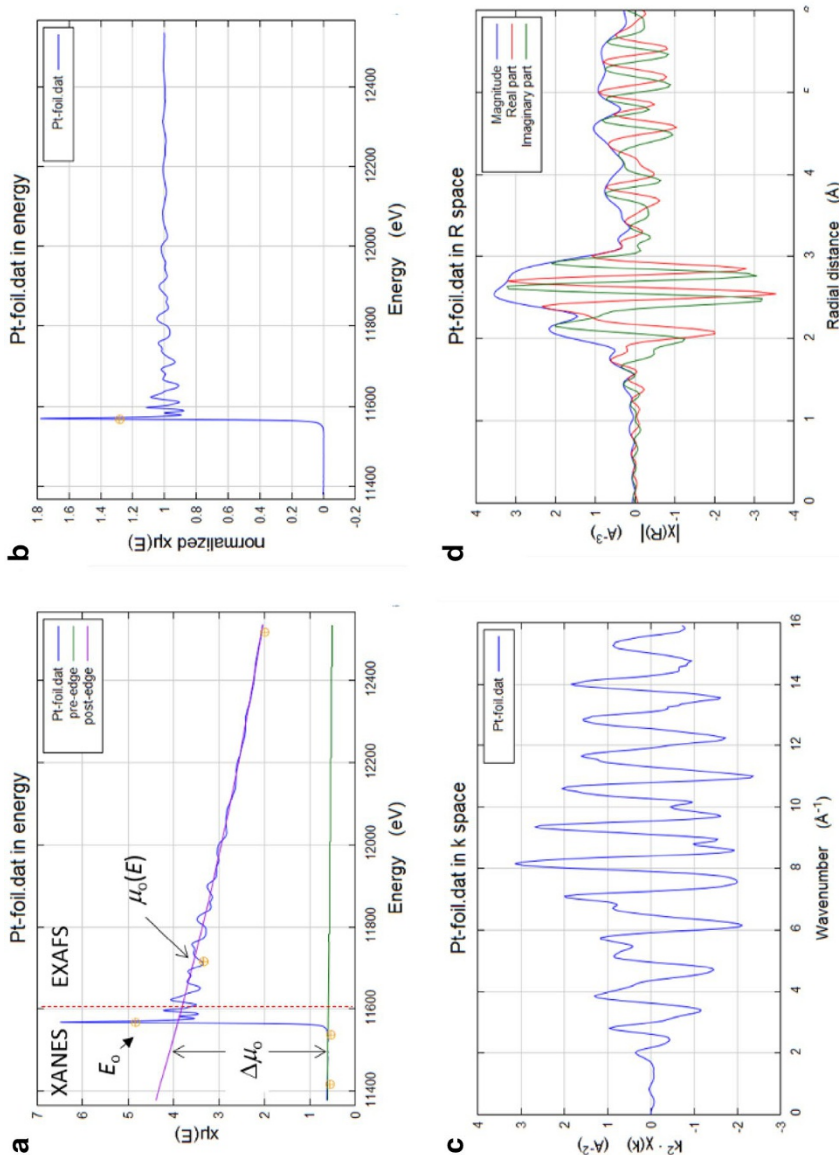


Fig. 3 Pt foil spectrum (**a**), normalized spectrum (**b**), processed in k -space (**c**), and in R -space (**d**)

absorption coefficient called the white line [71]. If the atom absorbing the X-rays (photoabsorber) were completely isolated, μ would continue to decline after the edge following the $\mu-E$ relation. Oscillations in the $\mu-E$ plot (Fig. 3a) are due to the interference of the photoelectron wave scattered off of the neighboring atoms with itself at the photoabsorber, and therefore the EXAFS contains information on the nature and position in space of atoms in photoabsorber's immediate surrounding. These oscillations, or "fine structure" of EXAFS, are extracted by subtracting the background $\mu_o(E)$ and dividing it by the edge step $\Delta\mu_o(E_o)$ to produce oscillations $\chi(E)$ normalized to one absorption event: $\chi(E)=[\mu(E)-\mu_o(E)]/\Delta\mu_o(E_o)$, thus obtaining the EXAFS spectrum (Fig. 3b). It is more convenient to express $\chi(E)$ as a function of photoelectron wave number, $k=0.512(E-E_o)^{1/2}$ (in Å⁻¹), where E_o is the edge energy. To amplify the oscillations at higher k values, $\chi(k)$ is often multiplied by k^2 or k^3 , producing the plot referred to as the EXAFS spectrum in k -space (Fig. 3c). By the Fourier transformation, this spectrum is converted into the plot in R space (Fig. 3d), where the real and imaginary part of the complex function and the magnitude are plotted as the function of radial distance (in Å). Radial distances are related to the actual distances between the photoabsorber and scatterer atoms but are usually offset by 0.3–0.5 Å due to phase shift. The actual distances between the atoms are revealed by subsequent fitting of the experimental spectrum to the theoretical one constructed from the crystal lattice of a selected model featuring scattered atoms, their coordination number, and the distance to the absorber.

Besides the necessity of a tunable X-ray source, for a good quality of XAS spectrum, the flux of the incident beam must be at least 10^{10} photons/s, and the width of the monochromatic beam should be smaller than 1 eV to obtain reasonable signal-to-noise ratio and spectral resolution, respectively. These requirements are only met with synchrotron radiation [70–75]. The XAS setup consists of two detectors measuring the incident and transmitted beam through the sample. The absorption coefficient is related to the ratio I/I_0 by Beer's law, similarly to that in the IR experiment described above. For weakly concentrated and/or X-ray opaque samples, fluorescence mode is often used with the detector positioned perpendicularly to the incidence beam path to reduce the intensity of the scattered X-rays.

The spectroelectrochemical cell for in situ measurements is presented in Fig. 4. The working electrode consists of the electrocatalyst deposited on a carbon cloth or carbon paper. Another strip of blank carbon cloth is used as the auxiliary (counter) electrode. If gas evolution on the counter electrode is extensive, it can be placed outside of the X-ray path. A Nafion membrane separates the working and counter electrodes. The working-auxiliary electrode pair, Teflon rings and spacers are all sealed in a grove of the acrylic body of the cell. When filled with electrolyte, the electrodes are in contact with a Ag/AgCl leak-tight reference electrode, placed away from the X-ray path. The cell can be used in both transmission and fluorescence mode. The EXAFS spectrum is measured at the constant potential once the current reaches the steady state [78, 79].

Processing of an EXAFS spectrum is accomplished by fitting the spectrum to a predicted structure. While there are several computer programs for this purpose, for the interpretation of the examples given here we used Demeter package. The freeeware includes the Athena program containing LCA, PCA, and spectral subtraction

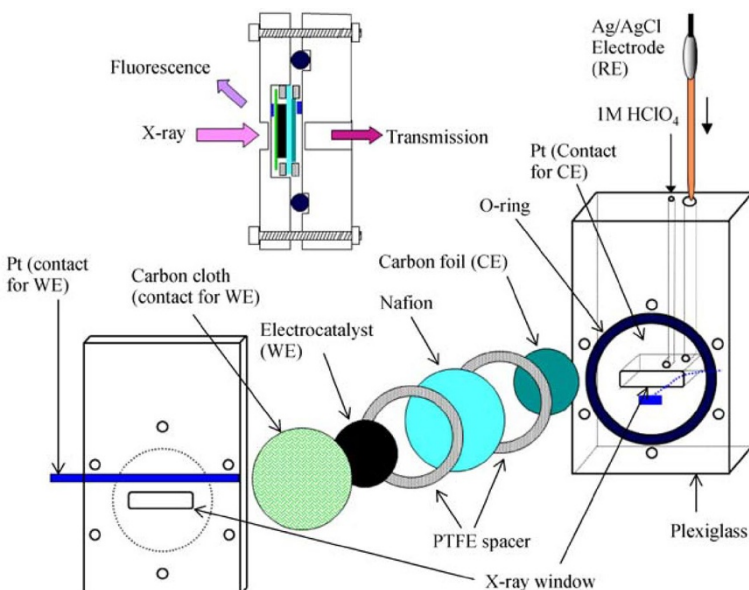


Fig. 4 Exploded view of the spectroelectrochemical cell used in the experiments (reprinted with permission from Ref. [79] with permission from Elsevier)

routines for XANES analysis, as well as data reduction and extraction of the sinusoidal EXAFS wave. The Artemis program is used for fitting the EXAFS spectrum to a predicted structure based on reasonable assumptions, or other information about the sample. The package also includes an automated program for ab initio multiple-scattering calculations for clusters of atoms (FEFF) as well as several helpful programs for data acquisition and processing [80].

3 In Situ FTIR Study of Ethanol Electrooxidation

3.1 In Situ IRRAS Study of Ternary Electrocatalysts for Oxidizing Ethanol to CO₂

Following the initial discovery of the multi-functional ternary Pt–Rh–SnO₂ electrocatalyst that is effective in splitting the C–C bond in ethanol at room temperature, a number of studies have been conducted [23, 26–30, 81–83]. Electrochemical measurements have proved that the addition of Rh is necessary for the enhanced activity and selectivity to CO₂ of the ternary system with respect to the optimized binary Pt–SnO₂ catalyst [84–86]. The enhanced kinetics and superior selectivity to total oxidation of the ternary catalyst is demonstrated by the electrochemical measurements and in situ FTIR studies. These and other techniques presented further and in other works have generated extremely valuable knowledge on the intermediates, products, and mechanism of this reaction, and provided guidance in designing highly active and efficient catalysts.

3.1.1 The Role of Rh in the Ternary Pt–Rh–SnO₂ Catalyst System

The catalytic property of the Pt–Rh–SnO₂ system is explained in terms of the synergistic effect among the three constituents [23]. Ethanol oxidation commences on Pt sites by dehydrogenate adsorption; Rh cleaves the C–C bond in ethanol and SnO₂ supplies oxygen-containing species for further oxidation of the intermediates, and also keeps Pt and Rh metallic. DFT calculations of ethanol decomposition on the PtRh/SnO₂(110) have explained that the path to the total ethanol oxidation pathway leads through an oxametallacyclic conformation (*CH₂CH₂O) intermediate, which further breaks into *CH₂ and *CH₂O radicals and two protons with a reasonable energy barrier of 1.29 eV. An oxidation pathway through acetaldehyde is unlikely, as it requires an extremely high energy of 3.82 eV. Furthermore, separate DFT studies on Rh(111) have shown that Pt in Rh–Pt alloy weakens the C–Rh interaction through electronic effect and helps the removal of carbonaceous species in the form of CO₂ [87].

Experimental confirmation that the addition of Rh enhances EOR activity via facilitating ethanol total oxidation to CO₂ was performed with single-crystal-based model catalysts [i.e., SnO₂/Pt(111) and RhSnO₂/Pt(111)] and carbon-supported nanoparticle catalysts (i.e., Pt–SnO₂/C and Pt–Rh–SnO₂/C) using IRRAS [21, 70]. For the single-crystal catalysts, Pt(111) single-crystal surface was first prepared by annealing in H₂/Ar mixture and cooling in the same stream, and then nanoclusters of SnO₂ or RhSnO₂ were deposited on it. Carbon-supported catalysts were synthesized via wet-chemistry methods, followed by the deposition of the nanocatalyst ink (catalysts dispersed in the mixture of ethanol, water, and Nafion) on an inactive support (polycrystalline gold electrode) in a similar manner described by Markovic et al. [88].

Figure 5a–d shows the *in situ* IRRAS spectra collected from the above catalysts during EOR in perchloric acid supporting solution. The two most prominent bands represent the electrolyte rearrangement near the electrode surface during the potential excursion, where perchlorate anions enter the electrolyte layer, producing the positive-going band near 1100 cm⁻¹, and replacing water molecules (negative-going band around 1600 cm⁻¹). The negative-going band at 1040 cm⁻¹ represents the ethanol consumption, whereas positive-going bands at 2343, 1280, and 933 cm⁻¹ represent the oxidation products consisting of CO₂, CH₃CHO, and CH₃COOH. Band assignments are listed in Table 1.

The selectivity of the catalyst towards the total oxidation pathway was evaluated by the intensity of the positive-going peak near 2343 cm⁻¹, the asymmetric stretch vibration of CO₂. It is evident that the intensity of the CO₂ band produced by the two Rh-containing catalysts [RhSnO₂/Pt(111) and Pt–Rh–SnO₂/C] is much higher when compared to the two Rh-free catalysts (SnO₂/Pt(111) and Pt–SnO₂/C). This fact confirms that the addition of Rh enhances catalysts' selectivity in C–C bond splitting and CO₂ production. In addition, a bipolar band around 2040 cm⁻¹, which is particularly strong at SnO₂/Pt(111) catalyst, appears due to the linearly bonded CO on the catalyst surface (CO_L). The bipolar shape of the band comes from the fact that CO_L is present at both sample and the reference potential but with different vibration frequencies, according to the Blyholder mechanism [89]. The band can

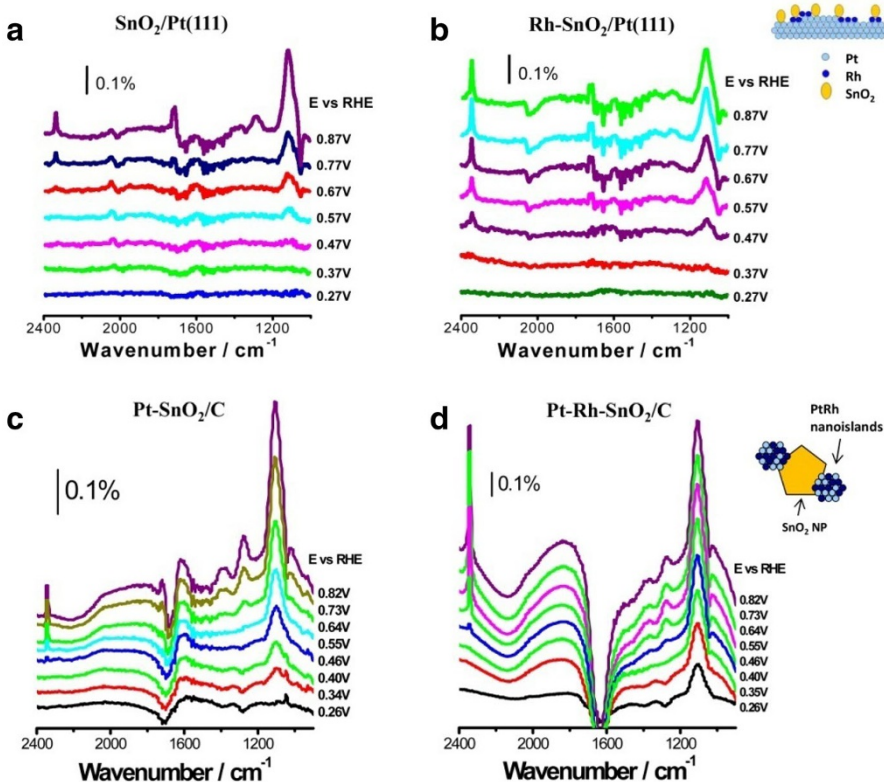


Fig. 5 In situ IRRAS spectra from the Rh-free and Rh-containing catalysts during EOR. Inserts are structural illustrations of respective catalysts. **a, b** Reprinted from Ref. [23], with permission from Springer Nature. **c, d** Reprinted from Ref. [84], with permission from Elsevier

Table 1 In situ IRRAS spectra band assignments [23, 84]

| Wavenumber/cm ⁻¹ | Assignment |
|-----------------------------|--|
| 2343 | CO ₂ asymmetric stretching |
| 2030–2065 | Linear-bonded CO |
| 1800–1840 | Bridge-bonded CO |
| 1705 | C=O stretching of CH ₃ CHO and CH ₃ COOH in solution |
| 1620–1635 | C=O stretching of adsorbed acetaldehyde and acetyl |
| ~1598 | H–O–H deformation of adsorbed water |
| 1396–1410 | O–C–O stretching of adsorbed acetate |
| 1368, 1108 | CH ₃ symmetric deformation and C–H wagging in CH ₃ CHO |
| ~1350 | CH ₃ in-plane bending of adsorbed acetate |
| 1280 | C–O stretching of CH ₃ COOH in solution |
| 1100 | Cl–O stretching ClO ₄ [−] |
| 1044 | C–O stretching of CH ₃ CH ₂ OH |
| 933 | C–C–O asymmetric stretching in CH ₃ CHO |

be used as a measure of the poisoning of the catalyst. It is obvious that the band is absent in the spectra of Pt–Rh–SnO₂, signifying the ability of the ternary catalyst to oxidize ethanol without surface poisoning. This is corroborated by DFT calculations, which reveal that the electron transfer from Rh to Pt weakens the interaction between *d*-states of Pt with dissociated oxygenates (including CO) and hydrocarbons, making them active only for dissociated H [23].

3.1.2 Quantitative Optimization of the Pt–Rh Ratio

In situ IRRAS studies have demonstrated the effect of Rh component and the superior performance of the Pt–Rh–SnO₂ ternary catalyst. Optimizing the content of Rh is of great importance because high EOR activity and high selectivity towards CO₂ formation are both essential goals in ethanol electrocatalysis. Moreover, Rh is a very rare and quite expensive metal and minimizing its content is essential for production of a viable catalyst. Four Pt–Rh–SnO₂/C catalysts with atomic ratio of Pt:Rh:Sn of 1:*x*:1, where *x* = 1, 1/2, 1/3, and 1/4, were synthesized via a seeded growth approach, and were employed to establish composition-selectivity correlation and to optimize the catalysts' composition [84]. Figure 6a–d displays in situ IRRAS spectra recorded from these catalysts. It can be observed that the two Pt–Rh–SnO₂/C with moderate Rh contents (i.e., Pt:Rh:Sn = 1:1/2:1 and 1:1/3:1) show considerably higher CO₂ production compared to the ones with too high or too low Rh content (i.e., Pt:Rh:Sn = 1:1:1 and 1:1/4:1).

3.1.3 In Situ FTIR as a Quantitative Analysis Method

In situ FTIR results were used for quantitative estimation of the products formed in studies of ethanol oxidation, EOR products distribution, and the dependence of the selectivity of Pt–Ru catalysts on Ru contents [2, 90–92]. To compare the selectivity of the four Pt–Rh–SnO₂/C electrocatalysts and to understand the effect of Rh content on the catalysts' capability in C–C bond cleavage, the quantity of different oxidation products is determined following the method described by Weaver's group [90]. The EOR total oxidation current efficiency, defined as the ratio between charge contribution from total oxidation pathway (C_{CO₂}) and charge contribution from both total oxidation and partial oxidation pathways (C_{CO₂+CH₃COOH+CH₃CHO}), is directly correlated to the capability of the catalysts to split the C–C bond. The integrated band intensities of CO₂, CH₃CHO, and CH₃COOH at 2343 cm^{−1}, 933 cm^{−1}, and 1280 cm^{−1}, respectively, obtained from the spectra in Fig. 6 were used to calculate the EOR total oxidation current efficiency for different Pt–Rh–SnO₂/C catalysts. CO₂ produces the strongest band in the spectra of Pt–Rh_{1/2}–SnO₂/C and Pt–Rh_{1/3}–SnO₂/C catalysts, while CH₃COOH bands are intensified for the Pt–Rh₁–SnO₂/C and Pt–Rh_{1/4}–SnO₂/C catalysts. CH₃CHO is only produced in small amounts in EOR of all four Pt–Rh–SnO₂/C catalysts. The variation of total oxidation efficiency versus applied potential is plotted in Fig. 7. For comparison purposes, those of Pt/C and Pt–SnO₂/C catalysts are also included.

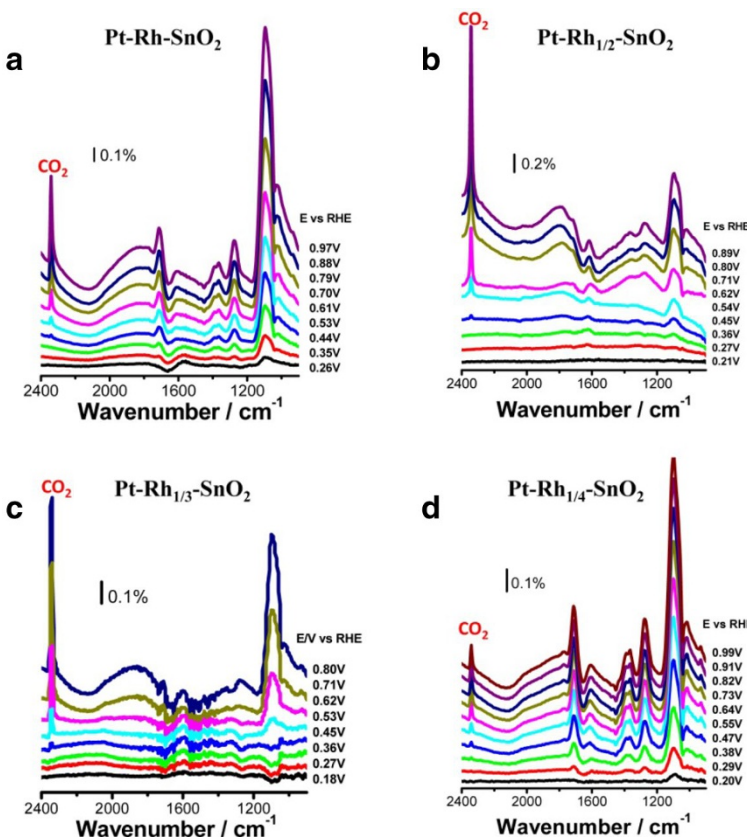


Fig. 6 In situ IRRAS spectra from four Pt–Rh–SnO₂/C nanocatalysts with different composition. Reprinted with Ref. [31] with permission from American Chemical Society

The amount of a given species inside the thin layer cavity, Q (mol/cm²), can be calculated using the ratio of respective integrated band intensities A_i , and effective absorption coefficient ϵ_{eff} , as:

$$Q = \frac{A_i}{\epsilon_{\text{eff}}}. \quad (5)$$

The values of ϵ_{eff} for CO₂, CH₃COOH, and CH₃CHO are taken as 3.5×10^4 , 5.8×10^3 , and 2.2×10^3 M⁻¹cm⁻², respectively [90]. Because the production of one molecule of CO₂, CH₃COOH, and CH₃CHO releases six, four, and two electrons, respectively, the total oxidation efficiency, C_{CO₂}/C_{CO₂+CH₃COOH+CH₃CHO}, is calculated as:

$$\frac{C_{\text{CO}_2}}{C_{\text{CO}_2} + C_{\text{CH}_3\text{COOH}} + C_{\text{CH}_3\text{CHO}}} = \frac{6 * Q_{\text{CO}_2}}{6 * Q_{\text{CO}_2} + 4 * Q_{\text{CH}_3\text{COOH}} + 2 * Q_{\text{CH}_3\text{CHO}}}. \quad (6)$$

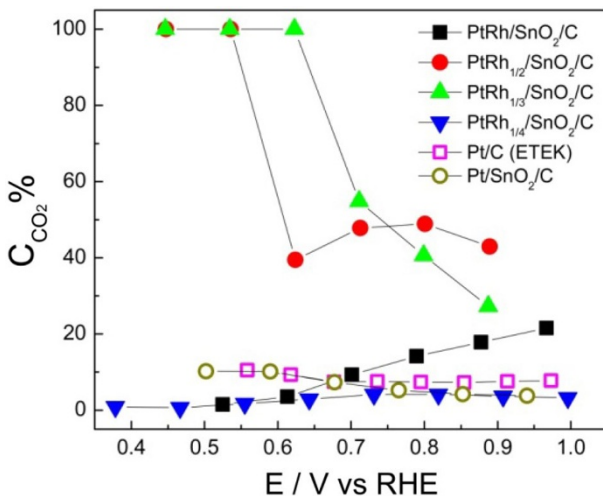


Fig. 7 The variation of different Pt–Rh–SnO₂/C catalysts’ EOR total oxidation current efficiency, i.e. $C_{CO_2}/(C_{CO_2}+CH_3COOH+CH_3CHO)$, versus applied potential. Reprinted from Ref. [31] with permission from American Chemical Society

It is evident that the Pt–Rh–SnO₂ catalysts with moderate Rh content (Pt:Rh = 1:0.5 and 1:0.33) give the optimal selectivity for C–C bond splitting and CO₂ formation, whereas the other two Pt–Rh–SnO₂/C catalysts (with Pt:Rh ratio of 1:1 and 1:0.25) show lowered capability for C–C bond splitting compared to pure Pt. Furthermore, in the potential region of practical interest for fuel cells (below 0.7 V), the total oxidation current efficiency for the optimal catalysts (Pt–Rh_{1/3}–SnO₂/C and Pt–Rh_{1/2}–SnO₂/C) is above 40%. To the best of our knowledge, these catalysts have achieved the highest ethanol conversion efficiency of all ethanol oxidation catalysts known to date. Therefore, the catalysts’ selectivity is highly dependent on their composition, i.e., Pt/Rh ratio, and a moderate Rh content yields the highest selectivity to CO₂. This phenomenon has been attributed to both the geometric “ensemble effect” and the electronic “ligand effect” [31].

We acknowledge that the in situ FTIR results should be taken with certain reservations for quantitative studies of EOR products distribution. Limitations come from both the instrument’s inability to detect certain products and the setup of the in situ FTIR experiment, as follows: (1) because the accumulation and diffusion of EOR products occur simultaneously, the total amount of product detected by the technique is lowered by the amount that diffuses away from the thin layer of electrolyte probed by the IR beam. However, various oxidation products are expected to have different diffusion rates. As the most volatile among the three major products, solvated CO₂ is likely to diffuse away faster than acetaldehyde and acetic acid. (2) Re-adsorption of products and their subsequent oxidation in thin-layer FTIR setup is probably different from the fuel cell environment. (3) The sensitivity of IRRAS is limited in detecting CH₄, leading to imprecise determination of its current efficiency assuming that methane was an important EOR product as claimed by Wieckowski et al. [93]. (4) The instrument sensitivity may be compromised because of the uneven surface

of studied electrodes (prepared by casting nanoparticle catalysts ink on an Au disk), the consequently thicker and uneven electrolyte layer, and the strong IR absorption by the amorphous carbon support.

On-line differential electrochemical mass spectroscopy (DEMS) has been accepted as a quantitative tool for determining ethanol electro-oxidation products. In the above studies, the Pt–SnO₂ catalyst shows lower CO₂ production than that on pure Pt catalyst, which is consistent with literature reports from both on-line DEMS and in situ FTIR studies [10, 11, 24]. The CO₂ production current efficiency on pure Pt appears to be 5–10% and it is consistent with the FTIR results reported by Camara and Iwasita [2]. However, this value is considerably higher than the values determined from DEMS measurements, which are mostly in the range of 2–3% [10, 11, 24]. Moreover, the IRRAS studies show a very low production of CH₃CHO, while DEMS determines considerably higher CH₃CHO generation (average current efficiency around 37% for CH₃CHO) in a similar electrolyte. We attribute the different results from the two techniques, IRRAS and DEMS, to their different reaction environments: thin-layer cell versus flow cell. In the thin-layer configuration, CH₃CHO is more likely to be re-adsorbed on the catalyst surface and further oxidized to CO₂ or CH₃COOH, while in the flow-cell setup in DEMS studies, CH₃CHO could easily desorb from catalyst surface once it formed. Nevertheless, IRRAS could be an important quantitative complement to the DEMS technique.

3.2 In Situ ATR-SEIRAS Study of Ethanol Oxidation on a Pt Electrode

The Kretschmann configuration for in situ FTIR studies on a thin metal film has mainly been used to study CO oxidation, because of the strong enhancement in IR bands of adsorbed CO molecules. It is also used to characterize the electrooxidation of small organic molecules such as formic acid, methanol, ethanol, dimethyl ether, etc., although the results are more difficult to interpret due the complexity of these reactions on metal surfaces [94–97].

Shao et al. carried out the study of ethanol oxidation on a polycrystalline Pt film electrode using the ATR-SEIRAS technique [97]. The Pt film was deposited on the flat side of a Si hemisphere by chemical deposition. The polished Si surface was treated with 4% HF for 1 min first to remove the surface oxide, and then 2 ml of plating solution (0.01 M K₂PtCl₆+10% HF) was repeatedly dropped on the Si surface for 30 min at room temperature.

The cyclic voltammetry curve of ethanol oxidation is shown in Fig. 8a, and the in situ ATR-SEIRAS spectra recorded during EOR in the first potential sweep are shown in Fig. 8c. The bands for the linear and bridge-bonded CO at 2030–2065 and 1800–1840 cm⁻¹, respectively, are clearly observed at all potentials. In addition, another prominent band located at 1396–1410 cm⁻¹ is attributed to the symmetric OCO stretching mode (ν_s OCO) of the adsorbed acetate, as its position matches that of the spectrum in the solution of 0.1 M HClO₄+0.1 M CH₃COOH at 0.6 V (dotted line in the bottom of Fig. 8c).

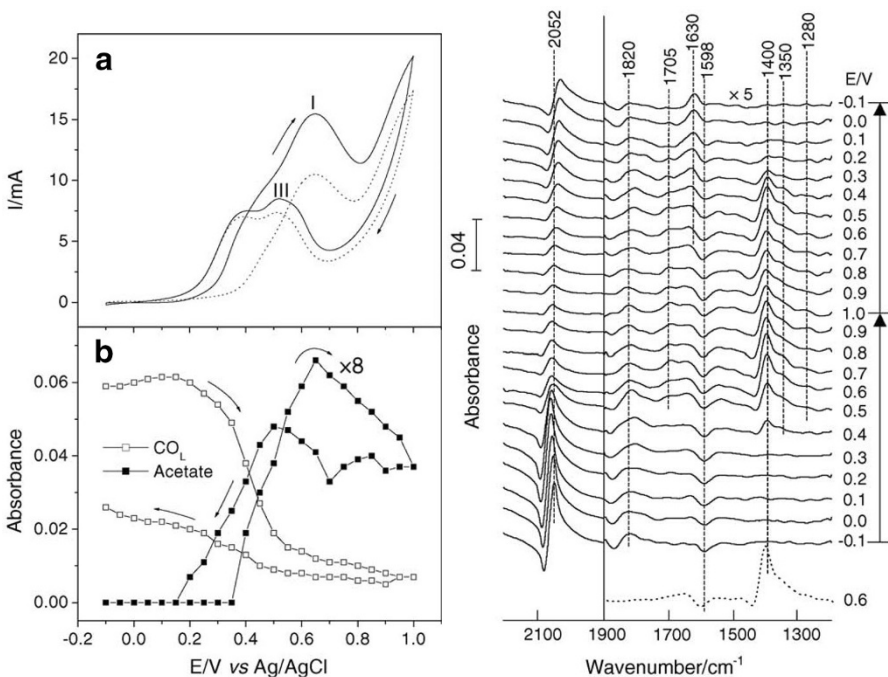


Fig. 8 **a** The first (solid line) and second (dotted line) potential sweep of the Pt electrode in 0.1 M HClO_4 + 0.1 M $\text{C}_2\text{H}_5\text{OH}$; sweep rate 5 mV s⁻¹; **b** the integrated band intensities of CO_L and adsorbed acetate taken from **c**; **c** in situ SEIRAS spectra recorded during EOR in the first potential sweep in **a**. The dotted line at the bottom is the spectrum of the Pt electrode in 0.1 M HClO_4 + 0.1 M CH_3COOH at 0.6 V normalized to the spectrum taken at -0.1 V in the same solution. Reprinted from Ref. [97] with permission from Elsevier

The bipolar shape of the linearly bonded carbon monoxide (CO_L) and its shift in frequency can be explained in terms of the Blyholder mechanism in a similar manner as in the Otto configuration, but could also be due to the optical behavior of the Pt thin film [89, 98]. The intensity changes of CO_L and $\nu_s\text{OCO}$ bands are plotted against electrode potential in Fig. 8b.

While the CO_L shows the expected potential behavior as rising at lower potentials and diminishing after 0.6 V when Pt becomes covered with oxygenating species to oxidize it to CO_2 , the intensity of the $\nu_s\text{OCO}$ band shows an interesting behavior that mimics closely the voltammogram shape up to 0.8 V. The maximum intensity of the band also matches closely to the peaks I and III in the CV. Even at high potentials, desorption of acetate is not obvious due to its strong adsorption at Pt surface. Hence, it is proposed that the bond strength of adsorbed acetate is detrimental for ethanol oxidation since the adsorbed acetate blocks Pt sites for further adsorption of ethanol.

4 In Situ XAS Study of Ethanol Oxidation

Metallic nanoparticles have gained special attention in heterogeneous catalysis, electrochemistry, and fuel cells because the catalytic phenomenon occurs mostly on the surface of the active catalyst, which is often made of one or more precious metals and their amount should be limited due to the rarity and its cost. Besides a large surface-to volume ratio necessary for active catalyst with minimal precious metals, nanoparticles have unique physical and chemical properties, which may further enhance the activity in supported metal catalysis [99]. However, their small size makes them difficult to characterize by ordinary techniques like transmission electron microscopy (TEM), XRD, or chemisorption. Instead, EXAFS became the technique of choice for the characterization because of its unique ability to: (a) elucidate the distances between atoms, (b) reveal the average particle size or particles smaller than ca. 3 nm (unlike XRD), (c) provide details on the shape of the nanoparticle (unlike chemisorption or XRD), as well as because (d) it can be used under *in situ* or *in operando* conditions (unlike TEM).

The content, and consequently the cost, of nanoparticle catalysts containing precious metals in fuel cells can be further reduced if they are mixed with non-noble metals while maintaining the electrochemical activity. Alternatively, the non-noble metal can provide the support for the active noble metal catalyst that is made in a thin shell surrounding the non-noble metal core of the nanoparticle. This type of catalyst has the lowest content of noble metals. Three types of metal–metal structures, a homogeneous solid solution (alloy) and two heterogeneous mixtures, i.e., core–shell and aggregate nanoparticles are shown in Fig. 9.

Mathematical formulas for calculation of average coordination numbers for face-centered cubic (fcc) nanoparticles of complete concentric shells (cuboctahedron and icosahedron) as well as the distribution of surface atoms of cuboctahedron and icosahedron as a function of particle size were derived [71, 100]. Fcc lattice structure is arguably the most important for catalysis not only because many catalytically important metals (Pt, Au, Rh, etc.) crystallize in it but also as a solid solution of metals of which one is the fcc metal often assumes fcc lattice [100, 101]. For metal–metal nanoparticles, it was shown that the coordination numbers and distances between metals measured by EXAFS could reveal its internal structure [101, 102]. For example, for the homogeneous solid solution of metals M_1 and M_2 where the atomic radius of M_1

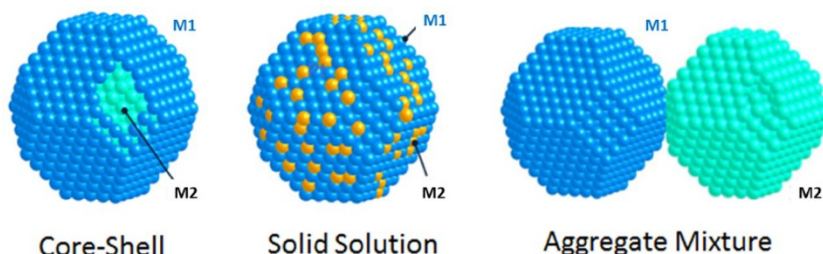


Fig. 9 Three possible structures of bimetallic particles

is larger than that of M_2 , it can be shown that: (a) the ratio of partial coordination numbers of the two metals is in direct relationship with the ratio of the mole fractions, viz. $x(M_1)/x(M_2)=N(M_2-M_1)/N(M_1-M_2)$; (b) the total coordination number of one metal must be equal to that of the other, i.e., $N(M_1-M_1)+N(M_1-M_2)$; and (c) the distances between the two metal atoms M_1-M_2 should be between that of M_1-M_1 and M_2-M_2 [102].

The relationship between coordination numbers and the interatomic distances can be also derived for the two heterogeneous mixtures in a similar manner [103, 104]. In core–shell nanoparticle, an atom of the core metal (M_{core}) is surrounded mostly with atoms of the same type, whereas the M_{shell} atom feels the presence of atoms of the same type that form the shell, as well as that of the other type of atoms forming the core; however, atoms in the shell always have lower coordination numbers. In addition, for a core–shell nanoparticle of a certain size, the total coordination number of the core atoms should be similar to the average coordination number for the nanoparticle of the same size composed of core atoms only, $N(M_{\text{core_nanoparticle}})$. Lastly, the distance between two atoms in the core should be similar to their bulk interatomic distance $R(M_{\text{core_bulk}})$, while the distance between two atoms in the shell can be either smaller or larger than bulk interatomic distance $R_{\text{shell_bulk}}$, depending on the relative sizes of the two metals comprising the core–shell particle.

Aggregate mixtures consist of two nanoparticles that are completely separated from one another, each consisting of one type of metal atoms only. Therefore, the coordination numbers N_1-N_2 and N_2-N_1 should be close to zero, and the distances between atoms of the same type should be close to that in the bulk [104].

4.1 Pt/Rh/SnO₂ Ternary Catalyst for Ethanol Oxidation

The ternary Pt–Rh–SnO₂ electrocatalyst that effectively splits the C–C bond at room temperature without production of adsorbed CO was prepared by synthesizing SnO₂ particles and absorbing them on carbon support, followed by deposition of Pt and Rh on top of the SnO₂ surface from their solutions by chemical displacement of previously deposited Pb. The diameters of the nanoclusters of SnO₂ and Pt–Rh clusters were measured by TEM and found to be larger than 10 nm and between 1 and 3 nm, respectively [23].

Operando XANES and EXAFS studies during the course of ethanol oxidation has shown only minor change in the Sn spectra collected from 0.21 to 0.91 V, i.e., between potentials at which no oxidation of ethanol is expected to that at which ethanol oxidation is in full progress. As seen in Fig. 10, EXAFS Sn K-edge spectrum showed a slight increase in intensity of the Sn–O scattering path. Electrical potential seems to have little influence on the behavior of the nonconducting SnO₂ surface, as its electrical state is controlled mostly by the solution's pH and its interaction with the environment is mediated by the “carpet” of OH groups resulted by the dissociative adsorption of water molecules [105, 106]. This effect probably shifts the onset of surface oxidation of both Rh and Pt to positive potentials, thus keeping Pt–Rh nanoparticles in zero-valent state in the potential region of practical interest for fuel cell technology ($0 < E < 0.6$ V).

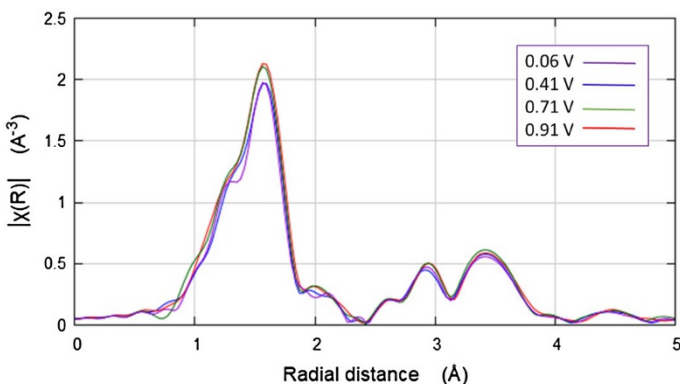


Fig. 10 EXAFS spectrum of Sn K-edge for the PtRhSnO₂/C electrocatalyst in 1 M HClO₄ solution taken in situ at various potentials during ethanol oxidation

4.1.1 EXAFS Fitting of Pt–Rh–SnO₂ Nanocatalyst

The internal structure of Pt/Rh nanoclusters were examined by in situ EXAFS. During the fit, only the amplitude reduction factors were kept constant and equal to the preceding fit of the Pt and Rh metal foils. The fitting results are shown in Fig. 11.

As shown earlier, the homogeneous solid solution is characterized with partial coordination numbers of two metals that are related to their mole fractions, equal total coordination numbers, and interatomic distances that are between their bulk values. Our EXAFS fitting gave the following results: $N(\text{Rh–Pt})/N(\text{Pt–Rh}) = 2.1 \pm 0.3$, whereas independent inductive coupled plasma (ICP) study showed similar value, $x(\text{Pt})/x(\text{Rh}) = 1.5 \pm 0.2$. The total coordination numbers obtained by concurrent fitting of Pt L₃-edge and Rh K-edge were equal within the error range, i.e., $N(\text{Pt–M}) = 9.5 \pm 0.8$ and $N(\text{Rh–M}) = 10.8 \pm 0.8$, suggesting that Pt and Rh atoms are homogeneously distributed throughout the PtRh nanoparticles. The bond lengths of Pt–Pt, Pt–Rh, and Rh–Rh found by the EXAFS analysis viz.: 2.743 ± 0.003 , 2.725 ± 0.004 , and 2.705 ± 0.005 Å, respectively, further support the above conclusion. It is expected that in the random alloy, the distances between atoms of the same type should be closer together than in pure nanoparticles (2.775 Å and 2.689 Å for Pt and Rh, respectively) [23]. Lastly, averaging the total coordination numbers for Pt–metal and Rh–metal to 10.0 ± 0.8 , the size of the nanoparticles is estimated to 2.7 ± 0.9 nm, which is in good agreement with the range found by TEM (1–3 nm) [104].

4.2 Optimizing Pt–Rh–SnO₂ Nanocatalyst

Catalytic properties of the ternary catalyst were improved by optimizing the molar fractions of the three constituents in Pt/Rh/SnO₂. As seen from part 3.1.2 above, in situ IR measurements indicated that the catalyst with the mole ratio of Pt:Rh = 1:1/3 produced the highest amount of CO₂ and the best selectivity toward

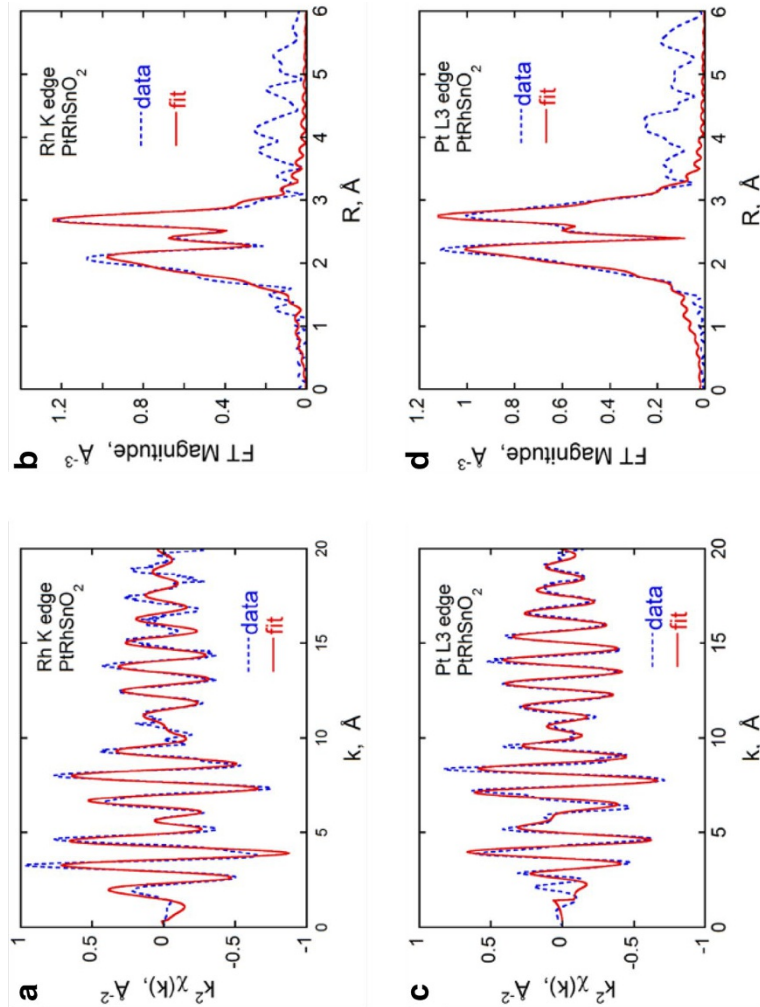


Fig. 11 Results of the first-shell fitting of the EXAFS spectra obtained during electrochemical oxidation of ethanol on the PtRhSnO₂/C electrocatalyst: **a, b** Rh K-edge; **c, d** Pt L₃ edge. The fits are presented in k -space (**a, c**), and Fourier transform magnitudes (**b, d**) for the catalyst held at 0.41 V vs. RHE. The Rh K-edge and Pt L₃-edge data were fitted concurrently to the theoretical signals while applying physically reasonable constraints. Reprinted from Ref. [23] with permission from Springer Nature

the total oxidation pathway of ethanol. This was ascribed to the electron donation from Rh to Pt through which the *d*-band states of both metals were changed so that the intermediates produced by splitting of C–C bond in ethanol become more mobile and able to reach oxygen-containing species covering the SnO₂ sites at the surface of the ternary catalyst and further oxidized to CO₂ [11].

To find the optimal SnO₂ sites, the mole fraction of Sn was varied while the Pt:Rh ratio was kept fixed to 3:1 [107]. Two carbon-supported catalysts with stoichiometric atomic ratio of Pt₂₁Rh₅Sn₃₉ and Pt₂₃Rh₅Sn₂₆ were obtained by simultaneous codeposition of all three metals from their soluble chlorides, followed by reduction in ethylene glycol and heating in air to oxidize Sn to SnO₂. The synthesized PtRh particles had an average size of 1.5 nm with a narrow distribution [84]. Their electrochemical activity was compared to the commercially available Pt/C and PtRu/C. When normalized to the total noble metal loading, the ethanol oxidation current densities of the two ternary catalysts are significantly higher and their oxidation onsets are shifted to lower potentials than those of the commercial ones (Fig. 12). The comparison of the two ternary catalysts reveals that the one with the lower Sn content shows higher activity and lower onset of ethanol oxidation. Subsequent chronoamperometric tests also showed that the catalyst with reduced Sn mole fraction has better stability. Because the two catalysts have roughly the same Pt:Rh ratio, the difference in their activity is ascribed to the variance in the content of SnO₂ [107].

As described before, besides the supply of oxygen-containing species, the role of SnO₂ is to keep Pt and Rh in metallic form. Figure 13 shows the *in situ* XANES spectra for Pt L₃-edge and Rh K-edge of the two catalysts at potentials ranging from 0.06 to 0.91 V. As seen in Fig. 13a, the spectra obtained from Pt₂₃Rh₅Sn₂₆/C at Pt edge at the three most negative potentials (0.06, 0.21, and 0.41 V) overlap and their shape is close to that of Pt foil. The changes in Pt XANES spectra are observed at potentials equal to or more positive than 0.71 V, but only in the intensity of the white line; however, no obvious shift in the edge energy (E_0) is seen. On the other hand, the changes in Rh XANES spectra are readily observed above 0.41 V, as white line increases and edge position shifts to the higher energies (Fig. 13c). A close observation of Fig. 13c further reveals isosbestic points at 23,256 and 23,300 eV, suggesting that Rh exists in two different chemical forms having the same total concentration. Thus, all Rh K-edge spectra can be reproduced with a linear combination of two XANES spectra, one of metallic Rh at 0.06 V, and the other of oxidized Rh at 0.91 V. During the potential excursion, Rh changes its oxidation state directly from Rh⁰ to Rh^{*n*+} (*n* is probably 3), without passing through lower oxidation states.

Figure 13b, d show the Pt L₃-edge and Rh K-edge XANES spectral region for the Pt₂₁Rh₅Sn₃₉/C catalyst obtained *in situ* at potentials ranging from 0.06 to 0.91 V. Like the behavior of the Pt₂₃Rh₅Sn₂₆/C catalyst, the changes in the intensity of the Pt white line (Fig. 13b) are noticed above 0.41 V. In contrast, the Rh K-edge (Fig. 13d) shows an abrupt oxidation that commences on or before 0.21 V, as observed from the increase of white line as well as the shift of the edge position to higher photon energies. It is interesting to note that the Pt white line for both catalysts is lower than that of the Pt foil at potentials below 0.41 V (cf. Figure 13a, b), whereas that of Rh foil is always lower than that of the catalysts (Fig. 13c, d). Since the white line of Rh K-edge represents the transition of an electron from 1s orbital to hybridized 5p and

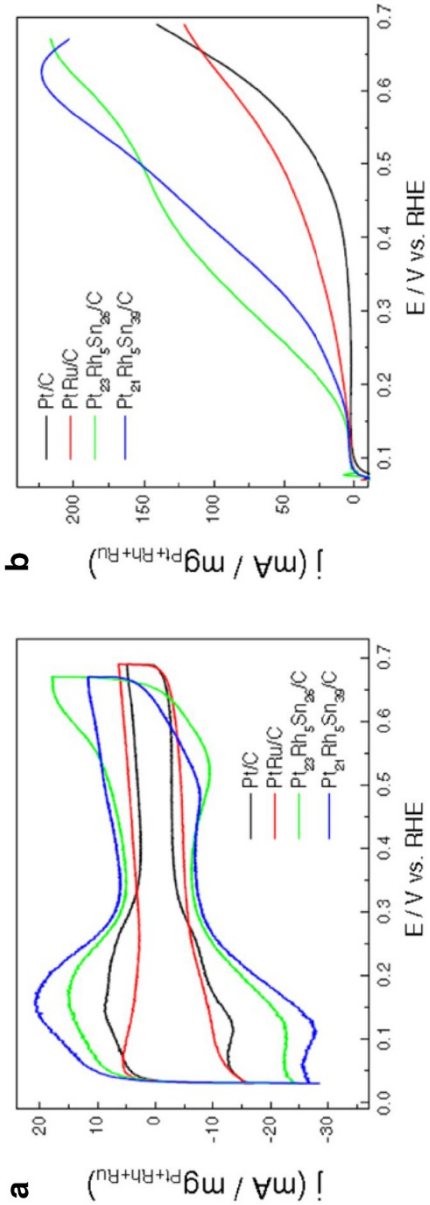


Fig. 12 Electrochemical measurements in 0.1 M HClO_4 (**a**), and anodic polarization curves in 0.5 M ethanol + 0.1 M HClO_4 (**b**) of commercial Pt/C, PtRu/C, $\text{Pt}_{23}\text{Rh}_5\text{Sn}_{26}/\text{C}$, and $\text{Pt}_{21}\text{Rh}_5\text{Sn}_{39}/\text{C}$; scan rate 10 mV/s; scan rate 10 mV/s. Reprinted from Ref. [107] with permission from Springer Nature

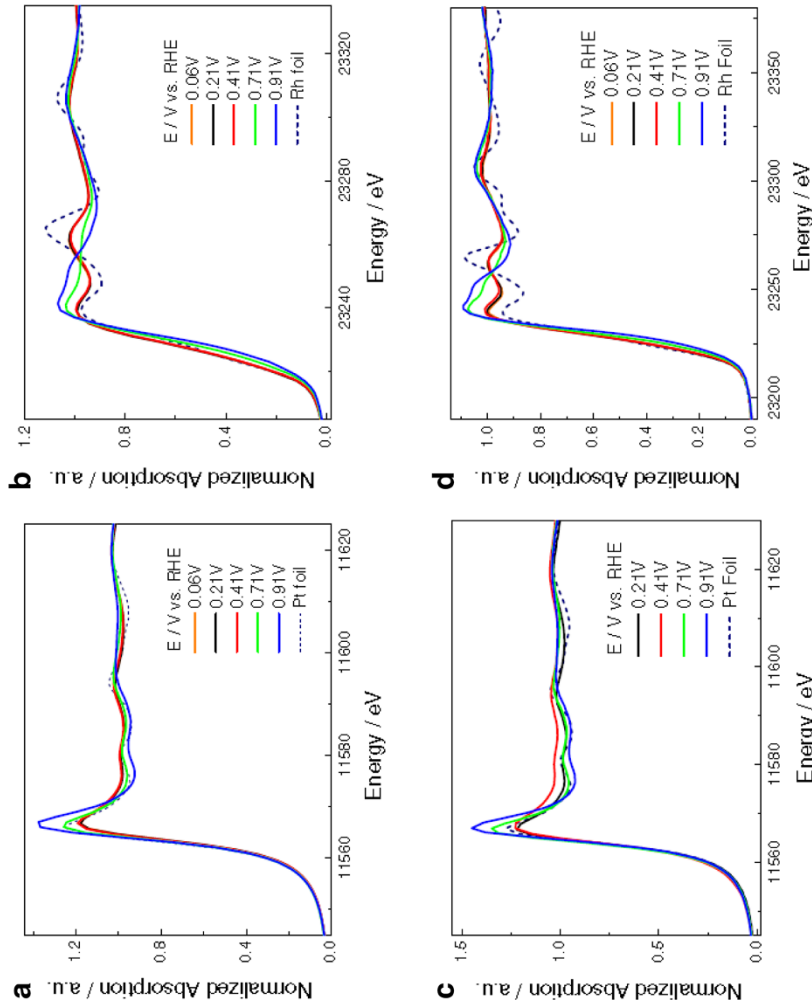


Fig. 13 In situ XANES spectra of $\text{Pt}_{23}\text{Rh}_5\text{Sn}_{39}/\text{C}$ catalyst (**a**, **b**) and $\text{Pt}_{21}\text{Rh}_5\text{Sn}_{39}/\text{C}$ catalyst (**c** and **d**) in 1 M HClO_4 ; **a**, **c** Pt L₃-edge; **b**, **d** Rh K-edge. Reprinted from Ref. [107] with permission from Springer Nature

4d orbitals, the up-shifted white line in the samples suggests a less filled *d*-band of Rh. Concurrently, the lower white line for Pt suggests more populated *d*-band. Both effects have been observed before in PtRh random alloys and are in line with our DFT calculations that predicted the electron transfer from Rh to Pt [23, 86].

Relative changes in white-line peaks of Pt L₃ and Rh K-edges of the two ternary catalysts as a function of applied potential are shown in Fig. 14. As seen, the intensity of the white line of Pt shows no effect on potential excursions to 0.41 V in either catalyst (Fig. 14a). Further increase of the potential affects the white lines of both catalysts, but the one with higher Sn content shows more abrupt change [31, 107]. On the other hand, while the white line of Rh in the catalyst with lower Sn content is unaffected by the potential excursion up to 0.41 V, that of Pt₂₁Rh₅Sn₃₉/C starts to change as early as 0.21 V and continues to increase with a steeper slope over the whole potential excursion (Fig. 14b).

It appears that a too high content of SnO₂ at the catalyst's surface can be detrimental for the catalyst's activity. The excess of oxygen-containing species uninvolved in oxidation of alcohols are spilled over from SnO₂ to Pt and Rh, blocking Pt sites for adsorption of ethanol and Rh sites for adsorption of the intermediate CH₂CH₂O*. In addition, the high content of SnO₂ in the Pt₂₁Rh₅Sn₃₉/C ternary catalyst affects the Rh oxidation, which is evident at Rh XANES spectra obtained during the potential excursion from 0.06 to 0.91 V.

Figure 15 shows the first-shell fitting results of the Pt–Rh–SnO₂/C electrocatalyst with Pt:Rh:Sn = 3:1:4 atomic ratio at the potential of 0.41 V where all parameters except the passive electron reduction factors (S_0^2) for the two metals were allowed to vary with no constraints. The fitting results are summarized in Table 2. As expected, the coordination numbers and bond lengths clearly show that the Pt and Rh form random alloy, as the ratio of their partial coordination numbers are consistent with mole fraction ratio obtained by ICP (Pt/Rh = 3.0), the total coordination numbers are close together, and the bond lengths are between those of the bulk values. Finally, the nanoparticle size can be estimated from the total coordination numbers of the two metals. Taking the average total coordination number $N(\text{Pt}–\text{M})=N(\text{Rh}–\text{M})=6.9$, the particle size is estimated to be 1.4 nm, which is in good agreement with the HR-STEM data.

4.3 Ir as an Alternative to Rh

Despite the superior activity of Pt–Rh–SnO₂ catalyst, further work was aimed to substitute the noble metals with cheaper and possibly more abundant metals so that the electrocatalyst can be used in mass production of portable fuel cells. While Pt cannot be replaced due to the unprecedented oxidative adsorption of ethanol, lower content of Rh in catalysts would significantly reduce the total cost as the current price of Rh is higher than that of Pt. Iridium and rhodium are in the same group of the periodic system and are expected to share adsorptive and catalytic properties. Regardless of the low abundance of Ir, it is considerably cheaper than Pt and Rh. Although Ir was studied as an EOR catalyst earlier, its capability in splitting the C–C bond was not investigated [108–110].

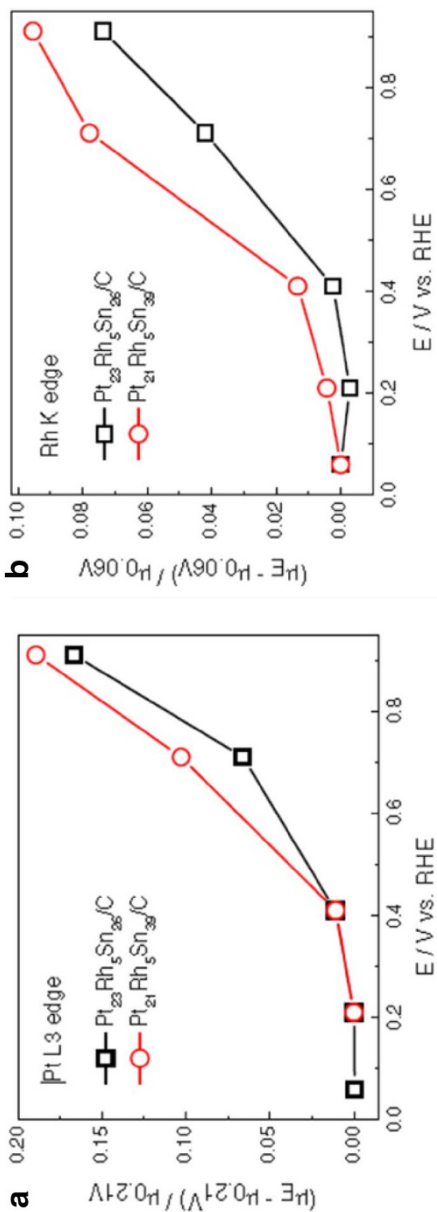


Fig. 14 Comparison of the change in absorption peaks at Pt L₃ edge (a) and at Rh K-edge (b) for two Pt-Rh-SnO₂/C electrocatalysts with different stoichiometry, plotted as a function of applied potentials. Reprinted from Ref. [107] with permission from Springer Nature

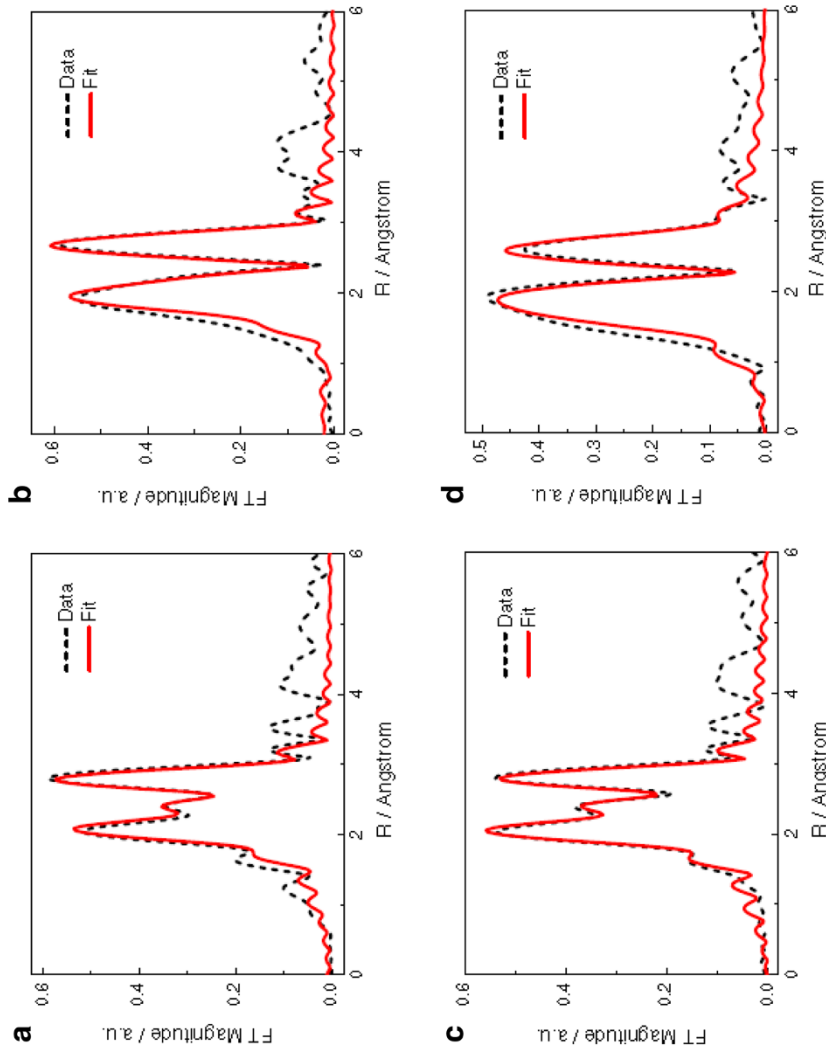


Fig. 15 Fourier transform magnitudes of Pt L₃ edge (**a**, **c**) and Rh K-edge (**b**, **d**) of two electrocatalysts with different Sn content held at 0.41 V in 1 M HClO₄ and the respective first-shell fits; Pt₂Rh₃Sn₂₆/C electrocatalyst (**a**, **b**) and Pt₂Rh₃Sn₃₉/C (**c**, **d**). See text for the fitting parameters. Reprinted from Ref. [107] with permission from Springer Nature

Table 2 Bond lengths and coordination numbers of Pt and Rh metals in the Pt–Rh–SnO₂/C catalyst held at 0.41 V in 1 M HClO₄ obtained by the first-shell fitting and comparison to those of bulk metals (from Ref. [84])

| | Bond length (Å) | Coordination number |
|-----------|-----------------|---------------------|
| Pt (bulk) | 2.775 | 12 |
| Rh (bulk) | 2.689 | 12 |
| Pt–Pt | 2.740 ± 0.004 | 5.1 ± 0.9 |
| Rh–Rh | 2.683 ± 0.006 | 1.9 ± 0.9 |
| Pt–Rh | 2.715 ± 0.004 | 1.7 ± 0.9 |
| Rh–Pt | 2.715 ± 0.004 | 5.1 ± 1.0 |

Our studies on several Pt–Ir–SnO₂ catalysts indicated that Ir could split the C–C bond in ethanol [31]. While it was difficult to obtain the internal structure of the nanoparticles with Ir and Pt due to the close proximity of their L₃ edges, the XANES spectra can be used to reveal the mole ratio of the two metals. In our study of the catalyst with Pt:Ir:Sn = 1:1:1 atomic ratio, we found that the edge step ($\Delta\mu_0$, cf. Fig. 2) of Ir L₃ and Pt L₃ are approximately equal (both ca. 0.5). Because their absorption intensities are close, the Pt/Ir ratio is approximately 1, which is consistent with the nominal value [111].

Furthermore, XANES spectra showed that Ir were in oxidized state even at the lowest potentials. As seen in Fig. 16, both Ir and Pt spectra show a dependence of the white lines on potential, indicating oxidation of both metals with the potential

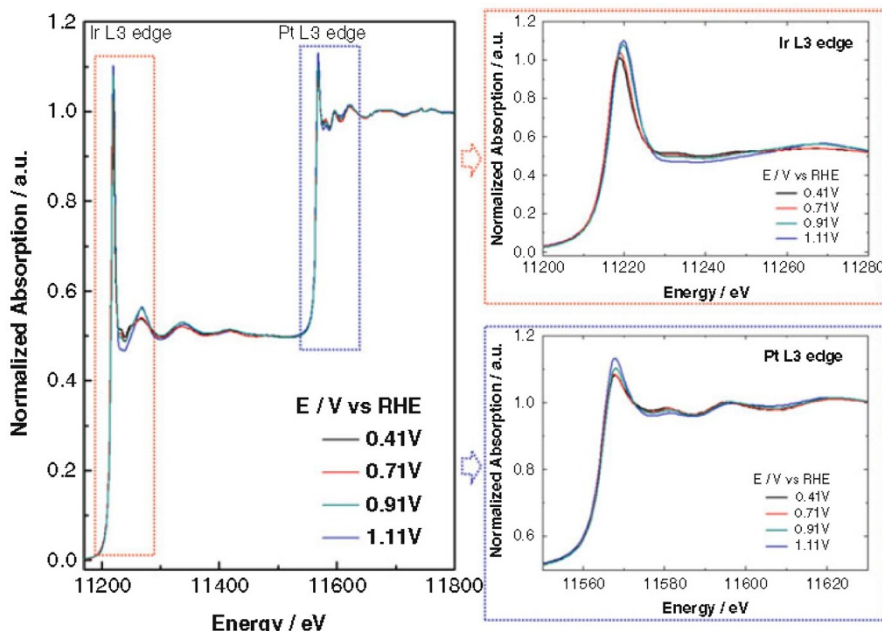


Fig. 16 In situ XANES spectra of Pt L₃ and Ir L₃ edges of PtIr/SnO₂/C electrocatalyst under different applied potentials. Reprinted from Ref. [31] with permission from American Chemical Society

increase. In a series of Pt/Ir/Rh/Sn catalysts, the highest activity for ethanol oxidation showed the ternary catalyst having $\text{Pt:Ir:Sn} = 1:1:1$ atomic ratio. Of the catalysts containing both Rh and Ir, the highest CO_2 production was found for the catalyst with atomic ratio $\text{Pt:Ir:Rh:Sn} = 1:1:1:1$. Nevertheless, even the best catalyst containing Ir was inferior in comparison to the optimized Pt–Rh– SnO_2 /C. We ascribe this phenomenon to the inability of SnO_2 to keep the Ir and Pt in metallic state, unlike its behavior in Pt–Rh– SnO_2 catalysts [31].

5 Platinum Monolayer Electrocatalysts for Ethanol Oxidation

Adzic et al. developed a new approach for designing and synthesizing electrocatalysts that can dramatically reduce the required Pt content, while affording possibilities to enhance their catalytic performance [112]. These electrocatalysts consist of a monolayer (one atom thick) of Pt on extended or supported nanoparticle metal or metal-alloy surfaces. The Pt-monolayer (Pt_{ML}) approach has several attractive features: (a) Close to complete Pt utilization since all Pt atoms are present on the surface and participate in catalytic reactions; (b) Tailored electrocatalytic properties consequent upon the combined geometric effect (substrate-induced strain) and ligand effect (the electronic interaction between Pt_{ML} and the substrate); (c) enhanced stability because of the decreased oxidation of the Pt_{ML} resulting from the interaction with the suitable substrate; (d) direct activity correlations between catalytic and physical properties of the Pt_{ML} as all Pt atoms involved in the reaction are sampled by the measuring technique [112].

Such Pt_{ML} electrocatalysts can be synthesized by depositing a Pt monolayer on different substrates via the galvanic displacement of an underpotentially deposited (UPD) Cu monolayer (Fig. 17). Scanning tunneling microscopy (STM) study of the resulting $\text{Pt}_{\text{ML}}/\text{Ru}(1010)$ surface revealed that Pt was deposited as a small three-dimensional (3D) island on Ru [113]. In some other Pt–M binary systems, for instance, Pt on Pd, a pseudomorphic monolayer of Pt was formed by the displacement of a Cu UPD layer [112]. EXAFS data on monolayer of Pt (Pt_{ML}) deposited on Pd revealed that the structure is indeed pseudomorphic, as the coordination numbers $N(\text{Pt–Pt})$ and $N(\text{Pt–Pd})$ were 5.8 ± 0.8 and 2.7 ± 0.7 , respectively. These coordination numbers are close to that expected on a flat Pt_{ML} on Pd(111), as an atom of Pt at the surface of (111) structure has six Pt nearest neighbors in the plane of the monolayer, and three Pd nearest neighbors below the surface. On a curved surface as in nanoparticles, those coordination numbers may differ slightly due to the presence of edges and vertices [79].

The Pt_{ML} electrocatalysts were systematically studied for the electrooxidation of methanol and ethanol. Pt_{ML} was deposited on different substrates via the galvanic displacement of a Cu UPD monolayer employing five single-crystal surfaces [$\text{Au}(111)$, $\text{Pd}(111)$, $\text{Ir}(111)$, $\text{Rh}(111)$, and $\text{Ru}(0001)$] as substrates. Because of the larger lattice, Au exerts on Pt a tensile strain in $\text{Pt}_{\text{ML}}/\text{Au}(111)$; in other $\text{Pt}_{\text{ML}}/\text{M}(111)$ surfaces ($\text{M} = \text{Pd, Ir, Rh, and Ru}$) Pt is under compressive strain as the metals have smaller lattice constants. Interestingly, a significant enhancement in the catalytic activity associated with the tensile strain, and decreased activity associates

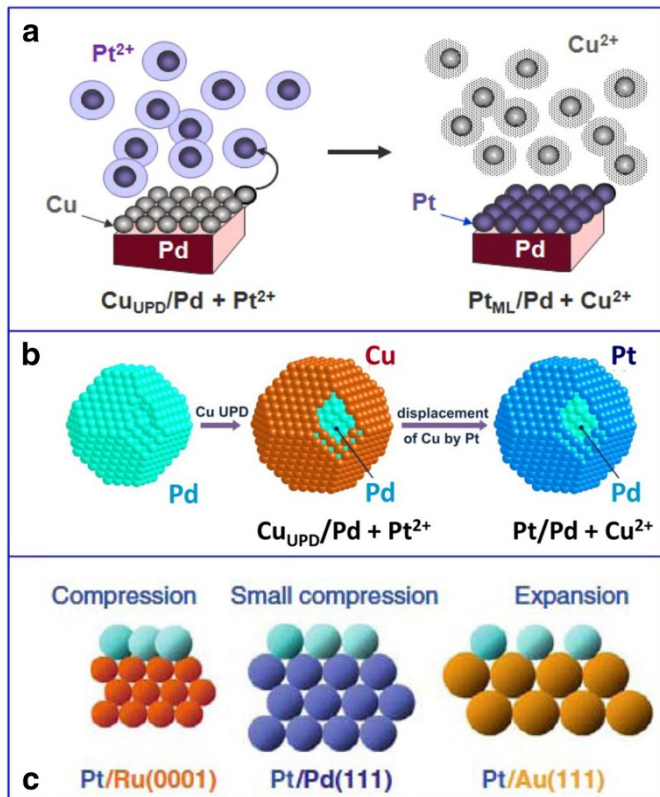


Fig. 17 Pt_{ML} deposition by galvanic displacement of a Cu UPD adlayer on the substrates of bulk Pd electrode (a) and Pd nanoparticle (b). Models of pseudomorphic monolayers of Pt on three different substrates (c) inducing compressive strain (Ru(0001) and Pd(111)) and expansive strain (Au(111)). Reprinted from Ref. [99] with permission from Springer

with the compressive strain is observed in both methanol and ethanol oxidation reactions (MOR and EOR). During the methanol oxidation (Fig. 18a), the Pt_{ML}/Au(111) exhibited a negatively shifted potential at the onset of the reaction, and over sevenfold enhancement in peak current density with respect to Pt(111) (the most active low-index plane of Pt). Similarly, during the ethanol oxidation (Fig. 18b), the stretched Pt_{ML} supported on Au(111) demonstrates slightly negatively shifted reaction-onset potential and over fourfold increase in peak current density. Along with more electrochemical studies, a trend is observable indicating that increased lattice compression lowers reactivity.

In situ infrared reflection absorption spectroscopy (IRRAS) study was carried out to identify the reaction intermediates and products during methanol and ethanol oxidation on Pt_{ML}/Au(111), as well as to gain insights into the substrate-induced change in the selectivity of Pt_{ML} and the mechanism of the greatly enhanced reaction kinetics.

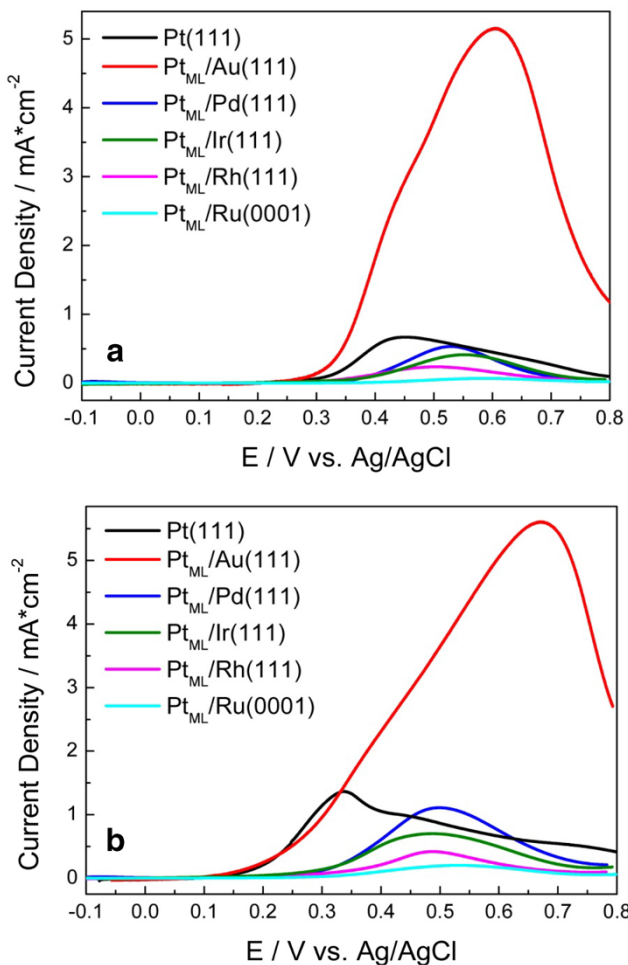


Fig. 18 Positive voltammetric scans for Pt(111) and Pt_{ML} supported on five different substrates [Au(111), Pd(111), Ir(111), Rh(111), and Ru(0001)] in 0.1 M HClO₄ containing 0.5 M methanol (**a**), or 0.5 M ethanol (**b**) with scan rate 10 mV/s. Reprinted from Ref. [32] with permission from American Chemical Society

In situ IRRAS spectra recorded on Pt_{ML}/Au(111) during MOR (Fig. 19a) indicate that methanol oxidation proceeds without formation of adsorbed CO, as observed by the lack of characteristic bipolar, potential dependent peak at ca. 2100 cm⁻¹; namely, the enhanced MOR activity in Pt_{ML}/Au(111) is due to the formation of COH_{ads} instead of the poisoning CO_{ads} species. On the other hand, in situ IRRAS spectra obtained during ethanol oxidation (Fig. 19b) show a complete absence of both the CO_{ads} and CO₂ bands, denoting that ethanol dissociative adsorption on Pt_{ML}/Au(111) does not occur, i.e., the EOR follows the partial oxidation pathway without cleavage of the C–C bond. Therefore, the high EOR activity on Pt_{ML}/Au(111) is a consequence of faster kinetics of partial oxidation

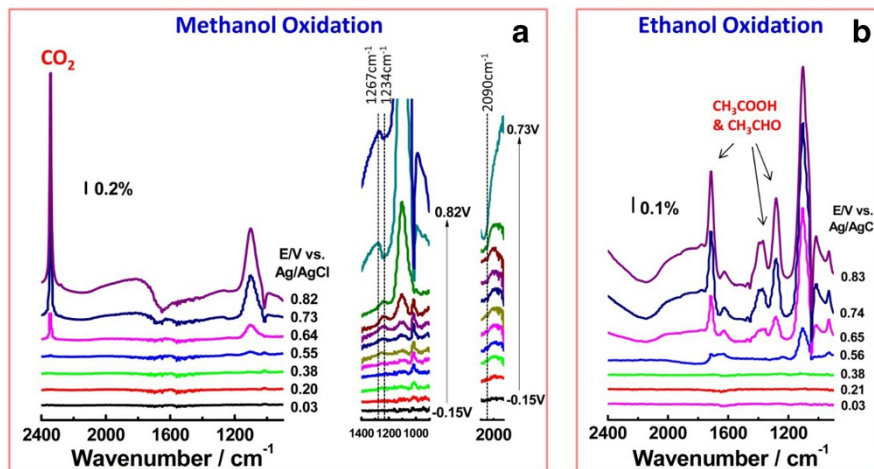


Fig. 19 In situ IRRAS spectra for identifying the intermediates and products of methanol and ethanol electrooxidation on $\text{Pt}_{\text{ML}}/\text{Au}(111)$. In situ IRRAS spectra recorded during MOR (**a**) and EOR (**b**) on the $\text{Pt}_{\text{ML}}/\text{Au}(111)$ electrode in 0.1 M HClO_4 containing 0.5 M methanol or 0.5 M ethanol. A total of 128 interferograms (resolution 8 cm^{-1}) were co-added to each spectrum. Reprinted from Ref. [32] with permission from American Chemical Society

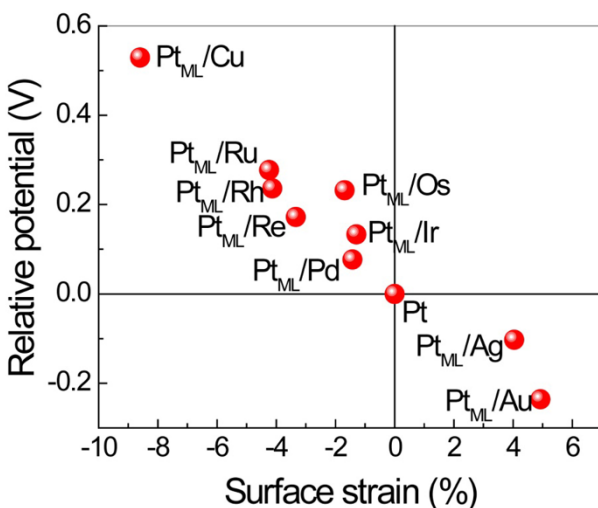


Fig. 20 DFT investigations of methanol oxidation on Pt_{ML} supported on different substrates. The DFT-calculated variation of the lowest potential to proceed methanol electrooxidation on the Pt_{ML} supported on Cu(111), Ru(0001), Rh(111), Re(001), Pd(111), Os(001), Ir(111), Ag(111), Au(111) surfaces with the surface strain. The surface stain was calculated by $[d(\text{Pt}_{\text{ML,surf}}) - d(\text{Pt})]/d(\text{Pt})$, where d is Pt–Pt bond length. The potential and surface strain were expressed with respect to the case of Pt(111). Reprinted from Ref. [32] with permission from American Chemical Society

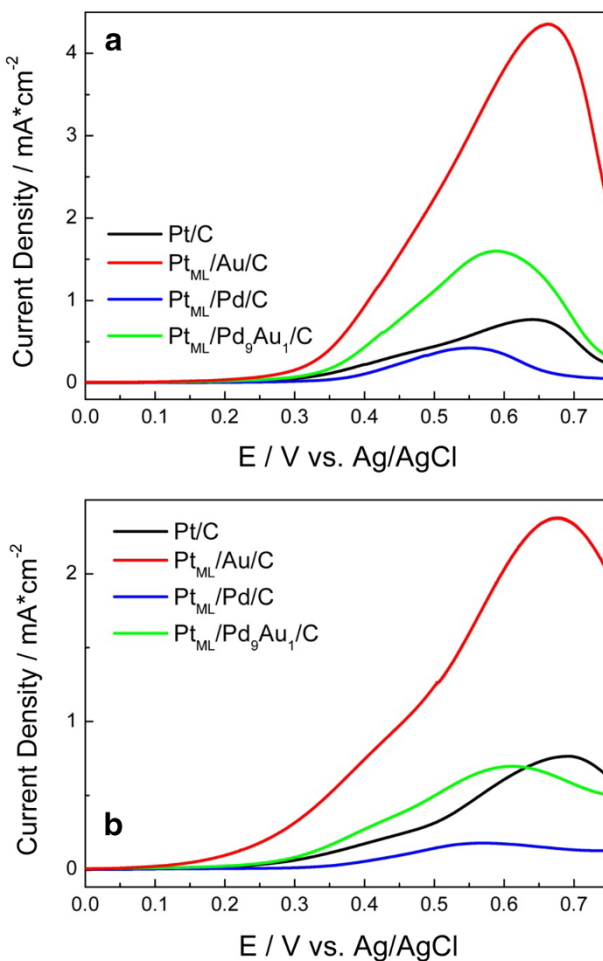


Fig. 21 Positive voltammetric scans for Pt/C and Pt_{ML} supported on different nanoparticle substrates in 0.1 M HClO₄ containing 0.5 M methanol (**a**) or 0.5 M ethanol (**b**) with scan rate 10 mV/s. Reprinted from Ref. [32] with permission from American Chemical Society

pathway that generates acetic acid and acetaldehyde. The complete oxidation of ethanol requires full dehydrogenation and C–C bond splitting, which might not be favored on a stretched Pt_{ML}.

DFT calculations were carried out to gain a better understanding of the methanol electrooxidation on the surfaces of Pt_{ML} supported on different substrates. The onset potential for methanol electrooxidation on the Pt_{ML}/metal surfaces was estimated by calculating the binding energies and free energies of CO and OH (Fig. 20). The DFT-predicted trend in reactivity, viz.: Pt_{ML}/Au(111) > Pt(111) > Pt_{ML}/Pd(111) > Pt_{ML}/Ir(111) > Pt_{ML}/Rh(111) > Pt_{ML}/Ru(0001), agrees well with the experimental data shown in Fig. 19. The activity

of Pt_{ML}/Au(111) is ascribed to Pt_{ML} that is stretched by over 4%. Such monolayer enhances dehydrogenative adsorption of alcohol molecules (Pt–CO) and the dissociation of water (Pt–OH formation). That is, the strain effect due to the Au support results in a Pt_{ML} that is able to bind the adsorbates strongly enough to activate methanol and carry on the reaction to the formation of CO₂, yet weakly enough to prevent CO poisoning [25].

Several Pt_{ML} nanocatalysts comprising Pt_{ML} supported on mono- or bi-metallic nanoparticle cores were studied (Fig. 21), and the activity for both methanol and ethanol electrooxidation reactions increased in the order of Pt_{ML}/Pd/C < Pt/C < Pt_{ML}/Au/C. Hence, a qualitatively similar trend is observed as with single-crystal surfaces, viz., activity of dilated Pt_{ML} is enhanced while that of compressed Pt_{ML} is decreased. Pt_{ML} supported on Pd–Au bimetallic alloy nanoparticles demonstrated an activity in between of Pt_{ML}/Pd/C and Pt_{ML}/Au/C, which suggests further that a tunable activity can be obtained from Pt_{ML} by manipulating its lateral strain [32].

6 Conclusions

Despite the renewed interest in ethanol oxidation reaction, there is still a long way to go before an active, cost-effective catalyst is found for the large-scale adaptation in direct ethanol fuel cells. At present, the best catalysts in acidic solution contain a certain amount of noble metals. Particularly, the best catalyst that leads to preferential production of CO₂ as the main product contains nanoparticles of Pt/Rh solid solution, where the role of the latter metal is to break the C–C bond of ethanol. However, Rh is several times more expensive than Pt, so reducing the amount of noble metals and/or replacing them with cheaper alternatives is the major challenge. Another possible pathway is through a design of core–shell nanoparticles with the active catalyst in a form of a monolayer deposited on an inexpensive and abundant core. The size, shape, and structure of nanoparticle supports can affect the reactivity, selectivity, and stability of the active monolayer in a complex way, where lateral strain of the monolayer may be an important factor. However, with advanced synthetic nanotechnology methods designing suitable, low-cost nanoparticle supports with enhancing properties is quite feasible.

Acknowledgements This research was performed at Brookhaven National Laboratory under contract DE-SC0012704 with the US Department of Energy, Office of Basic Energy Science, Material Science and Engineering Division, Division of Chemical Sciences, Geosciences and Biosciences Division. X-ray absorption studies were conducted on National Synchrotron Light Source (NSLS) at Brookhaven National Laboratory, in Upton, NY, and Stanford Synchrotron Light Source (SSRL) at SLAC National Accelerator Laboratory in Stanford, CA. The authors are indebted to the beamline staff Sayed Khalid (NSLS) and Matthew Latimer (SSRL) for their help. Beamlines X18a, X18b, and X19A at the NSLS, as well as BL 2–2 at the SSRL were supported in part by the Synchrotron Catalysis Consortium, U.S. Department of Energy Grant no. DE-SC0012335.

References

- Lamy C, Coutanceau C, Leger J-M (2009) The direct ethanol fuel cell: a challenge to convert bioethanol cleanly into electric energy. In: Barbaro P, Bianchini C (eds) *Catalysis for sustainable energy production*. WILEY-VCH Verlag GmbH & Co. KGaA, Weinheim
- Camara GA, Iwasita T (2005) Parallel pathways of ethanol oxidation: the effect of ethanol concentration. *J Electroanal Chem* 578:315–321
- Wang Y, Zou S, Cai W-B (2015) Recent advances on electro-oxidation of ethanol on Pt- and Pd-based catalysts: from reaction mechanisms to catalytic materials. *Catalysis* 5:1507–1534
- Kamarudin MZF, Kamarudin SK, Masdar MS, Daud WRW (2013) Review: direct ethanol fuel cells. *Int J Hydrog Energy* 38:9438–9453
- Lamy C, Rousseau S, Belgsir EM, Coutanceau C, Léger JM (2004) Recent progress in the direct ethanol fuel cell: development of new platinum–tin electrocatalysts. *Electrochim Acta* 49:3901–3908
- Rousseau S, Coutanceau C, Lamy C, Léger JM (2006) Direct ethanol fuel cell (DEFC): electrical performances and reaction products distribution under operating conditions with different platinum-based anodes. *J Power Sources* 158:18
- Iwasita T, Pastor E (1994) A DEMS and FTIR spectroscopic investigation of adsorbed ethanol on polycrystalline platinum. *Electrochim Acta* 39:531
- Lai SCS, Kleyn SEF, Rosca V, Koper MTM (2008) Mechanism of the dissociation and electrooxidation of ethanol and acetaldehyde on platinum as studied by SERS. *J Phys Chem C* 112:19080
- Wang H, Jusus Z, Behm RJ (2004) Ethanol electrooxidation on a carbon-supported Pt catalyst: reaction kinetics and product yields. *J Phys Chem B* 108:19413
- Wang Q, Sun GQ, Jiang LH, Xi NQ, Sun SG, Jiang YX, Chen SP, Jusys Z, Behm RJ (2007) Adsorption and oxidation of ethanol on colloid-based Pt/C, PtRu/C and Pt₃Sn/C catalysts: in situ FTIR spectroscopy and on-line DEMS studies. *Phys Chem Chem Phys* 9:2686–2696
- de Souza JPI, Queiroz SL, Bergamaski K, Gonzalez ER, Nart FC (2002) Electro-oxidation of ethanol on Pt, Rh, and PtRh electrodes. A study using DEMS and in-situ FTIR techniques. *J Phys Chem B* 106:9825–9830
- Antolini E (2007) Catalysts for direct ethanol fuel cells. *J Power Sources* 170:1–12
- Del Colle V, Berna A, Tremiliosi-Filho G, Herrero E, Feliu JM (2008) Ethanol electrooxidation onto stepped surfaces modified by Ru deposition: electrochemical and spectroscopic studies. *Phys Chem Chem Phys* 10:3766–3773
- Vigier F, Rousseau S, Coutanceau C, Leger J-M, Lamy C (2006) Electrocatalysis for the direct alcohol fuel cell. *Top Catal* 40:111–121
- Song SQ, Zhou WJ, Zhou ZH, Jiang LH, Sun GQ, Tsiakaras P, Xin Q, Leonditis V, Kontou S, Tsiakaras P (2005) Direct ethanol PEM fuel cells: the case of platinum based anodes. *Int J Hydrog Energy* 30:995–1001
- Jiang L, Colmenares L, Jusys Z, Sun GQ, Behm RJ (2007) Ethanol electrooxidation on novel carbon supported Pt/SnO_x/C catalysts with varied Pt:Sn ratio. *Electrochim Acta* 53:377–389
- Casado-Rivera E, Volpe DJ, Alden L, Lind C, Downie C, Vazquez-Alvarez T, Angelo ACD, DiSalvo FJ, Abruna HD (2003) Electrocatalytic activity of ordered intermetallic phases for fuel cell applications. *J Am Chem Soc* 126:4043–4049
- Petkovic LM, Rashkeev SN, Ginosar DM (2009) Ethanol oxidation on metal oxide supported platinum catalysts. *Catal Today* 147:107–114
- Watanabe M, Motoo S (1975) Electrocatalysis by ad-atoms: part II. Enhancement of the oxidation of methanol on platinum by ruthenium ad-atoms. *J Electroanal Chem* 60:267–273
- Van Veen JAR, Frelink T, Visscher W (1995) On the role of Ru and Sn as promoters of methanol electro-oxidation over Pt. *Surf Sci* 335:353–360
- Wang H, Jusys Z, Behm RJ (2006) Ethanol electro-oxidation on carbon-supported Pt, PtRu and Pt₃Sn/C catalysts: a quantitative study. *J Power Sources* 154:351–359
- Demirci UB (2007) Theoretical means for searching bimetallic alloys as anode electrocatalysts for direct liquid-feed fuel cells. *J Power Sources* 173:11
- Kowal A, Li M, Shao M, Sasaki K, Vukmirovic MB, Zhang J, Marinkovic NS, Liu P, Frenkel AI, Adzic RR (2009) Ternary Pt/Rh/SnO₂ electrocatalysts for oxidizing ethanol to CO₂. *Nat Mater* 8:325–330

24. Idriss H (2004) Ethanol reaction over the surfaces of noble metal/cerium oxide catalysts. *Platin Met Rev* 48:105–115
25. Haryanto A, Fernando S, Murali N, Adhikari S (2005) Current status of hydrogen production techniques by steam reforming of ethanol: a review. *Energy Fuels* 19:2098–2106
26. Erini N, Loukrakpam R, Petkov V, Baranova AL, Yang R, Teschner D, Huang Y, Brankovic SR, Straser P (2014) Ethanol electro-oxidation on ternary platinum–rhodium–tin nanocatalysts: insights in the atomic 3D structure of the active catalytic phase. *ACS Catal* 4:1859–1867
27. Bai J, Xiao X, Xue YY, Jiang JX, Zeng JH, Li XF, Chen Y (2018) Bimetallic platinum–rhodium alloy nanodendrites as highly active electrocatalyst for the ethanol oxidation reaction. *ACS Appl Mater Interfaces* 10(23):19755–19763
28. Lopez-Suarez FE, Perez-Cadenas M, Bueno-Lopez A, Carvalho-Filho CT, Eguiluz KIB, Salazar-Banda GR (2015) Platinum–rhodium–tin/carbon electrocatalysts for ethanol oxidation in acid media: effect of the precursor addition order and the amount of tin. *J Appl Electrochem* 45(10):1057–1068
29. Delpuech AB, Asset T, Chatenet M, Cremers C (2014) Electrooxidation of ethanol at room temperature on carbon-supported Pt and Rh-containing catalysts: a DEMS study. *J Electrochem Soc* 161:F918–F924
30. Cantane DA, Ambrosio WF, Chatenet M, Lima FHB (2012) Electro-oxidation of ethanol on Pt/C, Rh/C, and Pt/Rh/C-based electrocatalysts investigated by on-line DEMS. *J Electroanal Chem* 681:56–65
31. Li M, Cullen D, Sasaki K, Marinkovic NS, More K, Adzic RR (2013) Ternary electrocatalysts for oxidizing ethanol to carbon dioxide: making Ir capable of splitting C–C bond. *J Am Chem Soc* 135:132–141
32. Li M, Liu P, Adzic RR (2012) Pt monolayer electrocatalysts for oxidation of alcohol molecules. *J Phys Chem Lett* 3:3480–3485
33. Harrick NJ (1967) Internal reflection spectroscopy. Wiley, New York, pp 1–327
34. Bewick A (1986) A molecular structure and orientation in the electrode/electrolyte solution interface—in situ IR spectroscopy. In: Fernando Silva A (ed) Trends in interfacial electrochemistry, vol 179. Springer, Amsterdam, pp 331–358
35. Antonio Berna A, Rodes A, Feliu JM (2007) In-situ FTIR studies on the acid–base equilibria of adsorbed species on well-defined metal electrode surfaces. In: Sun S-G, Christensen PA, Wieckowski A (eds) In-situ spectroscopic studies of adsorption at the electrode and electrocatalysis. Elsevier, Amsterdam, pp 1–32
36. Leger J-M, Hahn F (2007) Contribution of in situ infrared reflectance spectroscopy in the study of nanostructured fuel cell electrodes. In: Sun S-G, Christensen PA, Wieckowski A (eds) In-situ spectroscopic studies of adsorption at the electrode and electrocatalysis. Elsevier, Amsterdam, pp 63–98
37. Korzeniewski C (2007) Recent advances in in situ infrared spectroscopy and applications in single-crystal electrochemistry and electrocatalysis. In: Sun S-G, Christensen PA, Wieckowski A (eds) In-situ spectroscopic studies of adsorption at the electrode and electrocatalysis. Elsevier, Amsterdam, pp 179–208
38. Osawa M (2009) In-situ surface-enhanced infrared spectroscopy of the electrode/solution interface. In: Alkire RC, Kolb DM, Lipkowski J, Ross PN (eds) Advances in electrochemical science and engineering. Diffraction and spectroscopic methods in electroelectrochemistry, vol 9. Wiley, New York, pp 269–314
39. Li M, Marinkovic NS (2013) In situ infrared spectroelectrochemistry: principles and applications. In: Cozzolino D (ed) Infrared spectroscopy: theory, developments and applications. Nova Science Publishers, Hauppauge, pp 307–332
40. Zamlynny V, Lipkowski J (2009) Quantitative SNIFTIRS and PM IRRAS of organic molecules at electrode surfaces. In: Alkire RC, Kolb DM, Lipkowski J, Ross PN (eds) Advances in electrochemical science and engineering. Diffraction and spectroscopic methods in electroelectrochemistry, vol 9. Wiley, New York, pp 315–376
41. Greenler RG (1966) Infrared study of adsorbed molecules on metal surfaces by reflection techniques. *J Chem Phys* 44:310–315
42. Greenler RG (1969) Reflection method for obtaining the infrared spectrum of a thin layer on a metal surface. *J Chem Phys* 50:1963–1968
43. Greenler RG (1975) Design of a reflection–absorption experiment for studying the IR spectrum of molecules adsorbed on a metal surface. *J Vac Sci Technol* 12:1410–1417

44. Bewick A, Kunimatsu K, Pons BS, Russell JW (1984) Electrochemically modulated infrared spectroscopy (EMIRS) experimental details. *J Electroanal Chem* 160:47–61
45. Davidson T, Pons BS, Bewick A, Schmidt PP (1981) Vibrational spectroscopy of the electrode/electrolyte interface. Use of Fourier transform infrared spectroscopy. *J Electroanal Chem* 125:237–241
46. Pons S, Davidson T, Bewick A (1983) Vibrational spectroscopy of the electrode–solution interface. 2. Use of Fourier transform spectroscopy for recording infrared spectra of radical ion intermediates. *J Am Chem Soc* 105:1802–1805
47. Russel JW, Overend J, Scanlon K, Severson M, Bewick A (1982) Infrared spectrum of carbon monoxide on a platinum electrode in acidic solution. *J Phys Chem* 86:3066–3068
48. Pons S (1983) The use of Fourier transform infrared spectroscopy for *in situ* recording of species in the electrode–electrolyte solution interphase. *J Electroanal Chem* 150:495–504
49. Corrigan DS, Leung LWH, Weaver MJ (1987) Single potential-alteration surface infrared spectroscopy: examination of absorbed species involved in irreversible electrode reactions. *Anal Chem* 59:2252–2256
50. Hippo KW, Crosby GA (1979) Applications of the photoelastic modulator to polarization spectroscopy. *J Phys Chem* 83:555–562
51. Golden WG, Kunimatsu K, Seki H (1984) Application of polarization-modulated Fourier transform infrared reflection–absorption spectroscopy to the study of carbon monoxide adsorption and oxidation of a smooth platinum electrode. *J Phys Chem* 88:1275–1277
52. Seki H, Kunimatsu K, Golden WG (1985) A thin-layer electrochemical cell for infrared spectroscopic measurements of the electrode/electrolyte interface. *Appl Spectrosc* 39:437–443
53. Golden WG, Saperstein DD, Severson MW, Overend J (1984) Infrared reflection–absorption spectroscopy of surface species: a comparison of Fourier transform and dispersion methods. *J Phys Chem* 88:574–580
54. Iwasita T, Nart FC (1997) *In situ* infrared spectroscopy at electrochemical interfaces. *Prog Surf Sci* 55:271–340
55. Faguy PW, Marinkovic NS (1996) Design and performance of a new infrared reflection accessory for spectroelectrochemical studies. *Appl Spectrosc* 50:394–400
56. Otto A (1968) A new method for exciting non-radioactive surface plasma oscillations. *Phys Stat Sol* 26:K99–K101
57. Mirabella FM (1993) History of internal reflection spectroscopy. In: Mirabella FM (ed) Internal reflection spectroscopy: theory and applications. Marcel Dekker, New York, pp 1–15
58. Marinkovic NS (2018) Optimization of *in situ* infrared spectro-electrochemical accessory with the aid of reflectance and electric field calculations. *Zast Mater* 59:273–281
59. <http://refractiveindex.info/?shelf=main&book=H2O&page=Hale>. <https://refractiveindex.info/?shelf=main&book=ZnSe&page=Querry>. Accessed 30 Mar 2019
60. Kretschmann E, Reather H (1968) Radiative decay of non-radiative surface plasmons excited by light. *Z Naturf* 23:2135–2136
61. Hartstein A, Kirtley JR, Tsang JT (1980) Enhancement of the infrared absorption from molecular monolayers with thin metal overlayers. *Phys Rev Lett* 45:201
62. Hatta A, Chiba Y, Suetaka W (1985) Infrared absorption study of adsorbed species at metal/water interface by use of the Kretschmann configuration. *Surf Sci* 158:616–623
63. Osawa M, Kuramitsu M, Hatta A, Suetaka W, Seki H (1986) Electromagnetic effect in enhanced infrared absorption of adsorbed molecules on thin metal films. *Surf Sci* 175:L787–L793
64. Hansen PW (1968) Electric fields produced by the propagation of plane coherent electromagnetic radiation in a stratified medium. *J Opt Soc Am* 58:380–390
65. Marinkovic NS (2018) Optimization of *in situ* infrared spectro-electrochemical accessory with the aid of reflectance and electric field and calculations. *Zast Mater* 59(2):273–281
66. Marinkovic NS (2019) (**To be submitted**)
67. Faguy PW, Marinkovic NS (1995) Sensitivity and reproducibility in infrared spectroscopic measurements at single-crystal electrode surfaces. *Anal Chem* 67:2791–2799
68. Faguy PW, Marinkovic NS, Adzic RR (1996) An *in situ* infrared study on the effect of pH on anion adsorption at Pt(111) electrodes from acid sulfate solutions. *Langmuir* 12:243–247
69. Faguy PW, Marinkovic NS, Adzic RR (1996) Infrared spectroscopic analysis of anions adsorbed from bisulfate-containing solutions on Pt(111) electrodes. *J Electroanal Chem* 407:209–218
70. Bunker G (2010) Introduction to XAFS: a practical guide to X-ray absorption fine structure spectroscopy. Cambridge University Press, Cambridge

71. Calvin S (2013) XAFS for everyone. CRC Press/Taylor, Boca Raton
72. Koningsberger DC, Prins R (eds) (1988) X-ray absorption: principles, applications, techniques of EXAFS, SEXAFS, and XANES, in chemical analysis, vol 92. Wiley, New York
73. McBreen J, Mukerjee S (1999) In situ X-ray absorption studies of carbon-supported Pt and Ptc alloy nanoparticles. In: Wieckowski A (ed) Interfacial electrochemistry: theory, experiment and applications. Marcel Dekker, New York, pp 895–914
74. Newville M (2014) Fundamentals of XAFS. *Rev Mineral Geochem* 78:33–74
75. Stern EA (1974) Theory of the extended X-ray-absorption fine structure. *Phys Rev B* 10:3027–3037
76. Ramaker DE, Koningsberger DC (2010) The atomic AXAFS and $\Delta\mu$ XANES techniques applied to heterogeneous catalysis and electrocatalysis. *Phys Chem Chem Phys* 12:5514–5534
77. Arruda TM, Shyam B, Ziegelbauer JM, Mukerjee S, Ramaker DE (2008) Investigation into the competitive and site-specific nature of anion adsorption on Pt using in situ X-ray absorption spectroscopy. *J Phys Chem C* 112:18087–18097
78. Sasaki K, Marinkovic NS, Isaacs H, Adzic RR (2016) Synchrotron-based in situ characterization of carbon-supported platinum and platinum monolayer electrocatalysts. *ACS Catal* 6:69–76
79. Sasaki K, Wang JX, Naohara H, Marinkovic N, More K, Inada H, Adzic RR (2010) Recent advances in platinum monolayer electrocatalysts for oxygen reduction reaction: scale-up synthesis, structure and activity of Pt shells on Pd cores. *Electrochim Acta* 55:2645–2652
80. Ravel B, Newville M (2005) ATHENA, ARTEMIS, HEPHAESTUS: data analysis for X-ray absorption spectroscopy using IFEFFIT. *J Synchrotron Rad* 12:537–541
81. Chang S-C, Leung LWH, Weaver MJ (1990) Metal crystallinity effects in electrocatalysis as probed by real-time FTIR spectroscopy: electrooxidation of formic acid, methanol, and ethanol on ordered low-index platinum surfaces. *J Phys Chem* 94:6013–6021
82. Colmati F, Tremiliosi-Filho G, Gonzalez ER, Berna A, Herrero E, Feliu JM (2009) The role of the steps in the cleavage of the C–C bond during ethanol oxidation on platinum electrodes. *Phys Chem Chem Phys* 11:9114–9123
83. Shin J, Tornquist WJ, Korzeniewski C, Hoaglund CS (1996) Elementary steps in the oxidation and dissociative chemisorptions of ethanol on smooth and stepped surface planes of platinum electrodes. *Surf Sci* 364:122–130
84. Li M, Kowal A, Sasaki K, Marinkovic NS, Su D, Korach E, Liu P, Adzic RR (2010) Ethanol oxidation on the ternary Pt–Rh–SnO₂/C electrocatalysts with varied Pt:Rh:Sn ratios. *Electrochim Acta* 55:4331–4338
85. Kowal A, Gojkovic SL, Leed KS, Olszewski P, Sung Y-E (2009) Synthesis, characterization and electrocatalytic activity for ethanol oxidation of carbon supported Pt, Pt–Rh, Pt–SnO₂ and Pt–Rh–SnO₂ nanoclusters. *Electrochim Commun* 11:724–727
86. Du W, Wang Q, LaScala CA, Zhang L, Su D, Frenkel AI, Mathura VK, Teng X (2011) Ternary PtSnRh–SnO₂ nanoclusters: synthesis and electroactivity for ethanol oxidation fuel cell reaction. *J Mater Chem* 21:8887–8892
87. Choi Y, Liu P (2011) Understanding of ethanol decomposition on Rh(111) from density functional theory and kinetic Monte Carlo simulations. *Catal Today* 165:64–70
88. Stamenkovic V, Arenz M, Ross PN, Markovic NM (2004) Temperature-induced deposition method for anchoring metallic nanoparticles onto reflective substrates for in situ electrochemical infrared spectroscopy. *J Phys Chem B* 108:17915–17920
89. Blyholder G (1964) Molecular orbital view of chemisorbed carbon monoxide. *J Phys Chem* 68:2772–2777
90. Gao P, Chang S-C, Zhou Z, Weaver MJ (1989) Electrooxidation pathways of simple alcohols at platinum in pure nonaqueous and concentrated aqueous environments as studied by real-time FTIR spectroscopy. *J Electroanal Chem* 272:161–178
91. Camara GA, de Lima RB, Iwasita T (2004) Catalysis of ethanol electrooxidation by PtRu: the influence of catalyst composition. *Electrochim Commun* 6:812–815
92. Camara GA, de Lima RB, Iwasita T (2005) The influence of PtRu atomic composition on the yields of ethanol oxidation: a study by in situ FTIR spectroscopy. *J Electroanal Chem* 585:128–131
93. Kutz RB, Braunschweig B, Mukherjee P, Behrens RL, Dlott DD, Wieckowski A (2011) Reaction pathways of ethanol electrooxidation on polycrystalline platinum catalysts in acidic electrolytes. *J Catal* 278:181–188
94. Samjeske G, Miki A, Ye S, Osawa M (2006) Mechanistic study of electrocatalytic oxidation of formic acid at platinum in acidic solution by time-resolved surface-enhanced infrared absorption spectroscopy. *J Phys Chem B* 110:16559–16566

95. Chen YX, Miki A, Ye S, Sakai H, Osawa M (2003) Formate, an active intermediate for direct oxidation of methanol on Pt electrode. *J Am Chem Soc* 125:3680–3681
96. Shao MH, Adzic RR (2005) Electrooxidation of ethanol on a Pt electrode in acid solutions: *in situ* ATR-SEIRAS study. *Electrochim Acta* 50:2415–2422
97. Shao MH, Warren J, Marinkovic NS, Faguy PW, Adzic RR (2005) *In situ* ATR-SEIRAS study of electrooxidation of dimethyl ether on a Pt electrode in acid solutions. *Electrochim Commun* 7:459–465
98. Burgi T (2001) ATR-IR spectroscopy at the metal–liquid interface: influence of film properties on anomalous band-shape. *Phys Chem Chem Phys* 3:2124–2130
99. Bell AT (2003) The impact of nanoscience on heterogeneous catalysis. *Science* 299(5613):1688–1691
100. Benfield RE (1992) Mean coordination numbers and the non-metal–metal transition in clusters. *J Chem Soc Faraday Trans* 88:1107–1110
101. Beale AM, Weckhuysen BM (2010) EXAFS as a tool to interrogate the size and shape of mono and bimetallic catalyst nanoparticles. *Phys Chem Chem Phys* 12:5562–5574
102. Frenkel A (2007) Solving the 3D structure of metal nanoparticles. *Zeitschrift fur Kristallographie* 222:605–611
103. Sasaki K, Marinkovic NS (2016) X-ray absorption spectroscopic characterization of nanomaterial catalysts in electrochemistry and fuel cells. In: Kumar CSSR (ed) X-ray and neutron techniques for nanomaterials characterization, chapter 6. Springer, New York, pp 315–365
104. Marinkovic NS, Sasaki K, Adzic RR (2018) Determination of single- and multi-component nanoparticle sizes by X-ray absorption spectroscopy. *J Electrochim Soc* 165(15):J3222–J3230
105. Trasatti S (1999) In: Wieckowski A (ed) *Interfacial electrochemistry: theory, experiment, and applications*. Marcel Dekker, New York, pp 769–788
106. Batzill M, Diebold U (2005) The surface and materials science of tin oxide. *Prog Surf Sci* 79:47–154
107. Li M, Marinkovic N, Sasaki K (2012) *In situ* characterization of ternary Pt–Rh–SnO₂/C catalysts for ethanol electrooxidation. *Electrocatalysis* 3:376–385
108. de Tacconi NR, Lezna RO, Beden B, Hahn F, Lamy C (1994) *In-situ* FTIR study of the electrocatalytic oxidation of ethanol at iridium and rhodium electrodes. *J Electroanal Chem* 379:329–337
109. Cao L, Sun G, Li H, Xin Q (2007) Carbon-supported IrSn catalysts for a direct ethanol fuel cell. *Electrochim Commun* 9:2541–2546
110. Du W, Wang Q, Saxner D, Aaron Deskins N, Su D, Krzanowski JE, Frenkel AI, Teng X (2011) Highly active iridium/iridium–tin/tin oxide heterogeneous nanoparticles as alternative electrocatalysts for the ethanol oxidation reaction. *J Am Chem Soc* 133:15172–15183
111. Zhang J, Sasaki K, Sutter E, Adzic RR (2007) Stabilization of platinum oxygen-reduction electrocatalysts using gold clusters. *Science* 315(5809):220–222
112. Adzic RR, Zhang J, Sasaki K, Vukmirovic MB, Shao M, Wang JX, Nilekar AU, Mavrikakis M, Valerio JA, Uribe F (2007) Platinum monolayer fuel cell electrocatalysts. *Top Catal* 46:249–262
113. Sasaki K, Adzic RR (2008) Monolayer-level Ru- and NbO₂-supported platinum electrocatalysts for methanol oxidation. *J Electrochim Soc* 105:B180–B186

Publisher's Note Springer Nature remains neutral with regard to jurisdictional claims in published maps and institutional affiliations.

Affiliations

Nebojsa S. Marinkovic¹  · **Meng Li**² · **Radoslav R. Adzic**²

 Nebojsa S. Marinkovic
marinkov@bnl.gov

¹ Synchrotron Catalysis Consortium and Columbia University, New York, NY, USA

² Brookhaven National Laboratory, Upton, NY, USA



REVIEW

Recent Advances in the Electro-Oxidation of Urea for Direct Urea Fuel Cell and Urea Electrolysis

Ke Ye^{1,2} · Gang Wang¹ · Dianxue Cao¹ · Guoxiong Wang²

Received: 22 August 2018 / Accepted: 9 October 2018 / Published online: 26 October 2018
© Springer Nature Switzerland AG 2018

Abstract

This paper provides an overview of recent advances in urea electro-oxidation. Urea sources are abundant from human urine, urea-containing wastewater, and industrial urea, thus becoming an attractive option as anodic fuel for the application in direct urea fuel cells (DUFCS). Besides, as a hydrogen-rich chemical fuel, urea can also be electrolyzed to produce hydrogen for energy storage in the near future. The exact mechanisms of urea decomposition are pretty different in alkaline or neutral mediums and are separately discussed in detail. More importantly, the development of anodic electro-catalysts is of great significance for improving the electrochemical performance of both DUFCS and urea electrolysis cells, which is systematically summarized in our review. Challenges and prospects on the future development of urea electro-oxidation are particularly proposed.

Keywords Fuel cells · Electrolysis · Urea · Electro-oxidation · Electro-catalyst

Ke Ye and Gang Wang contributed equally to this work.

Chapter 2 was originally published as Ye, K., Wang, G., Cao, D. & Wang, G. Topics in Current Chemistry (2018) 376: 42. <https://doi.org/10.1007/s41061-018-0219-y>.

✉ Dianxue Cao
caodianxue@hrbeu.edu.cn

✉ Guoxiong Wang
wanggx@dicp.ac.cn

¹ Key Laboratory of Superlight Materials and Surface Technology of Ministry of Education, College of Materials Science and Chemical Engineering, Harbin Engineering University, Harbin 150001, People's Republic of China

² State Key Laboratory of Catalysis, CAS Center for Excellence in Nanoscience, Dalian National Laboratory for Clean Energy, Dalian Institute of Chemical Physics, Chinese Academy of Sciences, Dalian 116023, People's Republic of China

1 Introduction

Human society consumes a large amount of fossil energy, which triggers serious environmental concerns and excessive emission of greenhouse gases. In order to maintain the normal operation of the global economy and preserve the ecological balance, new and clean power alternatives of petrochemical energy must be searched for and developed [1, 2]. Hydrogen is a clean and novel energy resource, but the production, storage, and transportation of hydrogen still suffer from great challenges that severely restrict the large-scale application of hydrogen energy. Therefore, exploring a qualified hydrogen energy carrier is one of the main ways to overcome these technical obstacles. In general, normal hydrogen energy carriers need to be considered in several ways, such as environmental compatibility, safety and cost, etc. [3–7].

Urea, as an organic material that contains carbon, nitrogen, oxygen, and hydrogen elements, is considered a hydrogen-rich chemical fuel (hydrogen content reaches 6.67 wt%) [8, 9]. Therefore urea is attractively focused on as an alternative anodic fuel for application in fuel cells [10]. In fact, urea sources are abundant from human urine, urea-containing waste water, and industrial urea. On the one hand, human urine contains 2–2.5 wt% of urea, which is equal to the average molar concentration of 0.33 mol l^{-1} . On the other hand, industrial production discharges amounts of urea-containing waste water with different urea contents. However, the urea-rich waste water or urine can be naturally hydrolyzed to ammonia (NH_3) if without any treatment and released to the atmosphere, accelerating the formation of acid rain as well as causing damage to the environment [11]. In addition, ammonia is unstable in the air, which means it is easily oxidized to form pollutants such as nitrates, nitrites, and nitrogen oxides. These harmful nitrogenous substances will directly infiltrate the soil and drinking water as rainwater, posing a great threat to the ground and human health. Furthermore, because of the high energy density of urea, direct emissions may cause a great deal of energy waste. Therefore, the utilization of rational methods to remove nitrogen-containing components from effluent and make better treatment for urea is becoming an increasingly important energetic and environmental issue [12]. Traditional urea treatments mainly include hydrolysis [12, 13], adsorption [14–17], biodegradation [18, 19], and chemical oxidation [20–23], but the high cost of required equipment of these methods as well as excessive energy consumption greatly limit their broader application. For instance, in order to obtain a better degradation effect, these methods are usually operated under high temperature conditions, which may result in inactivation and denaturation of the biological active enzymes (such as urease) [14, 24, 25].

Fortunately, the electro-oxidation method of urea possesses the advantages of simple operation, large quantity of processing, long operation cycle, and stable production of non-toxic CO_2 , N_2 with available H_2 (in basic solution). More significantly, urea electro-oxidation under alkaline condition can be effectively realized without the utilization of precious metals, which greatly reduces the catalyst cost and increases the possibility of practical application. As a matter of fact,

research work related to urea electro-oxidation started early in the 1970s and was applied in the field of bioengineering, such as portable bio-electrochemical sensors and artificial kidney rejuvenation. Actually, as long as supplying certain electrical energy to an aqueous solution that contains urea, urea will be oxidized to other inorganic materials. More recently, the technology of urea electro-oxidation is mainly developed and applied in direct urea fuel cells (DUFCs) as anodic reaction or the field of urea electrolysis for H₂ production.

This review summarizes the current advances in urea electro-oxidation. Adequate literature is available in the whole review and some main issues not mentioned in the existing literature are also addressed in this review. Specifically, a detailed survey of the applications for urea electro-oxidation, which mainly include direct urea fuel cells and urea electrolysis, are organized in Sect. 2. In-depth mechanisms of urea electro-oxidation in neutral or alkaline media are discussed in Sect. 3. The development of anodic catalysts is of great significance towards DUFCs and urea electrolysis, thus are mainly introduced and classified in Sect. 4, where the major challenges and remedies are also mentioned as a matter of interest. Finally, future challenges and prospects are proposed in Sect. 5.

2 Application of Urea Electro-Oxidation

2.1 Direct Urea Fuel Cells (DUFCs)

The fuel cell is a new type of high-efficiency, low-pollution power generation device, which has been highly favored since its invention [26–37]. Simultaneously, DUFCs are recently considered as promising advanced fuel cells, of which the fuel sources mainly come from industrial urea effluent or animal urine. This type of device, which uses the above urea as anodic fuels while O₂ or H₂O₂ as cathodic oxidants, can generate electricity as well as degrade waste water [38–46].

Tao et al. [10] firstly designed the working urea fuel cell and successfully applied this technology to generate electricity. The urea electro-oxidation takes place in the anodic compartment of this cell, and oxygen reduction reaction occurs in the cathodic compartment. They also found that when Pt/C catalyst was used for both cathode and anode, the open circuit voltage (OCV) reaches ~0.5 V, while the peak power density was about 0.55 mW cm⁻². Later in 2011, Tao et al. [47] made further efforts to optimize the anode catalyst and continued to increase the open circuit voltage and power density of DUFCs. Nickel nanoparticles with sizes between 2 and 3 nm were designed and firstly reported as anodic catalyst in the urine fuel cell. The power density was greatly enhanced to 1.5 mW cm⁻² while the OCV was also broadened to 0.65 V. Recently, Basumatary et al. developed an alkaline air cathode DUFC using Cu/ZnO@MWCNT, which demonstrated power outputs of 12 mW cm⁻² in 0.35 M urea at 20 °C (the highest power output reported at room temperature) with an OCV of 0.9 V [41]. Compared with other alkaline fuel cells (AFC), DUFCs' electrical output performance is relatively low [48–51]. Nevertheless, it is still considered that urea can be promising anodic fuels mainly due to their special merits as follows: (1) they have higher volumetric energy density (16.9 MJ l⁻¹)

than compressed hydrogen gas (5.6 MJ l^{-1}) or 28 wt% NH_4OH (1.17 MJ l^{-1}); (2) urea sources are abundant from animals' urine (contents ca. 2–2.5 wt%). Compared with conventional H_2 , direct utilization of wastewater rich in urea as fuels is more efficient for power generation; (3) the storage and transportation of urea are more convenient than hydrogen gas for its non-toxic and incombustible features; (4) the oxidative reaction products of urea are safely stable carbonate and nitrogen. On the other hand, Serban et al. employed Ni/MWCNTs–Pt/C as twin electrodes to form direct urea/ H_2O_2 fuel cell (DUPFC) that performed a maximum power density of 0.05 mW cm^{-2} with the OCV of 0.25 V. Then it caught the researchers' attention to focus on the cathodic oxidant of DUFCs and choose liquid hydrogen peroxide (H_2O_2) as the oxidants for their priorities. In certain DUPFC, the anodic electro-oxidation of urea occurs in a basic media, while the cathodic electro-reduction of H_2O_2 can react both in basic and acidic media [52, 53]. A specific type of acidic fuel cell in Cao et al.'s [54] work that used H_2O_2 as cathodic oxidant and Pd/CFC as the cathodic catalyst increased the OCV to $\sim 0.8 \text{ V}$ and the power density reached $\sim 5 \text{ mW cm}^{-2}$. The cell performance was much higher than that used oxygen as oxidant ($0.65 \text{ V}, 1.5 \text{ mW cm}^{-2}$). This was probably ascribed to the fact that H_2O_2 used as oxidants of DUFCs can enhance theoretical OCV of the cell to 2.51 V, much better than O_2 as oxidant (for basic media: OCV = 1.15 V) [55].

According to the differences of cathodic oxidant and media, DUFCs can be roughly divided into three of the most common and practical types: oxygen reduction reaction in basic media, hydrogen peroxide electro-reduction reaction in basic media, and hydrogen peroxide electro-reduction reaction in acidic media. Both of the fuel cell systems utilize cation exchange membrane (CEM) as separator. When the electrons flow from anode to cathode throughout external circuit, then K^+ flows from anode to cathode throughout the CEM, thus forming a current loop. The schematic representation of different DUFC configurations is displayed in Fig. 1 and their overall reactions are described in Table 1.

Although the anodic reactions of the three fuel cells are the same, their output voltage distinguishes a lot from each other. Observing the above reaction equations, it is known that for the cell (a) and (b) in Fig. 1, 1 mol of urea molecules are electro-oxidized to generate 6 mol of potassium ions at anode area, which happens to combine with 6 mol of hydroxide ions at the cathode to reversibly generate 6 mol of KOH. For the cell (c) in Fig. 1, 6 mol of potassium ions combine with 3 mol of sulfate ions produced by the cathode to form 3 mol of potassium sulfate. By comparison, thermodynamic parameters of these three types of fuel cells, including theoretical cell voltage (ΔE^θ), energy efficiency (η), entropy change (ΔS), and output

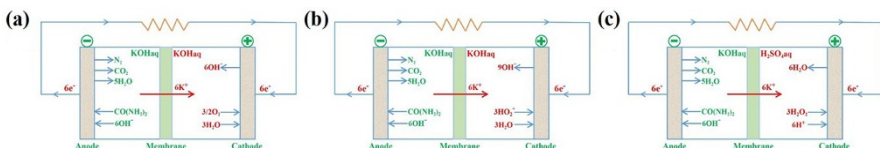


Fig. 1 Schematic diagram of three typical types of DUFCs. **a** Direct urea- O_2 (alkaline) fuel cells; **b** direct urea- H_2O_2 (alkaline) fuel cells; **c** direct urea- H_2O_2 (acidic) fuel cells

Table 1 Summary of reaction equations of different types of DUFCs (K^+ is taken as the cation for example)

| | Direct urea- O_2 (alkaline) fuel cell | Direct urea- H_2O_2 (alkaline) fuel cell | Direct urea- H_2O_2 (acidic) fuel cell |
|-------------------|---|--|---|
| Anodic reaction | $\text{CO}(\text{NH}_2)_2 + 6 \text{KOH} \rightleftharpoons \text{N}_2 + \text{CO}_2 + 5\text{H}_2\text{O} + 6\text{K}^+ + 6\text{e}^-$ $E^\theta = -0.75 \text{ V}$ | $\text{CO}(\text{NH}_2)_2 + 6 \text{KOH} \rightleftharpoons \text{N}_2 + \text{CO}_2 + 5\text{H}_2\text{O} + 6\text{K}^+ + 6\text{e}^-$ $E^\theta = -0.75 \text{ V}$ | $\text{CO}(\text{NH}_2)_2 + 6 \text{KOH} \rightleftharpoons \text{N}_2 + \text{CO}_2 + 5\text{H}_2\text{O} + 6\text{K}^+ + 6\text{e}^-$ $E^\theta = -0.75 \text{ V}$ |
| Cathodic reaction | $3/2\text{O}_2 + 3\text{H}_2\text{O} + 6 \text{K}^+ + 6\text{e}^- \rightleftharpoons 6\text{KOH}$ $E^\theta = 0.40 \text{ V}$ | $3\text{H}_2\text{O}_2 + 6 \text{K}^+ + 6\text{e}^- \rightleftharpoons 6\text{KOH}$ or $3\text{HO}_2^- + 9 \text{K}^+ + 3\text{H}_2\text{O} + 6\text{e}^- \rightleftharpoons 9\text{KOH}$ $E^\theta = 0.88 \text{ V}$ | $3\text{H}_2\text{O}_2 + 3\text{H}_2\text{SO}_4 + 6\text{e}^- \rightleftharpoons 6\text{H}_2\text{O} + 3\text{SO}_4^{2-}$ $E^\theta = 1.76 \text{ V}$ |
| Overall reaction | $\text{CO}(\text{NH}_2)_2 + 3/2\text{O}_2 \rightarrow \text{N}_2 + \text{CO}_2 + 2\text{H}_2\text{O}$ $E^\theta = 1.15 \text{ V}$ | $\text{CO}(\text{NH}_2)_2 + 3\text{H}_2\text{O}_2 \rightarrow \text{N}_2 + \text{C}$ $\text{O}_2 + 5\text{H}_2\text{O}$ or $\text{CO}(\text{NH}_2)_2 + 3\text{HO}_2^- + 3 \text{K}^+ \rightarrow 3\text{KOH} + \text{N}_2 + \text{CO}_2 + 2\text{H}_2\text{O}$ $E^\theta = 1.63 \text{ V}$ | $\text{CO}(\text{NH}_2)_2 + 3\text{H}_2\text{O}_2 + 6\text{KOH} + 3\text{H}_2\text{SO}_4 \rightarrow \text{N}_2 + \text{CO}_2 + 11\text{H}_2\text{O} + 3\text{K}_2\text{SO}_4$ $E^\theta = 2.51 \text{ V}$ |

Table 2 Comparison of thermodynamic parameters of the three types of DUFCs

| Types of DUFCs | Theoretical cell voltage ($\Delta E^0/V$) | Energy efficiency ($\eta/\%$) | Entropy change ($\Delta S/J \text{ mol}^{-1} \text{ K}^{-1}$) | Output power ($\Delta W/\text{Wh g}_{\text{urea}}^{-1}$) |
|--|---|---------------------------------|---|--|
| Direct urea-O ₂ (alkaline) fuel cell | 1.15 | 106.3 | 132.97 | 3.08 |
| Direct urea-H ₂ O ₂ (alkaline) fuel cell | 1.63 | 107.1 | 218.84 | 4.37 |
| Direct urea-H ₂ O ₂ (acid) fuel cell | 2.51 | 109.5 | 703.94 | 6.73 |
| Calculation formulas | $\Delta E^0 = -\Delta G^0/nF$ | $\eta = \Delta G^0/\Delta H^0$ | $(\partial \Delta E^0/\partial T)_p = \Delta S/nF$ | $\Delta W = I\Delta E^0$ |

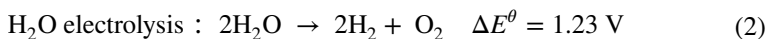
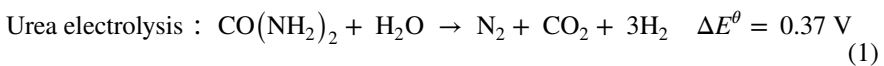
power (ΔW), are summarized in Table 2, respectively. Comprehensively considering these several factors, the direct urea–H₂O₂ (acid) fuel cell (Fig. 1c) shows considerable advantages for further applications. In this case, the efforts for researchers should be concentrated on increasing power density of the DUPFCs, especially achieving higher open circuit voltage as much as possible. To achieve these goals, a breakthrough of anodic catalysts, which devoted most contributions to the cell performance, might be realized in the near future. This part will be discussed in detail in Sect. 4, only then we may expect commercial applications of DUPFCs.

2.2 Urea Electrolysis

Under the background of energy shortage, hydrogen has attracted great attention due to its high calorific value, abundant reserves, and no pollution of products. Therefore it is believed to lead the upsurge of a new energy era and form a “hydrogen energy economy” system over the world. Urea exactly fulfill the current DOE (Department of Energy, USA) goals for hydrogen storage in transportation fields owing to its gravimetric hydrogen content up to 6.71 wt%, as we mentioned previously in this paper [10, 56]. While this value is equal conversion to 7.95 wt% of stoichiometric aqueous urea-containing solution with the additional H₂ molecule in the presence of steam reforming water. At present, a large-scale production of hydrogen in the domestic petrochemical industry mainly uses natural-gas steam reforming, light-oil steam reforming, or water–gas reforming, among which the natural gas steam reforming is the most common technology. However, due to the fossil energy shortage, reliance on the conventional energy sources still remains unsolved. Hydrogen production from electrolyzed water that needs to be performed at a high pressure of 3.0–5.0 MPa and high temperature of 120–250 °C encounters excessive electricity of conventional energy and relatively low electrolysis efficiency [12]. Recently, bio-hydrogen production has caught many researchers’ attention and was confirmed to a complicated strategy for producing hydrogen [18]. Pure photosynthetic or anaerobic bacteria used as catalysts and carbohydrates as hydrogen donors to produce hydrogen can be realized at room temperature without cost of fossil fuel. Nevertheless, the inadequacy lies

in the high demands of technologic devices, especially a series of biofilters with non-selective bacterial strain, accordingly difficult to widely operate or achieve industrialization [19, 57, 58].

Boggs et al. [56] investigated the urea electrolysis for the production of hydrogen. They pointed out that not only urea or urine can be degraded when it is electrolyzed under the alkaline condition but also hydrogen was obtained at the other compartment of electrolytic cell in the meantime. The urea molecules as raw materials are dissociated by imputing electrical energy, and H₂ is produced through hydrolysis of water molecules. In order to break the urea molecules, a standard voltage of 0.37 V needs to be applied across the alkaline cell, where urea electro-oxidized in anodic part at –0.46 V (vs. SHE) and water reduced in cathodic part at the required –0.83 V (vs. SHE). The voltage of urea electrolysis for hydrogen production (Eq. 1) is obviously smaller than that required to directly split the water molecules (1.23 V, Eq. 2). From the perspective of economic cost and energy consumption, Boggs et al. gave a comparison of the energy consumption for hydrogen production between the electrolysis of urea and water. When selecting the voltages of two electrolysis methods at the same current of 20 mA for calculation, they found that the energy consumption for hydrogen production from urea electrolysis is reduced by 30%, and the economic cost can be reduced by 36% (as shown in Table 3).



Considering that the hydrogen production from urea electrolysis needed an extra power input, Kim et al. [59] came up with an advanced hybrid photovoltaic (PV) arrays-electrochemical system, which jointly manages a power–water system using solar energy as imported source and urea/urine as hydrogen carrier (shown in Fig. 2a). They studied the PV system as an alternative technology for electrolysis of urea/urine and synchronous production of H₂. Three different electrolytes (Na₂SO₄, LiClO₄, NaCl) were employed in this PV system using BiO_x–TiO₂ as anodic catalyst. In sodium chloride electrolyte, the electrolysis of urea was observed to improve the production of H₂ by 20% in a relatively low urea concentration by comparison with water electrolysis (Fig. 2b). In addition, the energy harvested quantity from hydrogen can repay about 10% of the power consumed for the treatment of urea. Finally, this energy compensation is equivalent to 320 kJ of energy as the urine amount produced from one person for 24 h is electrolyzed, indicating promising applications in accordance with urea electrolysis for solar hydrogen.

Table 3 Energy consumption and cost of urea electrolysis and water electrolysis for hydrogen production (the price is calculated as \$0.07 kWh⁻¹)

| Electrolytic substance | Theoretical voltage (V) | Energy consumption (Wh g ⁻¹) | Price for H ₂ production (\$ kg ⁻¹) |
|------------------------|-------------------------|--|--|
| Urea | 0.37 | 37.5 | 2.63 |
| Water | 1.23 | 53.6 | 4.13 |

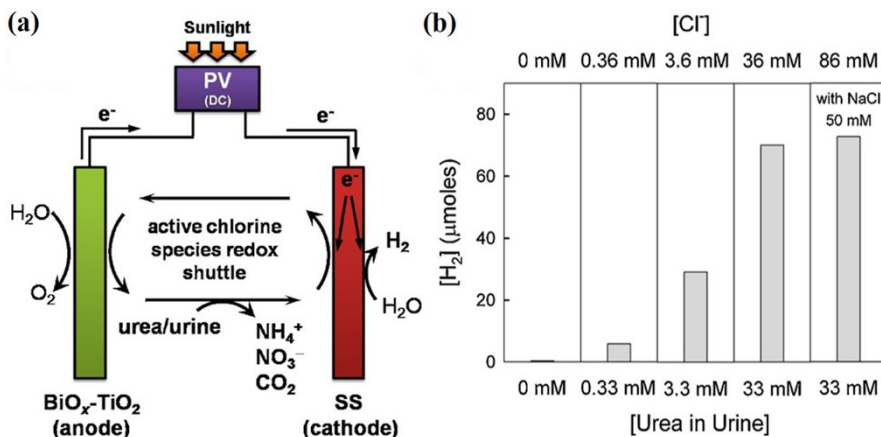


Fig. 2 **a** Diagrammatic drawing and working mechanism of PV electrical power system in sodium chloride solution; **b** the production of hydrogen in the process of urine or urea electrolysis without adding external electrolyte Reproduced with permission from Ref. [59]

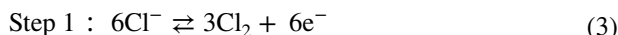
In this part, we briefly introduced some advanced achievements in the application of urea electrolysis. It is found that hydrogen production from electrolysis seems to be more meaningful for future energy storage. Nevertheless, this process exists a demand of difficult operation devices and conditions, which restricts their industrial applications. Otherwise, more consideration should be taken into the amount of urine-containing waste water, the further purification of waste water will increase the electrolysis cost.

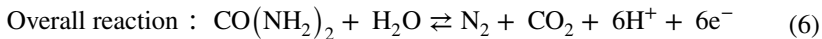
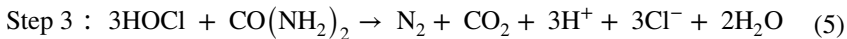
3 Mechanism of Urea Electro-Oxidation

In above introduction part about the urea electro-oxidation applied in DUFCS, urea is generally oxidized in alkaline or acid medium, the products of which are non-toxic N_2 and CO_2 . However, some initial investigations concerning urea electro-oxidation were carried out in neutral NaCl medium, the products of which include not only N_2 and CO_2 but also extra H^+ . Therefore, the accurate mechanisms might be different for the decomposition of urea in various media. Furthermore, the treatment of waste water also possibly includes some intermediates.

3.1 Mechanism in Neutral Cl^- Medium

In the neutral NaCl solutions, Cl^- is firstly electro-oxidized to Cl_2 , and then Cl_2 is disproportionated in aqueous solution to form HClO . Finally, urea is oxidized by HClO and meanwhile HClO itself is reduced to Cl^- (Eqs. 3–6). In fact, Cl^- acts as a transition oxidant throughout the overall process, with no change in quantity before and after reactions.





Since H^+ is produced and discharged into the solution, acid-resistant precious metal catalysts are used as the anode catalysts. Previous reports based on neutral NaCl medium have confirmed that urea (less than 0.2 M) can be degraded with a nearly equal molar amount of chloride ion on the noble-metal oxide catalysts such as IrO_2 , RuO_2 , and PtO_2 [12, 60–62]. For instance, Wright et al. [63] decomposed urea into CO_2 and N_2 accompanied with forming the chlorourea and subsequent dichlorourea on the surface of $\text{RuO}_2\text{-TiO}_2$ -coated titanium electrode. In this electrochemical process, OCl^- and HOCl of free reactive species formed as a primary oxidant that can promote the decomposition of urea, and chloramines usually appeared as the reactive intermediates. In recent studies, chlorine radicals generated by electrochemical reaction was proved to be able to effectively reduce the demanding chemical oxygen in human urine or industrial waste water [64, 65]. Under this condition, reactive chlorine species (RCS) was raised out as the total name of free chlorines (as Cl^\cdot) and chlorine radicals (as Cl_2^\cdot), while the most common RCS in typical urea degradation might be NaOCl . Based on these analyses, Cho et al. [66, 67] point out a further chloride-mediated mechanism of the electro-oxidation of urea in neutral RCS media. Figure 3 shows a proposed reaction pathway towards the urea electro-oxidation in the chlorine electrolyte for the generation of RCS. Actually, the chloramines and chloramides evolved from the RCS electrolyte are bare intermediates of the overall reaction. At first, chloride ions appear to form gaseous chlorine as

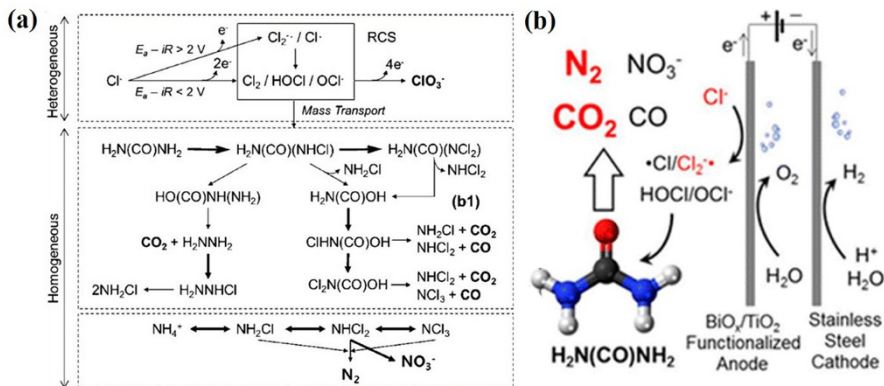


Fig. 3 **a** Electro-generated reactive chlorine in the reaction approach of urea deterioration; **b** schematic diagram of reaction mechanism in the urea electrolysis cell in sodium chloride solution Reproduced with permission from Ref. [66]

the potential is more positive than 2 V (vs. NHE) or to form chlorine radicals when lower than 2 V (vs. NHE). Because the electron receptor effect of substitutional chlorine will weaken bond strength of adjacent amido H, the first step of chlorate evolution tends to be a rate-determining procedure. At the same time in the first step, the other reaction of the OCl^- electro-oxidation might generate the ClO_2^- through a four-electron transfer. Afterwards, the reaction productions between urea and chlorate will undergo a rapid hydrolysis and convert to CO_2 , NHCl , and NH_2Cl through the chlorinated carbamic acid route or to CO_2 and NCl_3 through the chlorinated hydrazine route, while CO appears as a minor product, respectively. In the final step, the inorganic chloramine undergoes a breakage chlorination route to primarily form nitrogen or otherwise oxidization to a small amount of nitrate.

3.2 Mechanism in Alkaline OH^- Medium

Unfortunately, the electro-oxidation of urea under a neutral medium suffers from some disadvantages. Firstly, the anodic catalyst should be a noble metal, which increases the cost of urea-degradation technology. Secondly, the Cl_2 released by the oxidation reaction pollutes the atmosphere and is harmful to human health. Thirdly, the standard electrode potential of Cl_2 evolution is 1.36 V, which is higher than that of oxygen evolution (1.23 V). Therefore, there may exist a side reaction of oxygen evolution, which might greatly reduce the current efficiency. If urea is electro-oxidized in alkaline solution, non-precious metals can be used. Overviewing the amounts of reported literature, it can be concluded that compared to platinum, palladium and other precious metal catalysts, nickel metal, nickel hydroxide (or oxide), or nickel-based composites have behaved more excellent electro-catalytic performance for urea electro-oxidation. This characteristic of nickel-based catalysts can be explained by introducing the catalysis of urease. Figure 4a displays a schematic view of the nickel center in urease from *Klebsiella aerogenes* [68]. By definition, urease is composed of two Ni(II) ions, which are linked to two water molecules. According to the study of Suarez et al. [69], nickel and hydroxyl groups are the reactive sites where the dissociation of urea molecular takes place. Urea molecular is combined in a bidentate manner with two active nickel sites, one of which is connected to the oxygen atom on urea, and the other nickel atom is an amine group attached to

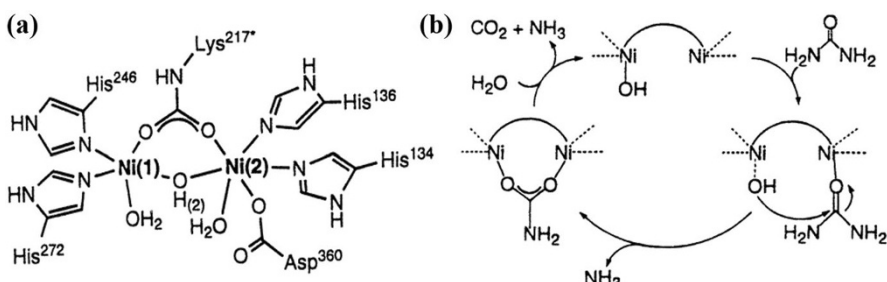
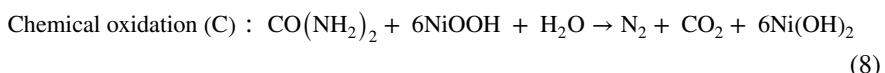


Fig. 4 **a** Schematic view of the active site of urease from *K. aerogenes*; **b** simulation of urea decomposition catalyzed by urease at the active site of the enzyme Reproduced with permission from Ref. [68]

urea molecular. Whereas, the bridging hydroxyl group is thought to participate in this process by supplying protons to the amino group that is linked to the nickel site. Figure 4b gives a simulation of urea decomposition catalyzed by urease at the active site of the enzyme, which can exactly explain why Ni element promotes the urea electro-oxidation reaction. Actually, almost all of these catalysts towards urea electro-oxidation are based on nickel element. These nickel-containing catalysts have one thing in common during the catalyzing process, namely that the onset oxidation potential (OOP) of urea is exactly consistent with that of NiOOH generated from $\text{Ni}(\text{OH})_2$. This phenomenon makes it clear that NiOOH instead of metallic Ni is the active site for urea electro-oxidation. Combined with *in situ* Raman spectroscopy and *in situ* X-ray diffraction patterns by Vedharathinam et al. [70–73], it can be preliminarily presumed that the electro-oxidation reaction mechanism of urea on nickel-based electrode surface is the electro-oxidation (E)-chemical oxidation (C) mechanism. As shown in Eqs. (7) and (8), $\text{Ni}(\text{OH})_2$ loses electrons to form NiOOH at first, and then urea undergo chemical oxidation to form CO_2 and N_2 while NiOOH is electro-reduced to form $\text{Ni}(\text{OH})_2$.



In order to further understand the electrochemical oxidation process, Botte et al. studied the various mechanisms of urea decomposition into HNCO, NCO^- , NH_3 , CO_2 , and N_2 , and adopting density functional theory (DFT) to forecast the product of urea decomposition using NiOOH as active catalyst [74]. The reaction process and relative rate-determination steps suggest three possible mechanisms for urea electro-oxidation in basic media. Among three reaction pathways, urea molecules are adsorbed on NiOOH through the same way of “bridge” connections in the first step, as shown in Fig. 5. The proposed connection method is based on the binding mode of urea decomposition catalyzed by urease. The Ni atom in the urease molecule is connected to the N atom or O atom in urea molecule, and the O atom of the urease molecule is linked to the C atom of urea molecule. This structure was confirmed as the most possible adsorption of urea on the catalyst surface. By comparison with the rate constants and free energies for each step of the corresponding

Fig. 5 Optimal construction of bridge-connected urea on NiOOH (N2 atom was among H4 and H3) Reproduced with permission from Ref. [74]

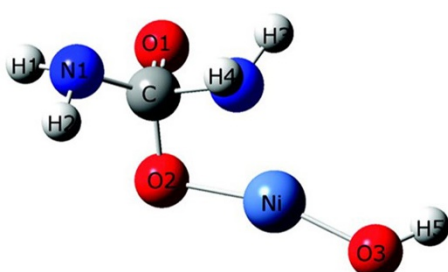


Table 4 Summary of rate constants and free energies of the intermediate steps ($M = \text{NiOOH}$)

| Step | Reaction pathways | Rate constants ($1 \text{ mol}^{-1} \text{ s}^{-1}$) | Free energies (kJ mol^{-1}) |
|------|---|--|--|
| 1 | $\text{CO}(\text{NH}_2)_2 + M \rightarrow [\text{M}\cdot\text{CO}(\text{NH}_2)_2]_{\text{ads}}$ | Not elementary | 66.2 |
| 2 | $[\text{M}\cdot\text{CO}(\text{NH}_2)_2]_{\text{ads}} + \text{OH}^- \rightarrow [\text{M}\cdot\text{CO}(\text{NH}_2\cdot\text{NH})]_{\text{ads}} + \text{H}_2\text{O} + e^-$ | 1.4×10^{-17} | -28.9 |
| 3 | $[\text{M}\cdot\text{CO}(\text{NH}_2\cdot\text{NH})]_{\text{ads}} + \text{OH}^- \rightarrow [\text{M}\cdot\text{CONH}\cdot\text{NH}]_{\text{ads}} + \text{H}_2\text{O} + e^-$ | 2.3×10^{-21} | -185.1 |
| 4 | $[\text{M}\cdot\text{CO}\cdot\text{NHNH}]_{\text{ads}} + \text{OH}^- \rightarrow [\text{M}\cdot\text{CO}\cdot\text{NHN}]_{\text{ads}} + \text{H}_2\text{O} + e^-$ | 4.1×10^7 | 75.4 |
| 5 | $[\text{M}\cdot\text{CO}\cdot\text{NHN}]_{\text{ads}} + \text{OH}^- \rightarrow \text{M}\cdot\text{CO}\cdot\text{N}_2 + \text{H}_2\text{O} + e^-$ | 8.8×10^{15} | -178.2 |
| 6 | Urea molecule deprotonated by the OH^- ions | Not elementary | |
| 7 | $[\text{M}\cdot\text{CO}\cdot\text{N}_2]_{\text{ads}} + \text{OH}^- \rightarrow [\text{M}\cdot\text{CO}\cdot\text{OH}]_{\text{ads}} + \text{N}_2 + e^-$ | 7.3×10^8 | 392.7 |
| 8 | $[\text{M}\cdot\text{CO}\cdot\text{OH}]_{\text{ads}} + \text{OH}^- \rightarrow [\text{M}\cdot\text{CO}_2]_{\text{ads}} + \text{H}_2\text{O} + e^-$ | 1.6 | -156.6 |
| 9 | $[\text{M}\cdot\text{CO}_2]_{\text{ads}} \rightarrow \text{M} + \text{CO}_2$ | 4.3×10^{-65} | 1242.2 |
| | Total | | 1227.7 |

reaction mechanism, the activation energy can be minimized to 1227 kJ mol^{-1} through a certain reaction profile, as described in Table 4.

Similarly, it can be concluded from the rate constants in each intermediate elementary reaction that the desorption of CO_2 from NiOOH catalyst in ‘step 9’ is the rate-determining step, because its rate constant value ($4.3 \times 10^{-65} \text{ mol}^{-1} \text{ s}^{-1}$) is the smallest among all the steps. The thermodynamic calculation can also explain this phenomenon because the final step ($\Delta G = 1242.2 \text{ kJ mol}^{-1}$) tends to make the greatest contribution to the change of free energy during the entire reaction. By summarizing the experimental results, it is known that when CO_2 is generated on the catalyst surface, the reaction of urea molecules will be blocked due to the aggregation of CO_2 molecules. Cao et al. [75, 76] further made an electrochemical study on the mechanism for alkaline urea electro-oxidation by cyclic voltammograms (CVs) and electrochemical impedance spectroscopy (EIS). In Fig. 6a, the OOP of

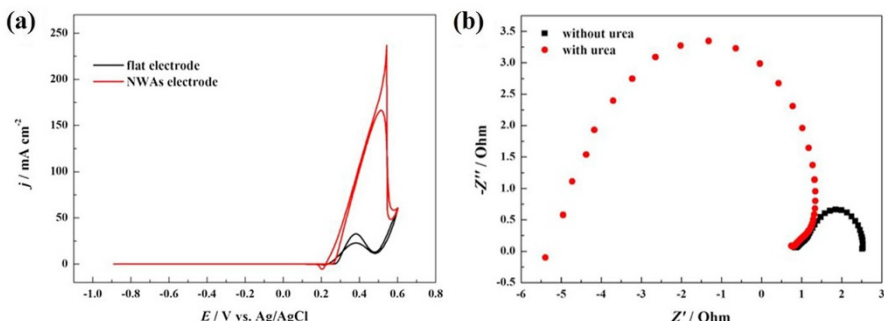


Fig. 6 **a** Cyclic voltammograms (CVs) of Ni plate and Ni nanowire array electrodes (solution: 5.0 M KOH + 0.33 M urea); **b** Nyquist plots of Ni nanowire array electrode at 0.47 V (solution: 5.0 M KOH with and without 0.33 M urea) Reproduced with permission from Ref. [75]

urea electro-oxidation on nickel nanowire arrays electrode reaches 0.25 V (vs. Ag/AgCl), which corresponds to the generation potential of NiOOH from $\text{Ni}(\text{OH})_2$, thus corresponding to indirect E-C mechanism. Compared to the nickel plate electrode, the OOP of the nickel nanowire electrode shows a certain degree of negative shift (-21 mV), which can attribute to the superior nanostructure of nickel catalyst. The reversed CV curve that suffers a sharp peak at 0.55 V is interpreted as secondary oxidation caused by the reaction intermediate. According to the DFT calculations, the surface of nickel catalyst might be covered by the intermediate product CO or CO_2 species and then the catalyst was poisoned. Ojani et al. [77] have studied the AC impedance curves of methanol electro-oxidation on the surface of Pt–Pd binary catalysts. They found that the Nyquist semi-arc showed clockwise and counterclockwise changes with the polarization potential. According to their conclusions, the reverse half arc at potentials 0.2–0.5 V (vs. SCE) represents that the electrode surface is adsorbed and covered by CO intermediate species. Afterwards, in alkaline urea oxidation process, the intermediate product CO was further electro-oxidized to form CO_2 at the high potential with the reversed scanning. The generated CO_2 follows on reacting with the alkali, resulting in a large number of surface active sites instantaneously exposed. Thus, a sudden rise of the current density appeared in the reversed CV curves (Fig. 6a). This means that the coverage and poisoning by CO_2 species on the catalyst surface was slowed down. On the other hand, because CO appeared as the intermediate product or final product, an odd reverse semi-circle was observed at 0.47 V in the Nyquist plots (Fig. 6b). Daramola et al. [74] thought that this phenomenon was due to the fact that CO and OH^- was easy to be adsorbed on Ni electrode surface during the electrochemical oxidation course. As a result, the catalyst gets poisoned on its surface, limiting the activity and causing electrode deactivation. Therefore, in order to further promote the development of alkaline urea electrolysis cells, it is imperative to develop anode catalytic materials with high activity and excellent stability.

4 Development of Anodic Catalysts for Urea Electro-Oxidation

For the purpose of improving the electrical output performance of DUFCs and the effectiveness of hydrogen production from urea electrolysis, the most significant pathway is to develop anode catalysts that can reduce onset oxidation potential (OOP) while perform their high activity. Initially, precious metal catalysts such as Ti–Pt–Ir, Ti–Pt, and Ru– TiO_2 were utilized to enhance the urea electro-catalytic performance, which obtained no obvious effect but high cost. Instead, since NiOOH has been proved as the intermediate transition catalyst towards urea electro-oxidation, recent research has paid more attention to increase the NiOOH formation efficiency of nickel-based catalyst [76]. In the literatures, nickel-based catalysts with various micromorphology and elemental composition have been optimized in order to perform low OOP while high oxidation current density. Specifically, present research work on the anodic catalyst mainly focuses on nickel-based metals, nickel-based hydroxides, nickel-based oxides, novel nickel-based compounds, and supported

nickel-based compounds, respectively. The detailed classification is summarized as follows.

4.1 Nickel-Based Metals

4.1.1 Single Nickel Metal

At the beginning, the work on nickel-based catalysts starts from the pure nickel metal. Kaulen et al. [78] proposed that nickel metal with its surface oxidant will form $\text{Ni}(\text{OH})_2$ in basic solution and further converted to NiOOH as the applied potential gradually shifts to positive. Simultaneously, the morphology and structure of the catalyst affect the catalytic performance in case that the urea electro-oxidation reaction takes place on the three-phase interface of catalyst. Low-dimensional nanostructures (such as nanowires or nanosheets) have a unique exposed crystal surface and high specific surface area, so as to provide more active sites and exhibit higher catalytic activity. Tao et al. [47] synthesized nickel nanoparticles with a size of 2–3 nm using KBH_4 reduction method, which is the smallest nickel particle reported in the literature. Compared to commercial nickel catalyst (particle size reaches 4–10 μm), their anodic nickel nano-catalysts had a much smaller size and larger surface area, resulting in a peak power density of 14.2 mW cm^{-2} in DUFCS when operated at 60°C with 1 mol l^{-1} urea as fuels and humidified air as oxidants. Yan et al. [79] and Cao et al. [75] successfully synthesized nickel nanowires with a length of several micrometers and a diameter of several tens of nanometers by means of electrodeposition method with the anodized aluminum oxide template and polycarbonate template, respectively. The nickel nanowires prepared by Yan et al. have a regular structure with a diameter of 90 nm and electrochemically active surface area (EASA) of $79.1 \text{ cm}^2 \text{ mg}^{-1}$, which performed a current density of 40 mA cm^{-2} at 0.55 V (vs. Hg/HgO). In addition, the nickel nanowire arrays prepared by Cao et al. behave a diameter of 50 nm for a single wire and an active surface area of 25.21 cm^2 . The typical SEM images of the nickel nanowire electrodes at different magnifications are shown in Fig. 7. All nanowires stand on the surface of the nickel

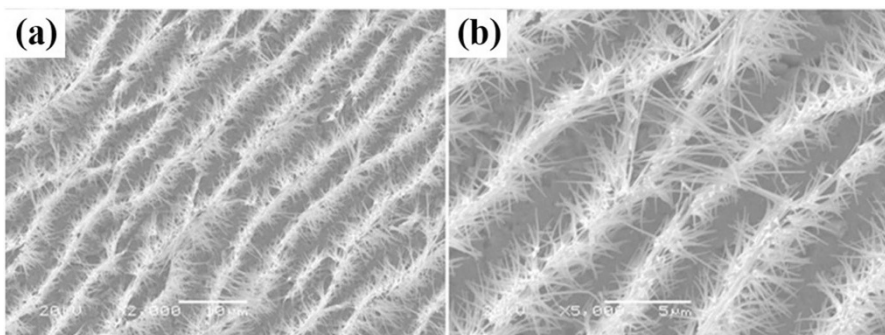


Fig. 7 SEM images of wheat-spike nickel nanowire arrays electrode at **a** low magnification and **b** high magnification Reproduced with permission from Ref. [75]

plate with the shape of “wheat ears”, leaving a gap between the “wheat” and “ear”, and the distance between the individual nanowires is also far away from each other. Electrochemical tests indicate the burr-like nickel nanowire catalyst can electro-catalyze urea oxidation at a lower OOP of 0.25 V vs. Ag/AgCl with a higher current density of 160 mA cm^{-2} in the 0.33 M urea and 5 M KOH solution at 0.50 V (Ag/AgCl). This kind of open three-dimensional array structure is conducive for diffusing the fuel to the electrode surface and fully contacting with the active sites, while the reaction product can also quickly diffuse away to the bulk solution.

4.1.2 Nickel-Noble Metal Alloys

As we mentioned above, pure nickel catalysts are prone to be poisoned during the electro-oxidation process, which may deactivate the active NiOOH. What's more, nickel catalysts always suffer shortcomings of higher starting potentials and greater polarization losses when catalyzing the oxidation of urea. Therefore, nickel is usually doped with other metals (such as noble metal or transition metal) for the preparation of binary or multicomponent metal catalysts to overcome these difficulties. King et al. [80] found some precious metals showing special resistance to be poisoned in the catalytic oxidation of urea. They introduced an electrodeposition method to synthesis Rh–Ni, Ru–Ni, Pt–Ir–Ni, and Pt–Ni alloy electrodes on the Ni substrate and compared their properties with the pure Ni catalyst. It was observed that the Ni–Rh alloy catalyst exhibited the best electro-catalytic property and stability (the maximum current density reached 80 mA cm^{-2}), which was probably owing to the doping of Rh that selectively adsorbed CO or OH^- to a certain extent, thus inhibiting the CO poisoning phenomenon and enhancing the stability of the catalyst. From the perspective of micromorphology, there existed many cracks on the relatively rough surface of Pt–Ir–Ni and Rh–Ni electrodes, leading to a high specific surface area. Therefore, the introduction of Rh and Pt–Ir can not only obtain a higher current density (about 200 times than that of the pure Ni) but also extend their catalytic life to a large extent. As a matter of fact, Rh has no catalytic activity towards urea electro-oxidation, which demonstrates that the incorporation of Rh increases the formation efficiency of NiOOH (generation potential reaches $\sim 0.45 \text{ V}$ vs. Hg/HgO) and suppresses the CO poisoning phenomenon. It is the synergy between Rh and Ni that makes the catalytic activity higher and more stable. Subsequently, Miller et al. [81] studied the influence of deposition potential and Rh loading on the catalyst morphology and current efficiency. Additionally, they found that the more negative the deposition potential, the lower current efficiency in the electrode position process. When Rh was deposited at a low potential, Rh–Ni alloy formed with a high alloying degree. Nonetheless, electrochemical results showed that when the two metals were not alloyed, which means Rh metal was deposited only on the surface of Ni, and showed the highest activity.

4.1.3 Nickel-Transition Metal Alloys

King et al. has come up with a promising research direction for the development of nickel-based alloy materials as anodic electro-catalysts in DUFCs. Unfortunately,

the high cost of Ni-Rh or other Ni-noble catalysts remains an objective problem that restricts their large-scale application for the alkaline urea electrolytic cells in the future. By contrast, cheap transition metals provide an effective solution due to the fact that doping the transition metal (such as Co, Fe, Zn, Mn, Cr, etc.) into Ni catalyst can induce more defects of nickel crystal structure to form more electrochemical active sites, thereby reducing the onset oxidation potential. Furthermore, the addition of these transition metals can also hinder the electrolysis of water (side reactions), so as to improve the electro-catalytic performance. Taking this into consideration, the researches on binary or multivariate nickel-based alloy catalysts have gradually achieved significant success in recent years. Yan et al. [82] successfully electrodeposited Ni-Co alloy on the Ti substrate. From the experimental data, it was observed that the Ni-Co alloy catalyst can greatly reduce the over-potential of urea oxidation at a maximum of 150 mV, so that the interference of side reactions such as oxygen evolution can be reduced or avoided for less energy consumption. Cao et al. [54] utilized a dynamic hydrogen template method to prepare three-dimensional porous Ni-Co electrode on nickel foam substrates. By changing the composition of the electrodeposition solution (nickel salt: cobalt salt = 10:0, 8:2, 5:5, 2:8, 0:10), they obtained Ni-Co@Ni foam electrode with different structures and morphologies (noted as Ni 10, Ni 8, Ni 5, Ni 2, Ni 0). As the corresponding SEM images shown in Fig. 8, all the deposits were porous and loose, consisting of abundant micron-sized particles. Benefiting from the unique micromorphology, Ni 2 electrode had a maximum real surface area (461.50 cm^2) as the geometric area fixed at 1 cm^2 . When applied as the anodic catalyst of DUPFC, the Ni 2 electrode also performed the best power density of 13.8 mW cm^{-2} at a low OCV (0.8 V), contributing to a proper doping of Co element, which was beneficial to the expose of more nickel active sites and the generation of NiOOH. However, the oxidation current density produced by Ni-Co catalyst is accidentally lower than the Ni catalyst in the case of equivalent amounts of Ni-Co and pure Ni catalyst. That is mainly ascribed to: (1) during the co-deposition process, the deposition rate of Co atoms is faster that might lead to partially covering the surface of Ni atoms, reducing the catalytic sites of the active ingredient Ni; (2) Co has no activity towards the electro-oxidation of urea. On

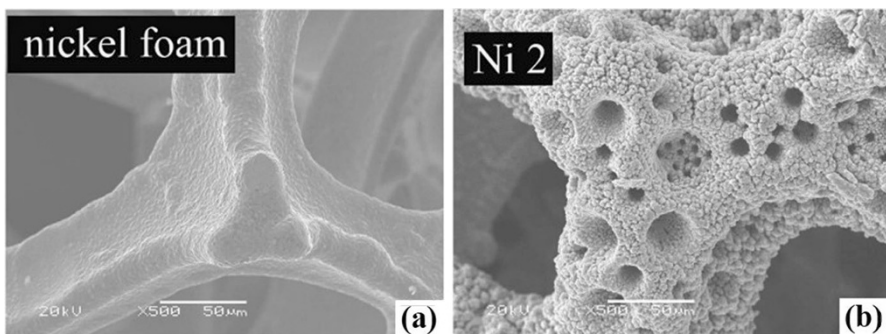
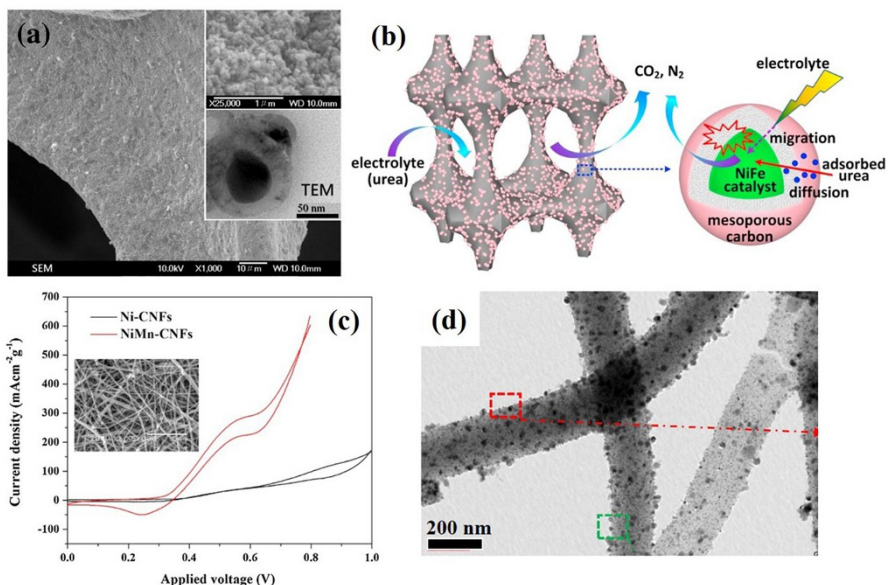


Fig. 8 SEM images of Ni foam (a) and Ni 2 (b) electrode prepared by hydrogen template method Reproduced with permission from Ref. [54]

account of the premise of equal mass for each catalyst, the absolute content of the main active component Ni changed to be lacked with gradually increasing the Co content. To sum up, although the Co-doping reduces the reaction over-potential, the current density decreased on the contrary. To overcome this drawback, Zn was further co-deposited with Ni and Ni–Co for fabricating multivariate nickel-based alloy catalysts by Botte et al. [83]. More interestingly, the electrochemical performance of Ni–Zn catalysts was three times that of Ni, while OOP was reduced by ~0.04 V. Otherwise, Ni–Zn–Co catalyst further decreased OOP by 0.08 V without dropping the current density.

Except for Co element, the doping of other transition metal elements has achieved preliminary results in the field of urea electro-oxidation more recently. Wu et al. [84] fabricated carbon-coated nickel–iron alloy nanoparticles with further adhered to the macroporous Ni foam (noted as C@Ni–Fe/NF) as unique catalysts with core–shell structure for high-efficiency electrolysis of urea. SEM and TEM images in Fig. 9a indicated an obvious carbon shell coated on Ni–Fe nanoparticles to form the ordered mesoporous structure with a diameter of 50 nm. Diagrammatic drawing of the electrolysis of urea (Fig. 9b) demonstrated that the unique C@Ni–Fe/NF electrode contributed to prevent the cores of the catalyst from being structurally damaged and allow the electrolyte to migrate and diffuse into the cavate carbon. CVs test in the 0.33 M urea and 1 M KOH solution showed that the C@Ni–Fe/NF electrode maintained a competitive current density of 100 mA cm^{-2} and OOP of 0.27 V (vs. SCE).



Remarkably, in the urea electrolysis cell employed 2 selfsame electrodes for the sake of sustaining urea electrolysis and hydrogen production, the C@Ni–Fe/NF reached a greater current efficiency value ca. 62% at 0.6 V than NiFe/NF (52%) or Ni/NF (44%). Barakat et al. [85] decorated nickel and manganese nanoparticles on carbon nanofibers (noted as NiMn-CNFs) by high-temperature calcination of electrospun mats method. The normal TEM image (Fig. 9d) displayed that the prepared nanofibers composed of amorphous matrix decorated by uniformly distributed nanoparticles. CVs as shown in Fig. 9c, the NiMn-CNFs electro-catalyst performed the catalytic activity of $300 \text{ mA cm}^{-2} \text{ g}^{-1}$ at 0.5 V with an OOP of 290 mV. Compared with pure Ni-CNFs, the incorporation of Mn elements distinctly enhanced the electro-catalytic activity as well as lowered the OOP toward urea electro-oxidation. Considering that the Cr element was rarely noticed in the nickel-based multi-metal field, Singh et al. [86] used direct borohydride reduction to synthesize NiCr/C electrode as a stable catalyst for urea oxidation. The Cr content in the electro-catalyst layers was optimal by dominating the atomic ratio of nickel salt and chromium salt in the reaction solution. The results showed that the electro-catalyst with 40% amount of Cr (noted as Ni₆₀Cr₄₀/C) exhibited the best catalytic performance of 90 mA cm^{-2} at a potential of 0.55 V vs. Ag/AgCl, which confirmed the increase in the Ni²⁺/Ni³⁺ active sites on the electrode surface. Tafel slope of the Ni₆₀Cr₄₀/C catalyst was observed as $16 \text{ mV decade}^{-1}$, which was worse than $30 \text{ mV decade}^{-1}$ of Ni/C, indicating improved charge-transfer kinetics. On the other hand, Shi et al. [87] noticed that the doping of Mo species was also selectable for enhancing the catalytic performance of bare Ni catalyst since the Mo-doping catalyst exhibited a strong anti-poisoning characteristic for the carbon monoxide intermediate. Therefore, they fabricated Ni–Mo composite nanocatalysts on graphene support (Ni–Mo/graphene) by simple reduction methods. The effect of doping amount of Mo species on the catalyst structure as well as properties was investigated in detail. Consequently, the optimal Ni₂Mo₁/graphene catalyst with selected meso-porous construction (particle size: 20–40 nm, pore size: 3.75 nm) exhibited higher catalytic current (128 mA cm^{-2} at 0.53 V) and decent kinetics (Tafel slope: 120 mV dec^{-1} , OOP: 0.39 V) by comparison with the Ni/graphene catalyst in 0.33 M urea and 1 M KOH electrolytes. It was the premium structural/electronic effects between Mo species and Ni³⁺ that contributed to the outstanding activity for the electro-oxidation of urea at the Ni–Mo/graphene catalyst.

4.2 Nickel-Based Hydroxide

4.2.1 Monovalent Nickel Hydroxide

Nickel hydroxide has a distinctive layer structure that results in two types of crystals: $\alpha\text{-Ni(OH)}_2$ and $\beta\text{-Ni(OH)}_2$. The randomly stacked non-stoichiometric Ni(OH)_{2-x} formed the c-axis of $\alpha\text{-Ni(OH)}_2$ (i.e., layered stacking direction), therefore, extraneous anions are able to intercalate between layers to counteract the positive charge of based layer. According to the size of the inserted anion, the spacing of $\alpha\text{-Ni(OH)}_2$ on the bottom surface is distributed as 7.5–31.7 Å, which is conducive

for the electrolyte ions to transfer on the inner surface of layer. In addition, Liang et al. [88] mentioned that Ni(OH)_2 monolayers separated from its matrix can provide more contact surfaces for the molecules and catalysts, thus exhibiting a higher electrochemical performance. However, $\alpha\text{-Ni(OH)}_2$ was unstable in basic environments, which was simply changed to $\beta\text{-Ni(OH)}_2$ according to the research of Kamath et al. [89]. The closely arranged internal $\beta\text{-Ni(OH)}_2$ layers with minimal interlayer spacing (surface area) hinder the liquid electrolyte from entering the $\beta\text{-Ni(OH)}_2$ layer, therefore causing the low electrochemical activity. From the above principle, although much attention has been paid to the structure and morphology, the crystal form of Ni(OH)_2 is also worth investigating [90].

Wang et al. [91] successfully fabricated two-dimensional Ni(OH)_2 nanosheets catalyst by polishing layered Ni(OH)_2 , the size of which range from several hundred nanometers to $1\ \mu\text{m}$ in length and $1\ \text{nm}$ in thickness. XRD results showed that the layered sheets with an interlayer distance of $2.67\ \text{nm}$ were arranged along the c axis, judging as $\alpha\text{-Ni(OH)}_2$ phase. From the electrochemical measurements, the $\alpha\text{-Ni(OH)}_2$ nanosheets reduced the OOP by $100\ \text{mV}$ and enhanced the oxidation current by $154\ \text{mA cm}^{-2}\ \text{mg}^{-1}$ relative to bulk Ni(OH)_2 , whereas this synthetic strategy has a low yield that needs to be ameliorated. Wang et al. prepared one-dimensional (1D) Ni(OH)_2 nanoribbons by convenient hydrothermal strategy [92]. The as-synthesized nanoribbons displayed a thickness of $15\text{--}20\ \text{nm}$ with several micrometers in length and a surface area of $54.9\ \text{m}^2\ \text{g}^{-1}$ via BET test. From the XRD pattern, it was seen that the nanoribbon belong to $\beta\text{-Ni(OH)}_2$ phase. The current density was ca. $7\ \text{mA cm}^{-2}\ \text{mg}^{-1}$, greatly lower than the α phase. These differences demonstrate that the crystal form of Ni(OH)_2 has a great influence on the urea electro-oxidation performance.

Low-dimensional nanomaterials have been recognized to exhibit superior physicochemical properties, which can greatly reduce the over-potential and increase the current density. Ji et al. [93, 94] fabricated open-ended Ni(OH)_2 nanotubes via electrochemical deposition method using hexagonal zinc oxide sphere templates. This kind of nanostructure with openness and connectivity make it easier to transport electrons and urea molecules. Its electro-oxidation current reached a competitive value of $100\ \text{mA cm}^{-2}\ \text{mg}^{-1}$ while the OOP was lowly obtained at $0.29\ \text{V}$. Recently, Ye et al. [95] successfully prepared 3D Ni(OH)_2 catalysts on Ni foam substrate with different nanostructures (Fig. 10) through a facile template-free strategy. Remarkably, nano-sheet Ni(OH)_2 with ultrathin thickness exhibited special 3D structures, allowing the reactants to touch the surface of the electro-catalysts. The oxidation current density of nano-sheet Ni(OH)_2 catalyst reaches the highest current of $337\ \text{mA cm}^{-2}$ at $0.45\ \text{V}$ in $5\ \text{mol l}^{-1}\ \text{KOH}$ solutions containing $0.6\ \text{mol l}^{-1}$ urea (Fig. 11a). The DUPFC employing nano-sheet $\text{Ni(OH)}_2/\text{Ni}$ foam as anode and Pd NP/C@TiC as cathode displays an OCV at $0.86\ \text{V}$ and the highest power density at $19.7\ \text{mW cm}^{-2}$ among the obtained Ni(OH)_2 anodic catalysts (Fig. 11b).

4.2.2 Doped Nickel-Based Hydroxide

Based on the excellent electrochemical activity of nickel-based bimetallic or poly-metallic catalysts, the introduction of doped nickel-based hydroxide is aimed at the

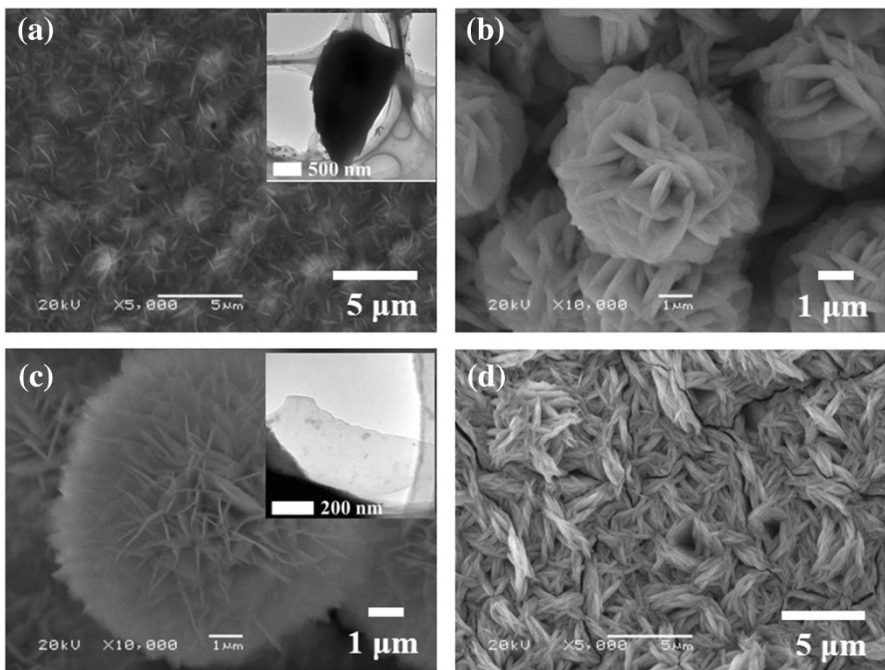


Fig. 10 SEM images of the sheet-like (**a**); flower-like (**b**); nano-sheet (**c**); twine-like (**d**) $\text{Ni(OH)}_2/\text{Ni}$ foam, respectively. The inset of **a**, **c** shows TEM images of the corresponding sheets Reproduced with permission from Ref. [95]

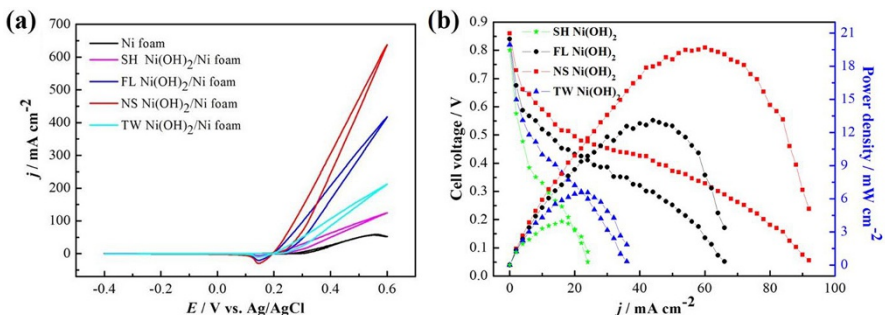


Fig. 11 Comparative CVs of four $\text{Ni(OH)}_2/\text{Ni}$ foam with different morphologies (**a**); comparative cell performance of DUPFC on these four anodes and Pd/C@TiC cathodes, catholyte was 2.0 M H_2O_2 and 2.0 M H_2SO_4 (**b**) Reproduced with permission from Ref. [95]

same goal of decreasing over-potential as well as obtaining considerable electro-catalytic properties. Specifically, followed by the object of Ni-Co bimetallic catalyst, Botte et al. [96] fabricated the $\text{Ni}_x\text{Co}_y(\text{OH})_2$ ($x:y$ represents the observed atom ratio of Ni:Co in samples) catalysts using a similar electrodeposition method, and investigated the influence of various Ni/Co ratios on their electrochemical properties. It

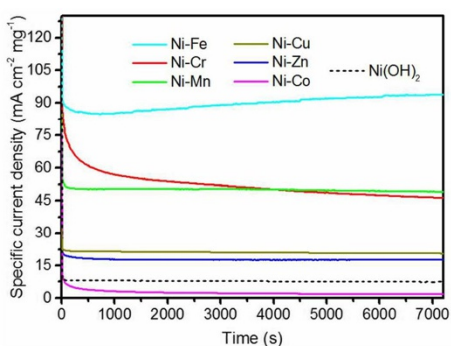
was observed that as the proportion of Co increased, the fragments of the Ni/Co hydroxide gradually decreased until the Co molar fraction reached 43% (atom%), forming an advantageous network structure while largely reducing the OOP by up to 150 mV. Nevertheless, when the molar fraction of Co was higher than 73%, its structure became suddenly tight with the surface area sharply dropped. On the other hand, the doping of other corresponding transition metal elements was further reflected in Xu et al.'s work [97]. Systematically, a series of various nickel-based bimetallic hydroxides (Ni–M hydroxide; M = Fe, Co, Cu, Cr, Mn, Zn, respectively) were fabricated on carbon cloth via one-step hydrothermal growth to investigate the effect of different element compositions on urea electro-oxidation performance. Consequently, the Ni–M bimetallic hydroxides showed several distinct morphologies as the Ni–Zn and Ni–Mn nanosheet, Ni–Co and Ni–Cu nanowire, as well as Ni–Cr and Ni–Fe nanoparticle. Correspondingly, the Ni–M hydroxides with their respective nanostructures showed a certain degree of electro-catalytic effect toward urea electro-oxidation. As shown in Fig. 12, in comparison to Ni(OH)_2 ($7.5 \text{ mA cm}^{-2} \text{ mg}^{-1}$), Ni–Fe achieved a greatly enhanced current of $\sim 95 \text{ mA cm}^{-2} \text{ mg}^{-1}$ at 0.5 V, followed by Ni–Mn ($54 \text{ mA cm}^{-2} \text{ mg}^{-1}$), Ni–Cr ($52 \text{ mA cm}^{-2} \text{ mg}^{-1}$), Ni–Cu ($23 \text{ mA cm}^{-2} \text{ mg}^{-1}$), and Ni–Zn ($20 \text{ mA cm}^{-2} \text{ mg}^{-1}$), apart from the decreased activity of Ni–Co ($3.5 \text{ mA cm}^{-2} \text{ mg}^{-1}$). Simultaneously, the Ni–Mn and Ni–Co hydroxides showed another contribution to the onset oxidation potential by reducing from 0.42 V of Ni(OH)_2 catalyst to 0.35 V of Ni–Mn catalyst and 0.30 V of Ni–Co catalyst, respectively.

4.3 Nickel-Based Oxide

4.3.1 Monovalent Nickel Oxide

As mentioned above, highly active $\alpha\text{-Ni(OH)}_2$ tends to be simply converted to $\beta\text{-Ni(OH)}_2$ with low electrochemical activity in an alkaline environment. Therefore, Wu et al. [98] transformed $\alpha\text{-Ni(OH)}_2$ through an annealing treatment into NiO to maintain its stability. The ordered mesoporous NiO nanosheets were vertically and evenly arranged on the nickel foam with low crystallinity and small particle size (about 5 nm), in which the arrangement provided amounts of large

Fig. 12 Chronoamperometric curves of Ni–M hydroxides on CFC at 0.5 V (vs. Ag/AgCl) in the 1.0 M NaOH and 0.33 M urea solution Reproduced with permission from Ref. [97]



pore channels with a size of 300–500 nm. The pore size of NiO nanosheets was mainly distributed between 2 and 50 nm, and most of them were mesopores with a size of 4 nm, providing a larger open space and expediting the transport of urea, gases, and electrolyte. In 1 M KOH solution that contains 0.33 M urea, the NiO nanosheet/Ni foam demonstrated an enhanced current of 400 mA cm^{-2} and a relatively lower OOP of 0.27 V (vs. Ag/AgCl) by comparison with NiO bulk/Ni foam and NiO nanosheet/SS (stainless-steel film), implying the catalytic activity of NiO strongly depended on their configuration and substrate. Yue et al. [99] recently reported a versatile nickel oxide-hybrid nanoarray catalyst that grown on Ni foam substrate (NiO–Ni/NF). It was observed that the nano-sheet NiO–Ni appeared roughly and thickly with an average pore size of 53 nm between the arrayed sheets (Fig. 13a, b). Obviously, the Ni particles attached to the nano-sheet NiO surface (Fig. 13c). This 3D open nanoarray structure with Ni nanoparticle film adhered to the NiO nanosheets surface tends to form a synergistic effect on the contact interface of Ni and NiO, enlarged EASA, and improved conductivity. Specially, stable multistep chronopotentiometric curve (Fig. 13d) implied both good long-term stability and superior mass transport of NiO–Ni catalyst.

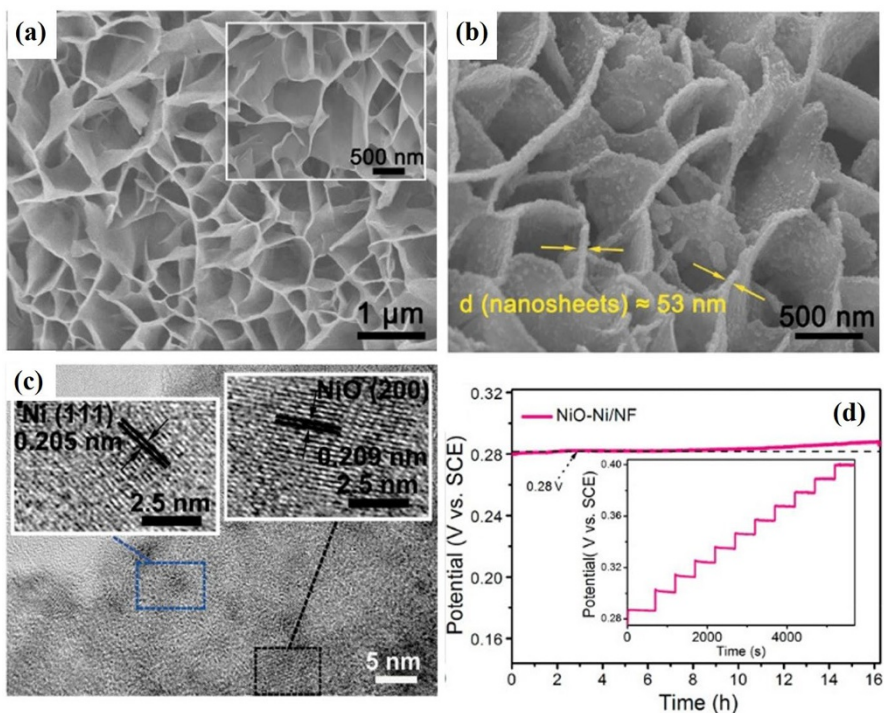


Fig. 13 SEM images of **a** NiO/NF and **b** NiO–Ni/NF; **c** HRTEM images of nano-sheet NiO–Ni; **d** chronopotentiometric curve of the NiO–Ni/NF electrode at constant 10 mA cm^{-2} . *Inset* displays the multipotential procedure under various currents Reproduced with permission from Ref. [99]

4.3.2 Nickel-Based Composite Oxides

Due to the deactivation of some pure nickel-based catalysts, the studies on the mixed oxides have been investigated extensively [100–102]. Ding et al. [103] successfully synthesized spinel-type NiCo_2O_4 as urea electro-catalyst by chemical deposition and simple annealing treatment. The formed NiCo_2O_4 nanoparticles have a size of about 10 nm, and these particles are agglomerated to form a rough surface with large coarse particles during the calcination stage. This loosely packed structure forms a lot of mesopores, while the pore size mostly distributed around 12 nm, providing a large surface area ($190.1 \text{ m}^2 \text{ g}^{-1}$). Electrochemical tests show that the current density of NiCo_2O_4 catalyst increased by twice the monovalent NiO , the onset potential decreased by 80 mV, and both the durability and stability were greatly enhanced. Thus, the composition and structure of composite oxides deserve further study [44]. More recently, spinel nickel manganese oxides (MnNi_2O_4 , NiMn_2O_4 , and $\text{Ni}_{1.5}\text{Mn}_{1.5}\text{O}_4$) were applied as the urea electro-catalyst by Sivakumar et al. [104]. Cyclic voltammetric measurements showed that the $\text{Ni}_{1.5}\text{Mn}_{1.5}\text{O}_4$ (loading as $50 \mu\text{g cm}^{-2}$) modified the electrochemical performance at 0.29 V with the highest current of 6.9 mA cm^{-2} (seven times better than the NiO and four times better than the MnNi_2O_4 and NiMn_2O_4), which was possibly attributed to the appearance of different phases. Liang et al. [88] fabricated the $\text{NiMoO}_4 \cdot x\text{H}_2\text{O}$ nanosheets on nickel foam ($\text{NiMoO}_4 \cdot x\text{H}_2\text{O}$ NS/NF) by hydrothermal synthesis at 160°C . The EASA of $\text{NiMoO}_4 \cdot x\text{H}_2\text{O}$ NS/NF calculated by Randles–Sevcik equation (Eq. 9) was valued at 0.47 cm^2 , which was 1.35 times that of Ni(OH)_2 NAs/NF. Electrochemical impedance spectroscopy (EIS) analysis also exhibited much lower impedance for the $\text{NiMoO}_4 \cdot x\text{H}_2\text{O}$ NAs than that of the Ni(OH)_2 NAs and resulted in a markedly faster kinetics towards urea electro-oxidation. As a consequence, it was meaningful that the incorporation of Mo elements could be beneficial to the elimination of surface deposition on the normal nickel hydroxide catalysts, thus providing a higher catalytic activity with good stability.

$$I_p = 2.99 \times 10^5 nAC_{\text{urea}} [(1 - \alpha)n_0]^{0.5} D^{0.5} v^{0.5} \quad (9)$$

Herein, I_p , A , n , C , v , and D represent the peak current, the EASA, the number of electrons involved in the reaction, the concentration of the reactant, the scan rate, and the diffusion coefficient of the reactant species, respectively.

More recently, highly porous rod-like Ni–Mo–O catalysts were designed for efficient water-to-hydrogen conversion via alkaline urea electrolysis [105]. Typically, the pre-synthesized $\text{NiMoO}_4 \cdot x\text{H}_2\text{O}$ nanorods (via one-step hydrothermal) were treated with Ar-protected annealing process to obtain the porous rod-like NiMoO_4 (named NiMoO-Ar). When switching the shielding gas from Ar to H_2/Ar , the annealing process generated the derived $\text{Ni}/\text{NiO}/\text{MoO}_x$ composite (named NiMoO-H_2). From the XPS results of NiMoO-Ar , it was noted that the incorporation of Mo with high oxidation state of +6 enabled an easier transition of Ni^{2+} to Ni^{3+} . Consequently, in an alkaline electrolyte, the porous rod-like NiMoO_4 performed exceptional electro-catalytic property for urea oxidation reaction (UOR) while derived $\text{Ni}/\text{NiO}/\text{MoO}_x$ exhibited platinum-like activity for hydrogen evolution

reaction (HER) (Fig. 14a, b). A mere voltage of 1.38 V was needed to reach the current of 10 mA cm^{-2} in this electrolytic cell, and the excellent catalytic performance can maintain an exceptional stability during the 25-h test (Fig. 14c). Actually, more similar bifunctional catalysts as the Ni–Mo–O will be further described in the next section.

4.4 Novel Nickel-Based Compounds

Furthermore, there have been exiting a series of novel nickel-based compounds (mainly referring to nickel-based sulfides, phosphides, selenides, etc.). Considering that these nickel-based sulfides, phosphides, and selenides have also been successfully applied in HER because of their good conductivity, excellent stability, and superior electrochemical performance, it seems more meaningful to design them as bifunctional catalysts for both highly efficient electrolysis of urea as well as electrochemical hydrogen production in the overall water splitting system (as shown in Fig. 15) [106–111]. More importantly, the development of these series of catalysts is hopeful for promoting the application of urea electrolysis in the field of future energy storage.

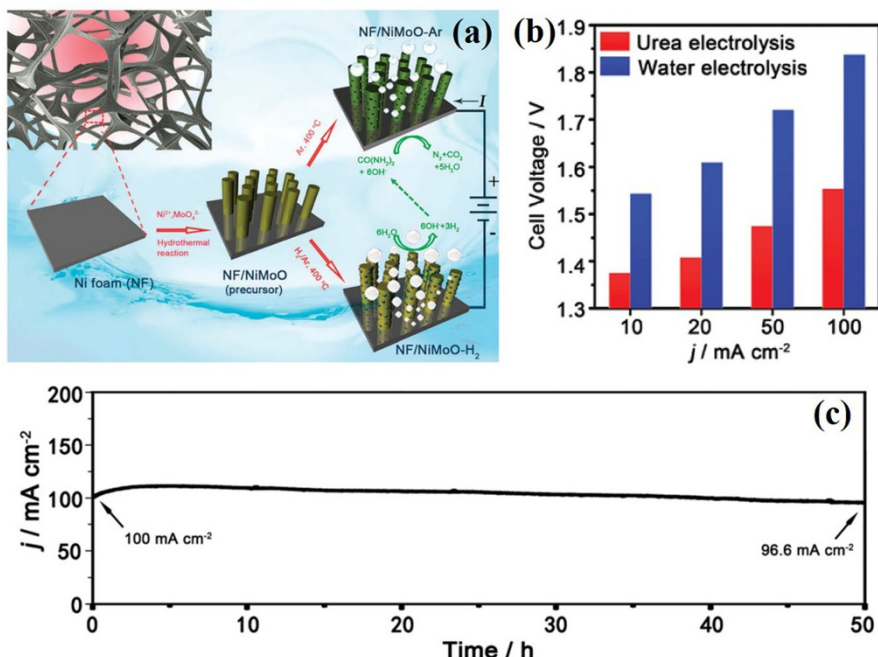


Fig. 14 **a** Schematic diagram of the preparation of NiMoO-Ar for UOR catalyst and NiMoO-H₂ for HER catalyst; **b** comparison of the cell voltage required to reach different current densities for urea electrolysis and water electrolysis; **c** long-term stability test of urea electrolysis (cell voltage = 1.58 V) Reproduced with permission from Ref. [105]

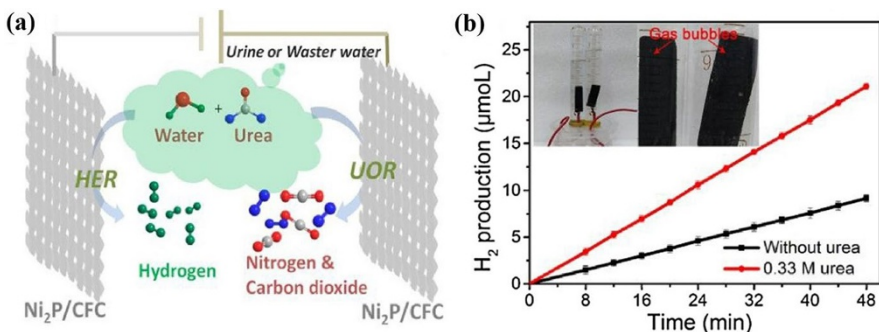


Fig. 15 **a** Schematic diagram of $\text{Ni}_2\text{P}/\text{CFC}$ catalysts for the two-electrode system of urea electrolysis; **b** a comparison of H_2 production amount for water-splitting system with and without urea at the cell voltage of 1.8 V Reproduced with permission from Ref. [106]

Earlier in 2016, mesoporous Ni–P nanomaterial was introduced as promising electrocatalysts for urea electro-oxidation by Ding et al. [65], considering its high electrical conductivity and metalloid properties. They proposed that non-metal phosphorus was a prospective doping element for enhancing the catalytic activity towards Ni-based hydroxide and oxide electro-catalysts, which could be primarily ascribed to the superiorities: firstly, the electronic configuration of Ni compounds can be effectually adjusted by adding the element of phosphorus for preventing their poisoned characters. Secondly, more efficient electro-active sites are available from changing the electronic density of Ni clusters [112]. In return, the peak current density of the Ni–P nanocatalysts reached 70 mA cm^{-2} , while the OOP was merely 1.37 V (vs. RHE), which showed a more enhanced performance than Ni nanocatalysts (62 mA cm^{-2} , 1.42 V). As followed, Ye et al. [113] designed a unique porous Ni_2P nanoflower by facile hydrothermal and phosphating methods. SEM and TEM images showed that Ni_2P performed an overall 3D flower-like morphology with many nano-sized holes (diameters ranging from 30 to 90 nm) presented on each single Ni_2P nanosheet surface (Fig. 16), which assured the reactants simply touch the catalyst surface and thus accelerated the interfacial reaction of urea electro-oxidation. Remarkably, the EASA value of porous Ni_2P nanosheet was ~ 7 times or higher than Ni(OH)_2 , thus indicative of more $\text{Ni(OH)}_2/\text{NiOOH}$ active sites. Except for achieving maximum current of 490 mA cm^{-2} at 0.5 V, the OOP of Ni_2P negatively shifted 30 mV to 0.24 V (vs. Ag/AgCl). For further application in urea-based electrolytic hydrogen generation systems, Liu et al. [114] prepared the nickel phosphide nanoflakes array on carbon cloth (Ni_2P NFs/CC) (Fig. 17a) as bifunctional UOR and HER electro-catalysts. As for UOR, it reached an outperforming current of 110 mA cm^{-2} at 0.45 V (vs. Ag/AgCl) in the 1.0 M KOH solution containing 0.5 M urea. As for both UOR and HER in the two-electrode alkaline electrolyzer system, it demanded a cell voltage of 1.30 V to obtain 50 mA cm^{-2} , 580 mV less than pure water splitting for achieving the same current density (Fig. 17b). Remarkably, the authors specially provided the XRD patterns and Raman spectra for Ni_2P before and after UOR electrolysis to demonstrate the unique formation of the NiOOH active

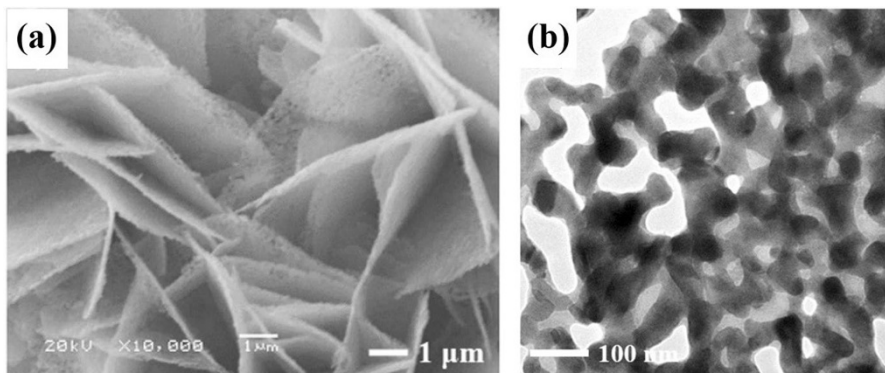


Fig. 16 SEM (a) and TEM (b) images of porous Ni_2P nanoflower Reproduced with permission from Ref. [113]

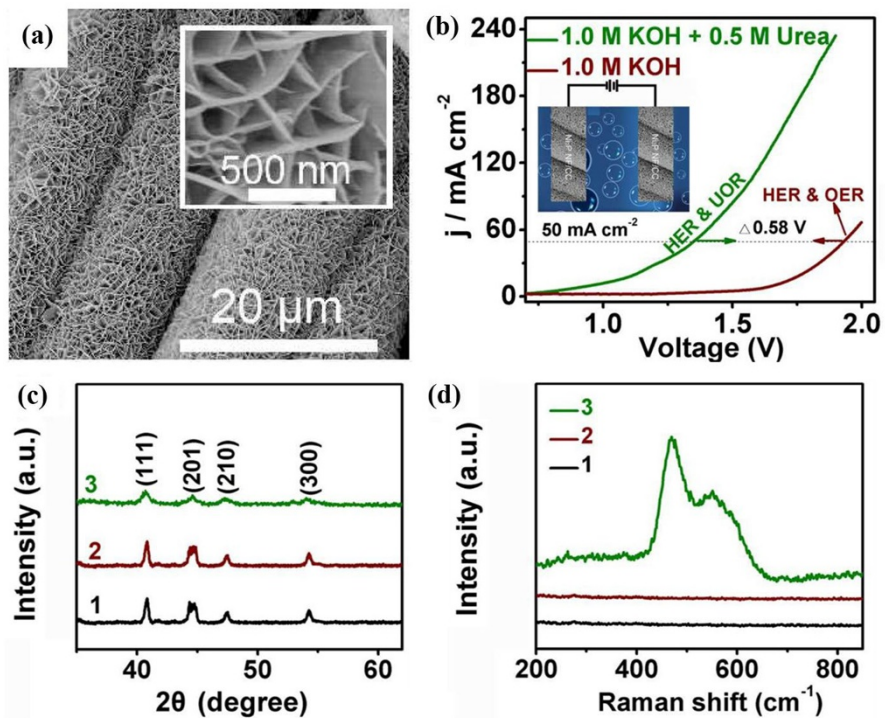


Fig. 17 **a** SEM images of Ni_2P nanoflakes array on carbon cloth in Liu's work; **b** this catalyst as an efficient and durable electrode for both UOR and HER; **c** XRD patterns and **d** Raman spectra for Ni_2P before (curve 1) and after HER (curve 2) and UOR (curve 3) electrolysis Reproduced with permission from Ref. [114]

species, indicating a similar E-C mechanism of nickel-based phosphides to the previous literature. More importantly, the voltage performance of Ni_2P for urea-based water splitting is better than that of the nano-sheet NiCoP arrays on carbon cloth (noted as NiCoP NS/CC) prepared by Xie et al. [115]. The two-electrode voltage of Ni_2P is durable with 1.45 V to afford 50 mA cm^{-2} .

Simultaneously, studies on sulfides and selenides are also emerging in the last 2 years [116]. Wang et al. [117] synthesized hierachic coral-like Ni-Mo sulfides supported on Ti mesh (HC-NiMoS/Ti) by simple hydrothermal and sulfuration treatment. The SEM images (Fig. 18a) displayed the outward nanorods on Ti mesh surface formed a special hierarchical coral-like nanostructure, offering a large number of exposed active sites with highly specific surface area. LSV curves were tested in the 0.5 M urea and 1.0 M KOH solution to obtain Tafel plots of the HC-NiMoS/Ti and comparative samples (2D-NiMoS/Ti, 2D-NiS₂/Ti, RuO₂/Ti) (Fig. 18b). It was found that the HC-NiMoS/Ti catalyst had the smallest Tafel slope of 19.2 mV dec^{-1} , much competitive with the reported nickel-based oxides, hydroxides or phosphide etc. Especially, Se-Ni(OH)₂@NiSe nanowires in situ formed on nickel foam in Tang et al.'s [118] study as efficient UOR catalysts, which demonstrated an achievement of only 0.37 V vs. SCE to drive the current density of 100 mA cm^{-2} . DFT calculations in Fig. 19 investigated the electronic structure of Se-Ni(OH)₂ [118]. It was observed that the incorporation of Se resulted in an obvious change of Ni(OH)₂ from primary semiconductive (band gap = 2.2 eV) to metallic state (band gap = zero) (Fig. 19a, b), which greatly enhanced the conductivity. As well, the adsorption strength of CO₂ on the surface of pristine Ni(OH)₂ was weakened from 0.92 to 0.20 eV on the surface of Se-Ni(OH)₂. What's more, the energy barrier of the carbon dioxide desorption was reduced from 1.11 to 0.31 eV, as displayed in Fig. 19c, d. That is, the DFT calculations further revealed that the reinforcement of UOR was mostly related to the lowered ad/desorption energy barrier of carbon dioxide on the surface of Se-Ni(OH)₂ with a rapid kinetics. Fortunately, their reports contribute to open up a promising new direction to develop catalysts with high performance for the application in fuel cells or energy-saving fields in the future.

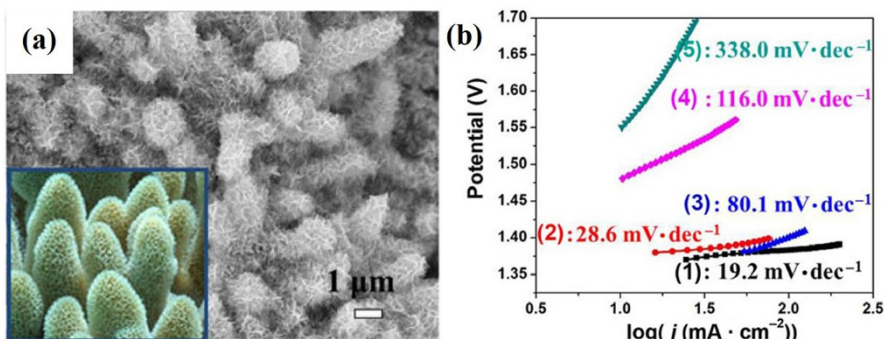


Fig. 18 **a** SEM image of HC-NiMoS/Ti electrode; **b** Tafel plots for UOR in the 1.0 M KOH solution containing 0.5 M urea: numbers represent (1) HC-NiMoS/Ti, (2) 2D-NiMoS/Ti, (3) 2D-NiS₂/Ti, (4) RuO₂/Ti, and (5) HC-NiMoS precursor/Ti, respectively. Reproduced with permission from Ref. [117]

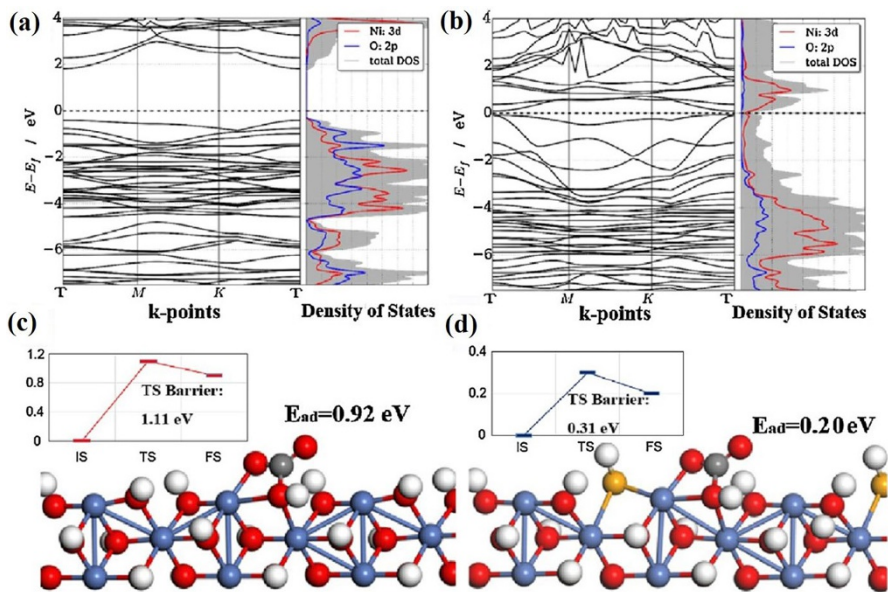


Fig. 19 The band structures and densities of state for **a** pristine and **b** Se–Ni(OH)₂ monolayer; carbon dioxide adsorptions on **c** pristine and **d** Se–Ni(OH)₂ surface (*insets* display the energy profile of the desorption process). *IS* initial state, *TS* transition state, *FS* final state; C, H, O, Ni and Se atoms are colored grey, white, red, blue, and yellow Reproduced with permission from Ref. [118]

4.5 Supported Nickel-Based Compounds

It is out of doubt that conventional carbon or non-carbon catalyst carriers (mainly referring to nickel foam, carbon fiber cloth, titanium mesh, etc.) have been proven as excellent stable current collectors for alkaline urea electro-oxidation. Nevertheless, novel catalyst supports such as graphene have strongly promoted the electrochemical reaction rate due to their superior electrochemical activities and favorable synergy between the catalyst and support, thereby attracting more attention in recent years. It is generally believed that suitable electrocatalyst supports should have good electrical conductivity, large specific surface area, reasonable pore structure, and good corrosion resistance. In view of the shortcomings of traditional conductive carbon black carriers, other advanced carbon materials (for instance: carbon nanotubes or graphene) and non-carbon materials are considered to be reliable urea electro-oxidation catalyst carriers. Briefly, the supported catalysts can be distinguished from several types of carriers as follows.

Graphene is defined as a 2D honeycomb crystal consisting of carbon atoms only one layer thick. The spheroidal arrangement between these carbon atoms can form a honeycomb-like framework, which commonly provides excellent mechanical properties, thermodynamic properties, electrical conductivity, chemical stability, and large surface area, respectively, and is therefore widely employed as the catalyst carrier [119, 120]. Wang et al. [121] prepared a Ni-graphene composite catalyst via the electrochemical reduction method and obtained the twice current density as

high as that of the pure nickel catalyst. On the one hand, it was due to the synergy between nickel and graphene that greatly increased the anti-CO poisoning ability of the active component. On the other hand, the large specific surface area and high electrical conductivity of graphene are in favor of the growth of more active sites for catalytic process. In turn, the catalytic performance was optimized.

Carbon nanotubes (CNT) as a type of one-dimensional hollow tubular carbon material equipped with good conductivity, stable chemical properties, and high mechanical strength, are also promising catalyst carriers for the employment in urea electro-oxidation [41, 56, 122, 123]. Wang et al. [124] fabricated the Ni-WC catalysts utilizing multi-walled carbon nanotubes (MWCNT) and activated carbon as carriers, respectively. It was found that the surface area of Ni-WC/MWCNT catalyst was nearly 1.5 times that of the WC/C catalyst under the premise of uniform carrier content. As a result, in the 0.33 M urea and 1 M KOH solution, the oxidant current on Ni-WC/MWCNT catalyst was three times that of the WC/C catalyst, and the resistance of the former was $4\ \Omega$ less than that of the latter, simultaneously. Kakati et al. [125] adopted a facile microwave-assisted method to design the MWCNT-supported sodium nickel fluoride with hollow nano-cube structures (SNF–MWCNT), according to an in situ template mechanism. The dispersed MWCNTs in the reaction medium provided amounts of attaching space for the adsorption of $[\text{BMIM}]^+$ ions and thereby anchored cubic NaF deposits on the surface of MWCNT. An interaction between F and Ni and the $\text{Ni}^{2+}/\text{Ni}^{3+}$ oxidation–reduction couple enriched Ni^{3+} surface was identified as the as-prepared SNF–MWCNT. Consequently, the hollow and porous SNF attached on MWCNT with the superior catalytic activity of $3.12\ \text{A cm}^{-2}\ \text{mg}^{-1}$ demonstrates a potential candidate for the urea electro-catalysts.

More interestingly, carbon sponge was initially designed with a three-dimensional (3D) porous structure as the efficient carrier for nickel electro-catalyst. This type of Ni@carbon sponge (Ni@CS) electro-catalysts with porous structure was prepared by the combination of carbonization and electro-deposition (Fig. 20a). Firstly, the progress began with a mild carbonization for the preparation of highly conductive 3D network-like carbon sponge, facilitating the entry

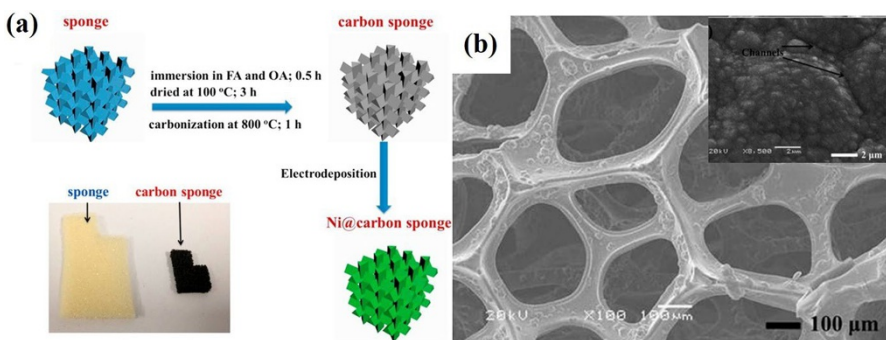


Fig. 20 **a** Schematic diagram of the preparation process of Ni@carbon sponge electrode; **b** low-magnification and high-magnification (inset image) SEM images of the Ni@carbon sponge electrode Reproduced with permission from Ref. [126]

and exit of reactant and product. Continuously, nickel nanoparticles were electro-deposited on the CS surface to form Ni@CS anode, which had a large surface area (Fig. 20b). The calculated EASA of Ni@CS anode was 18 times that of the Ni/Ti flat anode. The entire fabrication process avoided the introduction of binders and therefore exhibited a high catalytic activity, stability, and durability. Specifically, in the 0.1 M urea and 1 M NaOH, Ni@CS catalyst reached a peak current density of 290 mA cm^{-2} , which was 18 times that of the flat Ni/Ti catalyst. During the 20-min chronoamperometric test, the value of current density at the four applied potentials (0.45, 0.40, 0.35, and 0.30 V) demonstrated almost no attenuation owing to the robustness of the carbon sponge skeleton and deposited Ni catalyst [126].

5 Conclusions

A review of recent advances in the electro-oxidation of urea for DUFCs and urea electrolysis is presented. When urea is used for anodic fuel in DUFCs, the device can purify waste water as well as generate power in the meantime. In addition, as a hydrogen-rich chemical fuel, urea can also be electrolyzed to produce hydrogen for energy storage in the near future. The exact mechanisms of urea decomposition are pretty different in alkaline and neutral mediums and therefore separately discussed in detail. More importantly, the development of anodic electro-catalysts is significant for optimizing the electrochemical properties of both DUFCs and urea electrolysis cell, which is primarily summarized in our review (as shown in Table 5). Pure nickel, nickel oxides, or hydroxides still suffer from obstacles such as poor conductivity, inadequate stability, and lack of resistance to CO poisoning at present, which lead to high onset oxidant potential, poor cycling, or severe polarization. Therefore, future research on the nickel-based catalysts may be focused on solving the above challenges from several aspects: On the one hand, improving catalyst preparation methods is necessary to synthesize the nanostructured catalysts with controllable morphologies. The rapid development of nanotechnology provides a great technical support for fabricating catalysts with higher performance. On the other hand, novel nickel-based compounds such as phosphides and selenides show a competitive catalytic current density and relatively low over-potential. Moreover, the incorporation of other transition metals into these compounds is expected to satisfy the demands of bi-functional catalysts for both production of hydrogen and electrolysis of urea in the overall water splitting systems. The introduction of novel and promising catalyst supports manifests a great potential in improving the conductivity, stability, and electrochemical activity of the catalysts.

Table 5 Comparison of electro-catalytic performance of recent advanced Ni-based electro-catalysts derived from CVs in basic medium

| Anodic catalysts | Electrolytes | Current density (mA cm ⁻²) | Peak potential and OOP (V vs. Hg/HgO) | Refs. |
|---|-------------------------|---|--|-------|
| Ni nanoparticles | 0.33 M urea + 5 M KOH | 29 | 0.52/0.42 | [71] |
| Ni nanowires | 0.33 M urea + 1 M KOH | 95 | 0.65/0.50 | [79] |
| Ni nanowires | 0.33 M urea + 5 M KOH | 160 | 0.52/0.27 | [75] |
| Ru–Ni | 0.33 M urea + 1 M KOH | 72 | 0.70/0.45 | [80] |
| Rh–Ni | 0.33 M urea + 1 M KOH | 82 | 0.70/0.45 | [80] |
| Ni–Co nanowires/Ti | 0.33 M urea + 1 M KOH | 55 | 0.60/0.39 | [82] |
| Ni _x Co _y nanowires | 0.33 M urea + 5 M KOH | 170 (10:0) 380 (9:1) 180 (7:3) 165 (5:5) | 0.60/0.25 0.60/0.19 0.60/0.12 0.60/0.16 | [53] |
| Ni–Zn | 0.33 M urea + 5 M KOH | 67 | 0.52/0.39 | [83] |
| Ni–Zn–Co | 0.33 M urea + 5 M KOH | 24 | 0.50/0.35 | [83] |
| C–NiFe core shell/NF | 0.33 M urea + 1 M KOH | 100 | 0.60/0.27 | [84] |
| NiMn nanoparticle/CNFs | 1.00 M urea + 1 M KOH | 300 (mg ⁻¹) | 0.50/0.29 | [85] |
| Ni ₆₀ Cr ₄₀ /C | 0.33 M urea + 1 M KOH | 90 | 0.55/0.34 | [86] |
| Ni ₂ Mo ₁ nanoparticle/graphene | 0.33 M urea + 1 M KOH | 128 | 0.52/0.39 | [87] |
| α-Ni(OH) ₂ | 0.33 M urea + 5 M KOH | 154 (mg ⁻¹) | 0.55/0.32 | [91] |
| β-Ni(OH) ₂ | 0.33 M urea + 5 M KOH | 7 (mg ⁻¹) | 0.55/0.45 | [92] |
| Ni(OH) ₂ nanotube | 0.33 M urea + 1 M KOH | 100 (mg ⁻¹) | 0.60/0.29 | [93] |
| Sheet-like Ni(OH) ₂ /Ni foam | 0.60 M urea + 5 M KOH | 92 | 0.56/0.25 | [95] |
| Twine-like Ni(OH) ₂ /Ni foam | | 178 | 0.56/0.24 | [95] |
| Flower-like Ni(OH) ₂ /Ni foam | | 375 | 0.56/0.23 | [95] |
| Nano-sheet Ni(OH) ₂ /Ni foam | | 559 | 0.56/0.21 | [95] |
| Ni ₅₇ Co ₄₃ (OH) ₂ | 0.33 M urea + 5 M KOH | 47 | 0.60/0.25 | [96] |
| S-Ni(OH) ₂ nanosheets | 0.33 M urea + 1 M KOH | 35 | 0.52/0.32 | [90] |
| NiO nanosheets/Ni foam | 0.33 M urea + 1 M KOH | 400 (mg ⁻¹) | 0.50/0.27 | [98] |
| NiCo ₂ O ₄ | 0.33 M urea + 1 M KOH | 135 | 0.70/0.35 | [103] |
| Ni _{1.5} Mn _{1.5} O ₄ | 0.33 M urea + 1 M KOH | 6.9 | 0.50/0.29 | [104] |
| Ni–Co–Mn–O core shell | 0.05 M urea + 0.1 M KOH | 34 | 0.50/0.25 | [44] |
| NiMoO ₄ ·xH ₂ O nanosheets | 0.33 M urea + 1 M KOH | 830 (mg ⁻¹) | 0.50/0.28 | [88] |
| Ni ₅ Sm-P/C | 0.33 M urea + 5 M KOH | 327 (mg ⁻¹) | 0.46/0.32 | [112] |
| Ni ₂ P nanoflower/Ni foam | 0.33 M urea + 5 M KOH | 490 | 0.50/0.24 | [113] |
| Ni ₂ P nanoflake/carbon cloth | 0.50 M urea + 1 M KOH | 110 | 0.45/0.28 | [114] |
| NiCoP nanosheet/carbon cloth | 0.50 M urea + 1 M KOH | 50 | 0.45/0.24 | [115] |
| NiMoS coral-like/Ti mesh | 0.50 M urea + 1 M KOH | 260 | 0.40/0.30 | [117] |
| Se–Ni(OH) ₂ –NiSe nanowires | 0.33 M urea + 1 M KOH | 230 | 0.45/0.28 | [118] |
| NiSe nanowires | 0.33 M urea + 1 M KOH | 185 | 0.45/0.28 | [118] |
| NiSe nanoparticles | 0.33 M urea + 1 M KOH | 155 | 0.45/0.28 | [118] |
| Ni nanoparticle/graphene | 0.50 M urea + 1 M KOH | 93 | 0.60/0.32 | [123] |
| α-Ni(OH) ₂ @MWCNT | 0.33 M urea + 1 M KOH | 1300(mg ⁻¹) | 0.55/0.42 | [122] |

Table 5 (continued)

| Anodic catalysts | Electrolytes | Current density (mA cm ⁻²) | Peak potential and OOP (V vs. Hg/HgO) | Refs. |
|----------------------|-----------------------|--|---------------------------------------|-------|
| Nickel@carbon sponge | 0.10 M urea + 5 M KOH | 290 | 0.60/0.24 | [126] |

Acknowledgements This work was supported by the National Natural Science Foundation of China (51672056), the China Postdoctoral Science Foundation (2018M630307), the Heilongjiang Postdoctoral Scientific Research Developmental Fund (LBH-Q16044), and the Fundamental Research Funds for the Central Universities (HEUCF181007). G.X. Wang is thankful for the financial support from Outstanding Youth Talent Project of Dalian (Grant No. 2017RJ03) and CAS Youth Innovation Promotion (Grant No. 2015145).

References

1. Omer AM (2008) Energy, environment and sustainable development. *Renew Sustain Energy Rev* 12(9):2265–2300. <https://doi.org/10.1016/j.rser.2007.05.001>
2. Satyapal S, Petrovic J, Read C, Thomas G, Ordaz G (2007) The U.S. Department of Energy's National hydrogen storage project: progress towards meeting hydrogen-powered vehicle requirements. *Catal Today* 120(3–4):246–256. <https://doi.org/10.1016/j.cattod.2006.09.022>
3. Faungnawakij KTY, Shimoda N, Fukunaga T, Kikuchi R, Eguchi K (2007) Hydrogen production from dimethyl ether steam reforming over composite catalysts of copper ferrite spinel and alumina. *Appl Catal B* 74:144–151. <https://doi.org/10.1016/j.apcatb.2007.02.010>
4. Barbir F (2005) PEM electrolysis for production of hydrogen from renewable energy sources. *Sol Energy* 78(5):661–669. <https://doi.org/10.1016/j.solener.2004.09.003>
5. Christopher K, Dimitrios R (2012) A review on exergy comparison of hydrogen production methods from renewable energy sources. *Energy Environ Sci* 5(5):6640. <https://doi.org/10.1039/c2ee01098d>
6. Jiao Y, Zheng Y, Jaroniec M, Qiao SZ (2015) Design of electrocatalysts for oxygen- and hydrogen-involving energy conversion reactions. *Chem Soc Rev* 44(8):2060–2086. <https://doi.org/10.1039/c4cs00470a>
7. Zheng Y, Jiao Y, Zhu Y, Li LH, Han Y, Chen Y, Du A, Jaroniec M, Qiao SZ (2014) Hydrogen evolution by a metal-free electrocatalyst. *Nat Commun* 5:3783. <https://doi.org/10.1038/ncomm s4783>
8. Rahimpour MR, Mottaghi HR, Barmaki MM (2010) Hydrogen production from urea wastewater using a combination of urea thermal hydrolyser–desorber loop and a hydrogen-permselective membrane reactor. *Fuel Process Technol* 91(6):600–612. <https://doi.org/10.1016/j.fuproc.2010.01.006>
9. Edrisi A, Mansoori Z, Dabir B (2016) Urea synthesis using chemical looping process—techno-economic evaluation of a novel plant configuration for a green production. *Int J Greenhouse Gas Control* 44:42–51. <https://doi.org/10.1016/j.ijggc.2015.10.020>
10. Lan R, Tao S, Irvine JTS (2010) A direct urea fuel cell—power from fertiliser and waste. *Energy Environ Sci* 3(4):438. <https://doi.org/10.1039/b924786f>
11. Rollinson AN, Rickett GL, Lea-Langton A, Dupont V, Twigg MV (2011) Hydrogen from urea–water and ammonia–water solutions. *Appl Catal B* 106(3–4):304–315. <https://doi.org/10.1016/j.apcatb.2011.05.031>
12. Simka W, Piotrowski J, Robak A, Nawrat G (2009) Electrochemical treatment of aqueous solutions containing urea. *J Appl Electrochem* 39(7):1137–1143. <https://doi.org/10.1007/s10800-008-9771-4>
13. Mahalik K, Sahu JN, Patwardhan AV, Meikap BC (2010) Kinetic studies on hydrolysis of urea in a semi-batch reactor at atmospheric pressure for safe use of ammonia in a power plant for flue gas conditioning. *J Hazard Mater* 175(1–3):629–637. <https://doi.org/10.1016/j.jhazmat.2009.10.053>

14. Krajewska B, Ureases I (2009) Functional, catalytic and kinetic properties: a review. *J Mol Catal B Enzym* 59(1–3):9–21. <https://doi.org/10.1016/j.molcatb.2009.01.003>
15. Xue C, Wilson LD (2016) Kinetic study on urea uptake with chitosan-based sorbent materials. *Carbohydr Polym* 135:180–186. <https://doi.org/10.1016/j.carbpol.2015.08.090>
16. Liu X, Sun S, Tang Y, Li S, Chang J, Guo LA, Zhao Y (2012) Preparation and kinetic modeling of cross-linked chitosan microspheres immobilized Zn(II) for urea adsorption. *Anal Lett* 45(12):1632–1644. <https://doi.org/10.1080/00032719.2012.677785>
17. Zhu L-J, Liu F, Yu X-M, Gao A-L, Xue L-X (2015) Surface zwitterionization of hemocompatible poly(lactic acid) membranes for hemodiafiltration. *J Membr Sci* 475:469–479. <https://doi.org/10.1016/j.memsci.2014.11.004>
18. von Ahnen M, Pedersen L-F, Pedersen PB, Dalsgaard J (2015) Degradation of urea, ammonia and nitrite in moving bed biofilters operated at different feed loadings. *Aquacult Eng* 69:50–59. <https://doi.org/10.1016/j.aquaeng.2015.10.004>
19. Ieropoulos I, Greenman J, Melhuish C (2012) Urine utilisation by microbial fuel cells; energy fuel for the future. *Phys Chem Chem Phys* 14(1):94–98. <https://doi.org/10.1039/c1cp23213d>
20. Ananiev A (2003) The urea decomposition in the process of the heterogeneous catalytic denitrification of nitric acid solutions Part I. Kinetics of the reaction. *Appl Catal B: Environ* 45(3):189–196. [https://doi.org/10.1016/s0926-860x\(03\)00236-9](https://doi.org/10.1016/s0926-860x(03)00236-9)
21. Shen S, Li M, Li B, Zhao Z (2014) Catalytic hydrolysis of urea from wastewater using different aluminas by a fixed bed reactor. *Environ Sci Pollut Res Int* 21(21):12563–12568. <https://doi.org/10.1007/s11356-014-3189-9>
22. Lundström A, Snelling T, Morsing P, Gabrielsson P, Senar E, Olsson L (2011) Urea decomposition and HNCO hydrolysis studied over titanium dioxide, Fe-Beta and γ -Alumina. *Appl Catal B* 106(3–4):273–279. <https://doi.org/10.1016/j.apcatb.2011.05.010>
23. Bernhard AM, Peitz D, Elsener M, Wokaun A, Kröcher O (2012) Hydrolysis and thermolysis of urea and its decomposition byproducts biuret, cyanuric acid and melamine over anatase TiO₂. *Appl Catal B* 115–116:129–137. <https://doi.org/10.1016/j.apcatb.2011.12.013>
24. Daneshfar A, Matsuura T, Emadzadeh D, Pahlevani Z, Ismail AF (2015) Urease-carrying electrospun polyacrylonitrile mat for urea hydrolysis. *React Funct Polym* 87:37–45. <https://doi.org/10.1016/j.reactfunctpolym.2014.12.004>
25. Andrich L, Esti M, Moresi M (2010) Urea degradation kinetics in model wine solutions by acid urease immobilised onto chitosan-derivative beads of different sizes. *Enzyme Microb Technol* 46(5):397–405. <https://doi.org/10.1016/j.enzmictec.2009.12.010>
26. Mekhilef S, Saidur R, Safari A (2012) Comparative study of different fuel cell technologies. *Renew Sustain Energy Rev* 16(1):981–989. <https://doi.org/10.1016/j.rser.2011.09.020>
27. Lo Faro M, Stassi A, Antonucci V, Modafferi V, Frontera P, Antonucci P, Aricò AS (2011) Direct utilization of methanol in solid oxide fuel cells: an electrochemical and catalytic study. *Int J Hydrog Energy* 36(16):9977–9986. <https://doi.org/10.1016/j.ijhydene.2011.05.053>
28. Kamrudin SK, Hashim N (2012) Materials, morphologies and structures of MEAs in DMFCs. *Renew Sustain Energy Rev* 16(5):2494–2515. <https://doi.org/10.1016/j.rser.2012.01.073>
29. Shokrani R, Haghghi M, Jodeiri N, Ajamein H, Abdollahifar M (2014) Fuel cell grade hydrogen production via methanol steam reforming over CuO/ZnO/Al₂O₃ nanocatalyst with various oxide ratios synthesized via urea-nitrates combustion method. *Int J Hydrog Energy* 39(25):13141–13155. <https://doi.org/10.1016/j.ijhydene.2014.06.048>
30. Segura F, Durán E, Andújar JM (2009) Design, building and testing of a stand alone fuel cell hybrid system. *J Power Sources* 193(1):276–284. <https://doi.org/10.1016/j.jpowsour.2008.12.111>
31. Elmer T, Worall M, Wu S, Riffat SB (2015) Fuel cell technology for domestic built environment applications: state-of-the-art review. *Renew Sustain Energy Rev* 42:913–931. <https://doi.org/10.1016/j.rser.2014.10.080>
32. Wilberforce T, Alaswad A, Palumbo A, Dassisti M, Olabi AG (2016) Advances in stationary and portable fuel cell applications. *Int J Hydron Energy* 41(37):16509–16522. <https://doi.org/10.1016/j.ijhydene.2016.02.057>
33. Varcoe JR, Slade RCT (2005) Prospects for alkaline anion-exchange membranes in low temperature fuel cells. *Fuel Cells* 5(2):187–200. <https://doi.org/10.1002/fuce.200400045>
34. Chen Y, Zhuang L, Lu J (2007) Non-Pt anode catalysts for alkaline direct alcohol fuel cells. *Chin J Catal* 28(10):870–874. [https://doi.org/10.1016/s1872-2067\(07\)60073-4](https://doi.org/10.1016/s1872-2067(07)60073-4)
35. Merle G, Wessling M, Nijmeijer K (2011) Anion exchange membranes for alkaline fuel cells: a review. *J Membr Sci* 377(1–2):1–35. <https://doi.org/10.1016/j.memsci.2011.04.043>

36. Choudhury NA, Raman RK, Sampath S, Shukla AK (2005) An alkaline direct borohydride fuel cell with hydrogen peroxide as oxidant. *J Power Sources* 143(1–2):1–8. <https://doi.org/10.1016/j.jpowsour.2004.08.059>
37. An L, Zhao TS (2011) An alkaline direct ethanol fuel cell with a cation exchange membrane. *Energy Environ Sci* 4(6):2213. <https://doi.org/10.1039/c1ee00002k>
38. Xu W, Zhang H, Li G, Wu Z (2014) Nickel-cobalt bimetallic anode catalysts for direct urea fuel cell. *Sci Rep* 4:5863. <https://doi.org/10.1038/srep05863>
39. Chino I, Muneeb O, Do E, Ho V, Haan JL (2018) A paper microfluidic fuel cell powered by urea. *J Power Sources* 396:710–714. <https://doi.org/10.1016/j.jpowsour.2018.06.082>
40. Xu W, Wu Z, Tao S (2016) Urea-based fuel cells and electrocatalysts for urea oxidation. *Energy Technol* 4(11):1329–1337. <https://doi.org/10.1002/ente.201600185>
41. Basumatary P, Konwar D, Yoon YS (2018) A novel Ni-Cu/ZnO@MWCNT anode employed in urea fuel cell to attain superior performances. *Electrochim Acta* 261:78–85. <https://doi.org/10.1016/j.electacta.2017.12.123>
42. Ghouri ZK, Elsaied K, Al-Meer S, Barakat NAM (2017) Applicable anode based on $\text{Co}_3\text{O}_4-\text{SrCO}_3$ heterostructure nanorods-incorporated CNFs with low-onset potential for DUFCs. *Appl Nanosci* 7(8):625–631. <https://doi.org/10.1007/s13204-017-0601-z>
43. Yousef A, El-Newehy MH, Al-Deyab SS, Barakat NAM (2017) Facile synthesis of Ni-decorated multi-layers graphene sheets as effective anode for direct urea fuel cells. *Arab J Chem* 10(6):811–822. <https://doi.org/10.1016/j.arabjc.2016.12.021>
44. Senthilkumar N, Gnana kumar G, Manthiram A (2018) 3D Hierarchical core-shell nanostructured arrays on carbon fibers as catalysts for direct urea fuel cells. *Adv Energy Mater* 8(6):1702207. <https://doi.org/10.1002/aenm.201702207>
45. Nagao M, Kobayashi K, Hibino T (2015) A direct urine fuel cell operated at intermediate temperatures. *Chem Lett* 44(3):363–365. <https://doi.org/10.1246/cl.141067>
46. Xu W, Zhang H, Li G, Wu Z (2016) A urine/Cr(VI) fuel cell—electrical power from processing heavy metal and human urine. *J Electroanal Chem* 764:38–44. <https://doi.org/10.1016/j.jelechem.2016.01.013>
47. Lan R, Tao S (2011) Preparation of nano-sized nickel as anode catalyst for direct urea and urine fuel cells. *J Power Sources* 196(11):5021–5026. <https://doi.org/10.1016/j.jpowsour.2011.02.015>
48. Ma X, Ye K, Wang G, Duan M, Cheng K, Wang G, Cao D (2017) Facile fabrication of gold coated nickel nanoarrays and its excellent catalytic performance towards sodium borohydride electro-oxidation. *Appl Surf Sci* 414:353–360. <https://doi.org/10.1016/j.apsusc.2017.04.104>
49. Ye K, Ma X, Cang R, Wang G, Cheng K, Wang G, Cao D (2017) Nickel nanowires decorated with ultra-low palladium loading as an effective electrocatalyst for NaBH_4 oxidation. *Catal Sci Technol* 7(10):1991–1995. <https://doi.org/10.1039/c6cy02429g>
50. Liu H, Song C, Zhang L, Zhang J, Wang H, Wilkinson DP (2006) A review of anode catalysis in the direct methanol fuel cell. *J Power Sources* 155(2):95–110. <https://doi.org/10.1016/j.jpowsour.2006.01.030>
51. Liu R, Ye K, Gao Y, Zhang W, Wang G, Cao D (2015) Ag supported on carbon fiber cloth as the catalyst for hydrazine oxidation in alkaline medium. *Electrochim Acta* 186:239–244. <https://doi.org/10.1016/j.electacta.2015.10.126>
52. Fan Z, Kwon Y-H, Yang X, Xu W, Wu Z (2017) In-situ production of hydrogen peroxide as oxidant for direct urea fuel cell. *Energy Procedia* 105:1858–1863. <https://doi.org/10.1016/j.egypr.2017.03.544>
53. Guo F, Cheng K, Ye K, Wang G, Cao D (2016) Preparation of nickel-cobalt nanowire arrays anode electro-catalyst and its application in direct urea/hydrogen peroxide fuel cell. *Electrochim Acta* 199:290–296. <https://doi.org/10.1016/j.electacta.2016.01.215>
54. Guo F, Cao D, Du M, Ye K, Wang G, Zhang W, Gao Y, Cheng K (2016) Enhancement of direct urea-hydrogen peroxide fuel cell performance by three-dimensional porous nickel-cobalt anode. *J Power Sources* 307:697–704. <https://doi.org/10.1016/j.jpowsour.2016.01.042>
55. Jing X, Cao D, Liu Y, Wang G, Yin J, Wen Q, Gao Y (2011) The open circuit potential of hydrogen peroxide at noble and glassy carbon electrodes in acidic and basic electrolytes. *J Electroanal Chem* 658(1–2):46–51. <https://doi.org/10.1016/j.jelechem.2011.04.025>
56. Boggs BK, King RL, Botte GG (2009) Urea electrolysis: direct hydrogen production from urine. *Chem Commun (Camb)* 32:4859–4861. <https://doi.org/10.1039/b905974a>
57. Kapdan IK, Kargi F (2006) Bio-hydrogen production from waste materials. *Enzyme Microb Technol* 38(5):569–582. <https://doi.org/10.1016/j.enzmictec.2005.09.015>

58. Singh L, Wahid ZA (2015) Methods for enhancing bio-hydrogen production from biological process: a review. *J Ind Eng Chem* 21:70–80. <https://doi.org/10.1016/j.jiec.2014.05.035>
59. Kim J, Choi WJK, Choi J, Hoffmann MR, Park H (2013) Electrolysis of urea and urine for solar hydrogen. *Catal Today* 199:2–7. <https://doi.org/10.1016/j.cattod.2012.02.009>
60. Hernlem BJ (2005) Electrolytic destruction of urea in dilute chloride solution using DSA electrodes in a recycled batch cell. *Water Res* 39(11):2245–2252. <https://doi.org/10.1016/j.watres.2005.04.018>
61. Carlesi Jara C, Di Giulio S, Fino D, Spinelli P (2008) Combined direct and indirect electrooxidation of urea containing water. *J Appl Electrochem* 38(7):915–922. <https://doi.org/10.1007/s10800-008-9496-4>
62. Simka W, Piotrowski J, Nawrat G (2007) Influence of anode material on electrochemical decomposition of urea. *Electrochim Acta* 52(18):5696–5703. <https://doi.org/10.1016/j.electacta.2006.12.017>
63. Wright JC, Michaels AS, Appleby AJ (1986) Electrooxidation of urea at the ruthenium titanium oxide electrode. *AIChE J* 32:1450–1458. <https://doi.org/10.1002/aic.690320906>
64. Zollig H, Remmeli A, Fritzsch C, Morgenroth E, Udert KM (2015) Formation of chlorination byproducts and their emission pathways in chlorine mediated electro-oxidation of urine on active and nonactive type anodes. *Environ Sci Technol* 49(18):11062–11069. <https://doi.org/10.1021/acs.est.5b01675>
65. Ding R, Li X, Shi W, Xu Q, Wang L, Jiang H, Yang Z, Liu E (2016) Mesoporous Ni-P nanocatalysts for alkaline urea electrooxidation. *Electrochim Acta* 222:455–462. <https://doi.org/10.1016/j.electacta.2016.10.198>
66. Cho K, Hoffmann MR (2014) Urea degradation by electrochemically generated reactive chlorine species: products and reaction pathways. *Environ Sci Technol* 48(19):11504–11511. <https://doi.org/10.1021/es5025405>
67. Cho K, Kwon D, Hoffmann MR (2014) Electrochemical treatment of human waste coupled with molecular hydrogen production. *RSC Adv* 4(9):4596–4608. <https://doi.org/10.1039/c3ra46699j>
68. Barrios AM, Lippard SJ (2000) Interaction of urea with a hydroxide-bridged dinuclear nickel center: an alternative model for the mechanism of urease. *J Am Chem Soc* 122:9172–9177. <https://doi.org/10.1021/ja000202v>
69. Suarez D, Diaz D, Merz KM (2003) Ureases: quantum chemical calculations on cluster models. *J Am Chem Soc* 125:15324–15337. <https://doi.org/10.1021/ja030145g>
70. Vedharathinam V, Botte GG (2012) Understanding the electro-catalytic oxidation mechanism of urea on nickel electrodes in alkaline medium. *Electrochim Acta* 81:292–300. <https://doi.org/10.1016/j.electacta.2012.07.007>
71. Vedharathinam V, Botte GG (2014) Experimental investigation of potential oscillations during the electrocatalytic oxidation of urea on Ni catalyst in alkaline medium. *J Phys Chem C* 118(38):21806–21812. <https://doi.org/10.1021/jp5052529>
72. Vedharathinam V, Botte GG (2013) Direct evidence of the mechanism for the electro-oxidation of urea on $\text{Ni}(\text{OH})_2$ catalyst in alkaline medium. *Electrochim Acta* 108:660–665. <https://doi.org/10.1016/j.electacta.2013.06.137>
73. Wang Dan, Botte GG (2014) In Situ X-ray diffraction study of urea electrolysis on nickel catalysts. *ECS Electrochem Lett* 3:H29–H32. <https://doi.org/10.1149/2.0031409ee1%5d>
74. Daramola DA, Singh D, Botte GG (2010) Dissociation rates of urea in the presence of NiOOH catalyst: a DFT analysis. *J Phys Chem A* 114:11513–11521. <https://doi.org/10.1021/jp105159t>
75. Guo F, Ye K, Cheng K, Wang G, Cao D (2015) Preparation of nickel nanowire arrays electrode for urea electro-oxidation in alkaline medium. *J Power Sources* 278:562–568. <https://doi.org/10.1016/j.jpowsour.2014.12.125>
76. Guo F, Ye K, Du M, Huang X, Cheng K, Wang G, Cao D (2016) Electrochemical impedance analysis of urea electro-oxidation mechanism on nickel catalyst in alkaline medium. *Electrochim Acta* 210:474–482. <https://doi.org/10.1016/j.electacta.2016.05.149>
77. Ojani R, Hasheminejad E, Raoof JB (2014) Hydrogen evolution assisted electrodeposition of bimetallic 3D nano/micro-porous PtPd films and their electrocatalytic performance. *Int J Hydrog Energy* 39(16):8194–8203. <https://doi.org/10.1016/j.ijhydene.2014.03.162>
78. Lyalin BV, Petrosyan VA (2010) Oxidation of organic compounds on NiOOH electrode. *Russ J Electrochem* 46(11):1199–1214. <https://doi.org/10.1134/s1023193510110017>
79. Yan W, Wang D, Diaz LA, Botte GG (2014) Nickel nanowires as effective catalysts for urea electro-oxidation. *Electrochim Acta* 134:266–271. <https://doi.org/10.1016/j.electacta.2014.03.134>

80. King RL, Botte GG (2011) Investigation of multi-metal catalysts for stable hydrogen production via urea electrolysis. *J Power Sources* 196(22):9579–9584. <https://doi.org/10.1016/j.jpowsour.2011.06.079>
81. Miller AT, Hassler BL, Botte GG (2012) Rhodium electrodeposition on nickel electrodes used for urea electrolysis. *J Appl Electrochem* 42(11):925–934. <https://doi.org/10.1007/s10800-012-0478-1>
82. Yan W, Wang D, Botte GG (2015) Template-assisted synthesis of Ni–Co bimetallic nanowires for urea electrocatalytic oxidation. *J Appl Electrochem* 45(11):1217–1222. <https://doi.org/10.1007/s10800-015-0846-8>
83. Yan W, Wang D, Botte GG (2012) Electrochemical decomposition of urea with Ni-based catalysts. *Appl Catal B* 127:221–226. <https://doi.org/10.1016/j.apcatb.2012.08.022>
84. Wu M-S, Jao C-Y, Chuang F-Y, Chen F-Y (2017) Carbon-encapsulated nickel–iron nanoparticles supported on nickel foam as a catalyst electrode for urea electrolysis. *Electrochim Acta* 227:210–216. <https://doi.org/10.1016/j.electacta.2017.01.035>
85. Barakat NAM, El-Newehy MH, Yasin AS, Ghouri ZK, Al-Deyab SS (2016) Ni&Mn nanoparticle-decorated carbon nanofibers as effective electrocatalyst for urea oxidation. *Appl Catal A* 510:180–188. <https://doi.org/10.1016/j.apcata.2015.11.015>
86. Singh RK, Schechter A (2017) Electrocactivity of NiCr catalysts for urea oxidation in alkaline electrolyte. *ChemCatChem* 9(17):3374–3379. <https://doi.org/10.1002/cctc.201700451>
87. Shi W, Ding R, Li X, Xu Q, Liu E (2017) Enhanced performance and electrocatalytic kinetics of Ni-Mo/graphene nanocatalysts towards alkaline urea oxidation reaction. *Electrochim Acta* 242:247–259. <https://doi.org/10.1016/j.electacta.2017.05.002>
88. Liang Y, Liu Q, Asiri AM, Sun X (2015) Enhanced electrooxidation of urea using NiMoO₄·xH₂O nanosheet arrays on Ni foam as anode. *Electrochim Acta* 153:456–460. <https://doi.org/10.1016/j.electacta.2014.11.193>
89. Shukla AKKY, Munichandraiah N (1994) Stabilized α -Ni(OH)₂ as electrode material for alkaline secondary cells. *J Electrochem Soc* 141:2956–2959. <https://doi.org/10.1149/1.2059264>
90. Zhu X, Dou X, Dai J, An X, Guo Y, Zhang L, Tao S, Zhao J, Chu W, Zeng XC, Wu C, Xie Y (2016) Metallic nickel hydroxide nanosheets give superior electrocatalytic oxidation of urea for fuel cells. *Angew Chem Int Ed* 55(40):12465–12469. <https://doi.org/10.1002/anie.201606313>
91. Wang D, Yan W, Botte GG (2011) Exfoliated nickel hydroxide nanosheets for urea electrolysis. *Electrochem Commun* 13(10):1135–1138. <https://doi.org/10.1016/j.elecom.2011.07.016>
92. Wang D, Yan W, Vijapur SH, Botte GG (2012) Enhanced electrocatalytic oxidation of urea based on nickel hydroxide nanoribbons. *J Power Sources* 217:498–502. <https://doi.org/10.1016/j.jpowsour.2012.06.029>
93. Ji R-Y, Chan D-S, Jow J-J, Wu M-S (2013) Formation of open-ended nickel hydroxide nanotubes on three-dimensional nickel framework for enhanced urea electrolysis. *Electrochim Commun* 29:21–24. <https://doi.org/10.1016/j.elecom.2013.01.006>
94. Wu M-S, Ji R-Y, Zheng Y-R (2014) Nickel hydroxide electrode with a monolayer of nanocup arrays as an effective electrocatalyst for enhanced electrolysis of urea. *Electrochim Acta* 144:194–199. <https://doi.org/10.1016/j.electacta.2014.08.098>
95. Ye K, Zhang H, Zhao L, Huang X, Cheng K, Wang G, Cao D (2016) Facile preparation of three-dimensional Ni(OH)₂/Ni foam anode with low cost and its application in a direct urea fuel cell. *New J Chem* 40(10):8673–8680. <https://doi.org/10.1039/c6nj01648k>
96. Yan W, Wang D, Botte GG (2012) Nickel and cobalt bimetallic hydroxide catalysts for urea electro-oxidation. *Electrochim Acta* 61:25–30. <https://doi.org/10.1016/j.electacta.2011.11.044>
97. Xu W, Du D, Lan R, Humphreys J, Wu Z, Tao S (2017) Highly active Ni–Fe double hydroxides as anode catalysts for electrooxidation of urea. *New J Chem* 41(10):4190–4196. <https://doi.org/10.1039/c6nj04060h>
98. Wu M-S, Lin G-W, Yang R-S (2014) Hydrothermal growth of vertically-aligned ordered mesoporous nickel oxide nanosheets on three-dimensional nickel framework for electrocatalytic oxidation of urea in alkaline medium. *J Power Sources* 272:711–718. <https://doi.org/10.1016/j.jpowsour.2014.09.009>
99. Yue Z, Zhu W, Li Y, Wei Z, Hu N, Suo Y, Wang J (2018) Surface engineering of a nickel oxide–nickel hybrid nanoarray as a versatile catalyst for both superior water and urea oxidation. *Inorg Chem* 57(8):4693–4698. <https://doi.org/10.1021/acs.inorgchem.8b00411>
100. Das G, Tesfaye RM, Won Y, Yoon HH (2017) NiO–Fe₂O₃ based graphene aerogel as urea electrooxidation catalyst. *Electrochim Acta* 237:171–176. <https://doi.org/10.1016/j.electacta.2017.03.197>

101. Forslund RP, Mefford JT, Hardin WG, Alexander CT, Johnston KP, Stevenson KJ (2016) Nanostructured LaNiO₃ perovskite electrocatalyst for enhanced urea oxidation. *ACS Catal* 6(8):5044–5051. <https://doi.org/10.1021/acscatal.6b00487>
102. Wang L, Li M, Huang Z, Li Y, Qi S, Yi C, Yang B (2014) Ni-W/C nanocluster catalysts for urea electrooxidation. *J Power Sources* 264:282–289. <https://doi.org/10.1016/j.jpowsour.2014.04.104>
103. Ding R, Qi L, Jia M, Wang H (2014) Facile synthesis of mesoporous spinel NiCo₂O₄ nanostructures as highly efficient electrocatalysts for urea electro-oxidation. *Nanoscale* 6(3):1369–1376. <https://doi.org/10.1039/c3nr05359h>
104. Periyasamy S, Subramanian P, Levi E, Aurbach D, Gedanken A, Schechter A (2016) Exceptionally active and stable spinel nickel manganese oxide electrocatalysts for urea oxidation reaction. *ACS Appl Mater Interfaces* 8(19):12176–12185. <https://doi.org/10.1021/acsmami.6b02491>
105. Yu Z-Y, Lang C-C, Gao M-R, Chen Y, Fu Q-Q, Duan Y, Yu S-H (2018) Ni-Mo-O nanorod-derived composite catalysts for efficient alkaline water-to-hydrogen conversion via urea electrolysis. *Energy Environ Sci* 11(7):1890–1897. <https://doi.org/10.1039/c8ee00521d>
106. Zhang X, Liu Y, Xiong Q, Liu G, Zhao C, Wang G, Zhang Y, Zhang H, Zhao H (2017) Vapour-phase hydrothermal synthesis of Ni₂P nanocrystallines on carbon fiber cloth for high-efficiency H₂ production and simultaneous urea decomposition. *Electrochim Acta* 254:44–49. <https://doi.org/10.1016/j.electacta.2017.09.097>
107. Chen YY, Zhang Y, Zhang X, Tang T, Luo H, Niu S, Dai ZH, Wan LJ, Hu JS (2017) Self-templated fabrication of MoNi₄MoO_{3-x} nanorod arrays with dual active components for highly efficient hydrogen evolution. *Adv Mater*. <https://doi.org/10.1002/adma.201703311>
108. Fang M, Gao W, Dong G, Xia Z, Yip S, Qin Y, Qu Y, Ho JC (2016) Hierarchical NiMo-based 3D electrocatalysts for highly-efficient hydrogen evolution in alkaline conditions. *Nano Energy* 27:247–254. <https://doi.org/10.1016/j.nanoen.2016.07.005>
109. Gao MR, Liang JX, Zheng YR, Xu YF, Jiang J, Gao Q, Li J, Yu SH (2015) An efficient molybdenum disulfide/cobalt diselenide hybrid catalyst for electrochemical hydrogen generation. *Nat Commun* 6:5982. <https://doi.org/10.1038/ncomms6982>
110. Zhang J, Wang T, Liu P, Liao Z, Liu S, Zhuang X, Chen M, Zschech E, Feng X (2017) Efficient hydrogen production on MoNi₄ electrocatalysts with fast water dissociation kinetics. *Nat Commun* 8:15437. <https://doi.org/10.1038/ncomms15437>
111. Caban-Acevedo M, Stone ML, Schmidt JR, Thomas JG, Ding Q, Chang HC, Tsai ML, He JH, Jin S (2015) Efficient hydrogen evolution catalysis using ternary pyrite-type cobalt phosphosulphide. *Nat Mater* 14(12):1245–1251. <https://doi.org/10.1038/nmat4410>
112. Wang W, Chai D, Zhang J, Xue S, Wang Y, Lei Z (2017) Ni₅Sm-P/C ternary alloyed catalyst as highly efficient electrocatalyst for urea electrooxidation. *J Taiwan Inst Chem Eng* 80:326–332. <https://doi.org/10.1016/j.jtice.2017.07.017>
113. Wang G, Ye K, Shao J, Zhang Y, Zhu K, Cheng K, Yan J, Wang G, Cao D (2018) Porous Ni₂P nanoflower supported on nickel foam as an efficient three-dimensional electrode for urea electro-oxidation in alkaline medium. *Int J Hydron Energy* 43(19):9316–9325. <https://doi.org/10.1016/j.ijhydene.2018.03.221>
114. Liu D, Liu T, Zhang L, Qu F, Du G, Asiri AM, Sun X (2017) High-performance urea electrolysis towards less energy-intensive electrochemical hydrogen production using a bifunctional catalyst electrode. *J Mater Chem A* 5(7):3208–3213. <https://doi.org/10.1039/c6ta11127k>
115. Xie L, Liu Q, Luo Y, Liu Z, Xu Y, Asiri AM, Sun X, Xie F (2017) Bimetallic NiCoP nanosheets array for high-performance urea electro-oxidation and less energy-intensive electrolytic hydrogen production. *ChemistrySelect* 2(31):10285–10289. <https://doi.org/10.1002/slct.201702071>
116. Zhu W, Ren M, Hu N, Zhang W, Luo Z, Wang R, Wang J, Huang L, Suo Y, Wang J (2018) Traditional NiCo₂S₄ phase with porous nanosheets array topology on carbon cloth: a flexible, versatile and fabulous electrocatalyst for overall water and urea electrolysis. *ACS Sustain Chem Eng* 6(4):5011–5020. <https://doi.org/10.1021/acsschemeng.7b04663>
117. Wang X, Wang J, Sun X, Wei S, Cui L, Yang W, Liu J (2017) Hierarchical coral-like NiMoS nano hybrids as highly efficient bifunctional electrocatalysts for overall urea electrolysis. *Nano Res* 11(2):988–996. <https://doi.org/10.1007/s12274-017-1711-3>
118. Tang C, Zhao ZL, Chen J, Li B, Chen L, Li CM (2017) Se–Ni(OH)₂-shelled vertically oriented NiSe nanowires as a superior electrocatalyst toward urea oxidation reaction of fuel cells. *Electrochim Acta* 248:243–249. <https://doi.org/10.1016/j.electacta.2017.06.159>

119. Abdel Hameed RM, Medany SS (2017) NiO nanoparticles on graphene nanosheets at different calcination temperatures as effective electrocatalysts for urea electro-oxidation in alkaline medium. *J Colloid Interface Sci* 508:291–302. <https://doi.org/10.1016/j.jcis.2017.08.048>
120. Glass DE, Galvan V, Prakash GKS (2017) The effect of annealing temperature on nickel on reduced graphene oxide catalysts on urea electrooxidation. *Electrochim Acta* 253:489–497. <https://doi.org/10.1016/j.electacta.2017.09.064>
121. Wang D, Yan W, Vijapur SH, Botte GG (2013) Electrochemically reduced graphene oxide–nickel nanocomposites for urea electrolysis. *Electrochim Acta* 89:732–736. <https://doi.org/10.1016/j.electacta.2012.11.046>
122. Bian L, Du T, Du Q, Luo M, Li M (2017) Multiwalled carbon nanotubes twined α -nickel hydroxide microspheres as high-efficient urea electrooxidation catalysts. *J Appl Electrochem* 47(8):905–915. <https://doi.org/10.1007/s10800-017-1087-9>
123. Barakat NAM, Motlak M, Ghouri ZK, Yasin AS, El-Newehy MH, Al-Deyab SS (2016) Nickel nanoparticles-decorated graphene as highly effective and stable electrocatalyst for urea electrooxidation. *J Mol Catal A: Chem* 421:83–91. <https://doi.org/10.1016/j.molcata.2016.05.011>
124. Wang L, Du T, Cheng J, Xie X, Yang B, Li M (2015) Enhanced activity of urea electrooxidation on nickel catalysts supported on tungsten carbides/carbon nanotubes. *J Power Sources* 280:550–554. <https://doi.org/10.1016/j.jpowsour.2015.01.141>
125. Kakati N, Maiti J, Lee KS, Viswanathan B, Yoon YS (2017) Hollow sodium nickel fluoride nano-cubes deposited MWCNT as an efficient electrocatalyst for urea oxidation. *Electrochim Acta* 240:175–185. <https://doi.org/10.1016/j.electacta.2017.04.055>
126. Ye K, Zhang D, Guo F, Cheng K, Wang G, Cao D (2015) Highly porous nickel@carbon sponge as a novel type of three-dimensional anode with low cost for high catalytic performance of urea electro-oxidation in alkaline medium. *J Power Sources* 283:408–415. <https://doi.org/10.1016/j.jpowsour.2015.02.149>



REVIEW

Determination of Specific Electrocatalytic Sites in the Oxidation of Small Molecules on Crystalline Metal Surfaces

Manuel J. S. Farias¹ · Juan M. Feliu²

Received: 27 August 2018 / Accepted: 26 December 2018 / Published online: 10 January 2019
© Springer Nature Switzerland AG 2019

Abstract

The identification of active sites in electrocatalytic reactions is part of the elucidation of mechanisms of catalyzed reactions on solid surfaces. However, this is not an easy task, even for apparently simple reactions, as we sometimes think the oxidation of adsorbed CO is. For surfaces consisting of non-equivalent sites, the recognition of specific active sites must consider the influence that facets, as is the steps/defect on the surface of the catalyst, cause in its neighbors; one has to consider the electrochemical environment under which the “active sites” lie on the surface, meaning that defects/steps on the surface do not partake in chemistry by themselves. In this paper, we outline the recent efforts in understanding the close relationships between site-specific and the overall rate and/or selectivity of electrocatalytic reactions. We analyze hydrogen adsorption/desorption, and electro-oxidation of CO, methanol, and ammonia. The classical topic of asymmetric electrocatalysis on kinked surfaces is also addressed for glucose electro-oxidation. The article takes into account selected existing data combined with our original works.

Keywords Electrocatalysis · Single crystal surfaces · Active sites · Structure sensitivity · Asymmetric electrocatalysis

Chapter 3 was originally published as Farias, M. J. S. & Feliu, J. M. Topics in Current Chemistry (2019) 377: 5. <https://doi.org/10.1007/s41061-018-0228-x>.

✉ Juan M. Feliu
juan.feliu@ua.es

¹ Departamento de Química, Universidade Federal do Maranhão, Avenida dos Portugueses, 1966, São Luís, Maranhão CEP 65080-805, Brazil

² Instituto de Electroquímica, Universidad de Alicante Ap. 99, E-03080 Alicante, Spain

1 Introduction

Generally, catalysts consist of non-consumable chemicals capable of providing a favorable energy landscape for mediating steps of chemical reactions. Catalysts can be found everywhere in nature, as is the case of the enzymes in the living world, which are extremely selective [1]. In the case of inorganic catalysts, the efficiency almost always needs to be improved [2]. In heterogeneous catalysis, catalyst materials very often are solids—such as oxides or metals on a support—and the reactants are found in the fluid phase—as is the gaseous or liquid phase. The mechanism through which the reactions proceed on a catalyst surface is complex, involving many reaction intermediates, and it is worth mentioning that many parameters, which can be intrinsic and extrinsic to the catalyst surface, influence its overall efficiency [3]. The efficiency of catalysts can be (and had historically been [2]) improved by trial-and-error, but this strategy is very time-consuming and does not allow pushing the limits of the efficiency of the catalyst in terms of both activity and selectivity (and also long-term stability). The factors underlying the efficiency in heterogeneous electrocatalysis only can be reached if in-depth knowledge about the molecular relationships between the catalyst surface structure and the reactants/reactions taking place on it is successfully achieved. In this regard, from the theoretical viewpoint, it has been proposed that energy-scaling relations, i.e., for catalyzed reactions on the surface of some transition metals, the binding energies of adsorbed intermediates correlate with each other and these scaling relations likely limit the catalysis efficiency [3, 4]. This theoretical perception of catalysis has been extremely influential in the interpretation of heterogeneous catalysis at the solid/gas interface [5].

In electrocatalysis, catalysts are immersed in an electrolyte with which they interact, so that the catalyst surfaces are never unoccupied or “clean” as in ultra-high vacuum (where pressure below $\sim 10^{-9}$ torr is required so the surface is kept “clean” for up to about 1 h [6]). In this sense, beyond a parameter such as the external applied potential, also absent in ordinary heterogeneous catalysis, the catalyst surface in electrocatalysis permanently interacts also with, generally, a water-based electrolyte and its ions (and, not to say, the surface impurities coming from the electrolyte). This means that, during the attachment of the reactants to the catalyst surface, competitive reactions always take place. However, as in heterogeneous catalysis, the rate of reaction and the selectivity in electrocatalysis may be tactically tuned, playing with characteristics intrinsic to the electrode/catalyst surface, as the structure of the surfaces, as the shape of nanocrystals and step site density [7–9]. In addition, the catalytic activity can be modified based on parameters extrinsic to the catalyst surface, as is the electrolyte composition, the effect/influence of anions and, as more recently pointed out, cations (still not well understood) and pH of the solution [10, 11].

In controlled experiments, a structure’s sensitivity is successfully assessed by controlling the specific atomic configuration on the catalyst surfaces [12]. Despite surface-structure-sensitivity relationships being easily pointed out, the determination of the exact structure of the active sites involved in a specific reaction

pathway is not trivial and requires a great number of high-quality experiments in fundamental electrocatalysis. For electrocatalyzed reactions, this subject has been addressed in two review articles a few years ago [9, 13]. With regard to the surface structure, it is well established that studies of single crystal surfaces have historically played a prominent role in advancing understanding of molecular factors in heterogeneous catalysis at both solid/gas [6] and solid/liquid electrified interfaces [14]. The suitability of studies with single crystal surfaces—as a step in the direction for understanding the structure-activity relationships—is because the single crystal surfaces simplify enormously the number of variables of the catalytic process, and the single crystal, at a certain level, mimics the facets of the catalyst's nanoparticles used in real applications.

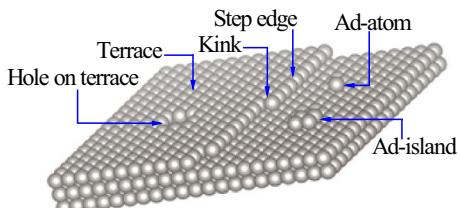
The identification of active sites requires the design of specific experiments for the description and investigation of the causes of the reactivity, catalytic activity and selectivity in heterogeneous electrocatalysis [15, 16]. In this article, we discuss efforts devoted to the establishment of relationships between reactivity and surface reaction pathways for the following electrochemical reactions: hydrogen adsorption/desorption reaction, electro-oxidation of CO, methanol, ammonia and glucose on platinum single crystal electrodes. It is worth noticing that the significance of these reactions in the field of electrocatalysis is because they are surface structure-sensitive reactions. The hydrogen adsorption/desorption and oxidation of carbon monoxide reactions can serve as surface model reactions. The oxidation of methanol and ammonia can serve as examples of potential fuel in low-temperature fuel cells. Moreover, the study of ammonia oxidation has a great appeal for environmental issues. Electro-oxidation of glucose is the best-documented case of enantiospecific interaction between a chiral molecule and an intrinsically chiral surface.

2 The Structure of the Catalytic Substrate

In heterogeneous electrocatalysis, the catalytic events, i.e., all the elementary reaction steps into the catalytic cycle, take place on the topmost layer of the atoms at the catalyst. The atomic ensemble at the surface where reaction takes place, involving the reaction intermediates and transition states, combines the effect of both electronic and geometric nature and is simplified under the name of surface active sites. In this sense, the active sites are far from being atoms, but structures that eventually may have some level of synergy. Historically, from a surface structure point of view, the insight on the active sites is attributed to Taylor and back to 1925 [17]. Taylor reviewed the mechanism of the catalytic action in solid surfaces, and he concluded that the occurrence of the reactions on surfaces was restricted to occur on unsaturated surface atoms [17]. In fact, in the real world, the surfaces of the catalyst consist of non-periodical arrangement of atoms, resulting in different local chemical environments [18]. As an example, the different configurations of atoms at the catalyst surfaces can be represented by a crystal surface model, as illustrated in Fig. 1 for crystals of the fcc (face-centered cubic) lattices.

The surface in Fig. 1 contains terrace, step edge, kink, ad-atom, ad-island and hole atoms. Under this framework, it is usually considered that the surface

Fig. 1 Hard sphere model of a Pt(111) surface, indicating different features: terrace, step, kink, hole, ad-atom and ad-island atoms



structure stays stable during the reaction, which could not be the case. Also, the uncontrolled crystallographic features such as holes, ad-atoms or ad-islands are not considered. In practice, unevenly distributed sites or the atom arrangement on surfaces are reflected in the variation of the local physical properties intrinsic to the surfaces, as the work function [19, 20], and imperfections, such as steps, create electronic perturbation on the terraces [21]. These modifications at the catalyst surface originate deep consequences in the catalytic properties and open the possibility of tuning the properties of the catalyst, in a controlled way. In fact, there are surface-catalyzed reactions which preferentially take place at the low coordination sites, typically at step or kink sites, while there are others reactions which occur preferentially at terraces [22].

Attempts to classify the electrocatalytic reactions as to their dependence on the surface structure (and size scale) of the electrocatalytic materials have appeared in literature [9]. However, beyond the structure of the topmost layer of atoms at the surface, combining the effects of electronic and geometric nature [23], the electrocatalytic properties very often depend on factors external to the structure of the catalyst surface, i.e., the electrochemical environments where the “active sites” exists at the catalyst surfaces. In this regard, the nature of an electrolyte’s anions, cations and its pH also exert influence on the performance of the catalyst. In fact, at different potentials, the nature of anions and their ability (and strength) to attach on the catalyst surface can induce preferential reaction pathways [24]. In the case of solution pH, the mechanisms by which this parameter affects the catalytic activity are much more complex than previously thought. In this sense, at the surface of a similar catalyst (consisting of non-equivalent sites), the change of solution pH passing from acidic toward alkalinity catalytically favored some kinds of sites [as highly coordinated Pt atoms, of (111) terrace sites], while the catalytic activity of the sites consisting of low-coordination atoms was inhibited [25]. Then, recognition of active sites in electrocatalysis involves at least two environmental aspects: one intrinsic to the catalyst surface, involving geometric and electronic factors (which include scale or size factors) and the possible influence of the local electrochemical environment (extrinsic to the catalyst surface). In the following, some of these aspects, such as surface structure, are considered constant unless otherwise stated, under the whole experiment, but others vary with applied potential.

3 Determination of Specific Electrocatalytic Sites

3.1 Fingerprints of Step and Terrace Sites on Pt Surfaces as Probed by Hydrogen Adsorption/Desorption

In Pt surface electrochemistry, the so-called hydrogen region is recognized to be a fast, surface-limited, faradaic charge transfer reaction as a result of protons discharging to adsorbed hydrogen and its reverse reaction: $H^+ + e^- + {}^*_{\text{active sites}} \rightleftharpoons H_{\text{ads}}$. These reactions correspond to the under-potential deposition of hydrogen (H_{UPD}), and is a characteristic signature of a few transition metals in the periodic table, such as Pt, Rh, Pd and Ir. At platinum electrodes in contact with different test electrolytes, as HClO_4 , H_2SO_4 , NaOH , those reactions develop well-defined reversible voltammetric features at potentials several mV higher than hydrogen evolution which serve as a fingerprint of Pt crystal facets and can be used to identify Pt active sites [26, 27]. In a spectro-electrochemistry study, in the region of H_{UPD} at $0.1 \text{ V}_{\text{RHE}}$, a band at $2080\text{--}2095 \text{ cm}^{-1}$, attributed to H_{ads} on top sites, was characterized by surface-enhanced infrared absorption spectroscopy [28]. A single band, assigned to the Pt- H_{ads} , also has been observed for Pt at the solid/gas interface [29]. However, other geometries of adsorbed hydrogen at potentials of H_{UPD} on Pt, as is the hollow sites, have been considered [28]. Then, because the potentials range of H_{UPD} the surface is predominantly covered with H_{ads} , it is plausible to assume that the proton discharging onto adsorbed hydrogen involves at least the reaction of water displacement from the Pt surface at potentials of H_{UPD} : $\text{Pt}-[(\text{H}_2\text{O})_m] + H^+ + e^- \rightleftharpoons \text{Pt}-H_{\text{ads}} + m\text{H}_2\text{O}$. As the potential increases in the positive direction, the characteristics of the electrified interface favor the Pt surface interaction with anions. Recently [30], attempts to provide a more complete description of the possible interfacial events responsible for the features in the “hydrogen” region include the possible participation of cations interacting with the Pt surface, and attempts to explain the non-Nernstian pH dependence of the “hydrogen” peak in voltammograms.

The voltammetric behavior of Pt single crystals in contact with a $0.1 \text{ M } \text{HClO}_4$ solution are displayed in Fig. 2, for three single crystal surfaces. The two stepped surfaces, namely Pt(554) and Pt(544), consist of 9-atom-wide (111) terraces, which are periodically broken by monoatomic steps with (110) and (100) orientations, respectively. The visible peaks caused by hydrogen adsorption/desorption at the (110) and (100) steps are distinctly separated by $\sim 156 \text{ mV}$. Figure 2 also shows a hard sphere model for each surface orientation, indicating the position of the monoatomic steps and two-dimensional (111) domains on the surfaces. The qualitative difference in the voltammetric profiles in the potential range of ~ 0.06 up to $\sim 0.35 \text{ V}_{\text{RHE}}$ concerns the existence of the remarkable peaks at ~ 0.128 and $\sim 0.284 \text{ V}_{\text{RHE}}$ due to the hydrogen adsorption/desorption at the (110) and (100) monoatomic steps, respectively. As we can see in the inset of Fig. 2 for the hard sphere model, the row of monoatomic steps consists of two parts: the top side and the bottom one, that would correspond to the positive and negative sides of the dipole steps, following the Smoluchowski model [31]. The reversible peaks

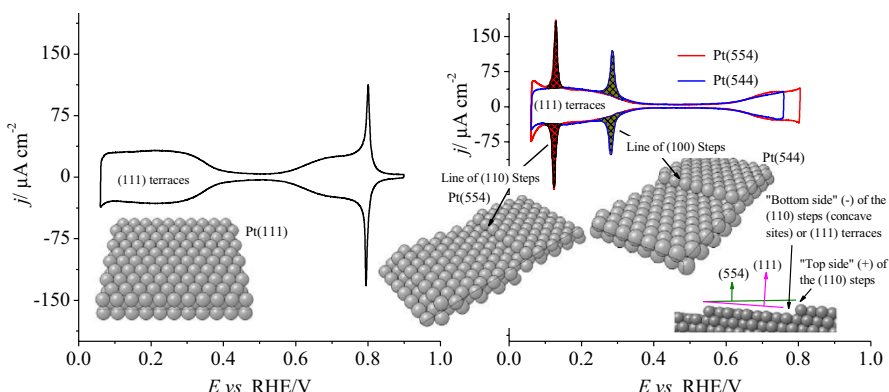


Fig. 2 Cyclic voltammograms of Pt crystal surfaces, namely, Pt(111), Pt(554) and Pt(544), in 0.1 M HClO_4 recorded at a potential sweep speed of 50 mV s^{-1} . Data include illustrations of hard sphere models for each surface orientation

in the corresponding voltammetries, therefore, are the fingerprint of the (110) and (100) step sites at Pt surfaces containing relatively wide (111) terraces. These peaks are completely absent in the cyclic voltammogram of Pt(111) surface, which should contain only the (111) terraces. Details on the voltammetric profile for a range of potentials up to the hydrogen region, especially for the Pt(111) surface in perchloric acid, are available elsewhere [32–34].

On the basis of H_{UPD} redox reactions taking place at site-specific Pt electrodes, it is possible to use the electric charge under the different states to estimate the coverage of blocking species which bind at the Pt sites stronger than H_{ads} does, and consequently displace H_{ads} from the surface. If the blocking species is site-selective, then by monitoring the changes of the voltammetric profile in the hydrogen region it would be possible to identify the specific electrocatalytic sites for an electrocatalytic reaction. The reverse is also possible, i.e., when a strongly blocking species leaves the surface and the vacancy sites become available for H_{UPD} . Therefore, it is possible to use the sequence of changes of the hydrogen region with the aim of surface site assignation for some electrocatalytic reaction. One of these reactions is CO electro-oxidation.

3.2 Electro-Oxidation of Carbon Monoxide

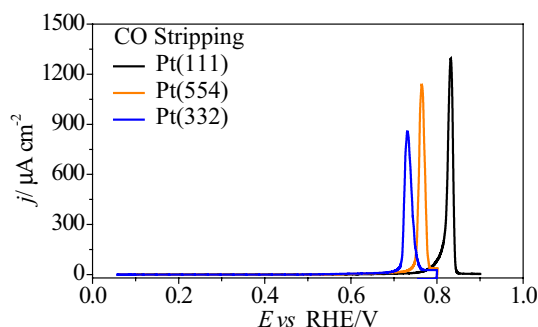
Similar to the solid/gas interface [35, 36], the adsorption and oxidation of CO can be considered a model in surface electrochemistry and electrocatalysis [37, 38]. From the fundamental research viewpoint, CO oxidation is widely used as a first test in heterogeneous catalysis and has been widely used as a model for the development of concepts in this field [35]. In surface electrochemistry, the adsorption of CO is employed in obtaining information about the structure of the electrified interface, as is the determination of the potential of zero total charge [39] for different electrodes. The charge that crosses the electrode/electrolyte interface during the

electro-oxidation of a CO monolayer can serve as a parameter for quantitative estimation of “electrochemically active surface area” (EASA) of the catalyst surfaces. Thus, the determination of EASA by CO stripping procedure has been revealed to be more accurate than the use of the charge from the H_{UPD} [40, 41], likely because the latter is more sensitive to surface contamination. It should be noted, however, that agreement is found if controlled experiments are performed [39]. On the other hand, adsorbed CO appears as an intermediate in the electro-oxidation of carbon-containing compounds (such as alcohols and other organic species [42]), and from the kinetics point of view, the self-generated CO_{ads} species acts as a catalytic poison.

Studies on the electro-oxidation of CO adlayer by voltammetry employing stepped Pt surfaces, as a general rule, revealed that the voltammetric stripping in acid media presents a single oxidation peak (not considering the possible pre-oxidation process), and the potential of CO oxidation peak shifts to lower values as the density of steps increases on the Pt surface [43], as shown in Fig. 3. In these specific experiments, the electrode preconditioning consisted of flame annealing and cooling under a controlled Ar/H₂ atmosphere. Additionally, the CO adlayer was deposited with the potential fixed at 0.100 V_{RHE}. The significance of highlighting this is because there are exceptions to that general rule [44], in which the catalytic activity of the platinum is greatly influenced by the catalyst preconditioning and the adsorption conditions of the CO adlayer. In alkaline media, on the other hand, the voltammetric CO stripping from Pt stepped surfaces exhibits more than one CO oxidation peak, as shown in Fig. 4. At Pt(111), the main peak is observed at 0.78 V, while the electrodes with (110) steps show another peak at 0.6 V and those with (100) steps at 0.7 V. At first glance, the catalytic behavior in alkaline media is not related to the greater “availability” of OH_{ads}, as is often suggested for experiments in alkaline media. The important issue that arises deals with the types of active sites that correspond to the different peaks of CO oxidation in the voltammograms, and the role that water plays in that reaction.

In CO electro-oxidation, different from the studies at the solid/gas interface, in which the oxygenated species is coming from molecular oxygen, at the aqueous electrified solid/liquid interfaces, it is accepted that the source of oxygenated species comes from the water molecules. It is also almost consensual that the mechanism of the electrocatalytic CO oxidation proceeds through the Langmuir–Hinshelwood

Fig. 3 Electro-oxidation of CO adlayer on Pt(111), Pt(554) and Pt(332) in 0.1 HClO₄. The CO adlayer was deposited at 0.10 V_{RHE}. Data was recorded at a sweep rate of 50 mV s⁻¹. The data were reproduced and adapted from the American Chemical Society [49] and Elsevier [25] with permission



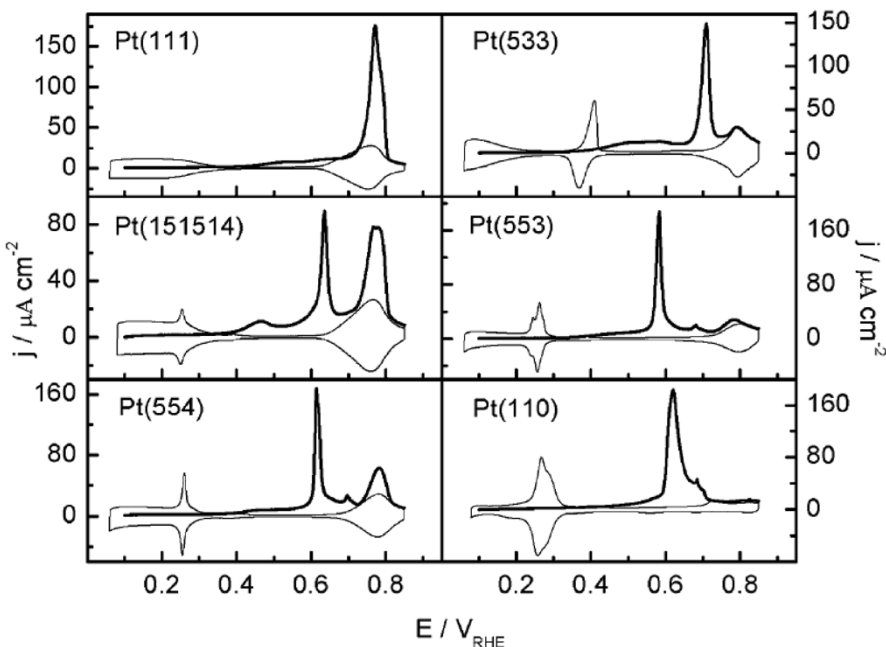
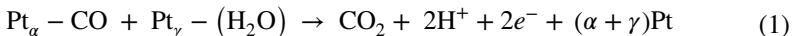


Fig. 4 CO stripping (thick solid line) and the subsequent cyclic voltammogram (thin solid line) for Pt(111), Pt(151514), Pt(554), Pt(533), Pt(553) and Pt(110) in 0.1 M NaOH. The CO adlayer was deposited at 0.10 V_{RHE}. Data were recorded at a sweep rate of 20 mV s⁻¹. The data were reproduced and adapted from the Royal Society of Chemistry [50] with permission

mechanism, in which bi-molecular interaction between two neighboring adsorbed species, i.e., CO_{ads} and (presumably) any sort of activated water, as proposed by Gilman [45], or incipient OH_{ads}, react to form the CO₂, which desorbs readily to free up the active sites on the surface. The overall reaction of CO electro-oxidation (disregarding any adsorption of anions, which certainly play an important role in the process [46]) can be written as:



in which the terms α and γ stand for the number of Pt atoms involved in the adsorption of each species. The standard potential for the reaction $\text{CO}_{(g)} + \text{H}_2\text{O}_{(l)} \rightleftharpoons \text{CO}_{2(g)} + 2\text{H}^+ + 2e^-$ is $E^0 \approx -0.104$ V_{SHE}.

In the catalytic process of electrochemical water dissociation to OH_{ads}, protons and electrons are expelled, i.e., $\text{H}_2\text{O} + {}^*\text{active sites} \rightarrow \text{OH}_{\text{ads}} + \text{H}^+ + e^-$. This reaction is expected to occur on Pt electrodes, at least at high potentials. In acidic media (0.1 M HF), Ueno et al. [47] using in situ infrared spectroscopy have provided evidence that the reaction of OH_{ads} formation, on stepped Pt surfaces [consisting of (111) terraces separated by monoatomic (110) or (100) steps, as in Fig. 2] starts at ~ 0.3 V_{RHE}. The reaction of OH_{ads} formation depends on the adsorption sites and the applied potential. At least at 0.9 V_{RHE}, the OH_{ads} on (111) terraces is dominant in comparison to the OH_{ads} on step sites; OH_{ads} coverage, i.e., the band intensity of δ_{PtOH} (in-plane

bending mode of OH_{ads}), decreased with the increase in step density [47]. If this (independent) reaction takes place in a step of the CO electro-oxidation, a possible intermediate species formed during CO_{ads} electro-oxidation would be the COOH_{ads} species, whose formation depends on the structure of the electrode, but its decomposition to CO_2 is potential-dependent, i.e., $\text{COOH}_{\text{ads}} \rightarrow \text{CO}_2 + \text{H}^+ + e^- + {}^*_{\text{active sites}}$. Santos et al. [48] had already proposed that COOH_{ads} might be a reaction intermediate during the electro-oxidation of CO_{ads} on Pt in acid media. However, the chemical nature of the oxygenated species that react with CO_{ads} remains an open question.

The identification of active sites in the CO electro-oxidation refers to experiments of CO stripping, which is when there is no CO beyond that adsorbed on the catalyst surface. The comparison between CO and H adsorption is useful because H cannot adsorb on CO-covered sites. In a full CO adlayer at Pt stepped surfaces such as those of Fig. 2, it is plausible to assume that all kind of sites are occupied by CO, i.e., either the (111) terrace sites and the step sites are blocked by CO. At this stage of full CO coverage (and in absence of solution CO), we can partially remove the CO adlayer and verify the kind of sites released after CO electro-oxidation. It is appropriate to anticipate that this experimental procedure is because the CO_{ads} adlayer apparently behaves as a typical poison (“immobile”) layer during the CO_{ads} oxidation. In the last 5 years, we have conducted a series of experiments in this direction in the entire pH range, and it was found that at stepped Pt surfaces the most active sites consist of (111) terraces [25, 51, 52]. The intrinsic catalytic activity of step and kink sites is lower compared to the catalytic activity at the (111) terraces of those kinds of surface. In this framework, concerning the determination of specific electrocatalytic sites in CO oxidation, another example is shown in Fig. 5 for a Pt(554) surface in 0.1 M NaOH, whose CO_{ads} adlayer was formed at 0.100 V_{RHE}. In Fig. 5, the (110)

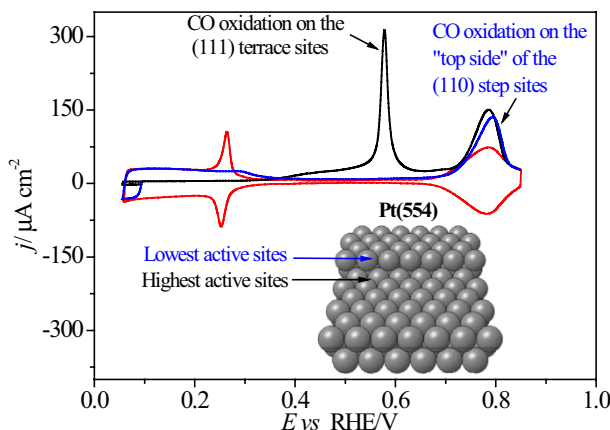


Fig. 5 Site specific determination for CO electro-oxidation on a Pt(554) surface in 0.1 NaOH. Black line: electro-oxidation of CO full coverage. Blue line: oxidation of CO only at the (110) step sites. Red line: black voltammetry. Inset: side view of the hard sphere model of the Pt(554) surface, highlighting the locally concave structure and convex one of the step site. Experiments were performed at a potential sweep speed of 0.05 V s^{-1} . The data were reproduced and adapted from the American Chemical Society [49] with permission

steps were selectively blocked by CO adsorption. In this case, in comparison to the blank cyclic voltammogram (red line), the reversible pair of peaks at ~0.264 V are fully blocked for hydrogen adsorption, and only the sites at the (111) terraces were free to adsorb hydrogen (Fig. 5, olive line). The oxidation of the CO only on (110) steps develops a peak at ~0.79 V. On the other hand, in the oxidation of full-coverage CO, where presumably all the kinds of sites were occupied by CO, the voltammetry develops multiple CO oxidation peaks. In the case of CO electro-oxidation on kinked Pt surfaces in alkaline media, three oxidation peaks arise in the CO stripping voltammogram [53]. For full coverage (Fig. 5), one prominent peak appears at ~0.58 V, and on the basis of partial CO stripping, it is due to the CO electro-oxidation along the (111) terrace sites of the Pt(554) surface. The position of this peak is extremely sensitive to the surface orientation (and flame annealing preconditioning). Then, in Fig. 5, the potential required for the CO electro-oxidation involving the (111) terraces is lower than that required for the CO oxidation at the (110) steps or top side of the step sites. Therefore, it is clear that the electro-oxidation of CO on Pt surfaces is a reaction which preferentially takes place at (111) terrace sites. Even the kink sites are less catalytically active toward CO electro-oxidation than the (111) terrace sites of the kinked Pt surfaces [51]. The identification of the (111) terraces of the stepped Pt surfaces as being the most active sites also has been possible by *in situ* FTIR analysis [51, 52, 54]. On the other hand, on the basis of theoretical (coordination-activity plot) modeling (and experimental data), Calle-Vallejo et al. [55] suggested that the Pt sites become activated at the lowest potentials are located at convex structures, being OH_{ads} at the top side of the steps, whereas the CO_{ads} were at the (111) domains from the upper side of the (111) terraces (close to the step occupied with OH_{ads}). Preferential CO electro-oxidation at the (111) terraces has also been observed on shape-controlled Pt nanoparticles (size ~8.5 nm) in alkaline media [56], and on commercial carbon-supported Pt nanoparticles (mean size 1.81 nm) in acid [57].

However, despite the higher catalytic activity along the (111) terraces of the stepped Pt surfaces, the catalytic activity of the Pt(111) electrode is lower than that observed for stepped surfaces in similar conditions. This can suggests that the break of the (111) terraces by steps induces variation in catalytic activity along the (111) terraces, not present in the “infinite” Pt(111) surface. In this way, on the basis of sequential sites for the CO adsorption and the oxidation at stepped Pt surfaces, it was suggested that there is a hierarchical energy gradient along the terraces [51]. In this sense, in terms of site occupancy, the top side of the step sites represents the set of sites that are preferentially occupied by CO adsorption, i.e., the set of sites to be first occupied, which also are the same sites which were the last released after CO electro-oxidation, in this particular case. At the solid/gas interface, in an experiment in which the CO_{ads} was forced to shift from steps to terraces and vice versa, as a function of a local thermal perturbation, it was observed that CO occupies preferentially the top of the steps, where it binds more strongly than on (111) terraces [58]. The set of sites close to the step sites from the bottom side (or terrace sites—see hard sphere model in Fig. 5) are concave sites and are the set of sites to be the last occupied by CO adsorption; but during the oxidation of the CO adlayer, these sites are released first [51]. Then, the most catalytically active sites correspond to the locally concave structures and the lowest catalytically active ones correspond to the

locally convex structures of the same local structure present at the Pt surfaces [51, 52] (see inset in Fig. 5). This means that the defects/steps do not partake in chemistry by themselves, but step sites act by modifying the catalytic properties of their neighboring sites. This seems to be a general characteristic of the sites vicinal to Pt(111) toward CO electro-oxidation. Recently, we have reported a case in which the activation pathway of CO oxidation on Pt was inhibited as the (111) planes become defect-rich. In this case, the CO adlayer was deposited during cooling of the Pt(111) surface in a CO atmosphere [44]. This means that the active site designation for the CO electro-oxidation requires a precise specification of the experiments.

In electrocatalysis of CO stripping experiments, after CO_{ads} oxidation at the most active sites, CO molecules do not occupy them again, because the CO_{ads} behaves as an “immobile” species during the process. This is a general characteristic of CO stripping on Pt electrodes in entire pH range [25, 51, 52]. Then, based on these arguments, in terms of site occupancy, the set of the most catalytically active sites become occupied only under conditions of full CO coverage or if there is CO in the solution side. If we consider the (111) terraces and steps/defects, the strength of CO adsorption at the specific sites is a parameter which must be considered in the kinetic analysis of the preferential electrocatalytic oxidation of CO, and this preference is directly linked to the local arrangement of atoms at the catalyst surface. In this regard, the influence of (100) steps in improving the catalytic activity of (111) terraces is lower in comparison to the catalytic shift in (111) terraces in the presence of (110) steps, despite the intrinsic catalytic activity of the (110) and (100) steps being very similar to each other [25].

In conclusion, the most active sites toward CO electro-oxidation at the Pt(111) vicinal surfaces consists of those located on the (111) terraces. A descriptive experiment which elucidates this issue starts by decoration of the (110) steps by ^{13}CO leaving all the (111) terraces sites of a Pt(332) surface free for electro-oxidation of the CO_{ads} coming from (10^{-3} to 10^{-1} M) ethanol dissociation [59]. It was shown that $^{13}\text{CO}_{\text{ads}}$ previously attached at the (110) steps oxidized at potentials higher than the electro-oxidation of CO_{ads} from ethanol dissociation at the (111) terraces of the stepped Pt surface. Again, a series of experiments including cyclic voltammetry (partial CO adlayer stripping), chronoamperometry (potential steps) and in situ FTIR employing well-defined Pt-based electrodes, indicate that CO_{ads} behaves as an immobile species during its oxidation [52, 60]. The oxidation of the CO adlayer initiates at sites at the bottom side of the steps, that belong to the (111) terraces. It is in this sense that we propose that the (111) domains of the stepped surfaces contain the most active sites toward CO electro-oxidation. The reaction proceeds along the (111) terraces, which became free for H_{UPD} , and the last set of sites at which the CO_{ads} was oxidized are the step sites, which were finally accessible to H_{UPD} .

3.3 Pathways of Methanol Electro-Oxidation Toward Carbon Dioxide

The main reason why the electrochemical oxidation reaction of methanol is so widely studied is because of its potential use in low-temperature fuel cells [61]. In terms of thermodynamics, the standard potential for the reaction $\text{CH}_3\text{OH}_{(l)} + \text{H}_2\text{O}_{(l)}$

$\rightleftharpoons \text{CO}_2^{(\text{g})} + 6\text{H}^+ + 6e^-$ is $E^0 \approx 0.016$ V_{SHE} and the theoretical fuel cell efficiency is $\approx 96.7\%$. At platinum electrodes, it is argued that the electrochemical oxidation reaction of C₁ molecules, as methanol, formaldehyde and formic acid, can proceed through two (parallel) pathways, termed direct and indirect [62, 63]. The terminologies for these reaction pathways have the CO_{ads} as a watershed in the reaction mechanism, and the preferred pathway depends on the nature and composition of the catalyst materials, as well as on the precise local geometric arrangement of the atoms at the catalyst surfaces, as deduced from the studies on the single crystalline surfaces [64, 65]. The direct pathway is kinetically faster and it is believed that the C₁ molecules goes to CO₂ without going through CO_{ads}. The indirect one is kinetically slower, and the C₁ molecules are finally transformed in CO₂, but through CO_{ads}. In the case of formic acid (HCOOH), the direct pathway involves its dehydrogenation and subsequent evolution to CO₂. The formate species adsorbed (HCOO_{ads}) through the carbon atom has been identified and its possible role in kinetics—if it acts like a catalytic poison or intermediate reaction—has been warmly debated in literature [66–68]. In the indirect pathway, the C₁ molecules are dehydrated toward CO_{ads}, which displays the role of a catalytic poison, as it is oxidized to CO₂ at high potentials.

The use of Pt single crystals in studying the electrocatalysis of methanol oxidation has revealed that the reaction is strongly sensitive to the catalyst surface structure [69]. Then, on platinum, the reaction yields formic acid and formaldehyde as soluble products, while CO_{ads} is detected at the electrode surface [69]. After a kinetic study employing stepped Pt surfaces, it was concluded that methanol dissociation takes place exclusively at the step sites [65]. In these unpoised terraces, it has been shown that the direct path of methanol electro-oxidation is a site-demanding process. The quantification of this statement was experimentally determined [70] employing a cyanide-Pt(111)-modified electrode, as shown in Fig. 6 [70]. In the series of in situ FTIR spectra in Fig. 6c, no bands due to the intermolecular stretching frequencies of adsorbed CO_{ads} were detected (which should appear at ~ 2060 – 2075 , and ~ 1850 cm⁻¹, due to the linearly and bridge-bonded CO, respectively [71]). The absence of CO_{ads} in the mechanism of methanol electro-oxidation on cyanide-Pt(111)-modified electrode also explains the stability of the voltammetry in the hydrogen region, even in the presence of methanol in solution (Fig. 6a). The band due to CO₂ appears in the in situ FTIR spectra at 2343 cm⁻¹ at ~ 0.6 V_{RHE}, that is the onset potential for the methanol oxidation to CO₂ on cyanide-Pt(111)-modified electrode.

Concerning the surface structure of the cyanide-modified Pt(111) electrode, Fig. 7a shows the pattern of the Pt sites occupied by cyanide. The configuration of the cyanide-modified Pt(111) electrode is a $(2\sqrt{3} \times 2\sqrt{3})R30^\circ$ structure and provides a limited arrangement of contiguous Pt atoms [72]. The formation of CO_{ads} requires a large atomic ensemble, at least three contiguous atoms of platinum [70]. This specific atomic configuration is not observed on the cyanide-modified Pt(111) electrode, explaining the direct oxidation of methanol toward CO₂, without going through CO_{ads}. Figure 7b, c displays the possible matches between the configurations involving three Pt atoms on the catalyst surface and the possible reaction pathways.

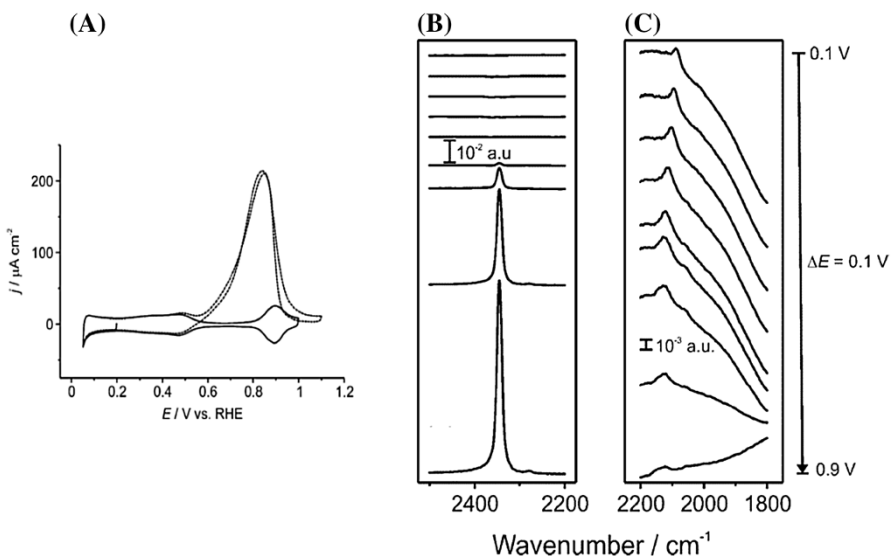


Fig. 6 Electro-oxidation of 0.2 M methanol on a cyclic voltammogram of a cyanide-modified Pt(111) electrode in 0.1 M HClO_4 . **a** Cyclic voltammograms (methanol electro-oxidation + blank cyclic voltammograms). **b, c** In situ FTIR spectra. The spectra in the frequency region between 2500 and 2200 cm^{-1} (**b**) were calculated using the spectrum at 0.05 V_{RHE} as reference, while the spectra in the frequency region between 2200 and 1800 cm^{-1} (**c**) were calculated using the spectrum at 1.30 V_{RHE} as reference. The original figures were modified. Data are reproduced from the American Chemical Society [70] with permission

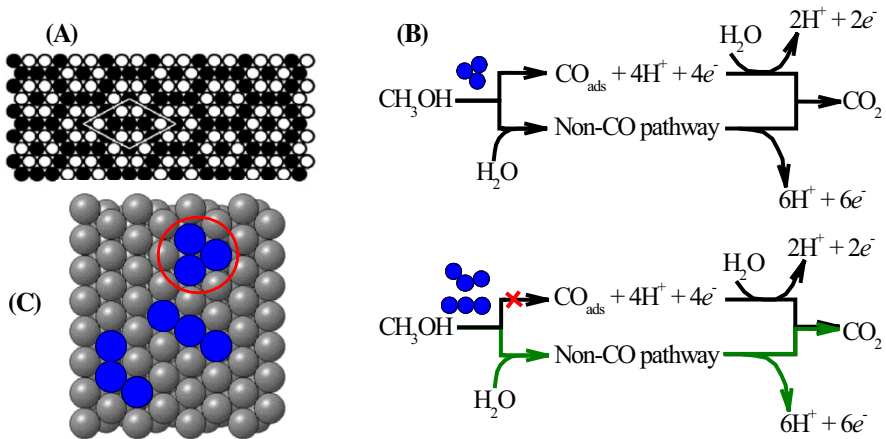


Fig. 7 **a** Ball model of the $(2\sqrt{3}\times 2\sqrt{3})R30^\circ$ structure of the cyanide layer on a Pt(111) surface. **b** Possible reaction pathways of specific geometric arrangement of three Pt atoms as (111) terraces. **c** Hard sphere model of a Pt(111) surface indicating three possible configurations involving three connected Pt atoms, and the configuration inside the circle being the only one that allows the CO_{ads} formation from the methanol dissociation. The schemes in **(a, b)** were reproduced and adapted from the American Chemical Society [70] with permission

At least in the case of the cyanide-Pt(111)-modified electrode, it was found that at least three contiguous atoms at the Pt surfaces are required for the formation of CO_{ads} , while at least two contiguous atoms are required for the activation pathway of CO_2 formation [73]. The set of atoms into the circle in Fig. 7c likely are the “active sites” in the indirect pathway for the methanol electro-oxidation toward CO_2 going through CO_{ads} . In the cyanide-Pt(111)-modified electrode, those three contiguous Pt atoms are not available and then the direct pathway takes place. As we can observe in Fig. 7a, the set of three atoms are a row of atoms and the condition of the three contiguous atoms is not fulfilled on cyanide-Pt(111)-modified surfaces. This elegant experiment provides exactly the narrow relationship existing between a specific set of atoms on the catalyst and the specific reaction pathways.

Similar restriction of at least three contiguous Pt atoms was also observed for formic acid electro-oxidized to CO_2 with going through CO_{ads} on cyanide-Pt(111)-modified electrodes [74]. In conclusion, the mechanisms of methanol electro-oxidation imply that at least two contiguous atoms of Pt are required for the activation of the reaction pathway of CO_2 formation, and at least three contiguous atoms are needed for the dehydrogenation of the methanol molecule toward CO_{ads} .

3.4 Electro-Oxidation of Ammonia

In this reaction, we approach one extreme case in which the electrocatalytic reaction takes place at a single kind of active site. Interest regarding ammonia electrochemical oxidation is because this toxic gas, or rather, the ammonium sulfate $(\text{NH}_4)_2\text{SO}_4$, used worldwide as a fertilizer, is a contaminant of water. As a result, the development of electrochemical sensors and selective catalysts for the degradation of ammonia to a harmless molecule such as N_2 gas are a subject of intense research in electrochemistry [75]. Other interest in ammonia electro-oxidation is because, from the electrochemical energy conversion point of view, ammonia is a potential candidate to be used as fuel in direct “ammonia” fuel cells [76, 77]. In extreme alkaline media, the standard potential for the ammonia oxidation reaction $\text{NH}_{3(\text{g})} + 3\text{OH}_{(\text{aq})}^- \rightleftharpoons 1/2\text{N}_{2(\text{g})} + 3\text{H}_2\text{O}_{(\text{l})} + 3e^- \text{is } E^0 \simeq -0.770 \text{ V}_{\text{SHE}} (\text{or } \sim 0.055 \text{ V}_{\text{RHE}})$ [76]. Then, it is interesting to study catalyst materials on which the selective electrochemical oxidation of ammonia toward N_2 gas is kinetically favored.

In terms of reaction mechanism, the accepted mechanism for the electrochemical oxidation of ammonia in alkaline media was proposed by Gerischer and Mauerer [78]; according to them, it occurs through a sequential dehydrogenation of adsorbed ammonia ($\text{NH}_{3,\text{ads}}$) resulting in NH_x species, i.e., $\text{NH}_{2,\text{ads}}$, $\text{NH}_{,\text{ads}}$, and N_{ads} . The main reaction intermediate is the NH_2 species, which dimerizes to adsorbed hydrazine-like $\text{N}_{2}\text{H}_{x+y,\text{ads}}$, which might easily oxidize to N_2 . The complete dehydrogenation of ammonia yields the N_{ads} species which is inert for the formation of N_2 , but in kinetics it was considered as a catalytic poison [78]. The essence of the Gerischer-Mauerer mechanism has been corroborated [79, 80] by using differential electrochemical mass spectrometry (DEMS) at Pt in alkaline solution, in which N_2 , NO_2 and NO [79] (byproduct of ammonia oxidation) were identified. In relation to the adsorbed species, Matsui et al. [81] by in situ

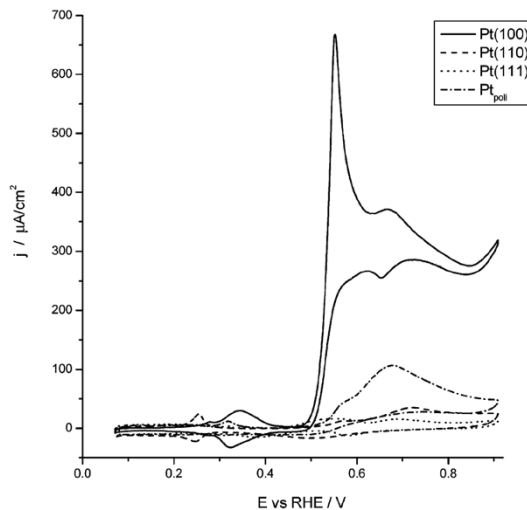
attenuated total reflection infrared (ATR-IR) spectroscopy identified bridge-bonded NO_{ads} species on the Pt surface in alkaline media as a catalytic poison (a band due to the NH_2 wagging mode of N_2H_4 was detected).

Studies employing Pt basal planes, namely, the Pt(111), Pt(110) and Pt(100), in alkaline media, showed that the electrochemical oxidation reaction of ammonia is extremely structure-sensitive and takes place almost exclusively on sites with (100) symmetry [82]. In line with this statement, different voltammetric profiles for ammonia electro-oxidation on Pt basal planes, in alkaline solution, are displayed in Fig. 8. The highest current density for the ammonia electro-oxidation on Pt(100) plane evidences the superior activity of this surface over the other basal planes. A local maximum occurs at $\sim 0.55 \text{ V}_{\text{RHE}}$, and at $\sim 0.65 \text{ V}_{\text{RHE}}$ a pair of redox peaks is observed. Subsequent studies employing stepped Pt surfaces consisting of (100) terraces separated by monoatomic steps of (111) or (110) symmetry revealed that the activity depends on the terrace width [83].

However, as pointed out above, different reaction products are formed from ammonia electro-oxidation on platinum [79]. Consequently, molecular details on the preference of reaction pathways (or selectivity) on Pt single crystals were obtained by DEMS, using a labelled ammonia (^{15}N) in 0.1 M NaOH, and detected [84] were $^{15}\text{N}_2$, ^{15}NO and $^{15}\text{N}_2\text{O}$, whose mass-to-charge ratio (m/z) data are reproduced in Fig. 9.

In Fig. 9 (left), the intensity for $m/z = 30$ ($^{15}\text{N}_2$) is about one order of magnitude higher for the Pt(100) plane than the other ones. At Pt(100), if we compare the (order of) magnitudes for $m/z = 30$ ($^{15}\text{N}_2$), $m/z = 46$ ($^{15}\text{N}_2\text{O}$) and $m/z = 31$ (^{15}NO), we conclude that the (100) facets are not only the most active sites, but they are also sites highly selective toward N_2 formation. Almost no current and NO were detected for ammonia electro-oxidation on Pt(110) and Pt(111) surfaces, and only a very small amount (low m/z ratio) of NO_2 molecules was formed on those surfaces.

Fig. 8 Cyclic voltammometric profiles of the oxidation of 10^{-3} M ammonia on Pt(100), Pt(111) and Pt(110) electrodes and polyoriented Pt single crystal in 0.1 M NaOH. Experiments were performed at a potential sweep speed of 10 mV s^{-1} . Data were reproduced from the American Chemical Society [83] with permission



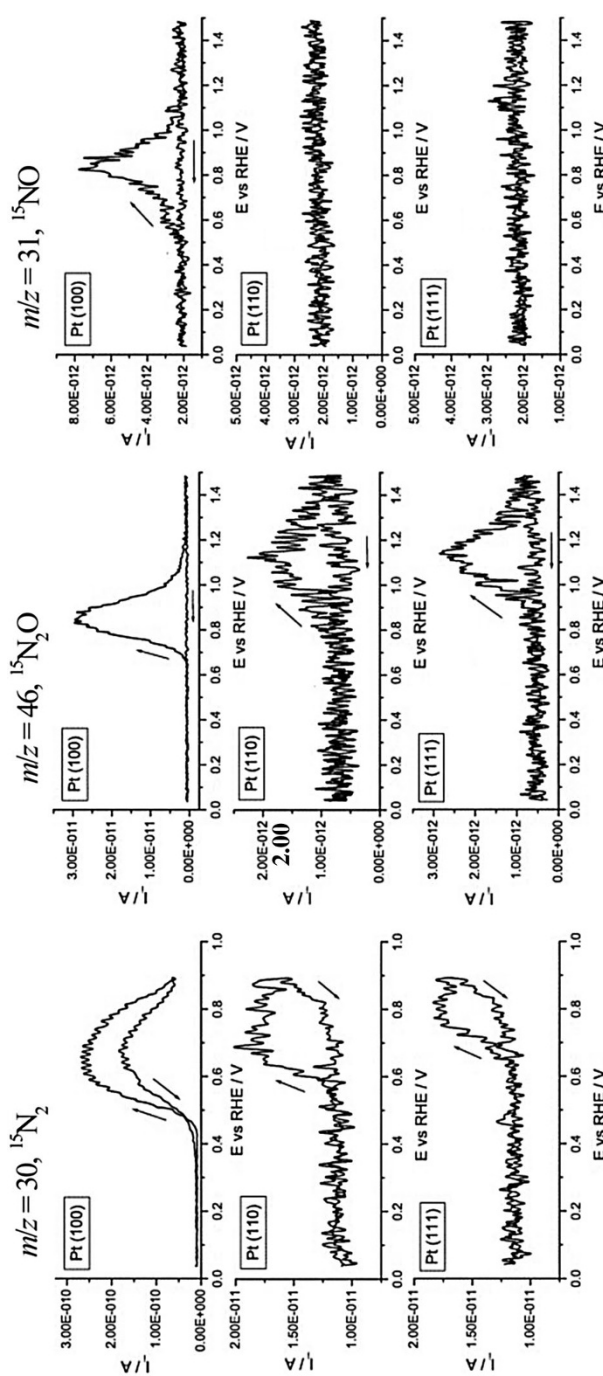


Fig. 9 Mass spectrometric cyclic voltammetry curves for the electro-oxidation of 10^{-3} M ammonia [$(^{15}\text{NH}_4)_2\text{SO}_4$] at three Pt basal surfaces, namely Pt(100), Pt(111) and Pt(110), in 0.1 M NaOH at a scan rate of 10 mV s^{-1} . The mass-to-charge ratios (m/z) for N_2 , N_2O and NO species are indicated in the figure. Data were modified and reproduced from Elsevier [84] with permission

In conclusion, the electro-oxidation of ammonia at Pt surfaces is, at least to the knowledge of these authors, the most sensitive electrocatalytic reaction to the structure of platinum, so that the electro-oxidation of ammonia has served as a guide for the characterization of shape-controlled Pt nanoparticles with (100) preferential orientation [85]. The electrochemical reduction of nitrite (NO_2^-) toward N_2 is another electrocatalytic reaction that preferentially takes place on the (100) facet of the Pt [86], whose reaction mechanism (in terms of intermediates of reactions) has been claimed to have some similarity with the oxidation mechanism of NH_3 to N_2 [87]. Returning to the reaction mechanism of ammonia electro-oxidation on Pt(100) in alkaline media, recently, Katsounaros et al. [80] proposed that the dimerization of NH_{ads} species to $\text{N}_2\text{H}_{2\text{ads}}$ ones, being the last of which is dehydrogenated to N_2 ; and the N_{ads} species serves as a reaction intermediate for the formation of byproducts as is the NO_{ads} species. Both N_{ads} and NO_{ads} act as catalyst poisons.

3.5 Asymmetric Electrocatalysis of the Glucose Oxidation in Intrinsically Chiral Pt Surfaces

As already reported above, the surface of the catalyst might consist of different active sites. The sophistication in heterogeneous catalysis and electrocatalysis is upgraded when enantioselective reactions are proposed to the catalyst surface. Comprehensive reviews on the origin of the chiral recognition and the enantioselectivity involving asymmetric catalyst surfaces have been published [88, 89]. Briefly, for fcc (face-centered cubic) metal lattices, the chiral recognition and the possible enantioselectivity are characteristics intrinsically linked to the kink sites. From the surface chemistry point of view, the elegance of the kinked surfaces lies in its intrinsic chiral character, and no matter the width of its terraces, all the kinked surfaces are intrinsically chiral [90]. The chiral surfaces cannot overlap with their mirror image. The kinked surfaces appear at the intercept of the three different basal planes, namely, the (111), (110) and (100), as shown in Fig. 8. Experimentally, they are obtained by cutting the surface of a stepped surface (intercept of two basal planes) with respect to the third basal plane [91] and the chirality obeys the follow condition $h \neq k \neq l$ and $h \times k \times l \neq 0$, in which the (hkl) are the Miller indices [92]. One pair of ideal (643)^{R&S} chiral faces (enantiomers) of the metals of fcc lattices is displayed in Fig. 10. The R (from the Latin *rectus*) and S (from the Latin *sinister*) terminology design the clockwise $(111) \rightarrow (100) \rightarrow (110)$ and counter-clockwise $(111) \leftarrow (100) \leftarrow (110)$ sequence of exposed planes on a surface (similar to the Cahn-Ingold-Prelog rules), taking into account the priority of the planes on the basis of its packing density $\rho_{(hkl)}$, i.e., $\rho_{(111)} > \rho_{(100)} > \rho_{(110)}$ [93].

Chiral properties, i.e., the chiral recognition and the enantioselectivity on solid catalysts, very often, is introduced by attachment of chiral compounds on non-chiral substrates [89], as the hybrid systems. The disadvantage is that the chiral modifiers may be leached from the solid surfaces, which would deactivate the chiral properties. The enantioselective recognition has also been obtained by generation of cavities in mesoporous Pt, by electrochemical reduction of Pt ions in presence of a “self-assembled liquid crystal” phase and chiral template molecules

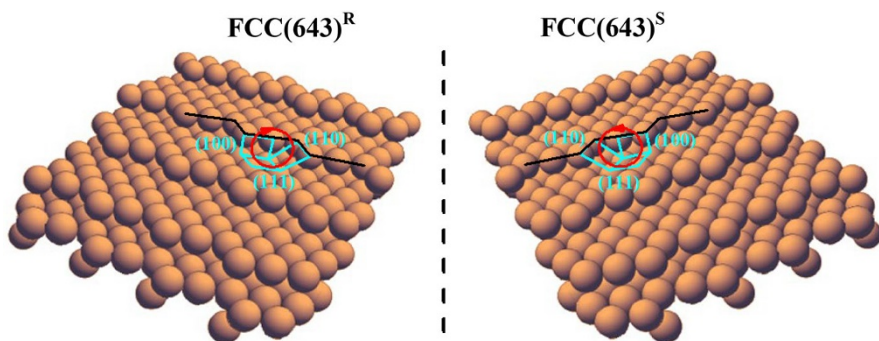


Fig. 10 Hard sphere model of a pair of $(643)^{R\&S}$ enantiomer surfaces of metals of fcc lattices. The enantiomer on the right side does not overlap with the surface on the left side. Figure reproduced and adapted from Springer Nature [96] with permission

[94, 95]. Inherently, the electro-deposited material seems to retain a chiral character after removal of the template molecules [94, 95]. However, in view of its well-defined surface structure, for understanding underlying factors controlling the chiral properties, the chiral surfaces must be designed, and in this case, the intrinsically chiral single crystal kinked surface is a suitable template for electro-catalytic studies.

As highlighted above, the enantiodifferentiation with kinked surfaces is due to the kink sites; consequently, they are the origin of the difference in electro-catalytic activity and discrimination of possible reaction pathway at this kind of surface. The first experimental example of enantiospecific interaction/adsorption of chirality on single crystal electrodes was provided in 1999 [97] for the electro-oxidation of D- and L-glucose at the Pt(643)^R and its enantiomorph Pt(643)^S surfaces, respectively, whose surfaces are shown in Fig. 10; the experiments are shown in Fig. 11 [90]. These kinked surfaces consist of three-atom-wide (111) terraces, separated by (110) monoatomic steps broken by the site's (100) symmetry, either R or S kink sites—see Fig. 10. Firstly, the voltammetry of the Pt(643)^{S&R} catalysts in the presence of the electrolyte (H_2SO_4 or $HClO_4$ solution) presents a pair of reversible peaks at ~ 0.07 and ~ 0.23 V due to the hydrogen adsorption/desorption at Pt sites [98]. These peaks were shifted toward less positive values in comparison to Fig. 2, because of the Pd reference electrode used. The survival of the peak at ~ 0.07 V suggests that the interaction of the glucose with (110) steps is weak or negligible at low potentials [97, 98], or at low potentials the interaction of either D- or L-glucose is not influenced by the handedness of the Pt(643) surfaces. The important difference in the voltammograms of the enantiomorph Pt(643)^{S&R} surfaces in the presence of D/L-glucose arose for potentials up to ~ 0.2 V. Then, in the case of the enantiomorph Pt(643)^R surface, a prominent oxidation peak at ~ 0.31 V arises for the electro-oxidation of D-glucose (Fig. 11b, and this referred peak is absent in electro-oxidation of D-glucose on the enantiomorph Pt(643)^S surface (Fig. 11a). For the electro-oxidation of L-glucose, the opposite is observed in Fig. 11c, d: cross reactivity appears. These examples evidence that the interaction/adsorption of an enantiomer molecule such

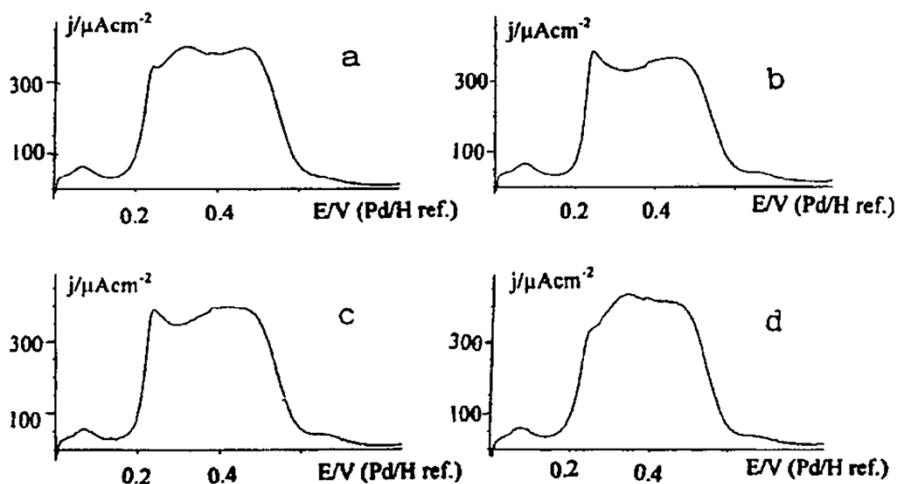


Fig. 11 Linear sweep voltammograms of 5×10^{-3} M D-glucose electro-oxidation on: **a** Pt(643)^S; **b** Pt(643)^R. Linear sweep voltammograms of 5×10^{-3} M L-glucose electro-oxidation on: **c** Pt(643)^S; **d** Pt(643)^R. Data obtained using 0.1 M H_2SO_4 at a potential sweep rate of 50 mV s⁻¹. Data reproduced from the American Chemical Society [90] with permission

as D- or L-glucose (whose molecule structure possesses multiple stereochemical centers) deeply depends on the chirality of the catalyst surfaces, either Pt(643)^R or Pt(643)^S.

Clearly, the origin of the enantiodifferentiation on the surfaces is due to the kink sites, likely because the enantiomer molecule fit better at one kinked surface than in its specular image. The electro-oxidation of L- and D-glucose is very similar on Pt(221) and Pt(332) stepped (non-kinked) surfaces (no chiral recognition) [97]. In fact, the increase in the ability in chiral recognition or enantioselectivity excess apparently coincides with the increase in surface density of kink sites on going from Pt(643) to Pt(321) to Pt(531) surfaces [90]. That the manifestation of enantioselective character on kinked surfaces requires the presence of kink sites suggests that kinks are the key part of the active sites. Therefore, the kinks in kinked surfaces likely impose the constraint for the interaction between the catalyst and the corresponding reactive stereoisomers. In this regard, at the solid/gas interface, kinetic studies of the desorption of alcohol enantiomers [(R)- and (S)-2-butanol] from the enantiomorph Ag(643)^R and Ag(643)^S surfaces reported no measurable enantio-specific energy differences of desorption heat, i.e., only ~ 0.4184 kJ mol⁻¹ [99], for those two alcohol enantiomers. In the case of a liquid/aqueous electrified interface [90], the difference in reactivity for two (alcohol) isomers is appreciable, which means that the difference of energy interactions might also be appreciable.

It is worth mentioning that the origin of the enantioselective character in kinked surfaces under electrochemical conditions is still much more complex. For example, the chiral recognition seems to depend on the nature of the anion in the electrolyte, due to, unexpectedly, the enantioselective difference being more marked in the presence of strong adsorbing anions (as is the sulfate) than the non-adsorbing anions

(as is the case of the perchlorate anion) [98]. Intuitively, the expected results would be of loss in ability of chiral recognition in the presence of strong adsorbing anions because this species could block the “active sites” [100], but it is known that anions, as is the (bi)sulfate anions, adsorb at higher potentials at the (111) terrace sites [101]. This fact can explain why there is no inhibition of the hydrogen region in the voltammogram of the Pt(643)^{R&S} surfaces in the presence of glucose in sulfuric acid (Fig. 11). Moreover, the kink stability is an incognita because surface reconstruction would modify the surface irreversibly. Indeed, glucose oxidation is too complex a problem to facilitate the understanding of enantiomeric reactivity [102] and clearly more work is needed to disentangle this problem using pure enough isomers (the key step) with low molecular weight.

4 Concluding Remarks and Prospects

This report illustrates some examples aimed at determining the specific active sites in electrocatalytic reactions which preferentially take place on specific facets of a catalyst consisting of non-equivalent sites. The determination of the active sites for the CO electro-oxidation requires a precise specification of the experimental conditions employed, especially because the catalytic activity of the Pt toward CO electro-oxidation deeply depends on the history of the CO adlayer. Then, for the cases in which a CO adlayer is deposited under potential control, i.e., in the hydrogen region, the main characteristic of the electro-oxidation of CO on Pt catalyst is that the reaction preferentially takes place at the (111) plane of defected surfaces. The preferred reaction on (111) terraces of the defected surfaces combines the action of steps in modifying the catalytic properties at (111) terraces, and the most active sites (that are locally concave structures) and the lowest active ones (that are locally convex structures) are facets of similar local structure at the Pt surfaces. The CO_{ads} is a reaction intermediate formed during the oxidation of methanol. The set of atoms able to activate the direct reaction pathway of methanol electro-oxidation toward CO₂ involve three contiguous atoms. Both surface defects and (111) terraces can provide this set of contiguous atoms. The active sites for a more complex reaction, such as glucose oxidation, cannot be determined with apparent simplicity like in the case of CO electro-oxidation. However, it is possible to note that the introduction of the kinks sites is responsible for the appearance of chiral recognition of glucose on kinked surfaces. On the other hand, the determination of the active sites in ammonia oxidation (and also other nitrogen-containing species, as nitrite reduction) is easily characterized as being (100) square symmetry, because the extreme difference of electrochemical reactivity among the different sites. Moreover, at this type of site, the reaction is entirely selective to the N₂ formation, which is the desired product.

This paper is only a step towards determining of the active site on the surfaces of catalysts in a macroscopic scale. It is mainly centered around Pt(111) and its vicinal surfaces. In this sense, there is a lot of work still necessary on single crystal vicinal to the other two basal planes to make breakthroughs in the identification of active sites and progress forward to incorporate more complex situations, e.g., those involving shape-controlled nanoparticles. The macroscopic crystals at some

level mimic the surfaces of the shape-controlled nanoparticles, and in this sense, it is interesting to investigate the concepts of stepped surfaces that fit the materials at the nanoscopic scale. Future works should follow these directions.

Acknowledgements M.J.S.F. is grateful to PNPD/CAPES (Brazil). J.M.F. thanks the MCINN (FEDER, Spain) project-CTQ-2016-76221-P.

References

1. Kirby AJ (1997) Efficiency of proton transfer catalysis in models and enzymes. *Acc Chem Res* 30:290–296
2. Robert S (2015) Heterogeneous catalysis. *Angew Chem Int Ed* 54:3465–3520
3. Vojdovic A, Nørskov JK (2015) New design paradigm for heterogeneous catalysts. *Nat Sci Rev* 2:140–143
4. Andersen M, Medford AJ, Nørskov JK, Reuter K (2017) Scaling-relation-based analysis of bifunctional catalysis: the case for homogeneous bimetallic alloys. *ACS Catal* 7:3960–3967
5. Nørskov JK, Studt F, Abild-Pedersen F, Bligaard T (2014) Fundamental concepts in heterogeneous catalysis. Wiley, New York
6. Somorjai GA, Li Y (2010) Introduction to surface chemistry and catalysis. Wiley, New York
7. Tian N, Zhou ZY, Sun SG, Ding Y, Wang ZL (2007) Synthesis of tetrahedahedral platinum nanocrystals with high-index facets and high electro-oxidation activity. *Science* 316:732–735
8. Seung WL, Chen S, Sheng W, Yabuuchi N, Kim YT, Mitani T, Vescovo E, Shao-Horn Y (2009) Roles of surface steps on Pt nanoparticles in electro-oxidation of carbon monoxide and methanol. *J Am Chem Soc* 131:15669–15677
9. Koper MTM (2011) Structure sensitivity and nanoscale effects in electrocatalysis. *Nanoscale* 3:2054–2073
10. Strmenik D, Kodama K, van der Vliet D, Greeley J, Stamenkovic VR, Marković NM (2009) The role of non-covalent interactions in electrocatalytic fuel-cell reactions on platinum. *Nat Chem* 1:466
11. Stoffelsma C, Rodriguez P, Garcia G, Garcia-Araez N, Strmenik D, Marković NM, Koper MTM (2010) Promotion of the oxidation of carbon monoxide at stepped platinum single-crystal electrodes in alkaline media by lithium and beryllium cations. *J Am Chem Soc* 132:16127–16133
12. Gale RJ, Salmeron M, Somorjai GA (1977) Variation of surface reaction probability with reactant angle of incidence: a molecular beam study of the asymmetry of stepped platinum crystal surfaces for H–H bond breaking. *Phys Rev Lett* 38:1027–1029
13. O'Mullane AP (2014) From single crystal surfaces to single atoms: investigating active sites in electrocatalysis. *Nanoscale* 6:4012–4026
14. Koper M, Wieckowski A (2009) Fuel cell catalysis: a surface science approach. Wiley, New York
15. Koper MTM (2005) Combining experiment and theory for understanding electrocatalysis. *J Electroanal Chem* 574:375–386
16. Seh ZW, Kibsgaard J, Dickens CF, Chorkendorff I, Nørskov JK, Jaramillo TF (2017) Combining theory and experiment in electrocatalysis: insights into materials design. *Science* 355:eaad4998
17. Taylor HS (1925) A theory of the catalytic surface. *Proc R Soc Lond Ser A* 108:105–111
18. Buurmans ILC, Weckhuysen BM (2012) Heterogeneities of individual catalyst particles in space and time as monitored by spectroscopy. *Nat Chem* 4:873–886
19. Wandelt K (1997) The local work function: concept and implications. *Appl Surf Sci* 111:1–10
20. Jia JF, Inoue K, Hasegawa Y, Yang WS, Sakurai T (1998) Variation of the local work function at steps on metal surfaces studied with STM. *Phys Rev B* 58:1193–1196
21. Pérez León C, Drees H, Wippermann SM, Marz M, Hoffmann-Vogel R (2016) Atomic-scale imaging of the surface dipole distribution of stepped surfaces. *J Phys Chem Lett* 7:426–430
22. Somorjai GA, Park JY (2008) Molecular factors of catalytic selectivity. *Angew Chem Int Ed* 47:9212–9228
23. Nørskov JK, Bligaard T, Hvolbæk B, Abild-Pedersen F, Chorkendorff I, Christensen CH (2008) The nature of the active site in heterogeneous metal catalysis. *Chem Soc Rev* 37:2163–2171

24. Batista EA, Malpass GRP, Motheo AJ, Iwasita T (2004) New mechanistic aspects of methanol oxidation. *J Electroanal Chem* 571:273–282
25. Farias MJS, Mello GAB, Tanaka AA, Feliu JM (2017) Site-specific catalytic activity of model platinum surfaces in different electrolytic environments as monitored by the CO oxidation reaction. *J Catal* 345:216–227
26. Clavilier J, El Achi K, Rodes A (1990) In situ probing of step and terrace sites on Pt(S)-[n (111)×(111)] electrodes. *Chem Phys* 141:1–14
27. Rodes A, El Achi K, Zamakhchari MA, Clavilier J (1990) Hydrogen probing of step and terrace sites on Pt(S)-[n (111)×(100)]. *J Electroanal Chem* 284:245–253
28. Kunimatsu K, Senzaki T, Samjeské G, Tsushima M, Osawa M (2007) Hydrogen adsorption and hydrogen evolution reaction on a polycrystalline Pt electrode studied by surface-enhanced infrared absorption spectroscopy. *Electrochim Acta* 52:5715–5724
29. Paleček D, Tek G, Lan J, Iannuzzi M, Hamm P (2018) Characterization of the platinum–hydrogen bond by surface-sensitive time-resolved infrared spectroscopy. *J Phys Chem Lett* 9:1254–1259
30. McCrum IT, Chen X, Schwarz KA, Janik MJ, Koper MTM (2018) Effect of step density and orientation on the apparent pH dependence of hydrogen and hydroxide adsorption on stepped platinum surfaces. *J Phys Chem C* 122:16756–16764
31. Smoluchowski R (1941) Anisotropy of the electronic work function of metals. *Phys Rev* 60:661–674
32. Climent V, Feliu JM (2011) Thirty years of platinum single crystal electrochemistry. *J Solid State Electrochem* 15:1297–1315
33. Gómez-Marín AM, Clavilier J, Feliu JM (2013) Sequential Pt(111) oxide formation in perchloric acid: an electrochemical study of surface species inter-conversion. *J Electroanal Chem* 688:360–370
34. Huang YF, Kooyman PJ, Koper MTM (2016) Intermediate stages of electrochemical oxidation of single-crystalline platinum revealed by in situ Raman spectroscopy. *Nat Commun* 7:12440
35. Freund HJ, Meijer G, Scheffler M, Schlägl R, Wolf M (2011) CO oxidation as a prototypical reaction for heterogeneous processes. *Angew Chem Int Ed* 50:10064–10094
36. van Spronsen MA, Frenken JWM, Groot IMN (2017) Surface science under reaction conditions: CO oxidation on Pt and Pd model catalysts. *Chem Soc Rev* 46:4347–4374
37. Beden B, Lamy C, de Tacconi NR, Arvia AJ (1990) The electrooxidation of CO: a test reaction in electrocatalysis. *Electrochim Acta* 35:691–704
38. Marković NM, Ross PN (2002) Surface science studies of model fuel cell electrocatalysts. *Surf Sci Rep* 45:117–229
39. Chen QS, Solla-Gullón J, Sun SG, Feliu JM (2010) The potential of zero total charge of Pt nanoparticles and polycrystalline electrodes with different surface structure: the role of anion adsorption in fundamental electrocatalysis. *Electrochim Acta* 55:7982–7994
40. Garrick TR, Moylan TE, Carpenter MK, Kongkanand A (2017) Electrochemically active surface area measurement of aged Pt alloy catalysts in PEM fuel cells by CO stripping. *J Electrochem Soc* 164:F55–F59
41. Moniri S, van Cleve T, Linic S (2017) Pitfalls and best practices in measurements of the electrochemical surface area of platinum-based nanostructured electro-catalysts. *J Catal* 345:1–10
42. Ye JY, Jiang YX, Sheng T, Sun SG (2016) In-situ FTIR spectroscopic studies of electrocatalytic reactions and processes. *Nano Energy* 29:414–427
43. Lebedeva NP, Koper MTM, Herrero E, Feliu JM, van Santen RA (2000) Cooxidation on stepped Pt[n (111)×(111)] electrodes. *J Electroanal Chem* 487:37–44
44. Farias MJS, Chequepán W, Tanaka AA, Feliu JM (2018) Requirement of initial long-range substrate structure in unusual CO pre-oxidation on Pt(111) electrodes. *Electrochim Commun* 97:60–63
45. Gilman S (1964) The mechanism of electrochemical oxidation of carbon monoxide and methanol on platinum. The “Reactant-Pair” mechanism for electrochemical oxidation of carbon monoxide and methanol. *J Phys Chem* 68:70–80
46. Angelucci CA, Nart FC, Herrero E, Feliu JM (2007) Anion re-adsorption and displacement at platinum single crystal electrodes in CO-containing solutions. *Electrochim Commun* 9:1113–1119
47. Ueno T, Tanaka H, Sugawara S, Shinohara K, Ohma A, Hoshi N, Nakamura M (2017) Infrared spectroscopy of adsorbed OH on n (111)-(100) and n (111)-(111) series of Pt electrode. *J Electroanal Chem* 800:162–166

48. Santos E, Leiva EPM, Vielstich W (1991) CO adsorbate on Pt(111) single crystal surfaces. *Electrochim Acta* 36:555–561
49. Farias MJS, Busó-Rogero C, Gisber R, Herrero E, Feliu JM (2014) Influence of the CO adsorption environment on its reactivity with (111) terrace sites in stepped Pt electrodes under alkaline media. *J Phys Chem C* 118:1925–1934
50. Garcia G, Koper MTM (2008) Stripping voltammetry of carbon monoxide oxidation on stepped platinum single-crystal electrodes in alkaline solution. *Phys Chem Chem Phys* 10:3802–3811
51. Farias MJS, Herrero E, Feliu JM (2013) Site selectivity for CO adsorption and stripping on stepped and kinked platinum surfaces in alkaline medium. *J Phys Chem C* 117:2903–2913
52. Farias MJS, Camara GA, Feliu JM (2015) Understanding the CO preoxidation and the intrinsic catalytic activity of step sites in stepped Pt surfaces in acidic medium. *J Phys Chem C* 119:20272–20282
53. Herrero E, Chen QS, Hernandez J, Sun SG, Feliu JM (2011) Effects of the surface mobility on the oxidation of adsorbed CO on platinum electrodes in alkaline media. The role of the adlayer and surface defects. *Phys Chem Chem Phys* 13:16762–16771
54. Lebedeva NP, Rodes A, Feliu JM, Koper MTM, van Santen RA (2002) Role of crystalline defects in electrocatalysis: CO adsorption and oxidation on stepped platinum electrodes as studied by *in situ* infrared spectroscopy. *J Phys Chem B* 106:9863–9872
55. Calle-Vallejo F, Pohl MD, Bandarenka AS (2017) Quantitative coordination—activity relations for the design of enhanced Pt catalysts for CO electro-oxidation. *ACS Catal* 7:4355–4359
56. Farias MJS, Vidal-Iglesias FJ, Solla-Gullón J, Herrero E, Feliu JM (2014) On the behavior of CO oxidation on shape-controlled Pt nanoparticles in alkaline medium. *J Electroanal Chem* 716:16–22
57. McPherson IJ, Ash PA, Jones L, Varambhia A, Jacobs RMJ, Vincent KA (2017) Electrochemical CO oxidation at platinum on carbon studied through analysis of anomalous *in situ* IR spectra. *J Phys Chem C* 121:17176–17187
58. Backus EHG, Eichler A, Kleyn AW, Bonn M (2005) Real-time observation of molecular motion on a surface. *Science* 310:1790–1793
59. Farias MJS, Chequepán W, Tanaka AA, Feliu JM (2018) Unraveling the nature of active sites in ethanol electro-oxidation by site-specific marking of a Pt catalyst with isotope-labeled ^{13}CO . *J Phys Chem Lett* 9:1206–1210
60. Farias MJS, Chequepán W, Tanaka AA, Feliu JM (2017) Nonuniform synergistic effect of Sn and Ru in site-specific catalytic activity of Pt at bimetallic surfaces toward CO electro-oxidation. *ACS Catal* 7:3434–3445
61. Vielstich W (2003) Electrochemical energy conversion: methanol fuel cell as example. *J Braz Chem Soc* 14:503–509
62. Cuesta A (2017) Electrooxidation of C_1 organic molecules on Pt electrodes. *Curr Opin Electrochem* 4:32–38
63. Herrero E, Feliu JM (2018) Understanding formic acid oxidation mechanism on platinum single crystal electrodes. *Curr Opinion Electrochem* 9:145–150
64. Grozovski V, Climent V, Herrero E, Feliu JM (2010) Intrinsic activity and poisoning rate for HCOOH oxidation on platinum stepped surfaces. *Phys Chem Chem Phys* 12:8822–8831
65. Grozovski V, Climent V, Herrero E, Feliu JM (2011) The role of the surface structure in the oxidation mechanism of methanol. *J Electroanal Chem* 662:43–51
66. Miki A, Ye S, Osawa M (2002) Surface-enhanced IR absorption on platinum nanoparticles: an application to real-time monitoring of electrocatalytic reactions. *Chem Commun* 150:1500–1501
67. Chen YX, Heinen M, Jusys Z, Behm RJ (2006) Bridge-bonded formate: active intermediate or spectator species in formic acid oxidation on a Pt film electrode? *Langmuir* 22:10399–10408
68. Osawa M, Komatsu KI, Samjseké G, Uchida T, Ikeshoji T, Cuesta A, Gutiérrez C (2011) The role of bridge-bonded adsorbed formate in the electrocatalytic oxidation of formic acid on platinum. *Angew Chem Int Ed* 50:1159–1163
69. Iwasita T (2002) Electrocatalysis of methanol oxidation. *Electrochim Acta* 47:3663–3674
70. Cuesta A (2006) At least three contiguous atoms are necessary for CO formation during methanol electrooxidation on platinum. *J Am Chem Soc* 128:13332–13333
71. Villegas I, Weaver MJ (1994) Carbon monoxide adlayer structures on platinum (111) electrodes: a synergy between *in situ* scanning tunneling microscopy and infrared spectroscopy. *J Chem Phys* 101:1648–1660
72. Kim YG, Yau SL, Itaya K (1996) Direct observation of complexation of alkali cations on cyanide-modified Pt(111) by scanning tunneling microscopy. *J Am Chem Soc* 118:393–400

73. Angel C (2011) Atomic ensemble effects in electrocatalysis: the site-knockout strategy. *ChemPhysChem* 12:2375–2385
74. Cuesta A, Escudero M, Lanova B, Baltruschat H (2009) Cyclic voltammetry, FTIRS, and DEMS study of the electrooxidation of carbon monoxide, formic acid, and methanol on cyanide-modified Pt(111) electrodes. *Langmuir* 25:6500–6507
75. Valentini F, Biagiotti V, Lete C, Palleschi G, Wang J (2007) The electrochemical detection of ammonia in drinking water based on multi-walled carbon nanotube/copper nanoparticle composite paste electrodes. *Sens Actuators B Chem* 128:326–333
76. Simons EL, Cairns EJ, Surd DJ (1969) The performance of direct ammonia fuel cells. *J Electrochem Soc* 116:556–561
77. Acevedo R, Poventud-Estrada CM, Morales-Navas C, Martínez-Rodríguez RA, Ortiz-Quiles E, Vidal-Iglesias FJ, Solla-Gullón J, Nicolau E, Feliu JM, Echegoyen L et al (2017) Chronoamperometric study of ammonia oxidation in a direct ammonia alkaline fuel cell under the influence of microgravity. *Microgravity Sci Technol* 29:253–261
78. Gerischer H, Mauerer A (1970) Untersuchungen zur anodischen oxidation von ammoniak an platin-elektroden. *J Electroanal Chem* 25:421–433
79. Wasmus S, Vasini EJ, Krausa M, Mishima HT, Vielstich W (1994) DEMS-cyclic voltammetry investigation of the electrochemistry of nitrogen compounds in 0.5 M potassium hydroxide. *Electrochim Acta* 39:23–31
80. Katsounaros I, Figueiredo MC, Calle-Vallejo F, Li H, Gewirth AA, Markovic NM, Koper MTM (2018) On the mechanism of the electrochemical conversion of ammonia to dinitrogen on Pt(1 0 0) in alkaline environment. *J Catal* 359:82–91
81. Matsui T, Suzuki S, Katayama Y, Yamauchi K, Okanishi T, Muroyama H, Eguchi K (2015) In situ attenuated total reflection infrared spectroscopy on electrochemical ammonia oxidation over Pt electrode in alkaline aqueous solutions. *Langmuir* 31:11717–11723
82. Vidal-Iglesias FJ, García-Aráez N, Montiel V, Feliu JM, Aldaz A (2003) Selective electrocatalysis of ammonia oxidation on Pt(100) sites in alkaline medium. *Electrochim Commun* 5:22–26
83. Vidal-Iglesias FJ, Solla-Gullón J, Montiel V, Feliu JM, Aldaz A (2005) Ammonia selective oxidation on Pt(100) sites in an alkaline medium. *J Phys Chem B* 109:12914–12919
84. Vidal-Iglesias FJ, Solla-Gullón J, Feliu JM, Baltruschat H, Aldaz A (2006) DEMS study of ammonia oxidation on platinum basal planes. *J Electroanal Chem* 588:331–338
85. Martínez-Rodríguez RA, Vidal-Iglesias FJ, Solla-Gullón J, Cabrera CR, Feliu JM (2014) Synthesis of Pt nanoparticles in water-in-oil microemulsion: effect of HCl on their surface structure. *J Am Chem Soc* 136:1280–1283
86. Duca M, Figueiredo MC, Climent V, Rodriguez P, Feliu JM, Koper MTM (2011) Selective catalytic reduction at quasi-perfect Pt(100) domains: a universal low-temperature pathway from nitrite to N₂. *J Am Chem Soc* 133:10928–10939
87. Finkelstein DA, Bertin E, Garbarino S, Guay D (2015) Mechanistic similarity in catalytic N₂ production from NH₃ and NO₂—at Pt(100) thin films: toward a universal catalytic pathway for simple N-containing species, and its application to in situ removal of NH₃ poisons. *J Phys Chem C* 119:9860–9878
88. Mallat T, Orglmeister E, Baiker A (2007) Asymmetric catalysis at chiral metal surfaces. *Chem Rev* 107:4863–4890
89. Zaera F (2017) Chirality in adsorption on solid surfaces. *Chem Soc Rev* 46:7374–7398
90. Attard GA (2001) Electrochemical studies of enantioselectivity at chiral metal surfaces. *J Phys Chem B* 105:3158–3167
91. Climent V, Feliu JM (2017) Surface electrochemistry with Pt single-crystal electrodes. *Advances in electrochemical science and engineering*. Wiley, New York, pp 1–57
92. Sholl DS, Asthagiri A, Power TD (2001) Naturally chiral metal surfaces as enantiospecific adsorbents. *J Phys Chem B* 105:4771–4782
93. Attard GA, Clavilier J, Feliu JM (2002) Chirality at well-defined metal surfaces. *Chirality: physical chemistry*. American Chemical Society, Washington, pp 254–268
94. Wattanakit C, Côme YBS, Lapeyre V, Bopp PA, Heim M, Yadnum S, Nokbin S, Warakulwit C, Limtrakul J, Kuhn A (2014) Enantioselective recognition at mesoporous chiral metal surfaces. *Nat Commun* 5:3325
95. Yutthalekha T, Wattanakit C, Lapeyre V, Nokbin S, Warakulwit C, Limtrakul J, Kuhn A (2016) Asymmetric synthesis using chiral-encoded metal. *Nat Commun* 7:12678

96. Gellman AJ, Ernst KH (2018) Chiral autocatalysis and mirror symmetry breaking. *Catal Lett* 148:1610–1621
97. Ahmadi A, Attard G, Feliu J, Rodes A (1999) Surface reactivity at “chiral” platinum surfaces. *Langmuir* 15:2420–2424
98. Attard GA, Harris C, Herrero E, Feliu J (2002) The influence of anions and kink structure on the enantioselective electro-oxidation of glucose. *Faraday Discuss* 121:253–266
99. McFadden CF, Cremer PS, Gellman AJ (1996) Adsorption of chiral alcohols on “chiral” metal surfaces. *Langmuir* 12:2483–2487
100. Schiffrrin DJ (2002) General discussion. *Faraday Discuss* 121:331–364
101. Mostany J, Herrero E, Feliu JM, Lipkowski J (2002) Thermodynamic studies of anion adsorption at stepped platinum (hkl) electrode surfaces in sulfuric acid solutions. *J Phys Chem B* 106:12787–12796
102. Popović KĐ, Tripković AV, Adžić RR (1992) Oxidation of D-glucose on single-crystal platinum electrodes: a mechanistic study. *J Electroanal Chem* 339:227–245

Publisher's Note Springer Nature remains neutral with regard to jurisdictional claims in published maps and institutional affiliations.



REVIEW

Bimetallic Electrocatalysts for CO₂ Reduction

Wenlei Zhu¹ · Brian M. Tackett² · Jingguang G. Chen² · Feng Jiao¹

Received: 11 September 2018 / Accepted: 20 October 2018 / Published online: 26 October 2018
© Springer Nature Switzerland AG 2018

Abstract

The increasing concentration of CO₂ in the atmosphere has caused various environmental issues. Utilizing CO₂ as the carbon feedstock to replace traditional fossil sources in commodity chemical production is a potential solution to reduce CO₂ emissions. Electrochemical reduction of CO₂ has attracted much attention because it not only converts CO₂ into a variety of useful chemicals under mild reaction conditions, but also can be powered by renewable electricity at remote locations. From this review article, we summarize recent literature on the topic of bimetallic electrocatalysts for CO₂ reduction. Both selectivity and activity of bimetallic catalysts strongly depend on their compositions and surface structures. Tuning the properties of a bimetallic catalyst could result in a wide range of products, including carbon monoxide, hydrocarbons, carboxylate and liquid oxygenates. By reviewing recent research efforts in the field of bimetallic electrocatalysts for CO₂ reduction, we aim to provide the community with a timely overview of the current status of bimetallic CO₂ electrocatalysts and to stimulate new ideas to design better catalysts for more efficient CO₂ electrolysis processes.

Keywords Bimetallic · Electrocatalysts · Carbon dioxide · CO₂ reduction

Chapter 4 was originally published as Zhu, W., Tackett, B. M., Chen, J. G. & Jiao, F. Topics in Current Chemistry (2018) 376: 41. <https://doi.org/10.1007/s41061-018-0220-5>.

- ✉ Jingguang G. Chen
jgchen@columbia.edu
- ✉ Feng Jiao
jiao@udel.edu

¹ Department of Chemical and Biomolecular Engineering, University of Delaware, Newark, DE 19716, USA

² Department of Chemical Engineering, Columbia University, New York, NY 10027, USA

1 Introduction

Over the past half century, atmospheric CO₂ concentration has increased dramatically. The current CO₂ concentration is the highest ever recorded since consistent measurements began in the 1950s. The high level of CO₂ concentration has resulted in global climate change and severe environmental damage [1–3]. Recently, much effort has been devoted to identifying potential methods to tackle CO₂ emission issues. A potential solution is to use CO₂ as the carbon source to produce value-added chemicals; however, reduction of CO₂ requires additional energy input to overcome activation barriers. If the required energy is obtained from fossil sources, the process does not necessarily have a negative (or even carbon neutral) CO₂ emission. Therefore, developing an effective catalyst that can lower activation barriers of CO₂ reduction, as well as utilize renewable energy is an important task in the field of carbon utilization.

In nature, green plants capture CO₂ directly from air and convert it to reduced carbon species through sunlight-driven photosynthesis processes. However, nature's photosynthesis processes are usually slow and they alone are not sufficient to offset the extremely large quantity of CO₂ emitted from human activities [4]. A variety of alternative CO₂ utilization approaches, including biological, thermochemical, photochemical, and electrochemical methods, are currently under investigation [5, 6]. Among them, electrochemical conversion of CO₂ has attracted much attention recently because this approach has several advantages, including fine control of production rates, wide scalability of modular electrolyzer designs, and the potential to produce a variety of high-value products [5, 7]. More importantly, the electrolysis system can be readily powered by carbon-free energy sources, such as wind, solar, and nuclear, providing a zero-CO₂ emission (or even negative) pathway for commodity chemical production. A recent scientific study on photovoltaics (PV) clearly showed a decrease of PV electricity price over time with a projected PV electricity price as low as \$0.03 per kWh in the near future [8]. A similar trend also holds for wind energy with the wind electricity price already at ~\$0.02 per kWh [9]. The low electricity price makes electrochemically driven CO₂ utilization technologies potentially profitable for commercial applications.

In a typical CO₂ electrolysis cell, there are three key components, a cathode for CO₂ reduction reaction, an anode for water oxidation reaction, and a membrane separator for physical separation of two electrode chambers. Because CO₂ reduction is a thermodynamically uphill reaction, external bias, often with a high overpotential, is required to drive the reaction [10, 11]. Additionally, hydrogen evolution reaction (the competing reaction) can occur under the CO₂ electrolysis conditions, which may substantially decrease selectivity and Faradaic efficiency (FE) of CO₂RR. Therefore, an efficient CO₂ reduction electrocatalyst is essential to achieve highly selective and energy efficient CO₂ electrolysis systems. In the past few decades, tremendous effort has been devoted to the investigation of CO₂ electrocatalysts. Systematic investigations of monometallic catalysts have been conducted [12–16]. Among all the monometallic CO₂ electrocatalysts, Cu is the

only metal that is able to reduce CO_2 to multi-carbon (C_{2+}) products, such as ethanol, ethylene, and n-propanol. Much effort has been devoted to engineering metallic Cu catalysts to enhance its CO_2 electrocatalytic properties; however, the range of products that can be produced is still limited and the product selectivity remains poor.

Recently, bimetallic catalysts have attracted much attention because the properties of a bimetallic catalyst can be tuned to be either between those of two individual metals (mixed alloy) or outside (core/shell structures) [17–21]. The unique and emergent properties of the latter arise from the hybridization of the atomic orbitals that shift the d-band center with respect to the Fermi level in a non-intuitive way. As a result, bimetallics enable one to access catalytic properties that cannot be mimicked by monometallics. More importantly, it may be possible to design a bimetallic catalyst, which is based on abundant elements only and can still effectively reduce CO_2 under mild overpotentials. Herein, we reviewed recent studies on bimetallic CO_2 electrocatalysts and organized the discussions based on CO_2RR products, such as CO, hydrocarbons, carboxylates and oxygenates.

2 Bimetallic Electrocatalysts for CO_2 Reduction

2.1 CO Selective Bimetallic Electrocatalysts

Table 1 summarizes recent literature reports on the topic of CO selective bimetallic electrocatalysts. It is evident that a variety of bimetallics can convert CO_2 into CO with > 90% FE. It should be noted that monometallic catalysts, such as Au and Ag, can also reduce CO_2 into CO with a high selectivity. Therefore, research efforts in developing bimetallic CO selective catalysts focused primarily on C_{2+} products using Cu-based bimetallics, while most of the attempts, such as AgCu [9, 22], AuCu [23, 24], and PdCu [25, 26], failed with CO as the major product.

As discussed previously, Cu is the most unique monometallic electrocatalyst for CO_2 reduction. Many research groups have studied Cu-based bimetallics with the hope to tune catalytic properties of Cu with a second metal. For example, Hori et al. showed that adding Cd onto a Cu electrode would prevent both HER and hydrocarbon formation, leading to a more selective catalyst toward CO [34]. Watanabe et al. investigated CO_2RR over Cu-containing alloys and showed that CO could be produced from $\text{Cu}_{52}\text{Zn}_{48}$ and $\text{Cd}_{62}\text{Cu}_{38}$ with relatively high FEs [40]. In another study, Cu–Ni and Cu–Fe were also synthesized using in situ deposition technique and studied as CO_2 electrocatalysts [41]. However, increasing the coverage of Ni or Fe on the Cu surface increased H_2 evolution, which is consistent with the observations in a recent study of water disassociation on Cu-based bimetallic surfaces [42]. Katoh et al. designed Cu–Sn and Cu–Zn alloy catalysts for CO_2 reduction and studied in detail about the relationship between the alloy structure and CO_2 reduction [29]. The authors found that some intermetallic compounds on the alloy surface, such as $\text{Cu}_{5.6}\text{Sn}$ and Cu_2Zn_8 , were the active phases for selective formation of CO from CO_2 at high production rates.

Table 1 Bimetallic electrocatalysts for CO₂ reduction to CO

| Catalysts | Electrolyte | Potential (V vs. RHE) | CO partial current density (mA/cm ²) ^a | CO partial current density (mA/cm ²) ^b | Faradaic efficiency (%) | References |
|---|---------------------------|-----------------------|---|---|-------------------------|------------|
| PLD Au _{0.87} Cu _{0.13} | 0.1 M KHCO ₃ | -0.8 | 4.34 | 2.9 | 90 | [23] |
| Cu ₈₅ Pt ₁₅ | 0.5 M KHCO ₃ | -1.11 | 1.5 | 0.17 | 25 | [27] |
| Cu–Sn | 0.1 M KHCO ₃ | -0.6 | 1.0 | 1.35 | 90 | [28] |
| Cu _{5.6} Sn | 0.05 M NaHCO ₃ | -0.87 | 0.6 | 0.54 | 67 | [29] |
| Cu ₅ Zn ₈ | 0.05 M NaHCO ₃ | -0.87 | 0.95 | 0.86 | 80 | [29] |
| AuCu (ordered) | 0.1 M KHCO ₃ | -0.77 | 3.6 | 1.4 | 80 | [30] |
| Ag ₅₇ Cu ₄₃ | 0.5 M KHCO ₃ | -1.05 | 5.7 | 1.9 | 12.5 | [9] |
| Ag/Cu foam | 0.5 M KHCO ₃ | -0.93 | 6.7 | 2.68 | 37 | [31] |
| Au ₅₇ Pt ₄₃ | 0.1 M KHCO ₃ | -0.7 | 0.32 | 0.84 | 30 | [32] |
| Au coated Cu NWs | 0.5 M KHCO ₃ | -0.65 | 12 | 6 | 30 | [24] |
| Cu ₈₇ Sn ₁₃ | 0.1 M KHCO ₃ | -1 | 0.55 | 0.46 | 60 | [33] |
| CdCu | 0.1 M KHCO ₃ | -1.24 | 5 | 4.5 | 61 | [34] |
| Cu–In | 0.1 M KHCO ₃ | -0.6 | 0.99 | 0.0034 | 90 | [35] |
| Pd ₈₅ Cu ₁₅ | 0.1 M KHCO ₃ | -0.89 | 6.9 | 0.28 | 86 | [26] |
| Cu _{0.75} In _{0.25} | 0.5 M NaHCO ₃ | -0.7 | 2.5 | 1.25 | 81 | [36] |
| Au ₃ Cu | 0.1 M KHCO ₃ | -0.73 | 3 | 1.17 | 60 | [37] |
| Cu/SnO ₂ | 0.5 M KHCO ₃ | -0.7 | 11 | 0.73 | 93 | [38] |
| Au–Fe | 0.5 M KHCO ₃ | -0.5 | N/A | 18 | 99 | [39] |

^aBased on geometric area of electrode^bBased on catalyst surface area; some values are estimated from the reported data

In principle, the strength of CO adsorption on metallic surface could be used to predict the catalyst selectivity in CO₂ electroreduction. Literature studies have demonstrated that the surface d-band center can be theoretically predicted, and experimental assessment showed a strong effect on surface adsorption [43–45]. The formation of bimetallic bonds often modifies the surface d-band center [46]. Kim et al. reported the CO₂ reduction results for AuCu alloy nanomaterials with different ratio of Au and Cu [37]. Among them, Au₃Cu nanoparticles (NPs) showed a high CO FE of 66% and a mass activity of 230A/g at -0.73 V vs. reversible hydrogen electrode (RHE, all voltages are on the RHE scale unless stated otherwise) in Fig. 1. Density functional theory (DFT) calculations revealed that the larger Au composition in CuAu induces a lower surface binding energy by modifying the d-band center. Lower binding energy for intermediates, such

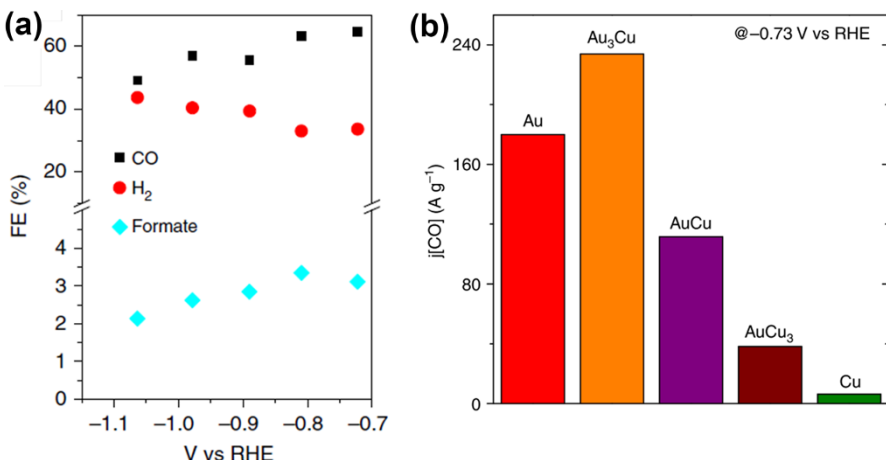


Fig. 1 **a** FE for CO, H₂ and formate produced with Au₃Cu. **b** mass activity of CO using AuCu bimetallic NPs with different composition at -0.73 V vs RHE. Reproduced with permission from Ref. [37]

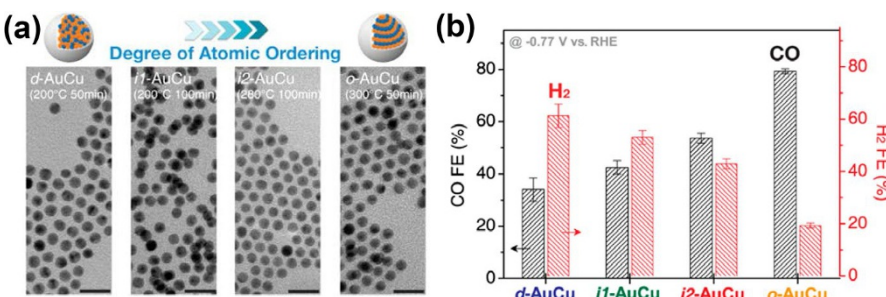


Fig. 2 **a** TEM images of AuCu bimetallic NPs with different degree of atomic ordering by tuning the reaction condition. Scale bar, 20 nm. **b** CO and H₂ FE from CO₂RR by using synthesized AuCu NPs. Reproduced with permission from Ref. [30]

as COOH, CO and H, increases the CO formation and suppresses the methane formation.

Utilizing the strain effect is another strategy to tune the surface d-band center. Kim et al. managed to introduce a compressive strain in surface Au through synthesizing an ordered AuCu catalyst [30]. AuCu NPs with different degrees of ordering were synthesized (Fig. 2a). The ordered AuCu exhibited a low onset potential (-0.31 V), high FE (80% at -0.77 V, Fig. 2b) and ultrahigh mass activity (800 A/g_{Au}) for CO formation. DFT calculations showed that the Au(211) active sites were characterized by a 6% compressive strain. The Au strain could reduce the limiting potential in the CO₂ reduction system, where COOH binding to the surface becomes the potential-limiting step.

Besides alloys, core/shell nanostructured materials can lead to both electronic modification and surface strain effects. Cu/SnO₂ NPs are an example [38]. The

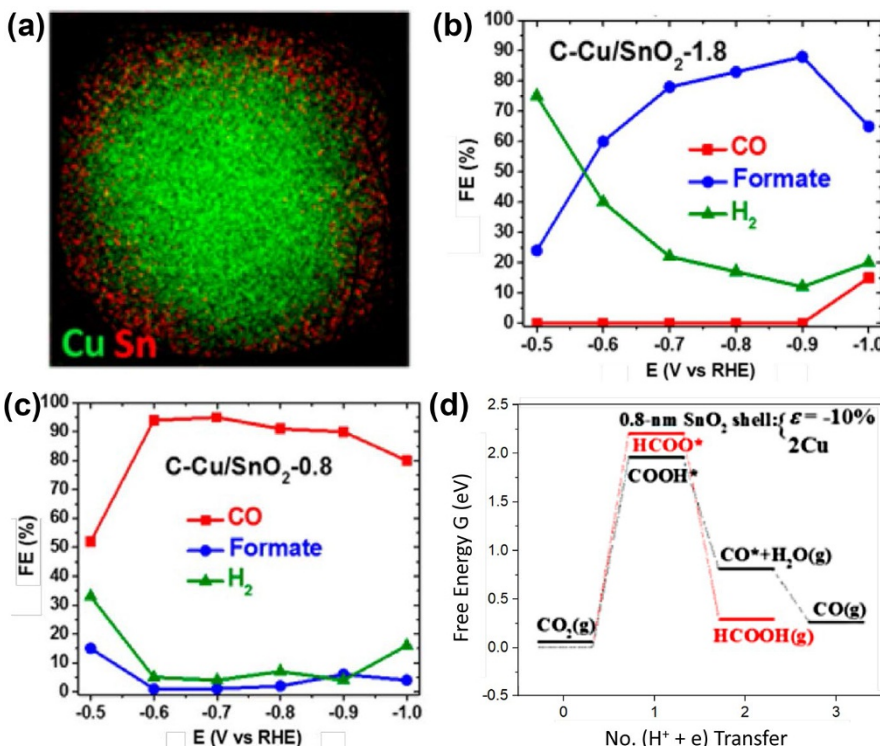


Fig. 3 **a** TEM image of Cu/SnO₂ core/shell NPs. FE for CO, H₂ and formate during CO₂RR by using **b** C-Cu/SnO₂-0.8 catalyst with a 0.8 nm shell and **c** C-Cu/SnO₂-1.8 catalyst with a 1.8 nm shell in CO₂-saturated 0.5 M KHCO₃ solution. **d** Free energy diagrams for CO and formate formation on 0.8 nm SnO₂ shell with both surface Cu atoms and 10% uniaxial compression. Reproduced with permission from Ref. [38]

Cu/SnO₂ NPs have a uniform SnO₂ shell on a spherical Cu core (Fig. 3a). They showed a SnO₂ thickness-dependent effect on CO₂RR. The NPs with thicker SnO₂ shell (1.8 nm) had similar products and FE as the pure SnO₂ NPs. They could produce 88% formate at -0.9 V (Fig. 3b). The NPs with thinner SnO₂ shell (0.8 nm) were not able to produce formate with high FE. However, they became CO selective with a 93% FE at -0.7 V (Fig. 3c). DFT modeling identified that the free energy of intermediate HCOO* was larger than COOH* due to the compressive strain effect and Cu doping on 0.8 nm SnO₂ shell (Fig. 3d). COOH* is the key intermediate for CO formation while the HCOO* intermediate can only produce formate. The overpotential for CO production was -1.87 V. The overpotential for formate production was -2.21 V. Thus, high selectivity for CO can be achieved because it has less negative overpotential.

In another case, a Cu-In alloy was synthesized and reported to have above 80% FE for CO [35]. The total current density was comparable to oxide-derived Cu. DFT calculations showed that indium (In) was preferentially located on the edge rather

than on the corner or flat sites. Sarfraz et al. showed that the Cu surface, when decorated with Sn, resulted in a CO FE of > 90% and a current density of -1.0 mA/cm^2 at -0.2 V [28]. DFT calculations for the parent Cu(100) and Cu(111) facets, with Cu atoms being replaced with Sn atoms, showed that the binding of hydrogen atoms can be reduced by 0.18 eV while CO adsorption was not affected.

Sun et al. showed that the AuFe core/shell NPs could reduce CO_2 to CO with ultrahigh selectivity (99% at -0.5 V vs RHE) and mass activity (150 mA/mg at -0.9 V vs RHE) [39]. AuFe core/shell NPs were formed by surface Fe leaching of the AuFe alloy during the first hour of electrolysis. This catalyst showed little to no current drop after 90-h tests. The surface defects from Fe leaching, as well as the subsurface alloy effect could be used to explain the increased selectivity and activity at low potential, compared with Au NPs and Au foils. PBE (Perdew–Burke–Ernzerhof) DFT calculations based on a Schottky defect on Au surface suggested that the formed Au defects could decrease the formation energy of ${}^*\text{COOH}$ and thus lower the onset potential.

2.2 Hydrocarbon Selective Bimetallic Electrocatalysts

Catalysts with the ability to convert CO_2 to hydrocarbons are more appealing in the field of CO_2RR . Various Cu-based bimetallic materials have been reported to show enhanced C_{2+} products yields. Table 2 summarizes recent work related bimetallic electrocatalysts for CO_2 reduction to hydrocarbons.

CO was identified as the key intermediate for further hydrocarbon formation [10, 54]. Metals with low CO binding energy, such as Au and Ag, might not form hydrocarbons because CO could be released easily from surface. In theory, strong CO binding energy could benefit the further reduction. However, for monometallic particles, only Cu appeared to have the proper CO binding energy to produce hydrocarbon. The CO binding on Ni, Pd, Pt and Rh was too strong, which could easily result in CO poisoning [54, 55]. The following mechanism was based on the reaction on Cu surfaces.

For the C1 hydrocarbon (methane) formation, the most widely accepted pathway was sequential hydrogenation of adsorbed CO^* until CH_4 . The potential rate determine step was the formation of CHO^* , and the subsequent reaction steps were exergonic. The formation of CO^* required COOH^* as an intermediate from initial CO_2 reduction [56] (Fig. 4a). If HCOO^* formed, the final product would be HCOOH [38]. Another C1 product, methanol, was also observed during CO_2RR . However, in this case, the intermediate was considered to be COH^* , which required that hydrogen should bond to the oxygen instead of carbon (Fig. 4b). The formation of COH^* usually showed a higher kinetic barrier than that of CHO^* . For the Cu(111) facet, methanol formation required 0.18 eV higher energy than the methane formation at -1.15 V [57].

The formation of C2 products was usually seen when using Cu based materials. The most important steps were the ability for C–C coupling. There were several different hypotheses about the intermediates before C–C coupling. Nie et al. calculated that CH and CH were possibly first coupled on the Cu(111) facet [57,

Table 2 Bimetallic electrocatalysts for CO₂ reduction to hydrocarbons

| Catalysts | Electrolyte | Selectivity @ potential | Partial current density @ potential | References |
|---------------------------------|---|--|--|------------|
| CuPd (phase separated) | 1 M KOH | C ₂ H ₄ ; 48% @ -0.74 V; C ₂ H ₅ OH; 15% @ -0.74 V | C ₂ H ₄ ; 173 mA/cm ² ; C ₂ H ₅ OH; 54 mA/cm ² @ -0.74 V; [47] | |
| Ag@Cu-20 | 0.1 M KHCO ₃ | C ₂ H ₄ ; 23%; CH ₄ ; 18%; @ -1.06 V | C ₂ H ₄ ; 1.1 mA/cm ² ; CH ₄ ; 0.4 mA/cm ² ; @ -1.06 V [22] | |
| Ag-Co | 0.5 M KHCO ₃ | CH ₄ ; 19.5% @ 2.0 V | N/A [48] | |
| CuAg (40%Cu) | 0.05 M Cs ₂ CO ₃ | C ₂ H ₄ ; 20.2%; CH ₄ ; 5%, @ -1.05 V | C ₂ H ₄ ; 1.58 mA/cm ² ; CH ₄ ; 0.39 mA/cm ² , @ -1.05 V [49] | |
| Au@Cu1 (6–7 Cu layers) | 94 mL of 1 M K ₂ HPO ₄ +6 mL of 1 M KH ₂ PO ₄ | 18% C ₂ H ₄ and 5% CH ₄ in total gases @ -0.6 V | N/A [50] | |
| Cu-Ag (porous Cu) | 0.1 M KHCO ₃ | C ₂ H ₆ +C ₂ H ₄ ; 14%; @ -0.74 V | C ₂ H ₆ +C ₂ H ₄ ; 1.5 mA/cm ² ; @ -0.74 V [51] | |
| Cu ₂ Pd | 0.1 M TBAPF ₆ /CH ₃ CN with 1 M H ₂ O | CH ₄ ; 50%; @ -1.8 V vs Ag/AgCl | CH ₄ ; 1.88 mA/cm ² ; @ -1.8 V vs Ag/AgCl [52] | |
| Cu ₉ Ag ₆ | 1 M KOH | C ₂ H ₄ ; 60%; C ₂ H ₅ OH; 25% @ -0.7 V | C ₂ H ₄ ; 180 mA/cm ² ; C ₂ H ₅ OH; 75 mA/cm ² , @ -0.7 V [53] | |

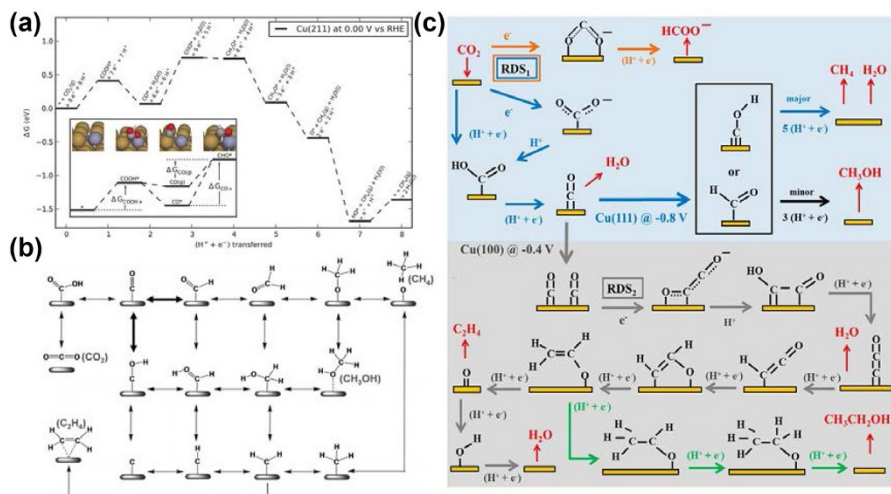


Fig. 4 **a** Proposed CO_2 reduction route for CH_4 formation on the $Cu(211)$ surface. **b** Proposed CO_2 reduction route for CH_4 , CH_3OH and C_2H_4 formation. **c** A possible route for C1 and C2 products from CO_2 RR. Reproduced with permission from Refs. [56, 57, 60]

[58]. Graza et al. showed that the C–C coupling first happened between CO and CHO [59]. The formed HOCCO could then go to either the ethylene or ethanol pathway. Kortlever et al. showed their proposed pathways based on DFT calculations and experimental observations (Fig. 4c). Two adsorbed CO^* could directly react with each other to form $OCCO^-$ on the $Cu(100)$ surface. This dimerization was the rate-determining step for the reduction of CO. The formed negatively charged intermediate then could be reduced by protonation. The subsequent reduction would lead to the final product to ethylene. Ethanol could form if the C=O double bond of CH_2CHO^* intermediate was hydrogenated. Further carbon addition on the same surface would lead to the formation of C3 or even longer carbon chain products [60].

Improved efficiency for C_2H_4 formation was reported using an Ag/Cu core/shell structure [22]. Ag/Cu core/shell NPs were synthesized by a co-reduction method from ethylene glycol (EG) solution containing $AgNO_3$, $Cu(OAc)_2 \cdot H_2O$ and PVP at 180 °C. 15 nm Cu shell thickness from 20 min heating time could achieve 29% FE for CO at –1.06 V. The CO adsorption was enhanced due to the tensile strain of the surface Cu strain, leading to more opportunity for C_{2+} transformation.

Au/Cu core/shell NPs were reported for electrochemical CO_2 reduction. Au nanocubes were first coated with Cu layers in $CuCl_2$ solutions to form the spherical Au/Cu NPs. The composition of the core/shell NPs was controlled by changing the Au NP solution's volume. The H_2 and CH_4 formation increased with more Cu layers while the formation of ethylene decreased. The author showed that 6–7 layers of Cu resulted in the proper tensile surface strain on Au/Cu that favored C–C bond formation [50].

In another study, CoCu catalysts showed a high C_2 selectivity with a Co content between 5 and 15% [61]. An intermediate species change from CHO to COH may help the C–C bond formation. A stronger CO binding on Co could also assist CO–CO dimerization. Both contribute to the enhanced C_2 product formation (C_2H_4 , C_2H_5OH).

Ma et al. showed that phase-separated Cu–Pd catalysts could reach as high as 50% FE for C_2H_4 [47]. Ordered, disordered, and phase separated Cu–Pd catalysts were synthesized (Fig. 5a). Major products were CO, CH_4 , C_2H_4 , and C_2H_5OH . The CO_2 reduction results of the Cu–Pd catalyst are shown in Fig. 5b–e. From all the samples tested, Cu NPs and phase separated CuPd showed strongest and weakest binding with CO based on the surface valence band photoemission spectra. However, both showed similar activity. Therefore, the authors determined that the geometric arrangement was more important than the electronic effect, with the orientation of the intermediate on the surface playing a key role for enhanced ethylene formation. Another related work also showed both high ethylene FE and activity on Cu can be achieved by optimizing the flow electrolyzer system [62].

From a theoretical point of view, tuning the binding energies of $*COOH$, $*OH$, $*COH$ and $*CHO$ is the key to improving C_{2+} selectivity [10]. Bell et al. designed an AgCu alloy system to give a compressive strain of Cu [49]. CO_2 reduction was conducted using 0.05 M Cs_2CO_3 aqueous solution. After reaction, surfaces of AgCu with 20–60% Cu bulk composition all changed to a more Cu-rich $Ag_{40}Cu_{60}$ surface due to the stronger interaction of CO with Cu than Ag. Comparing to a bulk Cu electrode under the same reaction conditions, more than a 10% total enhancement

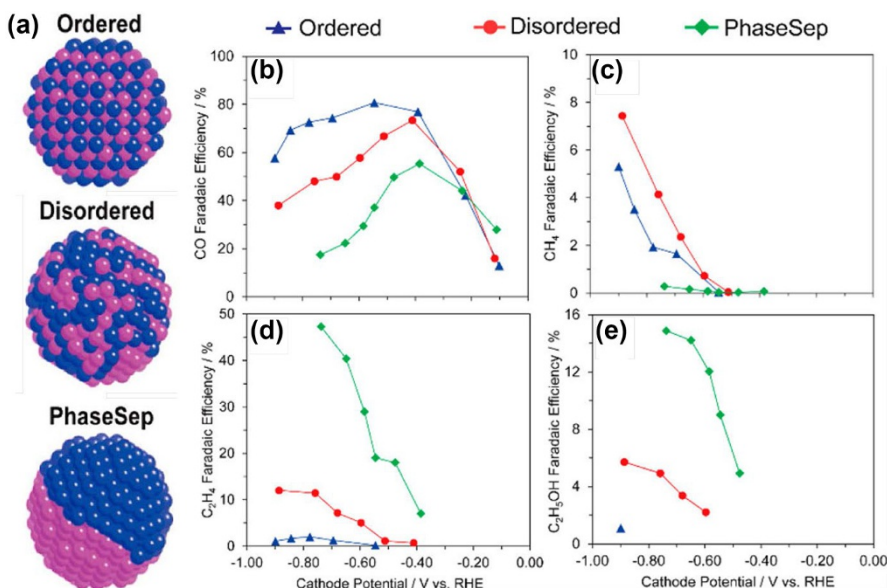


Fig. 5 **a** Illustration of prepared ordered, disordered and phase separated CuPd nanoalloys. FEs for **b** CO; **c** CH_4 ; **d** C_2H_4 ; **e** C_2H_5OH for CuPd nanoalloy catalyst in CO_2 RR. Reproduced with permission from Ref. [47]

of ethylene and liquid products was observed. AgCu showed a weaker CO binding energy due to the compressive strain of surface Cu. The authors suggested that reduced hydrogen and oxygen binding energies relative to CO could be the reason for improved performance.

Nie et al. reported DFT calculations for a promising CuFe electrocatalyst for producing C₂ hydrocarbons [58]. The combination of Cu and Fe enhanced CO₂ conversion by lowering the kinetic barriers, and consequently altered the selectivity preference to more C₂H₄ (or C₂H₆ with further hydrogenation) from CH₄ coupling on the surface of monometallic Fe.

Hoang et al. synthesized nanoporous Cu–Ag alloys on GDL. It was tested in a flow cell [53]. The Cu₉₄Ag₆ sample showed 60% ethylene and 25% ethanol FE at -0.7 V with a total current density of 300 mA/cm². The high selectivity towards C2 products was determined from the enhanced stabilization of the Cu₂O overlayer and the increased CO intermediate availability by adding Ag. The high pH of solvent was the possible reason for the high FE of ethylene.

Zhang et al. showed that Cu₂Pd nanoalloy on the polymeric film could produce up to 50% CH₄ as the reduction product [52]. This was tested in CO₂-saturated 0.1 M TBAPF₆/CH₃CN solutions with 1 M added H₂O. Interestingly, when considering the state-of-the-art work on CO₂ to CH₄, monometallic Cu NPs can achieve 80% FE for CH₄ [63], suggesting that current bimetallic catalysts did not show a significant improvement for methane production.

2.3 Oxygenate Selective Bimetallic Electrocatalysts

Previous studies showed that if the binding energy of *COOH intermediate is weak on a catalyst surface, formate will be produced. Another pathway suggests that CO₂ adsorbs as *OCHO, this can explain some formate formation at more negative potentials [10]. Table 3 summarizes some of the bimetallic electrocatalysts with a high selectivity towards formate.

Hahn et al. investigated electrocatalytic properties of thin film AuPd alloys for CO₂RR [72]. They found that using an electron-beam co-deposition method could produce phase-pure and uniform AuPd alloy films with different compositions (Fig. 6). Electrocatalytic results showed that both the selectivity and activity of the as-synthesized AuPd alloy films were higher for HCOO[−] than either pure Au or Pd metals, indicating that both metals can act synergistically. The Pd sites had reduced binding energy of CO, which allowed increased amounts of adsorbed H and consequently increased the probability of *H adjacent to COOH*.

Cu-modified Pd NPs synthesized by underpotential deposition showed a formate FE higher than 80% and a good stability [25]. The results were attributed to decreasing the adsorption strength of CO via modification of the Pd d-band, leading to an improved CO tolerance and an increased FE. In a related study, Ruud et al. established a new Pd-based electrochemical catalyst system, converting CO₂ to formic acid with a low overpotential [67]. Pd was electrodeposited on a polycrystalline Pt electrode. The onset potential for the formation of formic acid was -0.15 V vs. RHE at pH values of 2 and 6.7, compared with a -1.2 V onset potential of the bulk

Table 3 Bimetallic electrocatalysts for CO₂ reduction to formate

| Catalysis | Electrolyte | Selectivity @ potential | Partial current density @ potential | References |
|---------------------------------------|--|---|--|------------|
| Ag–Sn core/shell NPs | 0.5 M NaHCO ₃ | HCOOH: 87.2%; @ -0.9 V | HCOOH: 25.4 mA/cm ² ; @ -1.08 V | [64] |
| Cu–Ni | 0.05 M NaHCO ₃ | CH ₃ OH: 7% @ -0.52 V; HCOOH: 20%; @ -1.12 V | CH ₃ OH: 8 μA/cm ² @ -0.52 V; HCOOH: 0.28 mA/cm ² @ -1.12 V | [40] |
| Cu–Sn | 0.05 M NaHCO ₃ | HCOOH: 57% @ -1.02 V; | HCOOH: 1.43 mA/cm ² @ -1.02 V, | [40] |
| Cu–Pb | 0.05 M NaHCO ₃ | HCOOH: 50% @ -0.72 V | HCOOH: 1.45 mA/cm ² - 0.72 V | [40] |
| Pd/Pt/C | 1 M KHCO ₃ | HCOOH: 75% @ -0.3 V | HCOOH: 30 mA/cm ² - 0.3 V | [65] |
| CuAg (40%Cu) | 0.05 M Cs ₂ CO ₃ | C ₂ H ₅ OH: 13%; Acetaldehyde: 6.8%; Acetate: 6.3%; @ -1.05 V | C ₂ H ₅ OH: 1.02 mA/cm ² ; Acetaldehyde: 0.53 mA/cm ² ; Acetate: 0.49 mA/cm ² ; @ -1.05 V | [49] |
| Pd ₇₀ Pt ₃₀ | 0.1 M K ₂ HPO ₄ /0.1 KH ₂ PO ₄ | HCOOH: 91.8% @ -0.4 V | HCOOH: 5 mA/cm ² - 0.4 V | [66] |
| Sn _{56.3} Pb _{43.7} | 0.5 M KHCO ₃ | HCOOH: 79.8% @ -1.37 V | HCOOH: 45.7 mA/cm ² - 1.37 V | [67] |
| PdSn/C | 0.5 M KHCO ₃ | CH ₃ OH: >99% @ -0.43 V | CH ₃ OH: 2 mA/cm ² - 0.43 V | [68] |
| Ru–Rd | 0.5 M KHCO ₃ | HCOOH: 88% @ -0.7 V | HCOOH: 70 mA/cm ² - 0.7 V | [69] |
| Ag–Cu (phase-blended) | 0.1 M KHCO ₃ | C ₂ H ₅ OH: 34%; HCOOH: 11%; @ -1.2 V | C ₂ H ₅ OH: 0.68 mA/cm ² ; HCOOH: 0.22 mA/cm ² , @ -1.2 V | [70] |
| Au ₃ Cd | 0.1 M KHCO ₃ | HCOOH: 36%; @ -0.3 V | HCOOH: 0.01 mA/cm ² ; @ -0.3 V | [71] |
| Au _{0.20} Pd _{0.80} | 0.1 M KHCO ₃ | HCOOH: 10%; @ -0.87 V | HCOOH: 0.12 mA/cm ² ; @ -0.87 V | [72] |
| Cu ₄ Zn | 0.1 M KHCO ₃ | C ₂ H ₅ OH: 29.1%; @ -1.05 V | C ₂ H ₅ OH: 8.2 mA/cm ² ; @ -1.05 V | [73] |
| Pd ₈₃ Cu ₁₇ | 25% [Bmim]BF ₄ ; 75% water mixture (mol:mol) | CH ₃ OH: 80%; @ -2.1 V vs Ag/AgCl | CH ₃ OH: 31.8 mA/cm ² ; @ -2.1 V vs Ag/AgCl | [74] |
| Pd/SnO ₂ | 0.1 M NaHCO ₃ | CH ₃ OH: 54% @ -0.24 V | CH ₃ OH: 2.5 mA/cm ² ; @ -0.24 V | [75] |
| Bi–Sn | 0.5 M KHCO ₃ | HCOOH: 96% @ -1.1 V | HCOOH: 19.8 mA/cm ² - 1.1 V | [76] |

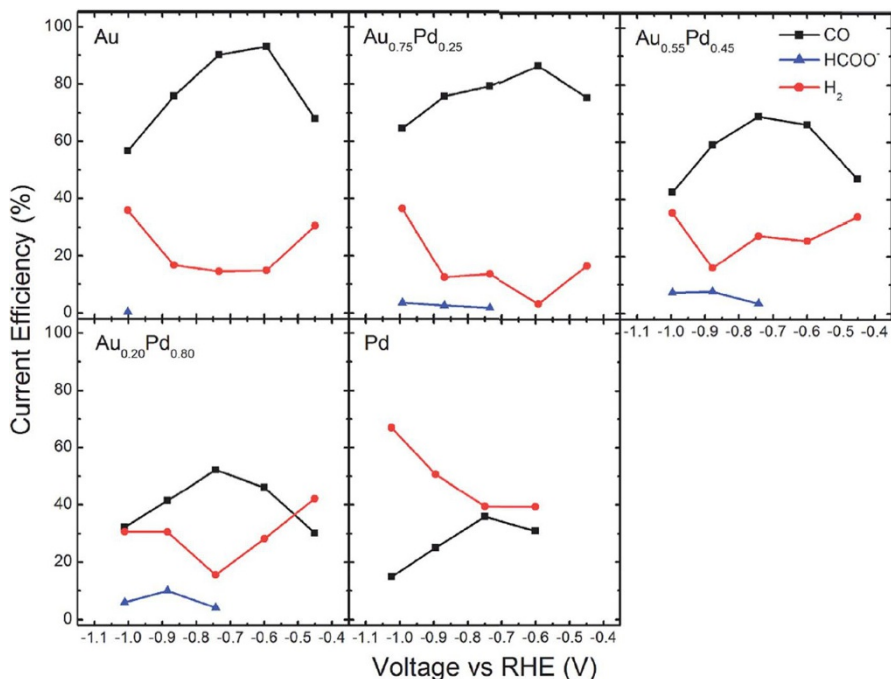


Fig. 6 Current efficiencies of $\text{Au}_{1-y}\text{Pd}_y$ alloys in a CO_2 purged environment. Current for CO (black), HCOO^- (blue) and H_2 (red) were recorded. Reproduced with permission from Ref. [72]

Pd electrode at pH of 6.7. The authors also demonstrated the reversible interconversion between CO_2 and formate by CV scanning around the equilibrium potential, suggesting that catalysts for formic acid oxidation should also be active for CO_2 reduction. The same group also developed a Pd–Pt/C bimetallic nano-catalyst for CO_2RR [66]. This nanocatalyst had an onset potential of -0.4 V vs. RHE, close to the theoretical equilibrium potential of 0.02 V. The $\text{Pd}_{70}\text{Pt}_{30}$ nanocatalyst also showed a very high FE of 88% at -0.4 V vs. RHE. Mixing Pd and Pt should alter the d-band center and reduce the numbers of neighboring Pt sites where CO poisoning happens, leading to high FE with high current density.

Additionally, Pd–Pt NPs with a Pd rich surface were also studied by Cai et al. [65]. Formate production was reached at relatively low overpotentials and the current density was dramatically increased. The author attributed the enhancement to the ease of H generation from the sublayer Pt.

AgPd nanodendrite-modified Au nanoprisms were reported as CO_2RR catalysts by increasing the H coverage to facilitate the interaction between H and $^{*}\text{CO}/^{*}\text{COOH}$ [77]. The author explained that Ag was the first electron donor and Pd was the H source. The catalyst produced formate at low overpotential (-0.18 V) with up to 49% FE.

Another interesting catalyst is AgSn/SnO_x core/shell bimetallic catalyst reported by Luc et al. [64]. By galvanically displacing a Sn nanosphere with Ag, AgSn with an ultra-thin SnO_x shell was formed (Fig. 7a). The bulk and surface

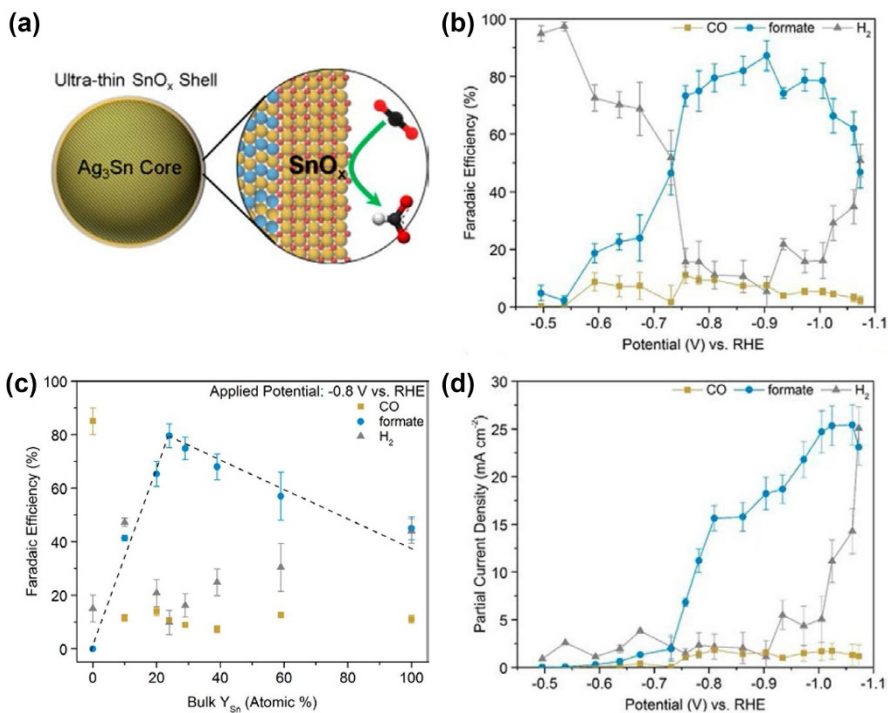


Fig. 7 **a** Illustration of AgSn particles with ultra-thin SnO_x shell for CO_2RR . **b** FE of CO , H_2 and formate for $\text{Ag}_{76}\text{Sn}_{24}$ catalyst at various potentials. **c** FE of CO , H_2 and formate for AgSn catalysts with different composition at -0.8 V, **d** partial current densities for $\text{Ag}_{76}\text{Sn}_{24}$ catalyst at various potentials. Reproduced with permission from Ref. [64]

compositions were verified by Wavelength Dispersive X-ray Fluorescence analysis and X-ray photoelectron spectroscopy. The FE values for H_2 , CO and formate with different Sn contents are shown in Fig. 7c. $\text{Ag}_3\text{Sn}/\text{SnO}_x$ was shown to produce up to 80% FE at -0.9 V and $25 \text{ mA}/\text{cm}^2$ formate partial current density at -1.25 V (Fig. 7b-d). DFT calculations revealed that the surface lattice expanded. A simulation of the strain effect on SnO oxygen-vacancy showed that lattice expansion gave a preferred energy driving force toward OCHO^* , favorable to HCOOH formation. However, a thicker SnO_x affected the electron conductivity. Therefore, a balance of surface lattice expansion and electrical conductivity must be considered.

Choi et al. used a similar idea to design a Sn-Pb alloy (SnO_x and Pb^0 on surface) on a carbon paper [68]. A higher electrical conductivity and stronger electron donating ability were observed, which was used to explain an enhanced performance of CO_2 reduction to formate [78]. A study with PdSnO_2 showed an exclusive formation of formic acid. The author proposed that the optimal Pd-Sn-O surface with highest oxygen occupancy could facilitate the $^*\text{OCHO}$ adsorption. In another case, Haruyama et al. developed a Cu-Sn alloy electrode

made from a simple electrodeposition method for converting CO_2 into CO and HCOO^- [33]. For the $\text{Cu}_{87}\text{Sn}_{13}$ electrode, high selectivity toward CO formation was observed at all applied potentials with maximum FE of 60% for CO at -0.99 V. Furthermore, good selectivity toward HCOO^- with maximum FE of 90% at -1.09 V was obtained on the $\text{Cu}_{55}\text{Sn}_{45}$ electrode. These results indicated the importance of the appropriate tuning of binding energies for the active intermediate species on the catalyst surface. The selectivity for HCOO^- formation was affected by the surface oxidation state of Sn, while the selectivity for CO was mainly affected by the crystal structures such as intermetallic compound formation.

Lu et al. showed that $\text{Pd}_{83}\text{Cu}_{17}$ bimetallic aerogels presented high FE (80.0%) and high current density (31.8 mA/cm^2) for methanol when a molar mixture of 25% [Bmim]BF₄ and 75% water was used as the electrolyte [74]. The superior performance was attributed to the high $\text{Pd}^0/\text{Pd}^{2+}$ and $\text{Cu}^{1+}/\text{Cu}^0/\text{Cu}^{2+}$ ratios and Cu/Pd grain boundaries from the nanochain structure.

Zhang et al. synthesized 2D hierarchical Pd/SnO₂ nanosheets for CO₂RR. They showed high FE (54.8%) for CO₂ to methanol at -0.24 V with a total current density of -2.5 mA/cm^2 . [75] The formation of the Pd–O–Sn interface was considered to be the key for the improved methanol formation.

Wen et al. demonstrated a highly selective Bi–Sn catalyst for CO₂ to formate [76]. The Bi NPs were deposited on Sn nanosheets. The catalyst could reach 96% FE and 0.74 mmol/h/cm^2 at -1.1 V. The stability test was conducted for 100 h with almost no FE loss. The Bi NPs could modify the density of states of Sn, resulting in a stronger binding of the HCOO^* intermediate that was attributed as a potential reason for high formate FE.

An alternative strategy to produce C₂₊ products in CO₂RR is to design a tandem micro-environment where one metal converts CO₂ to CO and the other metal does the further reduction of CO to form C₂₊ products. Oxide-derived Cu–Zn catalysts were reported to have higher ethylene and ethanol yield based on this strategy [73]. Ren et al. synthesized oxidized Cu–Zn films onto a polished Cu disk galvanically. Oxide-derived Cu–Zn with different compositions were tested in 0.1 M KHCO₃ electrolyte. The electrode surface was determined to be covered with phase segregated Cu⁰ and Zn⁰ crystallites during CO₂RR process (Fig. 8a). Operando Raman spectroscopy measurements revealed that Zn adsorbed CO weakly. The reduced CO on Zn could diffuse and spill over onto the Cu sites, leading to 29.1% FE for ethanol formation at -1.05 V (Fig. 8b) on Cu₂₀Zn. This concept was also applied on catalyst systems of CuNi and CuAg (Fig. 8c, d) by Lee et al. [70]. On Ag–Cu biphasic boundaries, CO on Ag could interact with the intermediate on the neighboring Cu site to form C₂H₅OH.

For Cu-based bimetallic catalysts, utilization of a second metal to strengthen CO adsorption energies was also studied. Zhang et al. placed Cu overlayers on tetrahedrahedral Pd NP surfaces [79]. The resulting high index Cu (310) surface could achieve a 0.3–0.4 V stronger binding for CO. This could result in a better selective ethanol formation. Jia et al. showed that FE of methanol (up to 15%) on nano-Cu_{63.9}Au_{36.1} (with nanoporous Cu as a support, dealloyed from Cu–Zn) was

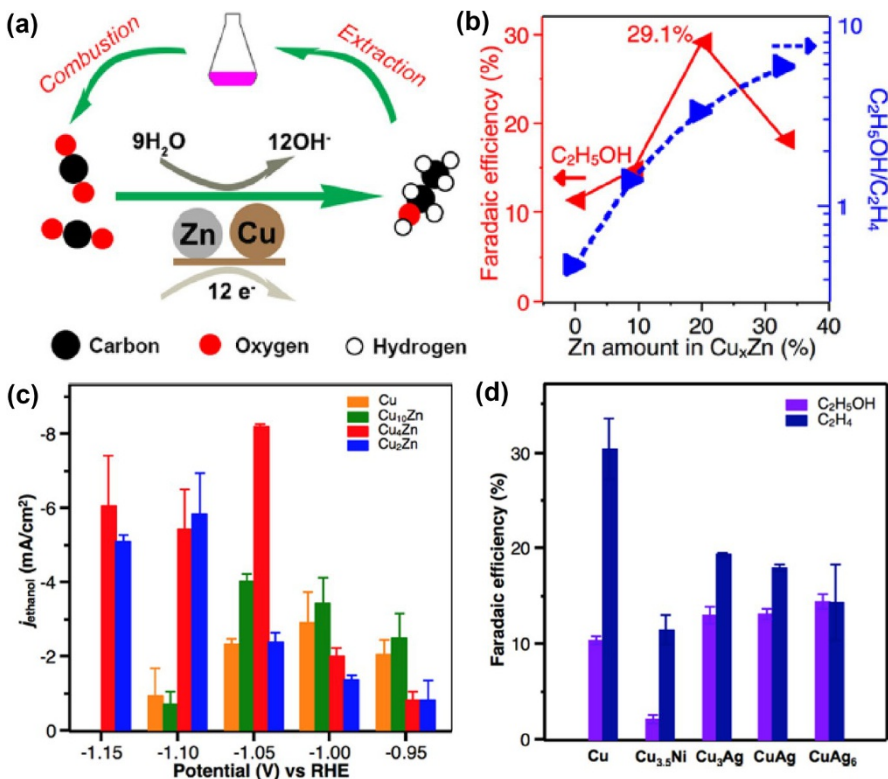


Fig. 8 **a** Cartoon for CO_2 electroreduction on $\text{Cu}-\text{Zn}$ catalysts. **b** FE and ethanol to ethylene ratio on $\text{Cu}-\text{Zn}$. **c** Partial current density of ethanol for CuZn with various composition between -0.95 V and -1.15 V. **d** FE of ethanol and ethylene using Cu , $\text{Cu}_{3.5}\text{Ni}$, Cu_3Ag , CuAg , and CuAg_6 catalysts. Reproduced with permission from Ref. [73]

nineteen times higher than that on Cu, although no clear explanation of the origin of this enhancement was provided [80].

DFT calculations predicted that titania-modified Ag electrocatalysts could be suitable for CO_2 reduction to produce CH_3OH as well as CH_4 [81], where Ag acts as an electron donor, reducing the supported $(\text{TiO}_2)_3$ partially. Thus, the surface became more reactive with CO_2 . Further reduction produces HCOO^* , H_2COO^* , H_2COOH^* , CH_3OH sequentially. Also, by calculating the intermediate surface free energies, Zhao et al. estimated that Ni/Ti, Cu/Ni, and strained Cu/Ni near-surface-alloys could lead to highly selective and efficient production of formic acid [24]. Even though there were several experimental and computational data for better multi-carbon species production, the detailed mechanism after CO adsorption were still under debate. The open questions include, for example, when and where the C-C coupling happens, and what helps the formation of C_{2+} products.

3 Challenges and Opportunities of Bimetallic Electrocatalysts for CO₂ Reduction

The literature review described has demonstrated the great potential of bimetallic materials for CO₂RR. Many bimetallic catalysts have been designed to enhance CO, hydrocarbon and oxygenate yields. Even though improvement in the selectivity, FE and activity was shown, the catalytic mechanisms have not been thoroughly revealed. A typical commercial catalyst would require an overpotential of less than 300 mV with a significant current density of higher than 10 mA/cm². The FE should be larger than 80% [71]. Therefore, the practical application of bimetallic materials for CO₂RR still faces several challenges: (1) high energy barrier for CO₂ activation, (2) mass transfer limitation for CO₂ gas to catalytic surfaces, (3) the sluggish kinetics, (4) high separation costs due to a wide range of products, (5) active sites poisoning from intermediates and impurities, and (6) low reduction selectivity for multi-carbon species. In most cases it remains unclear the exact reaction pathways for product formation, especially for the C–C coupling.

One important consideration for designing improved bimetallic CO₂RR catalysts is to tune the intermediate binding energy, which can be achieved by selecting the appropriate bimetallic components with guidance from DFT calculations. Core/shell structure is a viable way to control the surface strain, with the extent of the strain being controlled by shell thickness. Designing catalysts with grain boundaries and surface defects could also enhance CO₂RR selectivity and activity.

In general, the final CO₂RR products are controlled by the reaction intermediates. For example, if the target product is CO, a bimetallic catalyst with relatively low CO binding energy would be preferred in most cases. If methanol or methane is the target product, the tuned binding energy of CHO* and COH* is critical for high selectivity.

Enhanced reactant coverage should result in higher CO₂RR yields. Increasing CO₂ partial pressure near the catalyst surface can increase the activity for CO₂ reduction. Using organic solvents and ionic liquids can also help overcome the low solubility of CO₂ in water-based electrolytes. Many CO₂ reduction catalysts tested in organic solvent or with ionic liquid show an increased performance.

However, to successfully evaluate the true active sites and mechanisms of reactivity, catalyst samples must be carefully characterized using a variety of techniques. The surface and bulk compositions, structure and morphology before and after the CO₂RR should be examined. The identification of intermediates formed upon activation and reduction of CO₂ is essential to understanding the reaction mechanism. In-situ characterization methods such as infrared spectroscopy, ultraviolet-visible spectroscopy and Raman spectroscopy, as well as synchrotron-based techniques such as XRD and EXAFS, should be more extensively employed to understand effects of applied voltage on catalyst morphological changes and reaction mechanisms.

Acknowledgements Authors from Columbia University are partially supported by the US Department of Energy, Catalysis Program (DE-FG02-13ER16381). Authors at University of Delaware thank the financial support from the Department of Energy under Award Number DE-FE0029868. The authors also thank the National Science Foundation Faculty Early Career Development program (Award No. CBET-1350911).

References

- Beer C, Reichstein M, Tomelleri E, Ciais P, Jung M, Carvalhais N, Rödenbeck C, Arain MA, Baldocchi D, Bonan GB, Bondeau A, Cescatti A, Lasslop G, Lindroth A, Lomas M, Luyssaert S, Margolis H, Oleson KW, Roupsard O, Veenendaal E, Viovy N, Williams C, Woodward FI, Papale D (2010) Terrestrial gross carbon dioxide uptake: global distribution and covariation with climate. *Science* 329:834–838
- Solomon S, Plattner G-K, Knutti R, Friedlingstein P (2009) Irreversible climate change due to carbon dioxide emissions. *Proc Natl Acad Sci* 106:1704–1709
- Gillet NP, Arora VK, Zickfeld K, Marshall SJ, Merryfield WJ (2011) Ongoing climate change following a complete cessation of carbon dioxide emissions. *Nat Geosci* 4:83
- Malhi Y, Meir P, Brown S (2002) Forests, carbon and global climate. *Philos T R Soc A* 360:1567–1591
- Lu Q, Jiao F (2016) Electrochemical CO₂ reduction: electrocatalyst, reaction mechanism, and process engineering. *Nano Energy* 29:439–456
- Kondratenko EV, Mul G, Baltrusaitis J, Larrazabal GO, Perez-Ramirez J (2013) Status and perspectives of CO₂ conversion into fuels and chemicals by catalytic, photocatalytic and electrocatalytic processes. *Energ Environ Sci* 6:3112–3135
- Lu Q, Rosen J, Zhou Y, Hutchings GS, Kimmel YC, Chen JGG, Jiao F (2014) A selective and efficient electrocatalyst for carbon dioxide reduction. *Nat Commun* 5:3242
- Haegel NM, Margolis R, Buonassisi T, Feldman D, Froitzheim A, Garabedian R, Green M, Glunz S, Henning HM, Holder B, Kaizuka I, Kroposki B, Matsubara K, Niki S, Sakurai K, Schindler RA, Tumas W, Weber ER, Wilson G, Woodhouse M, Kurtz S (2017) Terawatt-scale photovoltaics: trajectories and challenges. *Science* 356:141–143
- Choi J, Kim MJ, Ahn SH, Choi I, Jang JH, Ham YS, Kim JJ, Kim S-K (2016) Electrochemical CO₂ reduction to CO on dendritic Ag–Cu electrocatalysts prepared by electrodeposition. *Chem Eng J* 299:37–44
- Peterson AA, Abild-Pedersen F, Studt F, Rossmeisl J, Norskov JK (2010) How copper catalyzes the electroreduction of carbon dioxide into hydrocarbon fuels. *Energ Environ Sci* 3:1311–1315
- Wu J, Huang Y, Ye W, Li Y (2017) CO₂ reduction: from the electrochemical to photochemical approach. *Adv Sci* 4:1700194
- Hori Y (2008) In: Vayenas CG, White RE, Gamboa-Aldeco ME (eds) Modern aspects of electrochemistry. Springer New York, New York, pp 89–189
- Hidetomo N, Shioichiro I, Yoshiyuki O, Kazumoto I, Masunobu M, Kaname I (1990) Electrochemical reduction of carbon dioxide at various metal electrodes in aqueous potassium hydrogen carbonate solution. *Bull Chem Soc Jpn* 63:2459–2462
- Yoshio H, Katsuhei K, Shin S (1985) Production of CO and CH₄ in electrochemical reduction of CO₂ at metal electrodes in aqueous hydrogencarbonate solution. *Chem Lett* 14:1695–1698
- Monnier A, Augustynski J, Stalder C (1980) On the electrolytic reduction of carbon dioxide at TiO₂ and TiO₂–Ru cathodes. *J Electroanal Chem Interfacial Electrochem* 112:383–385
- Hori Y, Wakebe H, Tsukamoto T, Koga O (1994) Electrocatalytic process of CO selectivity in electrochemical reduction of CO₂ at metal electrodes in aqueous media. *Electrochim Acta* 39:1833–1839
- Coq B, Figueras F (1998) Structure-activity relationships in catalysis by metals: some aspects of particle size, bimetallic and supports effects. *Coord Chem Rev* 178:1753–1783
- Ozin GA (1977) Very small metallic and bimetallic clusters: metal cluster-metal surface analogy in catalysis and chemisorption processes. *Catal Rev Sci Eng* 16:191–289
- Sinfelt JH (1977) Catalysis by alloys and bimetallic clusters. *Acc Chem Res* 10:15–20
- Sinfelt JH, Via GH, Lytle FW (1984) Application of EXAFS in catalysis-structure of bimetallic cluster catalysis. *Catal Rev Sci Eng* 26:81–140
- Wang DS, Li YD (2011) Bimetallic nanocrystals: liquid-phase synthesis and catalytic applications. *Adv Mater* 23:1044–1060
- Chang Z, Huo S, Zhang W, Fang J, Wang H (2017) The tunable and highly selective reduction products on Ag@Cu bimetallic catalysts toward CO₂ electrochemical reduction reaction. *J Phys Chem C* 121:11368–11379
- Roy C, Galipaud J, Fréchette-Viens L, Garbarino S, Qiao J, Guay D (2017) CO₂ electroreduction at AuxCu_{1-x} obtained by pulsed laser deposition in O₂ atmosphere. *Electrochim Acta* 246:115–122

24. Zhao Z, Chen Z, Lu G (2017) Computational discovery of nickel-based catalysts for CO₂ reduction to formic acid. *J Phys Chem C* 121:20865–20870
25. Takashima T, Suzuki T, Irie H (2017) Electrochemical carbon dioxide reduction on copper-modified palladium nanoparticles synthesized by underpotential deposition. *Electrochim Acta* 229:415–421
26. Yin Z, Gao D, Yao S, Zhao B, Cai F, Lin L, Tang P, Zhai P, Wang G, Ma D, Bao X (2016) Highly selective palladium-copper bimetallic electrocatalysts for the electrochemical reduction of CO₂ to CO. *Nano Energy* 27:35–43
27. Zhao X, Luo B, Long R, Wang C, Xiong Y (2015) Composition-dependent activity of Cu–Pt alloy nanocubes for electrocatalytic CO₂ reduction. *J Mater Chem A* 3:4134–4138
28. Sarfraz S, Garcia-Esparza AT, Jedidi A, Cavallo L, Takanabe K (2016) Cu–Sn bimetallic catalyst for selective aqueous electroreduction of CO₂ to CO. *ACS Catal* 6:2842–2851
29. Katoh A, Uchida H, Shibata M, Watanabe M (1994) Design of electrocatalyst for CO₂ reduction. V. Effect of the microcrystalline structures of Cu–Sn and Cu–Zn alloys on the electrocatalysis of CO₂ reduction. *J Electrochem Soc* 8:2054–2058
30. Kim D, Xie C, Becknell N, Yu Y, Karamad M, Chan K, Crumlin EJ, Nørskov JK, Yang P (2017) Electrochemical activation of CO₂ through atomic ordering transformations of AuCu nanoparticles. *J Am Chem Soc* 139:8329–8336
31. Lee H, Kim S-K, Ahn SH (2017) Electrochemical preparation of Ag/Cu and Au/Cu foams for electrochemical conversion of CO₂ to CO. *J Ind Eng Chem* 54:218–225
32. Ma M, Hansen HA, Valenti M, Wang Z, Cao A, Dong M, Smith WA (2017) Electrochemical reduction of CO₂ on compositionally variant Au–Pt bimetallic thin films. *Nano Energy* 42:51–57
33. Morimoto M, Takatsuji Y, Yamasaki R, Hashimoto H, Nakata I, Sakakura T, Haruyama T (2017) Electrodeposited Cu–Sn alloy for electrochemical CO₂ reduction to CO/HCOO[−]. *Electrocatalysis* 9:323–332
34. Yoshio H, Akira M, Shin-ya I (1990) Enhanced evolution of CO and suppressed formation of hydrocarbons in electroreduction of CO₂ at a copper electrode modified with cadmium. *Chem Lett* 19:1231–1234
35. Rasul S, Anjum DH, Jedidi A, Minenkov Y, Cavallo L, Takanabe K (2015) A highly selective copper–indium bimetallic electrocatalyst for the electrochemical reduction of aqueous CO₂ to CO. *Angew Chem Int Ed* 54:2146–2150
36. He J, Dettelbach KE, Salvatore DA, Li T, Berlinguette CP (2017) High-throughput synthesis of mixed-metal electrocatalysts for CO₂ reduction. *Angew Chem Int Ed* 56:6068–6072
37. Kim D, Resasco J, Yu Y, Asiri AM, Yang P (2014) Synergistic geometric and electronic effects for electrochemical reduction of carbon dioxide using gold–copper bimetallic nanoparticles. *Nat Commun* 5:4948
38. Li Q, Fu J, Zhu W, Chen Z, Shen B, Wu L, Xi Z, Wang T, Lu G, J-j Zhu, Sun S (2017) Tuning Sn-catalysis for electrochemical reduction of CO₂ to CO via the core/shell Cu/SnO₂ structure. *J Am Chem Soc* 139:4290–4293
39. Sun K, Cheng T, Wu L, Hu Y, Zhou J, MacLennan A, Jiang Z, Gao Y, Goddard WA, Wang Z (2017) Ultrahigh mass activity for carbon dioxide reduction enabled by Gold–iron Core–Shell nanoparticles. *J Am Chem Soc* 139:15608–15611
40. Watanabe M, Shibata M, Kato A, Azuma M, Sakata T (1991) Design of alloy electrocatalysts for CO₂ reduction: III. The selective and reversible reduction of on Cu alloy electrodes. *J Electrochem Soc* 138:3382–3389
41. Yoshio H, Akira M, Shin-ya I, Yuzuru Y, Osamu K (1989) Nickel and iron modified copper electrode for electroreduction of CO₂ by in situ electrodeposition. *Chem Lett* 18:1567–1570
42. Luc W, Jiang C, Chen JG, Jiao F (2018) Role of surface oxophilicity in copper-catalyzed water dissociation. *ACS Catal* 8:9327–9333
43. Hammer B, Morikawa Y, Nørskov JK (1996) CO chemisorption at metal surfaces and overlayers. *Phys Rev Lett* 76:2141–2144
44. Alayoglu S, Nilekar AU, Mavrikakis M, Eichhorn B (2008) Ru–Pt core–shell nanoparticles for preferential oxidation of carbon monoxide in hydrogen. *Nat Mater* 7:333
45. Gorzkowski MT, Lewera A (2015) Probing the limits of d-band center theory: electronic and electrocatalytic properties of Pd-shell–Pt-core nanoparticles. *The J Phys Chem C* 119:18389–18395
46. Chen JG, Menning CA, Zellner MB (2008) Monolayer bimetallic surfaces: experimental and theoretical studies of trends in electronic and chemical properties. *Surf Sci Rep* 63:201–254

47. Ma S, Sadakiyo M, Heima M, Luo R, Haasch RT, Gold JI, Yamauchi M, Kenis PJA (2017) Electrocatalysis of carbon dioxide to hydrocarbons using bimetallic Cu–Pd catalysts with different mixing patterns. *J Am Chem Soc* 139:47–50
48. Singh S, Gautam RK, Malik K, Verma A (2017) Ag–Co bimetallic catalyst for electrochemical reduction of CO₂ to value added products. *J CO₂ Util* 18:139–146
49. Clark EL, Hahn C, Jaramillo TF, Bell AT (2017) Electrochemical CO₂ reduction over compressively strained CuAg surface alloys with enhanced multi-carbon oxygenate selectivity. *J Am Chem Soc* 139:15848–15857
50. Monzo J, Malewski Y, Kortlever R, Vidal-Iglesias FJ, Solla-Gullon J, Koper MTM, Rodriguez P (2015) Enhanced electrocatalytic activity of Au@Cu core@shell nanoparticles towards CO₂ reduction. *J Mater Chem A* 3:23690–23698
51. Chang Z-Y, Huo S-J, He J-M, Fang J-H (2017) Facile synthesis of Cu–Ag bimetallic electrocatalyst with prior C2 products at lower overpotential for CO₂ electrochemical reduction. *Surf Interfaces* 6:116–121
52. Zhang S, Kang P, Bakir M, Lapides AM, Dares CJ, Meyer TJ (2015) Polymer-supported CuPd nanoalloy as a synergistic catalyst for electrocatalytic reduction of carbon dioxide to methane. *Proc Natl Acad Sci* 112:15809–15814
53. Hoang TTH, Verma S, Ma S, Fister TT, Timoshenko J, Frenkel AI, Kenis PJA, Gewirth AA (2018) Nanoporous copper–silver alloys by additive-controlled electrodeposition for the selective electroreduction of CO₂ to ethylene and ethanol. *J Am Chem Soc* 140:5791–5797
54. Peterson AA, Nørskov JK (2012) Activity descriptors for CO₂ electroreduction to methane on transition-metal catalysts. *J Phys Chem Lett* 3:251–258
55. Kuhl KP, Hatsukade T, Cave ER, Abram DN, Kibsgaard J, Jaramillo TF (2014) Electrocatalytic conversion of carbon dioxide to methane and methanol on transition metal surfaces. *J Am Chem Soc* 136:14107–14113
56. Hansen HA, Shi C, Lausche AC, Peterson AA, Nørskov JK (2016) Bifunctional alloys for the electroreduction of CO₂ and CO. *Phys Chem Chem Phys* 18:9194–9201
57. Nie X, Esopi MR, Janik MJ, Asthagiri A (2013) Selectivity of CO₂ reduction on copper electrodes: the role of the kinetics of elementary steps. *Angew Chem Int Ed* 52:2459–2462
58. Nie X, Wang H, Janik MJ, Chen Y, Guo X, Song C (2017) Mechanistic insight into C–C coupling over Fe–Cu bimetallic catalysts in CO₂ hydrogenation. *J Phys Chem C* 121:13164–13174
59. Garza AJ, Bell AT, Head-Gordon M (2018) Mechanism of CO₂ reduction at copper surfaces: pathways to C2 products. *ACS Catal* 8:1490–1499
60. Kuhl KP, Cave ER, Abram DN, Jaramillo TF (2012) New insights into the electrochemical reduction of carbon dioxide on metallic copper surfaces. *Energ Environ Sci* 5:7050–7059
61. Grote J-P, Zeradjanin AR, Cherevko S, Savan A, Breitbach B, Ludwig A, Mayrhofer KJJ (2016) Screening of material libraries for electrochemical CO₂ reduction catalysts—improving selectivity of Cu by mixing with Co. *J Catal* 343:248–256
62. Ma S, Sadakiyo M, Luo R, Heima M, Yamauchi M, Kenis PJA (2016) One-step electrosynthesis of ethylene and ethanol from CO₂ in an alkaline electrolyzer. *J Power Sources* 301:219–228
63. Manthiram K, Beberwyck BJ, Alivisatos AP (2014) Enhanced electrochemical methanation of carbon dioxide with a dispersible nanoscale copper catalyst. *J Am Chem Soc* 136:13319–13325
64. Luc W, Collins C, Wang S, Xin H, He K, Kang Y, Jiao F (2017) Ag–Sn bimetallic catalyst with a core-shell structure for CO₂ reduction. *J Am Chem Soc* 139:1885–1893
65. Cai F, Gao D, Si R, Ye Y, He T, Miao S, Wang G, Bao X (2017) Effect of metal deposition sequence in carbon-supported Pd–Pt catalysts on activity towards CO₂ electroreduction to formate. *Electrochim Commun* 76:1–5
66. Kortlever R, Peters I, Koper S, Koper MTM (2015) Electrochemical CO₂ reduction to formic acid at low overpotential and with high faradaic efficiency on carbon-supported bimetallic Pd–Pt nanoparticles. *ACS Catal* 5:3916–3923
67. Kortlever R, Balemans C, Kwon Y, Koper MTM (2015) Electrochemical CO₂ reduction to formic acid on a Pd-based formic acid oxidation catalyst. *Catal Today* 244:58–62
68. Bai X, Chen W, Zhao C, Li S, Song Y, Ge R, Wei W, Sun Y (2017) Exclusive formation of formic acid from CO₂ electroreduction by a tunable Pd–Sn alloy. *Angew Chem Int Ed* 56:12219–12223
69. Furuya N, Yamazaki T, Shibata M (1997) High performance RuPd catalysts for CO₂ reduction at gas-diffusion electrodes. *J Electroanal Chem* 431:39–41
70. Lee S, Park G, Lee J (2017) Importance of Ag–Cu biphasic boundaries for selective electrochemical reduction of CO₂ to ethanol. *ACS Catal* 7:8594–8604

71. Jovanov ZP, Hansen HA, Varela AS, Malacrida P, Peterson AA, Nørskov JK, Stephens IEL, Chorkendorff I (2016) Opportunities and challenges in the electrocatalysis of CO₂ and CO reduction using bifunctional surfaces: a theoretical and experimental study of Au–Cd alloys. *J Catal* 343:215–231
72. Hahn C, Abram DN, Hansen HA, Hatsukade T, Jackson A, Johnson NC, Hellstern TR, Kuhl KP, Cave ER, Feaster JT, Jaramillo TF (2015) Synthesis of thin film AuPd alloys and their investigation for electrocatalytic CO₂ reduction. *J Mater Chem A* 3:20185–20194
73. Ren D, Ang BS-H, Yeo BS (2016) Tuning the selectivity of carbon dioxide electroreduction toward ethanol on oxide-derived Cu_xZn catalysts. *ACS Catal* 6:8239–8247
74. Lu L, Sun X, Ma J, Yang D, Wu H, Zhang B, Zhang J, Han B (2018) Highly efficient electroreduction of CO₂ to methanol on palladium–copper bimetallic aerogels. *Angew Chem Int Ed*. <https://doi.org/10.1002/anie.201808964>
75. Zhang W, Qin Q, Dai L, Qin R, Zhao X, Chen X, Ou D, Chen J, Chuong TT, Wu B, Zheng N (2018) Electrochemical reduction of carbon dioxide to methanol on hierarchical Pd/SnO₂ nanosheets with abundant Pd–O–Sn interfaces. *Angew Chem Int Ed* 57:9475–9479
76. Wen G, Lee DU, Ren B, Hassan FM, Jiang G, Cano ZP, Gostick J, Croiset E, Bai Z, Yang L, Chen Z (2018) Orbital interactions in Bi–Sn bimetallic electrocatalysts for highly selective electrochemical CO₂ reduction toward formate production. *Adv Energy Mater*. <https://doi.org/10.1002/aenm.201802427>
77. Shan C, Martin ET, Peters DG, Zaleski JM (2017) Site-selective growth of AgPd nanodendrite-modified au nanoprisms: high electrocatalytic performance for CO₂ reduction. *Chem Mater* 29:6030–6043
78. Choi SY, Jeong SK, Kim HJ, Baek I-H, Park KT (2016) Electrochemical reduction of carbon dioxide to formate on tin-lead alloys. *ACS Sustain Chem Eng* 4:1311–1318
79. Zhang F-Y, Sheng T, Tian N, Liu L, Xiao C, Lu B-A, Xu B-B, Zhou Z-Y, Sun S-G (2017) Cu over-layers on tetrahedahedral Pd nanocrystals with high-index facets for CO₂ electroreduction to alcohols. *Chem Commun* 53:8085–8088
80. Zhu W, Zhang Y-J, Zhang H, Lv H, Li Q, Michalsky R, Peterson AA, Sun S (2014) Active and selective conversion of CO₂ to CO on ultrathin Au nanowires. *J Am Chem Soc* 136:16132–16135
81. Zhai L, Cui C, Zhao Y, Zhu X, Han J, Wang H, Ge Q (2017) Titania-modified silver electrocatalyst for selective CO₂ reduction to CH₃OH and CH₄ from DFT study. *J Phys Chem C* 121:16275–16282



REVIEW

Dispersive Single-Atom Metals Anchored on Functionalized Nanocarbons for Electrochemical Reactions

Jin-Cheng Li^{1,2,3} · Zidong Wei⁴ · Dong Liu³ · Dan Du³ · Yuehe Lin³ · Minhua Shao^{1,2}

Received: 11 August 2018 / Accepted: 29 December 2018 / Published online: 8 January 2019
© Springer Nature Switzerland AG 2019

Abstract

The use of dispersive single-atom metals anchored on functionalized carbon nanomaterials as electrocatalysts for electrochemical energy conversion reactions represents a burgeoning area of research, due to their unique characteristics of low coordination number, uniform coordination environment, and maximum atomic utilization. Here we highlight the advanced synthetic methods, characterization techniques, and electrochemical applications for carbon-based single-atom metal catalysts, and provide illustrative correlations between molecular/electronic structures and specific catalytic activity for O₂ reduction, water splitting, and other emerging reactions including CO₂ reduction, H₂O₂ production, and N₂ reduction. We also discuss fundamental principles for the future design of carbon-based single-atom metal catalysts for specific electrochemical reactions. In addition, we explore the challenges and opportunities that lie ahead in further work with carbon-based single-atom metal electrocatalysts.

Keywords Single-atom metal catalysts · Oxygen reduction · Water splitting · Carbon dioxide reduction · Nitrogen reduction

Chapter 5 was originally published as Li, J.-C., Wei, Z., Liu, D., Du, D., Lin, Y. & Shao, M. Topics in Current Chemistry (2019) 377: 4. <https://doi.org/10.1007/s41061-018-0229-9>.

✉ Minhua Shao
kemshao@ust.hk

¹ Fok Ying Tung Research Institute, Hong Kong University of Science and Technology, Guangzhou 511458, People's Republic of China

² Department of Chemical and Biological Engineering, Hong Kong University of Science and Technology, Clear Water Bay, Kowloon, Hong Kong, People's Republic of China

³ School of Mechanical and Materials Engineering, Washington State University, Pullman, WA 99164, USA

⁴ College of Chemistry and Chemical Engineering, Chongqing University, Chongqing 400044, People's Republic of China

1 Introduction

The exploitation of clean and renewable energy technologies as alternatives to traditional fossil fuels has become a compelling need, given the effects of rapid energy consumption and severe environmental pollution. Electrochemical energy conversion devices, which involve the conversion between electrical energy and chemical energy (Fig. 1), are widely acknowledged as the most promising in terms of sustainability. In this case, electrochemical processes of oxygen reduction reaction (ORR) in fuel cells and metal–air batteries, along with hydrogen evolution reaction (HER) and oxygen evolution reaction (OER) in water splitting, occupy a central role in energy conversion technologies [1–3]. In addition, various emerging clean energy reactions, including ORR for H_2O_2 production, CO_2 reduction, and N_2 reduction for the respective production of fuels/chemicals and fertilizers, have recently attracted great attention [4–7]. Although these processes align with the vision for a sustainable and green energy system, the electrochemical reactions involved are extremely slow, resulting in poor performance of the related energy devices. In this case, catalysts are needed to improve the reaction rate, efficiency, and selectivity of electrochemical devices (Fig. 1).

Noble metals are believed to be the best electrocatalysts in most cases. However, these metals are extremely scarce, resulting in high costs associated with the use of these materials. Extensive research advancements have been made through downsizing of noble metal particles to increase the utilization of noble metals. It has also been found that their catalytic activity is strongly dependent on particle size. With the reduction in particle size, its surface free energy and specific surface area increase, and a unique quantum size effect can occur, leading to higher specific

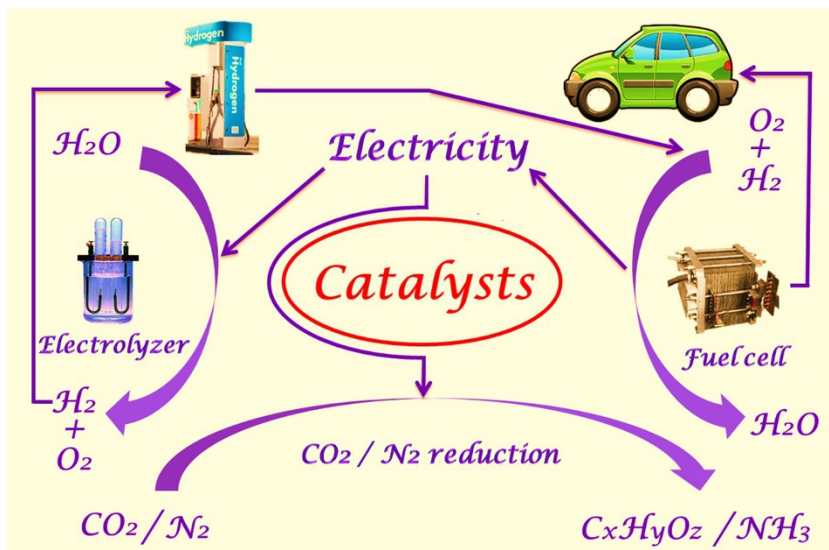


Fig. 1 Schematic showing electrochemical processes of hydrogen generation (electrolyzer) and utilization (fuel cell), CO_2 and N_2 reduction

catalytic activity (Fig. 2a) [8]. At present, the metal electrocatalysts commonly used commercially are nanosized counterparts. Further size reduction results in metal nanoclusters. Although some metal nanoclusters have shown good activity for certain reactions, they still contain multiple active centers [9, 10]. Such multiple sites make it difficult for researchers to understand the catalytic reaction process, thus impeding the future design of desirable catalysts. Compared to their bulk- and nanosized counterparts, single-atom metal catalysts have a well-defined single active center, which provides us with an ideal model for investigation of reaction mechanisms. In addition, single-atom metal catalysts demonstrate 100% atomic metal utilization and high specific catalytic activity. These unique features have motivated substantial research interest in single-atom catalysis.

The concept and validation of single-atom metal catalysts can be traced back to 2011 [11]. Qiao et al. fabricated an atomically dispersed Pt on FeO_x and demonstrated its excellent catalytic activity and high stability for CO oxidation. Combining experimental results and density functional theory (DFT) calculations, the authors claimed that the more vacant d orbitals of single Pt atoms induced through the electron transfer to FeO_x was responsible for its catalytic performance. Since this seminal work, numerous single-atom metals supported on various supports (metal

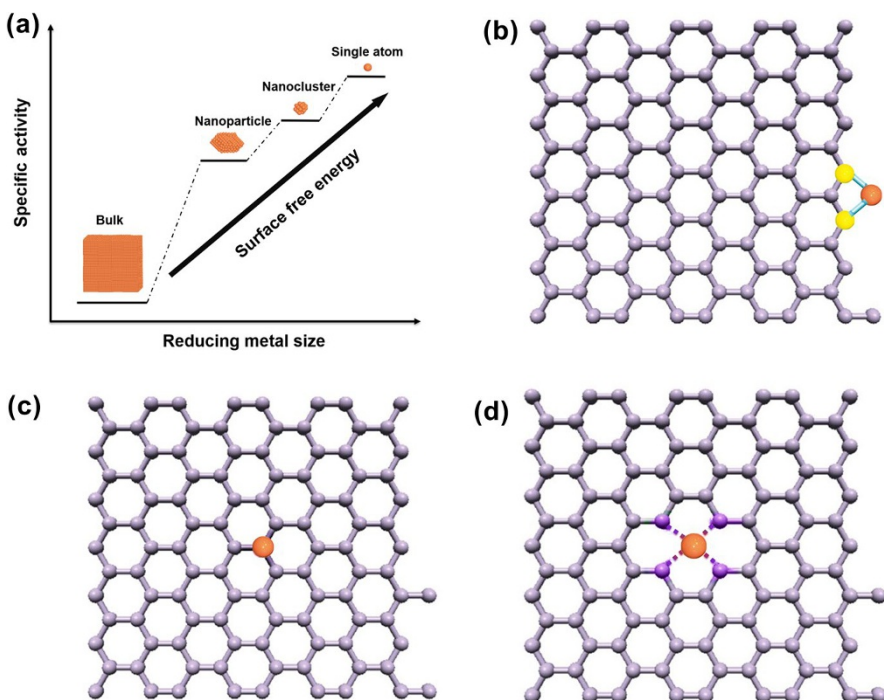


Fig. 2 **a** Schematic correlation between metal size and specific activity. **b** Single metal atom anchored at the edge of graphene. **c** Single metal atom substituting one carbon atom in graphene lattice. **d** Single metal atom coordinated with heteroatom atoms in graphene matrix

oxide/carbide/nitride/sulfide, carbons, etc.) have been developed across a wide array of catalytic systems [12–16]. The strong interactions between isolated metal atoms and supports play a significant role in preventing the aggregation of isolated metal atoms, leading to stable and well-dispersed single-atom metal catalysts.

Even though metal compounds (oxide/carbide/nitride/sulfide) have been widely used as supports for the fabrication of single-atom metal catalysts, they generally suffer from poor electrical conductivity. On the other hand, carbon materials offer many advantages, including large specific surface area (to host sufficient metal-based active sites), excellent electrical conductivity (to accelerate charge transfer), high chemical stability (to improve corrosion resistance), and flexibility with dopants (such as single metal atoms anchored at the edge of graphene due to the dangling bonds and pyridinic N (Fig. 2b) [17, 18], substitution of a single metal atom for one carbon atom in graphene lattice (Fig. 2c) [19], and a single metal atom coordinated with heteroatoms in graphene matrix (Fig. 2d) [20–23]). These unique features make them suitable for practical application in electrocatalysis. As a significant branch of single-atom metal catalysts, carbon-based single-atom metal electrocatalysts represent a burgeoning area of research [24–26]. In general, Fe/Co–N–C materials, in which pyridinic and/or pyrrolic N provides rich coordination sites for binding isolated Fe/Co atoms, are of great interest for use in various catalytic reactions including ORR, OER, HER, and CO₂ reduction [27–30].

Here, we highlight the advanced synthetic methods, characterization techniques, and electrochemical applications of recently advanced carbon-based single-atom metal catalysts. By providing illustrative correlations between geometric/electronic structures and specific activity for ORR, OER, HER, and other emerging reactions including CO₂ reduction, H₂O₂ production, and N₂ reduction, we extract fundamental principles for the future design of carbon-based single-atom metal catalysts for these electrochemical reactions. Finally, we explore the challenges and opportunities that lie ahead in further work with carbon-based single-atom metal electrocatalysts.

2 Synthesis of Carbon-Based Single-Atom Metal Catalysts

Because the high surface energy of isolated metal atoms tends to cause agglomeration during synthesis processes, the rational design of synthesis protocols is highly important for obtaining dispersive single-atom metals anchored on carbon nanomaterials. To date, three main strategies have been used: high-vacuum deposition technique, wet-chemical route, and high-temperature pyrolysis (Fig. 3).

2.1 High-Vacuum Deposition

High-vacuum deposition is a family of processes used to deposit material atom-by-atom or molecule-by-molecule on a solid support. These processes operate at a very low pressure, and the deposited thickness can range from one atom to millimeters. At present, arc-discharge and atomic layer deposition (ALD) are used to synthesize single metal atoms on carbon supports. For the arc-discharge approach, bulk metal

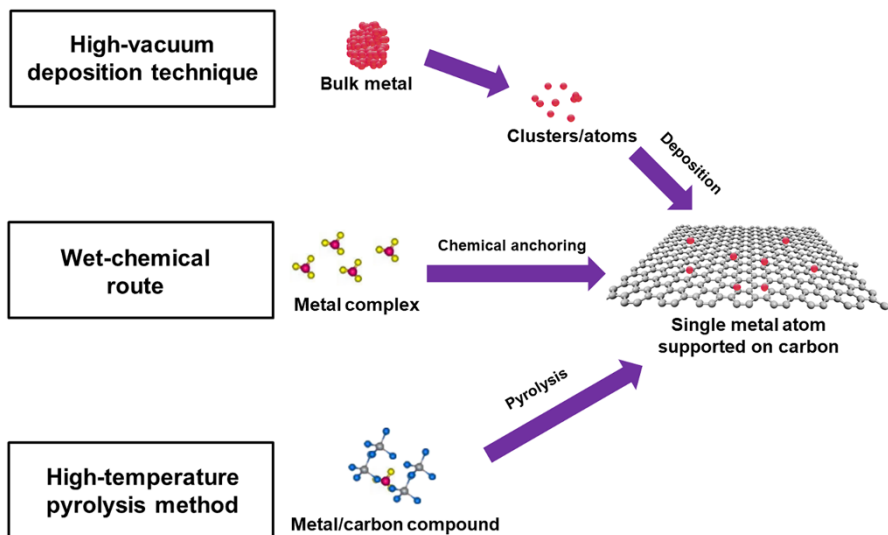


Fig. 3 Synthetic methods for preparation of carbon-based single-atom metal catalysts: high-vacuum deposition, wet-chemical route, and high-temperature pyrolysis

is usually used as the precursor, which undergoes arc-discharge evaporation, reaction with the decomposed carbon, and deposition on the cool walls of the chamber to produce carbon-supported single-atom metal catalysts. A typical example is a single-atom niobium in graphitic layer reported by Zhang et al. [31]. ALD is a more widely adopted strategy for the fabrication of carbon-based single-atom metal catalysts owing to its high level of controllability. Organic molecules containing metal atoms are used as the precursors. The Sun group first reported single Pt atoms on graphene nanosheets using (methylcyclopentadienyl)-trimethylplatinum as the precursor [32]. Subsequently, a series of carbon-based single-atom metal catalysts were synthesized by ALD [33–35].

To date, high-vacuum deposition has been the most common method used to prepare carbon-based single-atom noble metal catalysts. Owing to its good controllability, this technique may be a desirable strategy for fundamental studies in terms of metal–support interactions and size effect. However, this deposition method may not be suitable for large-scale industrial applications due to low catalyst yield and high cost. Thus there is an urgent need for the development of alternatives for the synthesis of carbon-based single-atom metal catalysts.

2.2 Wet-Chemical Route

Compared to the high-vacuum deposition technique, the wet-chemical route has been more widely used for the synthesis of carbon-based single-atom metal catalysts, as it does not involve specialized equipment [18, 36, 37]. Typically, single-atom metal species are anchored in the carbon supports by wet-chemical

reactions, during which they must avoid the aggregation of single metal atoms and dissolution. For example, Bulushev et al. synthesized single Pt-group metal (Ru, Pb, and Pt) atoms on N-doped carbon nanofibers via incipient wetness impregnation [17]. Experimental and theoretical simulation results revealed that these metal atoms are coordinated by pyridinic N, leading to an ionic/electron-deficient state of these single metal atoms, thereby preventing their aggregation. Choi et al. reported a sulfur-doped zeolite-templated carbon stabilizing high concentration of single Pt atoms (5 wt%) [21]. Interestingly, unlike conventional Pt-based materials that catalyze ORR with four-electron transfer, this catalyst selectively produces H₂O₂ with a two-electron pathway. This work suggests that the coordination environment of single Pt atoms plays a significant role in electrocatalysis and affects the reaction mechanisms.

In addition, this strategy can also be used to prepare carbon-based single-atom non-noble-metal catalysts. In nature, an iron porphyrin core structure in cytochrome c oxidase is recognized as the active site for catalyzing the ORR [38, 39]. To mimic the natural system, transition metal macrocyclic molecules supported on carbon materials have been designed and applied in electrocatalysis [40–42]. For example, Cao et al. reported iron phthalocyanine with an axial ligand anchored on single-walled carbon nanotubes (CNTs) [43], while Hijazi et al. prepared a covalent cobalt porphyrin network supported on CNT surfaces [44]. Wang et al. synthesized cobalt ions coordinated with N-, O-, S-doped graphene [45], and Ding et al. reported single cobalt ions bridged by ionic liquid polymer on CNT surfaces [46]. These carbon-based single-atom metal catalysts obtained through wet-chemical routes possess a relatively high concentration of single metal atoms, but they usually suffer from poor long-term stability.

2.3 High-Temperature Pyrolysis

High-temperature pyrolysis of precursors is the most widely adopted method for preparing carbon-based single-atom metal catalysts. Metal ions adsorbed on conducting polymer, metal–organic frameworks (MOFs), and transition metal macrocyclic molecules are the most common precursors [47–51]. During the high-temperature treatment (generally above 700 °C), isolated metal atoms can be directly doped into the carbon matrix or strongly coordinated by heteroatom-doped carbon, which gives isolated metal atoms high stability. Importantly, if the temperature is too high, coordination sites can be easily broken, leading to inactive nanosized metal species rather than enrichment of isolated metal atoms.

To date, a series of carbon-based single-atom metal (Pt, Ru, Fe, Co, Ni, Cu, and Zn) catalysts have been prepared using high-temperature pyrolysis [52–57]. More importantly, this method involves low-cost raw materials and apparatuses, and the final catalysts exhibit a robust structure and high performance. However, there is still a challenge in increasing the metal loading, as metal atoms are easily converted to nanoclusters and nanoparticles during high-temperature treatment.

3 Characterization of Carbon-Based Single-Atom Metal Catalysts

Characterization techniques are of great significance for studying carbon-based single-atom metal catalysts. Two main types of technique have been widely used to characterize these materials. One is electron microscopy and the other is spectroscopy.

3.1 Electron Microscopy Techniques

Scanning tunneling microscopy (STM) is used for imaging of surfaces at the atomic level. When a conducting tip approaches the surface of a sample and a bias voltage is applied between the two, a tunneling current is generated. By monitoring the current as the tip scans across the surface, we can acquire the surface information of the sample. Figure 4a shows a typical low-temperature STM image of a graphene-based single-atom Fe catalyst [25]. A single Fe atom, resolved as a bright spot, is coordinated by four N atoms embedded in the graphene matrix, which can be well reconstructed using a simulated STM image (Fig. 4b). However, the STM technique is not suitable for widespread use, as it requires extremely clean, smooth, and stable surfaces, sharp tips, excellent vibration control, and sophisticated electronics.

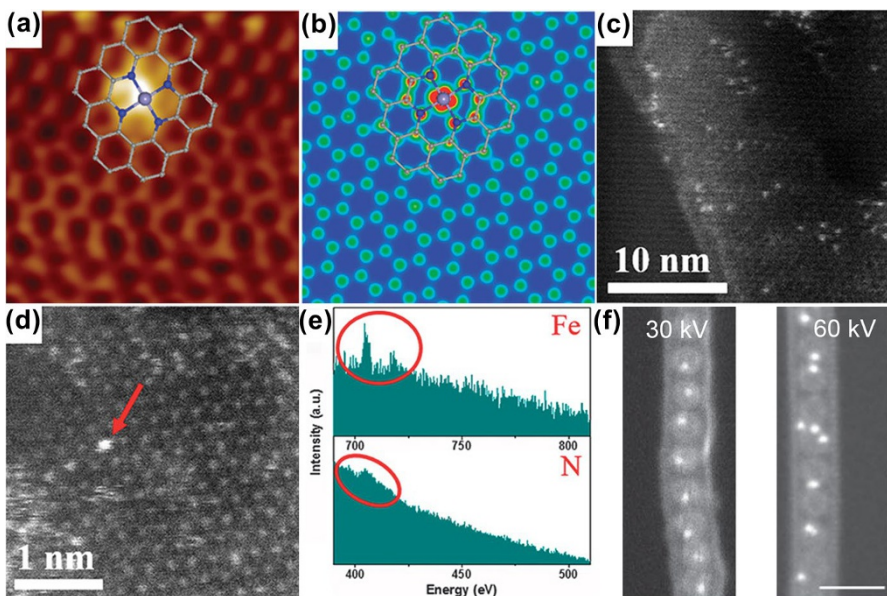


Fig. 4 **a** Low-temperature STM image of graphene-based single-atom Fe catalyst. **b** Simulated STM image for **a**. **c**, **d** HAADF-STEM images of graphene-based single-atom Fe catalyst. **e** The EELS atomic spectra of Fe and N elements from the bright dot marked by the red arrow in **d** [25]. **f** HAADF-STEM images of metallofullerene peapods in a single-wall carbon nanotube observed under 30 kV and 60 kV [61]

By contrast, aberration-corrected transmission electron microscopy (TEM) is a more popular technique for characterization of single-atom metal catalysts. Single metal atoms can be clearly observed in high-angle annular dark-field scanning transmission electron microscopy (HAADF-STEM) images, since the atomic number Z of a metal is much higher than that of carbon [58]. In addition, accessory electron energy-loss spectroscopy (EELS) and energy-dispersive X-ray spectroscopy (EDS) can be performed to detect the chemical composition of samples at the atomic level [59, 60]. Figure 4c–e shows the HAADF-STEM images and corresponding EELS data for a graphene-based single-atom Fe catalyst [25]. The bright spots are isolated Fe atoms, as determined on the basis of Z-contrast and EELS results. However, during imaging and chemical analysis of carbon-based single-atom metal catalysts, the electron beam irradiation can damage their structure. A comparison of HAADF-STEM images of metallofullerene ($\text{Er}@\text{C}_{82}$) peapods acquired at 30 kV and 60 kV is shown in Fig. 4f [61]. During the STEM experiment at 60 kV, the metallofullerenes were punctured, and single Er atoms escaped from their fullerene cage and traveled along the single-wall carbon nanotube (SWCNT). By contrast, the metallofullerene molecules observed at 30 kV largely retained an intact structure with a relatively low resolution. Thus, the rational choice of an appropriate operating voltage is critical for observing the real structure of single-atom metal catalysts.

TEM enables the direct observation of single metal atoms on carbon supports, but the visual field with these techniques is too small (several to dozens of nanometers). As a result, only partial information can be revealed. Thus, other techniques are needed that can provide average information for samples.

3.2 Spectroscopy Techniques

Spectroscopy techniques, including X-ray absorption spectroscopy [extended X-ray absorption fine structure (EXAFS) and X-ray absorption near-edge structure (XANES)], X-ray photoelectron spectroscopy (XPS), and Mössbauer spectroscopy, have been extensively applied for characterizing the chemical environments and content of metal atoms in carbon-based single-atom metal catalysts. Figure 5 shows a variety of spectroscopic techniques revealing the average information of $\text{Fe}-\text{N}-\text{C}$ catalysts (a typical carbon-based single-atom Fe catalyst) [62]. Compared to the reference samples of Fe foil and Fe_2O_3 (Fig. 5a), $\text{Fe}-\text{N}-\text{C}-600$ and $\text{Fe}-\text{N}-\text{C}-600$ prepared at 600 °C and 700 °C are lacking a prominent peak at the position of Fe–Fe coordination. This suggests that all Fe species are atomically dispersed in these $\text{Fe}-\text{N}-\text{C}$ catalysts, with no aggregation. However, there is a small peak of Fe–Fe coordination clearly observed in the sample synthesized at 800 °C, suggesting the formation of Fe aggregates. In addition, like the reference samples of FePc and $\text{Fe}(\text{phen})_x$, the $\text{Fe}-\text{N}-\text{C}$ catalysts show a main Fe–N coordination peak at 1.47 Å, indicating the presence of atomically dispersed Fe species. Importantly, the coordination numbers of Fe–N can be determined by fitting the EXAFS data. Combining the electrochemical evaluation and the EXAFS fitting results, correlations can be established between catalytic activity and the local environment of the metal centers, namely their coordination numbers of single-atom metal catalysts, providing a scientific basis for further study [50, 63]. The normalized

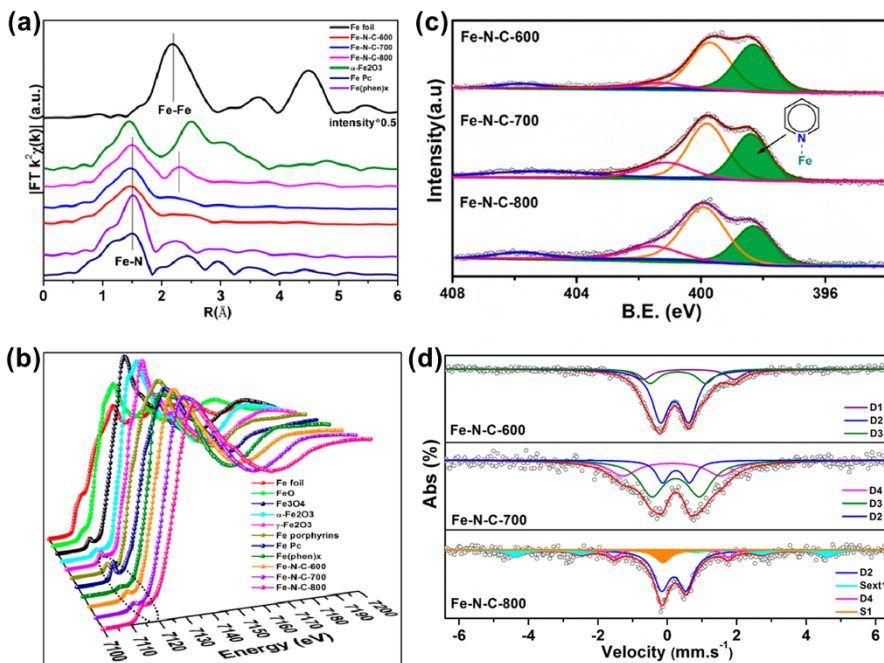


Fig. 5 **a** The k^2 -weighted Fourier transform spectra and **b** normalized XANES spectra at the Fe K-edge of carbon-based single-atom Fe catalyst and reference samples. **c** XPS N 1s spectra of carbon-based single-atom Fe catalysts prepared at different temperatures. **d** ^{57}Fe Mössbauer spectra of the Fe–N–C catalysts [62]

XANES spectra at the Fe K-edge of different samples are shown in Fig. 5b. A similar pre-edge peak at 7117 eV appears in the Fe–N–C catalysts and reference sample of FePc, indicating that the Fe–N–C materials contain a similar $\text{Fe}-\text{N}_4$ planar structure. Because of the small binding energy difference between pyridinic- and metal-N binding, XPS is used to qualitatively or semi-quantitatively evaluate the content of single metal atoms [64, 65]. Figure 5c shows the N 1s peak of the Fe–N–C catalysts. The pyridinic N content follows the order $\text{Fe}-\text{N}-\text{C}-600 > \text{Fe}-\text{N}-\text{C}-700 > \text{Fe}-\text{N}-\text{C}-800$, in good agreement with EXAFS results.

Mössbauer spectroscopy is a powerful technique for discriminating different Fe species in Fe-based catalysts [66–68]. As shown in Fig. 5d, the spectra of Fe–N–C–600 and Fe–N–C–700 can be fitted well with three doublets with the absence of a sextet and singlet (Fe_xC). By contrast, sextet and singlet signals exist in Fe–N–C–800. This result is consistent with EXAFS and XPS results.

4 Applications of Carbon-Based Single-Atom Metal Catalysts in Electrocatalysis

Compared to carbon-supported metal nanoparticle catalysts, carbon-hosted single-atom metal catalysts have remarkable advantages, including unsaturated configuration, maximal atomic utilization, well-defined coordination structure, and unique interaction between metal atoms and supports. These features lead to higher catalytic activity, selectivity, and durability in electrocatalytic reactions. Dispersive and isolated metal atoms anchored on conductive carbon supports are known as active centers in single-atom electrocatalysts. Different types of metal centers possess different electronic structures and, therefore, different catalytic activity in certain reactions. In addition, the coordination sites such as C, N, O, and S to metal atoms play a significant role in determining the electrocatalytic performance of single-atom metal catalysts.

4.1 Oxygen Reduction Reaction

The ORR is usually described as a process in which an oxygen molecule reacts with the protons (acidic media)/water (alkaline media) and electrons to form $\text{H}_2\text{O}/\text{OH}^-$ through a highly efficient four-electron pathway or a less efficient two-electron pathway involving the formation of $\text{H}_2\text{O}_2/\text{HO}_2^-$. Many electrochemical energy devices including proton exchange membrane fuel cells (acidic media), anion exchange membrane fuel cells (alkaline media), and Zn/Mg/Al-air batteries (alkaline media) involve the cathodic ORR. Since ORR kinetics is extremely sluggish, especially in acidic conditions, highly efficient electrocatalysts are needed to overcome this issue. Commercial Pt nanoparticles supported on carbon black are universally acknowledged as the best ORR catalysts, but they suffer from high cost and poor durability and selectivity. Therefore, the development of more advanced catalysts at low cost is critical for promoting these technologies.

The development of single-atom noble metals hosted on carbons is an effective strategy, providing maximized metal utilization, and unsaturated and uniform coordination environments. Liu et al. reported an N-doped carbon black-supported single-atom Pt catalyst (Pt1-N/BP) with Pt loading of 0.4 wt% [52]. Compared to a pure carbon black-supported single-atom Pt catalyst (Pt1-/BP), Pt1-N/BP showed much higher catalytic activity for the ORR, and a synergistic effect between doped-N and single Pt atoms was suggested for the enhanced ORR activity. When used in fuel cells, Pt1-N/BP demonstrated remarkable Pt utilization of $0.13 \text{ g}_{\text{Pt}} \text{ kW}^{-1}$, higher than that of a commercial Pt/C catalyst ($0.29 \text{ g}_{\text{Pt}} \text{ kW}^{-1}$). DFT calculations indicate that the single pyridinic N-anchored single-atom Pt centers are the main active sites. Zhang et al. synthesized single-atom niobium anchored in a carbon (atomic niobium carbide) catalyst through an arc-discharge method [31]. Experimental results coupled with theory calculations revealed that the single niobium atoms incorporated within the graphitic layers resulted in a redistribution of *d*-band electrons and became surprisingly reactive for O_2 adsorption and dissociation.

In addition to noble-metal catalysts, heteroatom-doped carbons [69–71], carbon-supported noble-metal-free nanoparticles [72, 73], and N-coordinated noble-metal-free atoms on carbons (M–N–C) [74, 75] have attracted great interest as ORR catalysts in fuel cells and metal-air batteries due to abundant sources of their precursors, easy preparation, and good ORR performance. Among these materials, N-doped carbon-anchored single M (M–N–C, M=Fe/Co) atoms showed the best ORR catalytic activity [76]. Current approaches to synthesizing M–N–C catalysts generally involve the pyrolysis of precursors containing C, N, and metal sources, in which metal nanoparticles are produced simultaneously. The ORR activity of these metal nanoparticles is much poorer than those of single-atom counterparts, leading to unsatisfactory ORR performance in the final catalysts. Recent works have focused extensively on optimizing carbon-supported single-atom Fe/Co catalysts. For example, Yin et al. reported that single-atom Co catalysts prepared by directly pyrolyzing bimetallic MOFs showed much better ORR performance than commercial Pt/C catalysts in alkaline conditions [63]. Sa et al. put forward a silica-protective-layer-assisted approach for preparation of single-atom Fe catalysts exhibiting ORR performance comparable to that of Pt/C in alkaline conditions, but the power density of the anion exchange membrane fuel cell was still poorer than that of Pt/C [49]. Compared to alkaline conditions, the development of low-cost electrocatalysts for ORR in acidic media is more cost-effective. Li et al. proposed a simple and scalable atomic isolation strategy for synthesizing single-atom Fe catalysts [77]. As shown in Fig. 6a, Zn acted as “inert” atoms to spatially isolate Fe, preferentially generating highly active single-atom Fe ($\text{Fe}-\text{N}_x$) sites while suppressing the formation of large Fe-based particles. Aberration-corrected TEM characterization results demonstrated that the final single-atom Fe catalyst had a density of $\sim 30 \pm 3$ atoms per 100 nm^2 (Fig. 6b), which is six times that of the traditional Fe–N–C catalyst. As a result, the single-atom Fe catalyst showed outstanding ORR performance comparable to commercial Pt/C catalysts in acidic media (Fig. 6c). After the ORR test, the density of single Fe atoms remained nearly unchanged, as revealed by aberration-corrected TEM characterization. This result provides direct evidence of the good stability of single-atom Fe catalysts. In addition, the method is quite versatile, as atomic Fe sites can be anchored on many different supports, and many compounds (LiCl, NaCl, KCl, etc.) can act as atom-isolating agents [77].

It is important to note that many strategies have been proposed for the preparation of single-atom Fe/Co catalysts, but significant differences in performance have been found among these methods based on rotating disk electrode (RDE) testing. For the materials themselves, they may possess different microstructures and chemical environments surrounding single metal atoms, resulting in completely different ORR performance. In addition, catalyst loading has a considerable impact on ORR performance—for example, higher loading usually leads to better RDE data [20]. However, excessively high loading in fuel cells can result in undesirable output power owing to poor mass transport [78]. Thus, a uniform standard is needed to evaluate ORR performance with the RDE technique and even fuel cells.

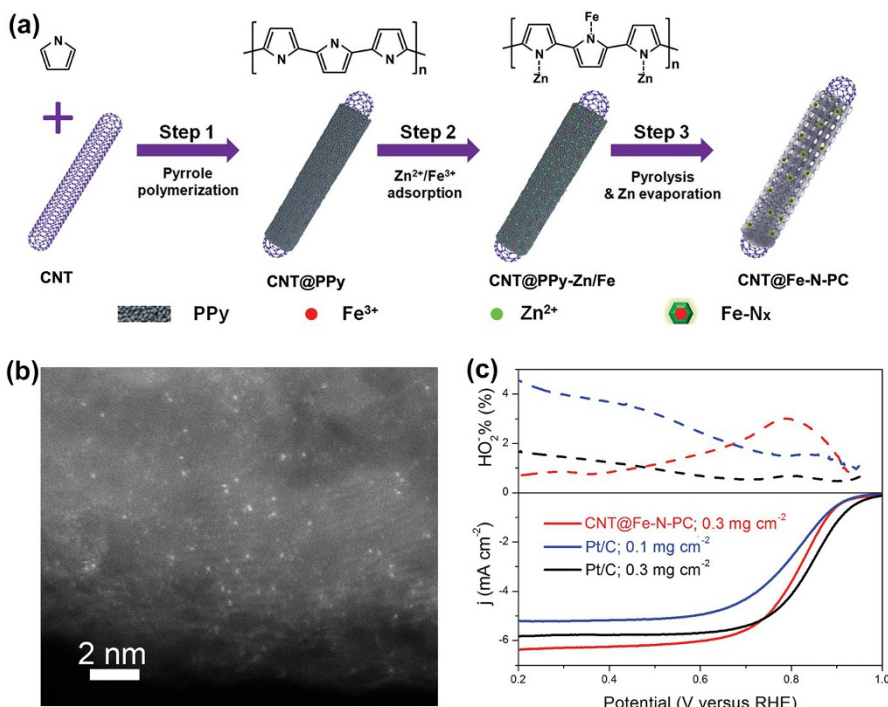


Fig. 6 **a** Schematic showing the preparation of N-doped CNT-based single-atom Fe catalyst. **b** HAADF-STEM image of CNT-based single-atom Fe catalyst. **c** ORR polarization curves of CNT-based single-atom Fe catalyst and reference samples in acidic media [77]

4.2 Water Splitting

Electrochemical water splitting, including HER at the cathode and OER at the anode, has attracted attention for hydrogen generation. To reduce the accompanying energy consumption, water electrolysis is usually carried out in either acidic or alkaline conditions [79, 80]. The efficiency of HER in acidic conditions is higher than that in alkaline conditions [81]. Intensive research has focused mainly on acidic HER catalysts [82–84]. The development of OER catalysts in acidic conditions has been relatively slow, because metal compounds are generally not stable under these harsh conditions, with the exception of noble Ir/Ru-based materials [81, 85], although great progress has been made in OER under alkaline conditions [86, 87]. To date, Pt/Pt–Ru have been found to be the best HER catalysts in both acidic and alkaline conditions, while Ir/Ru are the best OER catalysts in acidic media.

Like ORR, development of single-atom metal supported on carbons is an effective strategy for replacing nanosized noble metals for water splitting. Cheng et al. reported that single-atom Pt supported on N-doped graphene prepared by ALD showed significantly enhanced HER catalytic activity (up to 37 times) and high

stability in comparison with the state-of-the-art commercial Pt/C catalysts [34]. Liang et al. synthesized a novel type of catalyst using single cobalt atoms coordinated with N-doped carbon (CoN_x/C) by the pyrolysis of Co-N_4 macrocycles or Co/o-phenylenediamine composites and using silica colloids as a hard template [88]. Owing to well-dispersed molecular CoN_x active sites on the carbon support, the CoN_x/C materials showed excellent HER performance in both acidic (Fig. 7a) and alkaline (Fig. 7b) conditions, higher than those reported for other scalable non-precious metal HER catalysts. Dou et al. prepared atomic-scale CoO_x species in MOFs with even better OER activity than RuO_2 by O_2 plasma to activate the Co ions in MOFs [89]. Recently, Fei et al. proposed MN_4C_4 moieties as efficient OER catalysts, with activity following the trend $\text{Ni} > \text{Co} > \text{Fe}$ (Fig. 7c) [28]. DFT calculations showed that the OER catalytic mechanism of MN_4C_4 moieties depended strongly on the number of d electrons (N_d) of the metal in MN_4C_4 moieties. For Fe ($N_d=6$) and Co ($N_d=7$), all intermediates (OH^* , O^* and OOH^*) bind more strongly at the M site than the C site, and therefore the reaction proceeds through the single-site mechanism (Fig. 7d). However, for Ni ($N_d=8$), O^* and OH^* prefer to reside at the C site, while OOH^* is favorably adsorbed on the Ni atom; thus the reaction pathway involves a dual-site mechanism (Fig. 7e).

4.3 Other Electrochemical Reactions

Recent reports have emerged of energy reactions including H_2O_2 production, CO_2 reduction, and N_2 reduction, which have attracted much attention [4–7]. Since single-atom metal catalysts possess unique features of high activity and selectivity as well as good stability compared to bulk counterparts, researchers have initiated investigations of single-atom metal catalysts for these electrochemical reactions.

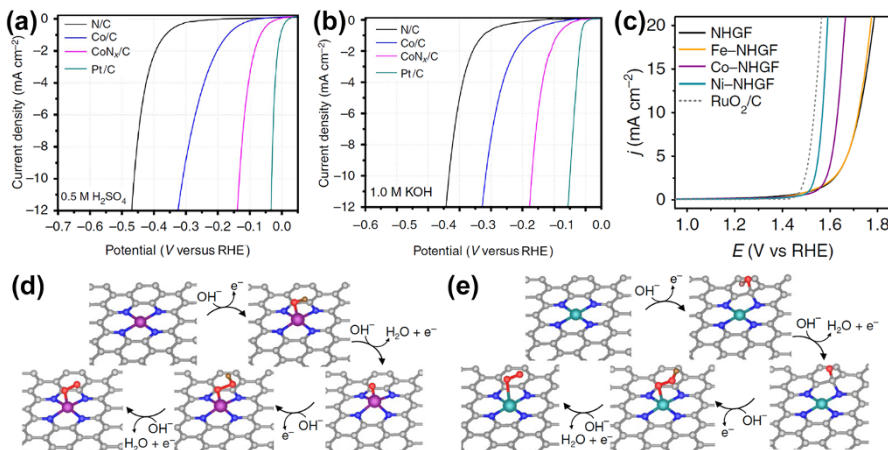


Fig. 7 HER polarization curves of N-doped carbon-based single-atom Co catalyst and reference samples in **a** acidic and **b** alkaline conditions [88]. **C** OER polarization curves of N-doped graphene-based single-atom Fe, Co, Ni catalysts and reference samples. The proposed reaction pathways of **d** single-site and **e** dual-site mechanisms for the OER [28]

For example, S-doped zeolite-templated carbon-supported single-atom Pt catalysts, containing relatively high Pt loading of 5 wt%, did not follow a conventional four-electron pathway producing water, but selectively produced H₂O₂ (Fig. 8a, b) [21]. Furthermore, it was found that high sulfur content (17 wt%) was beneficial for H₂O₂ yield, which indicates that the coordination environment has a significant impact on the selectivity of single-atom metal catalysts.

Back et al. used DFT calculations to study single transition metal atoms (Ag, Au, Co, Cu, Fe, Ir, Ni, Os, Pd, Pt, Rh, or Ru) anchored on defective graphene with single or double vacancies as catalysts for CO₂ reduction [90]. As shown in Fig. 8c, most single-atom metal catalysts were found to be highly selective for the CO₂ reduction over the competitive HER due to favorable adsorption of carboxyl (*COOH) or formate (*OCHO) over hydrogen (*H) on single-atom metal active sites. Subsequent experimental results demonstrated that single-atom Fe/Co/Ni catalysts indeed have high selectivity for CO₂ reduction [91–93]. Figure 8d shows that pristine N-doped graphene (N-G) possesses negligible CO₂ reduction activity. When it was decorated with metallic Ni nanoparticles, the obtained catalyst (Ni-NG) showed improved

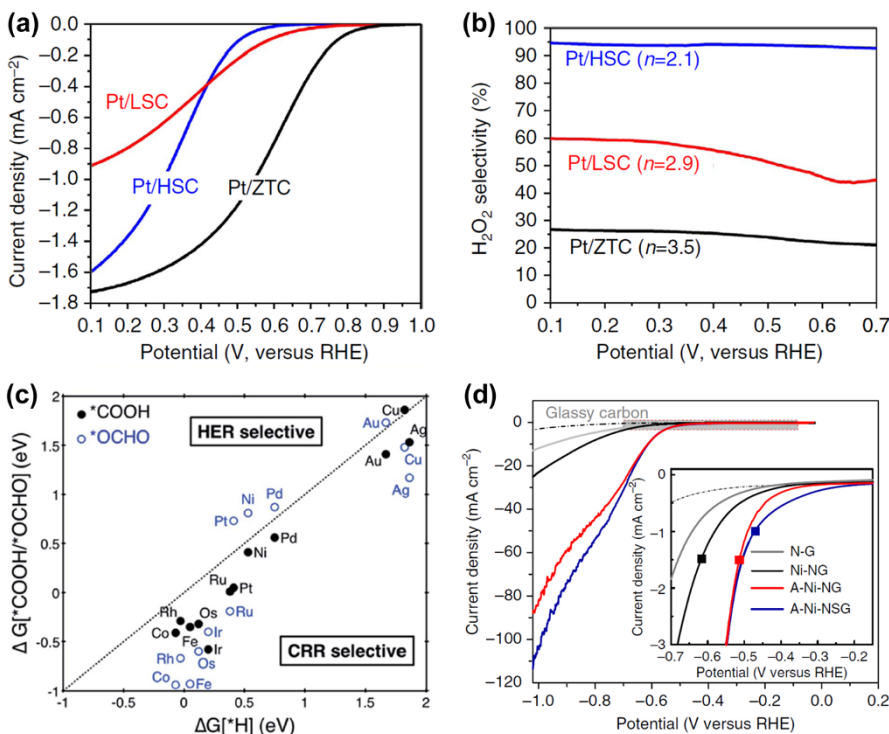


Fig. 8 **a** ORR polarization curves of S-doped carbon-based single-atom Pt catalysts and reference samples. **b** Corresponding H₂O₂ production estimated by RRDE experiments [21]. **c** Free energy change of the first protonation step in the CO₂ reduction reaction and HER on various graphene-based single-atom metal catalysts [90]. **d** CO₂ reduction reaction curves of N, S-doped graphene-based single-atom Ni catalyst and reference samples acquired in CO₂-saturated 0.5 M KHCO₃ solution [91]

activity and selectivity for CO₂ reduction. Further reducing the size of the Ni particles to single atoms in A–Ni–NG and A–Ni–NSG provided catalysts with markedly improved performance. These results suggest that the outlook is good for the use of single-atom metal catalysts in CO₂ reduction.

E lectrocatalytic N₂ reduction is still in its early stage. Like CO₂ reduction, the competing HER greatly reduces the faradaic efficiency of the N₂ reduction because the standard HER potential is comparable to that of the N₂ reduction. Recently, an atomically dispersed Au catalyst was prepared to catalyze the N₂ reduction, and its NH⁴⁺ yield rate was found to be 22.5 times that of the nanosized counterpart [94]. Conversely, doping Fe into the N-doped carbon facilitates the strong competitor of the HER to the N₂ reduction, resulting in a negative effect on ammonia products [95]. This result suggests that not all single-atom metal catalysts are good for N₂ reduction. Many scientific issues remain to be explored. In other words, there is huge room for growth in developing single-atom metal catalysts for N₂ reduction.

5 Summary and Perspectives

Dispersive single-atom metals hosted on carbon structures have shown fascinating activity for many electrochemical reactions owing to their unique characteristics of low coordination number, uniform coordination environment, and maximum atomic utilization. Here, we summarized the synthesis strategies, characterization methods, and electrocatalytic applications for carbon-based single-atom metal catalysts. Table 1 shows a summary of typical carbon-based single-atom metal catalysts, including preparation methods, coordination sites, metal centers, and electrochemical applications. Nitrogen is the most common coordination site for anchoring metal atoms. Such species coordinated with Fe atoms are as active as Pt for ORR. By contrast, Ni-doped carbon materials are generally efficient for HER and OER. Although a number of strategies, including high-vacuum deposition techniques, wet-chemical routes, and high-temperature pyrolysis, have been used for the preparation of carbon-based single-atom metal catalysts, the catalysts produced usually contain very limited metal loading. Compared to other methods, high-temperature pyrolysis, especially for the synthesis of non-noble metal catalysts, can offer greater reliability and cost-effectiveness because it involves simple facilities. The final products synthesized using this method also have robust structures and show better catalytic activity and durability. However, prevention of agglomeration of metal atoms is still a great challenge in preparing catalysts with high atomic metal loading. Advanced electron microscopy and spectroscopy techniques are the basis for mechanistic investigation at the atomic level and can be complementary.

Carbon-based single-atom metal catalysts have been demonstrated to be active in some electrochemical reactions (ORR, HER, OER, H₂O₂ production, CO₂ reduction, and N₂ reduction). The catalytic activity is strongly dependent on the type of metal atoms in the catalyst and coordination environments, that is, their electronic structures. M–N_x moieties are found to be active sites for the OER following the activity trend Ni>Co>Fe, while the opposite is shown for the ORR. It is traditionally acknowledged that Pt is the best ORR catalyst, and single Pt atoms anchored

Table 1 A summary of carbon-based single-atom metal catalysts

| Coordination sites | Metal centers | Preparation methods | Electrochemical applications | References |
|--------------------|---------------|----------------------------|--|-----------------------|
| Carbon | Nb | High-vacuum deposition | ORR | [31] |
| | Ni | High-temperature pyrolysis | HER OER | [19] [96] |
| Nitrogen | Fe | High-temperature pyrolysis | ORR ORR/OER | [50] [97] |
| | | | CO ₂ reduction | [93] |
| Nitrogen | Co | Wet-chemical route | ORR | [98] |
| | | High-temperature pyrolysis | ORR ORR/OER | [63] [55] |
| | | | HER CO ₂ reduction | [29] [99] |
| | Ni | Wet-chemical route | ORR | [44] |
| | | | OER | [46] |
| | | High-temperature pyrolysis | OER HER CO ₂ reduction | [28] [100] [91] |
| Pt | Pt | High-temperature pyrolysis | ORR | [52] |
| | | High-vacuum deposition | HER | [34] |
| | | Wet-chemical route | HER | [17] |
| Ru | Ru | High-temperature pyrolysis | ORR | [26] |
| | | | – | [35] |
| Oxygen | Pd | High-vacuum deposition | – | [35] |
| Sulfur | Pt | Wet-chemical route | H ₂ O ₂ production | [21] |

on N-doped carbons indeed show much better ORR activity than commercial nano-sized counterparts. However, single Pt atoms supported on S-doped carbons follow an inefficient two-electron-transfer pathway, beneficial for H₂O₂ formation. The stability of single-atom metal catalysts is also a significant factor. Most research results have shown that carbon-based single-atom metal catalysts exhibit good stability at room temperature in liquid cells, but it is not clear whether they can meet the durability requirements in full electrochemical cells under harsher operating conditions.

Based on the above discussions, we believe that strategies for the future development of carbon-based single-atom metal catalysts for highly efficient electrocatalysis should focus mainly on (1) understanding the correlation between electronic properties and catalytic activity, and (2) increasing atomic metal loading in catalysts. The total catalytic performance of a catalyst is directly proportional to turnover frequency (TOF, evaluating the catalytic activity per active site) and concentration of active sites. The TOF of single-atom metal sites is dependent on the types of metal atoms as well as their surrounding coordination environments. The addition or removal of any heteroatoms surrounding single metal atoms can greatly alter the

electronic structures and TOFs for electrocatalysis. At this point, advanced techniques are required to understand molecular structures of single-atom metal sites. Combining experiments with theoretical simulations should help to understand the correlation between the electronic structures and catalytic activity at the atomic level. The findings of this fundamental research can provide scientific evidence for the rational design of high-performance electrocatalysts. On the other hand, creative strategies are needed for increasing the metal loading in single-atom metal catalysts. In addition, electrochemical energy devices such as fuel cells and electrolyzers should be assembled to further evaluate the reliability and practicality of carbon-based single-atom metal catalysts.

Acknowledgements This work was supported by the National Key R&D Program of China (No. 2017YFB0102900), the Research Grant Council (N_HKUST610/17) of the Hong Kong Special Administrative Region, Guangdong Special Fund for Science and Technology Development [Hong Kong Technology Cooperation Funding Scheme (201704030019 and 201704030065)].

References

1. Seh ZW, Kibsgaard J, Dickens CF, Chorkendorff I, Nørskov JK, Jaramillo TF (2017) Combining theory and experiment in electrocatalysis: insights into materials design. *Science* 355(6321):eaad4998
2. Zhu YP, Guo C, Zheng Y, Qiao S-Z (2017) Surface and interface engineering of noble-metal-free electrocatalysts for efficient energy conversion processes. *Acc Chem Res* 50(4):915–923
3. Shao M, Chang Q, Dodelet J-P, Chenitz R (2016) Recent advances in electrocatalysts for oxygen reduction reaction. *Chem Rev* 116(6):3594–3657
4. Zhu S, Jiang B, Cai W-B, Shao M (2017) Direct observation on reaction intermediates and the role of bicarbonate anions in CO₂ electrochemical reduction reaction on Cu surfaces. *J Am Chem Soc* 139(44):15664–15667
5. Yao Y, Zhu S, Wang H, Li H, Shao M (2018) A spectroscopic study on the nitrogen electrochemical reduction reaction on gold and platinum surfaces. *J Am Chem Soc* 140(4):1496–1501
6. Liu K-H, Zhong H-X, Li S-J, Duan Y-X, Shi M-M, Zhang X-B, Yan J-M, Jiang Q (2018) Advanced catalysts for sustainable hydrogen generation and storage via hydrogen evolution and carbon dioxide/nitrogen reduction reactions. *Prog Mater Sci* 92:64–111
7. Lu Z, Chen G, Siahrostami S, Chen Z, Liu K, Xie J, Liao L, Wu T, Lin D, Liu Y, Jaramillo TF, Nørskov JK, Cui Y (2018) High-efficiency oxygen reduction to hydrogen peroxide catalysed by oxidized carbon materials. *Nat Catal* 1(2):156–162
8. Yang X-F, Wang A, Qiao B, Li J, Liu J, Zhang T (2013) Single-atom catalysts: a new frontier in heterogeneous catalysis. *Acc Chem Res* 46(8):1740–1748
9. Turner M, Golovko VB, Vaughan OPH, Abdulkin P, Berenguer-Murcia A, Tikhov MS, Johnson BFG, Lambert RM (2008) Selective oxidation with dioxygen by gold nanoparticle catalysts derived from 55-atom clusters. *Nature* 454:981
10. Zhang H, Liu G, Shi L, Ye J (2018) Single-atom catalysts: emerging multifunctional materials in heterogeneous catalysis. *Adv Energy Mater* 8(1):1701343
11. Qiao B, Wang A, Yang X, Allard LF, Jiang Z, Cui Y, Liu J, Li J, Zhang T (2011) Single-atom catalysis of CO oxidation using Pt1/FeOx. *Nat Chem* 3:634
12. Chen Y, Kasama T, Huang Z, Hu P, Chen J, Liu X, Tang X (2015) Highly dense isolated metal atom catalytic sites: dynamic formation and in situ observations. *Chem Eur J* 21(48):17397–17402
13. Deng J, Li H, Xiao J, Tu Y, Deng D, Yang H, Tian H, Li J, Ren P, Bao X (2015) Triggering the electrocatalytic hydrogen evolution activity of the inert two-dimensional MoS₂ surface via single-atom metal doping. *Energy Environ Sci* 8(5):1594–1601
14. Yang S, Kim J, Tak YJ, Soon A, Lee H (2016) Single-atom catalyst of platinum supported on titanium nitride for selective electrochemical reactions. *Angew Chem Int Ed* 55(6):2058–2062

15. Zhang B, Asakura H, Zhang J, Zhang J, De S, Yan N (2016) Stabilizing a platinum1 single-atom catalyst on supported phosphomolybdic acid without compromising hydrogenation activity. *Angew Chem Int Ed* 55(29):8319–8323
16. Wang X, He T, Chen S, Ni B, Gong Y, Wu Z, Song L, Gu L, Hu W (2018) Zirconium-porphyrin based metal-organic framework hollow nanotubes for immobilization of noble metal single atoms. *Angew Chem Int Ed* 57(13):3493–3498
17. Bulushev DA, Zacharska M, Lisitsyn AS, Podyacheva OY, Hage FS, Ramasse QM, Bangert U, Bulusheva LG (2016) Single atoms of Pt-group metals stabilized by N-doped carbon nanofibers for efficient hydrogen production from formic acid. *ACS Catal* 6(6):3442–3451
18. Bulushev DA, Zacharska M, Shlyakhova EV, Chuvilin AL, Guo Y, Beloshapkin S, Okotrub AV, Bulusheva LG (2016) Single isolated Pd^{2+} cations supported on N-doped carbon as active sites for hydrogen production from formic acid decomposition. *ACS Catal* 6(2):681–691
19. Qiu HJ, Ito Y, Cong W, Tan Y, Liu P, Hirata A, Fujita T, Tang Z, Chen M (2015) Nanoporous graphene with single-atom nickel dopants: an efficient and stable catalyst for electrochemical hydrogen production. *Angew Chem Int Ed* 54(47):14031–14035
20. Li J-C, Zhao S-Y, Hou P-X, Fang R-P, Liu C, Liang J, Luan J, Shan X-Y, Cheng H-M (2015) A nitrogen-doped mesoporous carbon containing an embedded network of carbon nanotubes as a highly efficient catalyst for the oxygen reduction reaction. *Nanoscale* 7(45):19201–19206
21. Choi CH, Kim M, Kwon HC, Cho SJ, Yun S, Kim H-T, Mayrhofer KJJ, Kim H, Choi M (2016) Tuning selectivity of electrochemical reactions by atomically dispersed platinum catalyst. *Nat Commun* 7:10922
22. Li J-C, Hou P-X, Zhao S-Y, Liu C, Tang D-M, Cheng M, Zhang F, Cheng H-M (2016) A 3D bi-functional porous N-doped carbon microtube sponge electrocatalyst for oxygen reduction and oxygen evolution reactions. *Energy Environ Sci* 9(10):3079–3084
23. Li J-C, Hou P-X, Liu C (2017) Heteroatom-doped carbon nanotube and graphene-based electrocatalysts for oxygen reduction reaction. *Small* 13(45):1702002
24. Wang J, Zhang H, Wang C, Zhang Y, Wang J, Zhao H, Cheng M, Li A, Wang J (2018) Co-synthesis of atomic Fe and few-layer graphene towards superior ORR electrocatalyst. *Energy Storage Mater* 12:1–7
25. Deng D, Chen X, Yu L, Wu X, Liu Q, Liu Y, Yang H, Tian H, Hu Y, Du P, Si R, Wang J, Cui X, Li H, Xiao J, Xu T, Deng J, Yang F, Duchesne PN, Zhang P, Zhou J, Sun L, Li J, Pan X, Bao X (2015) A single iron site confined in a graphene matrix for the catalytic oxidation of benzene at room temperature. *Sci Adv* 1(11):e1500462
26. Zhang C, Sha J, Fei H, Liu M, Yazdi S, Zhang J, Zhong Q, Zou X, Zhao N, Yu H, Jiang Z, Ringe E, Yakobson BI, Dong J, Chen D, Tour JM (2017) Single-atomic ruthenium catalytic sites on nitrogen-doped graphene for oxygen reduction reaction in acidic medium. *ACS Nano* 11(7):6930–6941
27. Li J-C, Tang D-M, Hou P-X, Li G-X, Cheng M, Liu C, Cheng H-M (2018) The effect of carbon support on the oxygen reduction activity and durability of single-atom iron catalysts. *MRS Commun* 8(3):1158–1166
28. Fei H, Dong J, Feng Y, Allen CS, Wan C, Voloskiy B, Li M, Zhao Z, Wang Y, Sun H, An P, Chen W, Guo Z, Lee C, Chen D, Shakir I, Liu M, Hu T, Li Y, Kirkland AI, Duan X, Huang Y (2018) General synthesis and definitive structural identification of MN4C4 single-atom catalysts with tunable electrocatalytic activities. *Nat Catal* 1(1):63–72
29. Fei H, Dong J, Arellano-Jiménez MJ, Ye G, Dong Kim N, Samuel ELG, Peng Z, Zhu Z, Qin F, Bao J, Yacaman MJ, Ajayan PM, Chen D, Tour JM (2015) Atomic cobalt on nitrogen-doped graphene for hydrogen generation. *Nat Commun* 6:8668
30. Pan F, Zhang H, Liu K, Cullen D, More K, Wang M, Feng Z, Wang G, Wu G, Li Y (2018) Unveiling active sites of CO_2 reduction on nitrogen-coordinated and atomically dispersed iron and cobalt catalysts. *ACS Catal* 8:3116–3122
31. Zhang X, Guo J, Guan P, Liu C, Huang H, Xue F, Dong X, Pennycook SJ, Chisholm MF (2013) Catalytically active single-atom niobium in graphitic layers. *Nat Commun* 4:1924
32. Sun S, Zhang G, Gauquelain N, Chen N, Zhou J, Yang S, Chen W, Meng X, Geng D, Banis MN, Li R, Ye S, Knights S, Botton GA, Sham T-K, Sun X (2013) Single-atom catalysis using Pt/graphene achieved through atomic layer deposition. *Sci Rep* 3:1775
33. Cheng N, Sun X (2017) Single atom catalyst by atomic layer deposition technique. *Chin J Catal* 38(9):1508–1514

34. Cheng N, Stambula S, Wang D, Banis MN, Liu J, Riese A, Xiao B, Li R, Sham T-K, Liu L-M, Botton GA, Sun X (2016) Platinum single-atom and cluster catalysis of the hydrogen evolution reaction. *Nat Commun* 7:13638
35. Yan H, Cheng H, Yi H, Lin Y, Yao T, Wang C, Li J, Wei S, Lu J (2015) Single-atom Pd1/graphene catalyst achieved by atomic layer deposition: remarkable performance in selective hydrogenation of 1,3-butadiene. *J Am Chem Soc* 137(33):10484–10487
36. Lee E-K, Park S-A, Woo H, Hyun Park K, Kang DW, Lim H, Kim Y-T (2017) Platinum single atoms dispersed on carbon nanotubes as reusable catalyst for Suzuki coupling reaction. *J Catal* 352(4):388–393
37. Li X, Bi W, Zhang L, Tao S, Chu W, Zhang Q, Luo Y, Wu C, Xie Y (2016) Single-atom Pt as Co-catalyst for enhanced photocatalytic H₂ evolution. *Adv Mater* 28(12):2427–2431
38. Yoshikawa S, Shimada A (2015) Reaction mechanism of cytochrome c oxidase. *Chem Rev* 115(4):1936–1989
39. Zhang W, Lai W, Cao R (2017) Energy-related small molecule activation reactions: oxygen reduction and hydrogen and oxygen evolution reactions catalyzed by porphyrin- and corrole-based systems. *Chem Rev* 117(4):3717–3797
40. Sa YJ, Park C, Jeong HY, Park S-H, Lee Z, Kim KT, Park G-G, Joo SH (2014) Carbon nanotubes/heteroatom-doped carbon core-sheath nanostructures as highly active, metal-free oxygen reduction electrocatalysts for alkaline fuel cells. *Angew Chem Int Ed* 53(16):4102–4106
41. Gentil S, Lalaoui N, Dutta A, Nedellec Y, Cosnier S, Shaw WJ, Artero V, Le Goff A (2017) Carbon-nanotube-supported bio-inspired nickel catalyst and its integration in hybrid hydrogen/air fuel cells. *Angew Chem Int Ed* 56(7):1845–1849
42. Wang X, Wang B, Zhong J, Zhao F, Han N, Huang W, Zeng M, Fan J, Li Y (2016) Iron polyphthalocyanine sheathed multiwalled carbon nanotubes: a high-performance electrocatalyst for oxygen reduction reaction. *Nano Res* 9(5):1497–1506
43. Cao R, Thapa R, Kim H, Xu X, Gyu Kim M, Li Q, Park N, Liu M, Cho J (2013) Promotion of oxygen reduction by a bio-inspired tethered iron phthalocyanine carbon nanotube-based catalyst. *Nat Commun* 4:2076
44. Hijazi I, Bourgetteau T, Cornut R, Morozan A, Filoromo A, Leroy J, Derycke V, Jousselme B, Campidelli S (2014) Carbon nanotube-templated synthesis of covalent porphyrin network for oxygen reduction reaction. *J Am Chem Soc* 136(17):6348–6354
45. Wang J, Ge X, Liu Z, Thia L, Yan Y, Xiao W, Wang X (2017) Heterogeneous electrocatalyst with molecular cobalt ions serving as the center of active sites. *J Am Chem Soc* 139(5):1878–1884
46. Ding Y, Klyushin A, Huang X, Jones T, Teschner D, Girsdsies F, Rodenas T, Schlägl R, Heumann S (2018) Cobalt bridged with ionic liquid polymer on carbon nanotube for enhanced oxygen evolution reaction activity. *Angew Chem Int Ed* 57(13):3514–3518
47. Kwak D-H, Han S-B, Lee Y-W, Park H-S, Choi I-A, Ma K-B, Kim M-C, Kim S-J, Kim D-H, Sohn J-I, Park K-W (2017) Fe/N/S-doped mesoporous carbon nanostructures as electrocatalysts for oxygen reduction reaction in acid medium. *Appl Catal B* 203:889–898
48. Hu K, Tao L, Liu D, Huo J, Wang S (2016) Sulfur-doped Fe/N/C nanosheets as highly efficient electrocatalysts for oxygen reduction reaction. *ACS Appl Mater Interfaces* 8(30):19379–19385
49. Sa YJ, Seo D-J, Woo J, Lim JT, Cheon JY, Yang SY, Lee JM, Kang D, Shin TJ, Shin HS, Jeong HY, Kim CS, Kim MG, Kim T-Y, Joo SH (2016) A general approach to preferential formation of active Fe-Nx sites in Fe–N/C electrocatalysts for efficient oxygen reduction reaction. *J Am Chem Soc* 138(45):15046–15056
50. Zhang H, Hwang S, Wang M, Feng Z, Karakalos S, Luo L, Qiao Z, Xie X, Wang C, Su D, Shao Y, Wu G (2017) Single atomic iron catalysts for oxygen reduction in acidic media: particle size control and thermal activation. *J Am Chem Soc* 139(40):14143–14149
51. Wang XX, Cullen DA, Pan Y-T, Hwang S, Wang M, Feng Z, Wang J, Engelhard MH, Zhang H, He Y, Shao Y, Su D, More KL, Spendelow JS, Wu G (2018) Nitrogen-coordinated single cobalt atom catalysts for oxygen reduction in proton exchange membrane fuel cells. *Adv Mater* 30(11):1706758
52. Liu J, Jiao M, Lu L, Barkholtz HM, Li Y, Wang Y, Jiang L, Wu Z, D-j Liu, Zhuang L, Ma C, Zeng J, Zhang B, Su D, Song P, Xing W, Xu W, Wang Y, Jiang Z, Sun G (2017) High performance platinum single atom electrocatalyst for oxygen reduction reaction. *Nat Commun* 8:15938
53. Wang X, Chen W, Zhang L, Yao T, Liu W, Lin Y, Ju H, Dong J, Zheng L, Yan W, Zheng X, Li Z, Wang X, Yang J, He D, Wang Y, Deng Z, Wu Y, Li Y (2017) Uncoordinated amine groups of metal-organic frameworks to anchor single Ru sites as chemoselective catalysts toward the hydrogenation of quinoline. *J Am Chem Soc* 139(28):9419–9422

54. Liu Q, Liu X, Zheng L, Shui J (2018) The solid-phase synthesis of an Fe–N–C electrocatalyst for high-power proton-exchange membrane fuel cells. *Angew Chem Int Ed* 57(5):1204–1208
55. Zheng Y, Jiao Y, Zhu Y, Cai Q, Vasileff A, Li LH, Han Y, Chen Y, Qiao S-Z (2017) Molecule-level g-C₃N₄ coordinated transition metals as a new class of electrocatalysts for oxygen electrode reactions. *J Am Chem Soc* 139(9):3336–3339
56. Song P, Luo M, Liu X, Xing W, Xu W, Jiang Z, Gu L (2017) Zn single atom catalyst for highly efficient oxygen reduction reaction. *Adv Funct Mater* 27(28):1700802
57. Wu H, Li H, Zhao X, Liu Q, Wang J, Xiao J, Xie S, Si R, Yang F, Miao S, Guo X, Wang G, Bao X (2016) Highly doped and exposed Cu(I)-N active sites within graphene towards efficient oxygen reduction for zinc-air batteries. *Energy Environ Sci* 9(12):3736–3745
58. Krivanek OL, Chisholm MF, Nicolosi V, Pennycook TJ, Corbin GJ, Dellby N, Murfitt MF, Own CS, Szilagyi ZS, Oxley MP, Pantelides ST, Pennycook SJ (2010) Atom-by-atom structural and chemical analysis by annular dark-field electron microscopy. *Nature* 464:571
59. Leapman RD (2003) Detecting single atoms of calcium and iron in biological structures by electron energy-loss spectrum-imaging. *J Microsc* 210(1):5–15
60. Lovejoy TC, Ramasse QM, Falke M, Kaeppel A, Terborg R, Zan R, Dellby N, Krivanek OL (2012) Single atom identification by energy dispersive X-ray spectroscopy. *Appl Phys Lett* 100(15):154101
61. Suenaga K, Izumi Y, Okazaki T (2011) Single atom spectroscopy with reduced delocalization effect using a 30 kV-STEM. *Eur Phys J Appl Phys* 54(3):33508
62. Liu W, Zhang L, Liu X, Liu X, Yang X, Miao S, Wang W, Wang A, Zhang T (2017) Discriminating catalytically active FeNx species of atomically dispersed Fe–N–C catalyst for selective oxidation of the C–H bond. *J Am Chem Soc* 139(31):10790–10798
63. Yin P, Yao T, Wu Y, Zheng L, Lin Y, Liu W, Ju H, Zhu J, Hong X, Deng Z, Zhou G, Wei S, Li Y (2016) Single cobalt atoms with precise N-coordination as superior oxygen reduction reaction catalysts. *Angew Chem Int Ed* 55(36):10800–10805
64. Liang H-W, Wei W, Wu Z-S, Feng X, Müllen K (2013) Mesoporous metal–nitrogen-doped carbon electrocatalysts for highly efficient oxygen reduction reaction. *J Am Chem Soc* 135(43):16002–16005
65. Li J-C, Hou P-X, Shi C, Zhao S-Y, Tang D-M, Cheng M, Liu C, Cheng H-M (2016) Hierarchically porous Fe–N-doped carbon nanotubes as efficient electrocatalyst for oxygen reduction. *Carbon* 109:632–639
66. Ferrandon M, Kropf AJ, Myers DJ, Artyushkova K, Kramm U, Bogdanoff P, Wu G, Johnston CM, Zelenay P (2012) Multitechnique characterization of a polyaniline–iron–carbon oxygen reduction catalyst. *J Phys Chem C* 116(30):16001–16013
67. Zitolo A, Goellner V, Armel V, Sougrati M-T, Mineva T, Stievano L, Fonda E, Jaouen F (2015) Identification of catalytic sites for oxygen reduction in iron- and nitrogen-doped graphene materials. *Nat Mater* 14(9):937–942
68. Sahraei NR, Kramm UI, Steinberg J, Zhang Y, Thomas A, Reier T, Paraknowitsch J-P, Strasser P (2015) Quantifying the density and utilization of active sites in non-precious metal oxygen electroreduction catalysts. *Nat Commun* 6:8618
69. Chai G-L, Qiu K, Qiao M, Titirici M-M, Shang C, Guo Z (2017) Active sites engineering leads to exceptional ORR and OER bifunctionality in P, N Co-doped graphene frameworks. *Energy Environ Sci* 10(5):1186–1195
70. Pei Z, Li H, Huang Y, Xue Q, Huang Y, Zhu M, Wang Z, Zhi C (2017) Texturing in situ: N, S-enriched hierarchically porous carbon as a highly active reversible oxygen electrocatalyst. *Energy Environ Sci* 10(3):742–749
71. Li J-C, Hou P-X, Cheng M, Liu C, Cheng H-M, Shao M (2018) Carbon nanotube encapsulated in nitrogen and phosphorus co-doped carbon as a bifunctional electrocatalyst for oxygen reduction and evolution reactions. *Carbon* 139:156–163
72. Hu H, Han L, Yu M, Wang Z, Lou XW (2016) Metal–organic-framework-engaged formation of Co nanoparticle-embedded carbon@Co9S8 double-shelled nanocages for efficient oxygen reduction. *Energy Environ Sci* 9(1):107–111
73. Zhou T, Du Y, Yin S, Tian X, Yang H, Wang X, Liu B, Zheng H, Qiao S, Xu R (2016) Nitrogen-doped cobalt phosphate@nanocarbon hybrids for efficient electrocatalytic oxygen reduction. *Energy Environ Sci* 9(8):2563–2570
74. Guan BY, Yu L, Lou XW (2016) A dual-metal–organic-framework derived electrocatalyst for oxygen reduction. *Energy Environ Sci* 9(10):3092–3096

75. Li J, Ghoshal S, Liang W, Sougrati M-T, Jaouen F, Halevi B, McKinney S, McCool G, Ma C, Yuan X, Ma Z-F, Mukerjee S, Jia Q (2016) Structural and mechanistic basis for the high activity of Fe-N-C catalysts toward oxygen reduction. *Energy Environ Sci* 9(7):2418–2432
76. Higgins D, Zamani P, Yu A, Chen Z (2016) The application of graphene and its composites in oxygen reduction electrocatalysis: a perspective and review of recent progress. *Energy Environ Sci* 9(2):357–390
77. Li J-C, Yang Z-Q, Tang D-M, Zhang L, Hou P-X, Zhao S-Y, Liu C, Cheng M, Li G-X, Zhang F, Cheng H-M (2018) N-doped carbon nanotubes containing a high concentration of single iron atoms for efficient oxygen reduction. *NPG Asia Mater* 10:e461
78. Sarapuu A, Kibena-Poldsepp E, Borghei M, Tammeveski K (2018) Electrocatalysis of oxygen reduction on heteroatom-doped nanocarbons and transition metal-nitrogen-carbon catalysts for alkaline membrane fuel cells. *J Mater Chem A* 6(3):776–804
79. Song J, Zhu C, Xu Bo Z, Fu S, Engelhard Mark H, Ye R, Du D, Beckman Scott P, Lin Y (2016) Bimetallic cobalt-based phosphide zeolitic imidazolate framework: CoPx phase-dependent electrical conductivity and hydrogen atom adsorption energy for efficient overall water splitting. *Adv Energy Mater* 7(2):1601555
80. Wang Y, Xie C, Zhang Z, Liu D, Chen R, Wang S (2018) In situ exfoliated, N-doped, and edge-rich ultrathin layered double hydroxides nanosheets for oxygen evolution reaction. *Adv Funct Mater* 28(4):1703363
81. Anantharaj S, Ede SR, Karthick K, Sam Sankar S, Sangeetha K, Karthik PE, Kundu S (2018) Precision and correctness in the evaluation of electrocatalytic water splitting: revisiting activity parameters with a critical assessment. *Energy Environ Sci* 11(4):744–771
82. Wu Z-Y, Hu B-C, Wu P, Liang H-W, Yu Z-L, Lin Y, Zheng Y-R, Li Z, Yu S-H (2016) Mo₂C nanoparticles embedded within bacterial cellulose-derived 3D N-doped carbon nanofiber networks for efficient hydrogen evolution. *NPG Asia Mater* 8:e288
83. Liu R, Zhang G, Cao H, Zhang S, Xie Y, Haider A, Kortz U, Chen B, Dalal NS, Zhao Y, Zhi L, Wu C-X, Yan L-K, Su Z, Keita B (2016) Enhanced proton and electron reservoir abilities of polyoxometalate grafted on graphene for high-performance hydrogen evolution. *Energy Environ Sci* 9(3):1012–1023
84. Liu W, Cui Y, Du X, Zhang Z, Chao Z, Deng Y (2016) High efficiency hydrogen evolution from native biomass electrolysis. *Energy Environ Sci* 9(5):467–472
85. Shi Q, Zhu C, Du D, Wang J, Xia H, Engelhard MH, Feng S, Lin Y (2018) Ultrathin dendritic IrTe nanotubes for an efficient oxygen evolution reaction in a wide pH range. *J Mater Chem A* 6(19):8855–8859
86. Cui X, Ren P, Deng D, Deng J, Bao X (2016) Single layer graphene encapsulating non-precious metals as high-performance electrocatalysts for water oxidation. *Energy Environ Sci* 9(1):123–129
87. Detzi E, Cook JB, Lesel BK, Turner CL, Liang Y-L, Robbenolt S, Tolbert SH (2016) Mesoporous Ni₆₀Fe₃₀Mn₁₀-alloy based metal/metal oxide composite thick films as highly active and robust oxygen evolution catalysts. *Energy Environ Sci* 9(2):540–549
88. Liang H-W, Bruller S, Dong R, Zhang J, Feng X, Mullen K (2015) Molecular metal-Nx centres in porous carbon for electrocatalytic hydrogen evolution. *Nat Commun* 6:7992
89. Dou S, Dong C-L, Hu Z, Huang Y-C, J-I Chen, Tao L, Yan D, Chen D, Shen S, Chou S, Wang S (2017) Atomic-scale CoOx species in metal-organic frameworks for oxygen evolution reaction. *Adv Funct Mater* 27(36):1702546
90. Back S, Lim J, Kim N-Y, Kim Y-H, Jung Y (2017) Single-atom catalysts for CO₂ electroreduction with significant activity and selectivity improvements. *Chem Sci* 8(2):1090–1096
91. Yang HB, Hung S-F, Liu S, Yuan K, Miao S, Zhang L, Huang X, Wang H-Y, Cai W, Chen R, Gao J, Yang X, Chen W, Huang Y, Chen HM, Li CM, Zhang T, Liu B (2018) Atomically dispersed Ni(I) as the active site for electrochemical CO₂ reduction. *Nat Energy* 3(2):140–147
92. Bi W, Li X, You R, Chen M, Yuan R, Huang W, Wu X, Chu W, Wu C, Xie Y (2018) Surface immobilization of transition metal ions on nitrogen-doped graphene realizing high-efficient and selective CO₂ reduction. *Adv Mater* 30(18):1706617
93. Pan F, Zhang H, Liu K, Cullen D, More K, Wang M, Feng Z, Wang G, Wu G, Li Y (2018) Unveiling active sites of CO₂ reduction on nitrogen-coordinated and atomically dispersed iron and cobalt catalysts. *ACS Catal* 8(4):3116–3122
94. Wang X, Wang W, Qiao M, Wu G, Chen W, Yuan T, Xu Q, Chen M, Zhang Y, Wang X, Wang J, Ge J, Hong X, Li Y, Wu Y, Li Y (2018) Atomically dispersed Au1 catalyst towards efficient electrochemical synthesis of ammonia. *Sci Bull* 63(19):1246–1253

95. Mukherjee S, Cullen DA, Karakalos S, Liu K, Zhang H, Zhao S, Xu H, More KL, Wang G, Wu G (2018) Metal-organic framework-derived nitrogen-doped highly disordered carbon for electrochemical ammonia synthesis using N₂ and H₂O in alkaline electrolytes. *Nano Energy* 48:217–226
96. Zhang L, Jia Y, Gao G, Yan X, Chen N, Chen J, Soo MT, Wood B, Yang D, Du A, Yao X (2018) Graphene defects trap atomic ni species for hydrogen and oxygen evolution reactions. *Chem* 4(2):285–297
97. Chen P, Zhou T, Xing L, Xu K, Tong Y, Xie H, Zhang L, Yan W, Chu W, Wu C, Xie Y (2017) Atomically dispersed iron-nitrogen species as electrocatalysts for bifunctional oxygen evolution and reduction reactions. *Angew Chem Int Ed* 56(2):610–614
98. Wei P-J, Yu G-Q, Naruta Y, Liu J-G (2014) Covalent grafting of carbon nanotubes with a biomimetic heme model compound to enhance oxygen reduction reactions. *Angew Chem Int Ed* 53(26):6659–6663
99. Pan Y, Lin R, Chen Y, Liu S, Zhu W, Cao X, Chen W, Wu K, Cheong W-C, Wang Y, Zheng L, Luo J, Lin Y, Liu Y, Liu C, Li J, Lu Q, Chen X, Wang D, Peng Q, Chen C, Li Y (2018) Design of single-atom Co–N₅ catalytic site: a robust electrocatalyst for CO₂ reduction with nearly 100% CO selectivity and remarkable stability. *J Am Chem Soc* 140(12):4218–4221
100. Fan L, Liu PF, Yan X, Gu L, Yang ZZ, Yang HG, Qiu S, Yao X (2016) Atomically isolated nickel species anchored on graphitized carbon for efficient hydrogen evolution electrocatalysis. *Nat Commun* 7:10667

Publisher's Note Springer Nature remains neutral with regard to jurisdictional claims in published maps and institutional affiliations.



REVIEW

Electrometabolic Pathways: Recent Developments in Bioelectrocatalytic Cascades

David P. Hickey¹ · Erin M. Gaffney¹ · Shelley D. Minteer¹

Received: 1 September 2018 / Accepted: 25 October 2018 / Published online: 3 November 2018
© Springer Nature Switzerland AG 2018

Abstract

In biological systems, the majority of chemistry occurs in enzymatic pathways. Pathways are essentially cascades of protein catalysts used for catabolism or metabolism. However, in cellular-free systems, catalytic cascades have been rarely studied until recently. This review will introduce the lessons that can be learned from *in vivo* enzymatic pathways and novel enzymatic pathways that have been developed for synthetic biology of electrochemical energy production and conversion. This review will also discuss the recent bio-inspired developments to utilize catalytic cascades for non-biological applications ranging from energy conversion to biosensing and the electrochemical production of important chemicals such as methanol from carbon dioxide and ammonia from agricultural waste runoff.

Keywords Bioelectrocatalysis · Enzymes · Mediated electron transfer · Catalytic cascades · Electrocatalysis

1 Enzyme-Based Catalytic Cascades

Metabolic and catabolic pathways comprise the energetic engine to convert and distribute chemical energy in living cells. These pathways are enzymatic cascades that catalyze sequential reactions for chemical energy conversion. Saccharides are the primary fuel source for eukaryotic metabolism, where they can be utilized to generate cellular energy while simultaneously acting as precursor carbon sources in many biosynthetic pathways. Metabolism of saccharides *in vivo* occurs via glycolysis and the pentose phosphate pathways resulting in the formation of pyruvate, which subsequently undergoes pyruvate metabolism via the Kreb's cycle.

Chapter 6 was originally published as Hickey, D. P., Gaffney, E. M. & Minteer, S. D. Topics in Current Chemistry (2018) 376: 43. <https://doi.org/10.1007/s41061-018-0221-4>.

✉ Shelley D. Minteer
minteer@chem.utah.edu

¹ Departments of Chemistry and Materials Science and Engineering, University of Utah, 315 S 1400 E Rm 2020, Salt Lake City, UT 84112, USA

Saccharides boast high theoretical energy densities that are extracted *in vivo* by a series of enzymes that catalyze the oxidation of sugars to CO₂ while utilizing ATP as a means of exchanging chemical energy. Such high energy densities make saccharides and other biologically derived metabolic intermediates attractive fuel sources for electrical energy generation. However, the full utilization of these biofuels requires multiple sequential oxidative steps to extract all of the electrons from a single molecule of fuel. While cellular metabolism offers a roadmap of possible reaction pathways for the complete oxidation of biofuels, methods to convert ATP hydrolysis to electrical energy remain in their infancy [1, 2]. Consequently, alternative catalysts must be selected to convert chemical bonds into electrons at each step of the metabolic pathway in the form of electrochemical oxidation.

This review aims to provide an overview of recent developments in research to utilize enzymatically inspired catalytic cascades in the context of electrochemical energy conversion. Of particular interest is work to bias the advantages that catalytic cascades afford with respect to overcoming diffusional and kinetic limitations that arise when multiple catalysts are used to maximize the depth of substrate oxidation. While many of the electrocatalytic oxidation cascades described herein are direct electrochemical adaptations of a natural metabolic pathway, we will also provide an update on recent work being done to design artificial electrocatalytic oxidation pathways, herein referred to as electrometabolic pathways. This term is meant to describe a newly emerging field of artificial cascades, which can consist of (1) native metabolic pathways, in which one or more enzyme is replaced with an electrochemically interfaced enzyme or non-enzymatic electrocatalyst, (2) sequential non-natural electrochemical oxidation reactions in which more than one electrocatalyst (enzymatic or otherwise) is employed, or (3) native metabolic pathways, in which one or more pairs of sequential enzymes has/have been modified (translationally, post-translationally, or synthetically) to manipulate spatial orientation of corresponding enzymes.

Biofuels, broadly speaking, contain a diverse array of chemical functionalities, and therefore their complete electrochemical oxidation offers a unique challenge. Specifically, there has been a growing effort to design molecular architectures containing promiscuous electrocatalysts capable of deep biofuel oxidation [3–8]. The earliest attempts to facilitate multiple electrocatalytic oxidations for energy conversion were in the context of a direct methanol fuel cell [9]. Direct liquid fuel cells (DLFCs) employ transition metals (usually Pt and Pt alloys) to electrochemically reduce O₂ to water at the cathode while oxidizing a carbon-based fuel to CO₂ at the anode. While research into DLFCs remains active, these electrocatalytic reactions tend to exhibit relatively low efficiencies, and rely on a single catalyst for multiple reactions [10–13]. As the focus of the current review is aimed at the simultaneous utilization of multiple electrocatalysts for cascade reactions, DLFCs are outside the scope of this work. However, several reviews exist on recent research and advancements in DLFC technologies [11]. In contrast to the heterogeneous transition metal electrocatalysts found in DLFCs, enzymes operate under mild conditions at ambient temperatures and near neutral pH. It is this ubiquitous reaction environment that enables combinations of redox enzymes

to be implemented simultaneously, and thus making metabolic enzymes ideal as a platform around which to design oxidative cascades.

2 Enzymatic Cascades for Electrometabolic (Oligo)Saccharide Oxidation Pathways

The majority of metabolic enzymes responsible for oxidation steps are dehydrogenase enzymes that utilize nicotinamide adenine dinucleotide (NAD^+) as a dissociable cofactor for oxidation. In what has become a common strategy for electrochemically interfacing enzymatic cascades, an enzyme, diaphorase, is added with an electrochemical mediator, such as viologen, to electrochemically regenerate NAD^+ from NADH (Fig. 1). This strategy was first employed by Palmore et al., where a three-enzyme cascade consisting of NAD^+ -dependent alcohol, aldehyde, and formate dehydrogenase (ADH, ALDH, and FDH, respectively) was used to catalyze the complete oxidation of methanol to CO_2 with an electrochemical diaphorase/methyl viologen mechanism for regenerating NAD^+ [14].

The use of multi-enzyme electrodes for cascade oxidations has subsequently expanded greatly, where additional specialized enzymes have been included to enable the complete oxidation of more complex fuels. Of particular interest has been the development of electroenzymatic pathways based on glycolytic metabolism. An extension of this approach demonstrated the possibility of immobilizing all nine enzymes (five dehydrogenases and four kinases) of the Kreb's cycle at a single bioanode to electrochemically oxidize pyruvate to CO_2 [15]. In this case, poly(methylene green) was used as an electrocatalyst to regenerate NAD^+ , while guanosine-5'-diphosphate (GDP) and phosphate were added to activate succinyl-CoA synthetase. Minteer and coworkers demonstrated that incremental increases in power output of a biofuel cell could be achieved with the addition of each sequential dehydrogenase of the citric acid cycle, then a large increase in power output was observed upon inclusion of malate dehydrogenase (completing the Kreb's cycle and minimizing the build up of inhibitory intermediates) (Fig. 2). This method illustrates a trend in native pathways where increased depth of substrate oxidation requires additional oxidoreductases.

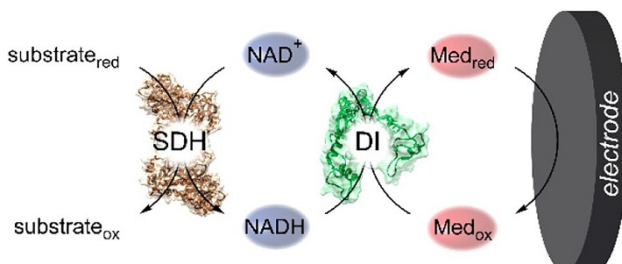


Fig. 1 Scheme depicting the electrochemically mediated regeneration of NAD^+ catalyzed by diaphorase (DI)

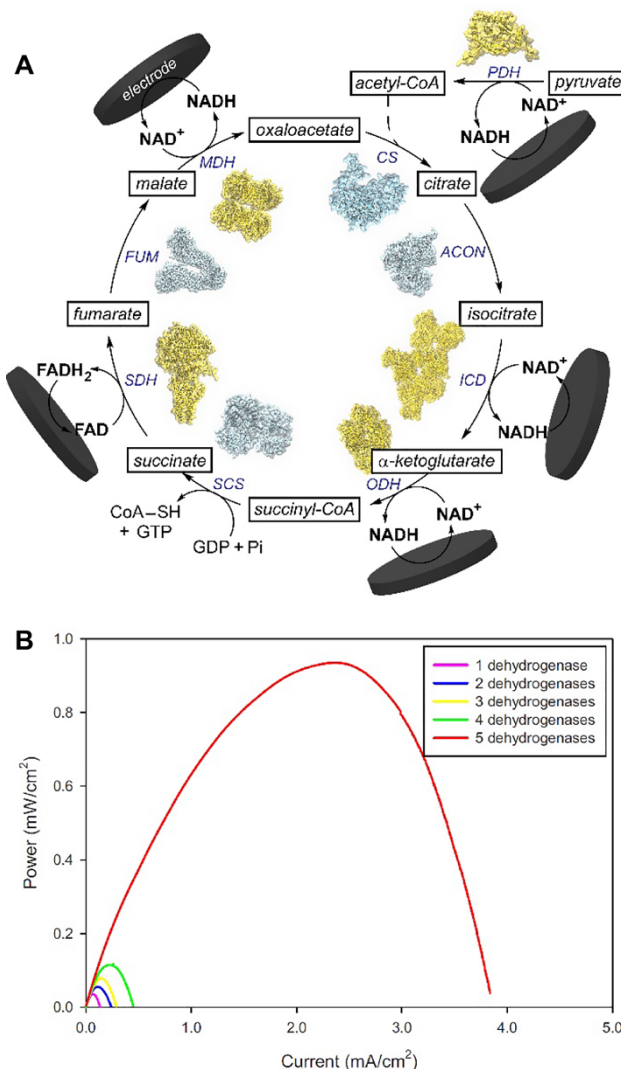


Fig. 2 Schematic overview **a** of the electrochemical adaptation of the Krebs cycle described by Minteer, in which NAD⁺ and flavin adenine dinucleotide (FAD) were regenerated electrochemically via poly(methylene green), and **b** the corresponding power curves generated from bioanodes composed of 1, 2, 3, 4, or 5 (all) dehydrogenase enzymes of the Krebs cycle. The plot shown in **b** was reproduced from [15]

An alternative approach to expanding the number of electrochemically interfaced enzymes (i.e. dehydrogenases) has been to employ secondary and tertiary isomerase- and transferase-based cycles to utilize oxidized fragments for regenerating the parent biofuel. Zhang and coworkers designed an electrometabolic pathway constructed from a series of four codependent enzyme cascades to electrochemically oxidize complex (oligo)saccharides to CO₂ [16–18]. All four cascade sequences were comprised of

combinations of recombinant thermostable enzymes and employed an electrochemically mediated diaphorase system to regenerate NAD⁺ and extract electrons from the sugar mixtures. The first cascade sequence converts complex (poly)saccharides to glucose-6-phosphate via sucrose phosphorylase (SP), xylose isomerase (XI), polyphosphate glucokinase (PPGK), and phosphoglucomutase (PGM) [17, 18]. Both variants of this sequence require inorganic polyphosphate. The second cascade sequence consists of glucose-6-phosphate dehydrogenase (G6PDH) and 6-phosphogluconate dehydrogenase (6PGDH) to sequentially oxidize glucose-6-phosphate and 6-phosphogluconate while cleaving CO₂ from the latter, ultimately producing ribulose-5-phosphate [16]. This sequence requires NAD⁺ and enables the electrochemical interface required for energy conversion. The third cascade sequence employs a series of kinases and isomerases to convert six equivalents of ribulose-5-phosphate into five equivalents of glucose-6-phosphate. This sequence consists of ribose-5-phosphate isomerase (RPI), ribulose-5-phosphate-3-epimerase (RuPE), transketolase (TK), transaldolase (TA), and phosphoglucose isomerase (PGI) to convert two equivalents of ribulose-5-phosphate into one equivalent of glyceraldehyde-3-phosphate and glucose-6-phosphate that feeds back into the second (electrochemical) cascade sequence. Finally, three additional enzymes were included to convert glyceraldehyde-3-phosphate to glucose-6-phosphate, thereby preventing it from building up and causing product inhibition. Those three enzymes were triose phosphate isomerase (TPI), aldolase (ALD), and fructose-1,6-biphosphatase (FBP) [18] (Fig. 3).

Despite exemplifying the robustness of the multi-enzyme electrode approach to electrocatalytic cascades, this work importantly highlights an inherent limitation to the use of overly specialized catalysts. The sequential nature of both Zhang's pseudoglycolysis pathway and Minteer's immobilized Kreb's cycle necessitates that the overall catalytic rate will be limited by the slowest catalytic step. Furthermore, the buildup of reaction intermediates and a multitude of enzymatic cofactors due to unbalanced kinetics can result in multiple competitive inhibition pathways, effectively shutting down the entire cascade. Two solutions to this fundamental problem have emerged: (1) the use of compartmentalization and microscopic spatial orientation to control the movement of intermediates and cofactors (which will be discussed in a later section), and (2) a collective movement of researchers towards fewer, but more promiscuous electrocatalysts. Some of the early research using promiscuous enzymatic cascade electrodes has been based on reaction pathways that mimic glycolysis [19, 20].

Glucose oxidase and glucose dehydrogenase catalyze the oxidation of glucose, and have been widely investigated for bioelectrode designs, because of the importance of electrochemical glucose sensing. However, in the context of energy conversion, these enzymes are only capable of extracting two electrons per molecule of glucose via oxidation of the C1 carbon. Gorton and coworkers demonstrated that pyranose dehydrogenase (PDH) from *Agaricus meleagris* is capable of electrochemically oxidizing both the C2 and C3 positions of glucose [19]. Therefore, by co-immobilizing PDH with the dehydrogenase domain of cellobiose dehydrogenase from *Corynascus thermophiles* (an enzyme that, like glucose dehydrogenase, oxidizes glucose at C1), a bienzyme-modified electrode can electrochemically oxidize the C1, C2, and C3 positions while collecting six electrons per molecule of glucose

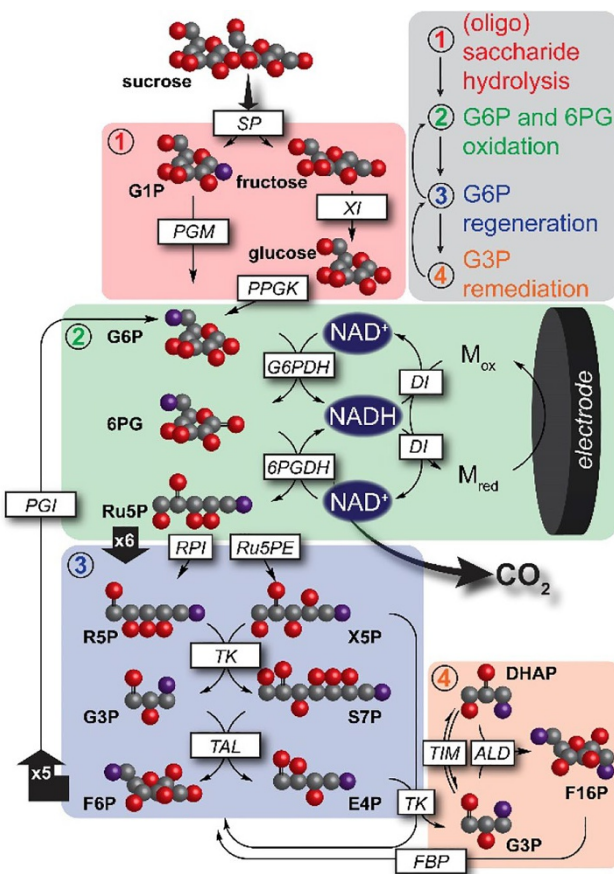


Fig. 3 Schematic of the *in vitro* 15-enzyme electrometabolic pathway described by Zhang and coworkers

[21]. This concept was later expanded upon by Holade et al. to enable multistep oxidation of a broad range of (oligo)saccharides. In the follow-up work, cellobiose dehydrogenase was replaced with a broad glucose oxidase (bGOx) capable of oxidizing the anomeric carbon of galactose, lactose, maltose, cellobiose, and xylose in addition to glucose. Therefore, the combination of PDH and bGOx was capable of extracting up to six electrons per molecule of fuel in a complex mixture of (oligo)saccharides [22]. While deep glucose oxidation remains an area of extreme interest for bioenergy conversion, several interesting lessons have been learned recently in attempts to utilize glycerol as a fuel source.

3 Hybrid Cascades for Electrometabolic Glycerol Oxidation Pathways

Glycerol is a promising biofuel due to its low cost, abundance (it is a biproduct of industrial biodiesel production) and its high energy density [23]. This is highlighted by the fact that concentrated glycerol solutions boast theoretical energy densities (6260 W h L^{-1}) that are comparable to than gasoline [24]. However, designing electrometabolic pathways from glycerol that mimic natural metabolism is complicated by the number of enzymes required for its activation to oxidation (as highlighted by the complex pathways described above). Recent efforts to electrochemically oxidize glycerol to CO_2 have shifted towards a simpler artificial pathway by employing catalysts with lower substrate specificity. Arechederra et al. demonstrated that three promiscuous enzymes [PQQ-dependent alcohol and aldehyde dehydrogenase and oxalate oxidase (OxO)] can be used to catalyze the complete bioelectrooxidation of glycerol to CO_2 [25]. The combination of alcohol and aldehyde dehydrogenases was able to oxidize alcohol and aldehyde intermediates (five steps) along the electrometabolic glycerol pathway, eventually converting glycerol into mesoxalic acid [26]. Then, oxalate oxidase was employed to cleave CO_2 from both mesoxalate and oxalate to complete the cascade, while collecting 12 electrons per glycerol molecule [25]. The primary drawback to this approach comes from the decreasing relative activity as the catalytic cascade progresses. As such, the rate of electroenzymatic glycerol oxidation (step 1) is much slower than the rate of tartronic acid oxidation (step 5), which stems from the fact that, despite being a promiscuous enzyme, alcohol dehydrogenase maintains an activity bias for primary alcohols. To simplify the system further and enable a more uniform reactivity, a novel strategy was developed utilizing hybrid catalytic motifs.

Enzymes have evolved to exhibit exceptional catalytic activities towards a relatively limited range of substrates, while small molecular catalysts have been designed to comparatively moderate catalytic activity towards a much broader substrate scope. Given the demands of complex electrooxidative cascades, it was postulated that hybrid catalytic combinations could combine the benefits of each catalytic motif. Hickey et al. employed a homogeneous small molecular catalyst, 2,2,6,6-tetramethylpiperidin-1-yl)oxyl (TEMPO), known to electrochemically oxidize alcohols to aldehydes and subsequently to carboxylic acids under mild aqueous conditions to replace alcohol and aldehyde dehydrogenases from the electrometabolic glycerol pathway described above [27]. One particular amine-functionalized derivative, TEMPO-NH₂, was demonstrated to catalyze the first five steps of the electrochemical glycerol oxidation pathway (as well as step 7, glyoxalate to oxalate), thereby replacing the catalytic role of both alcohol and aldehyde dehydrogenase. Most importantly, TEMPO-NH₂ was found to exhibit exceptional catalytic activity in the oxidation of tartrate, which had been the limiting step for complete glycerol oxidation. The rate of electron transfer is substantially slower for OxO than TEMPO-NH₂. Consequently, most electrons from the OxO-catalyzed oxidative cleavage of mesoxalate and oxalate were likely leached to O₂ (the

native electron acceptor for OxO), thus < 12 electrons per molecule of glycerol were likely collected.

Use of hybrid catalytic motifs to enhance the overall rate-determining steps in this cascade was expanded upon in two important ways. The first altered the electrometabolic pathway for glycerol oxidation by replacing oxalate oxidase (which exhibits only minor activity for the oxidative cleavage of CO₂ from mesoxalate) with formate dehydrogenase, an NAD⁺-dependent enzyme that can more efficiently oxidize mesoxalate to form glyoxalate. Unlike previously described NAD⁺ regeneration systems (that require additional enzymes or coelectrocatalysts), the FDH/TEMPO hybrid cascade utilizes TEMPO-NH₂ dually to oxidize alcohols/aldehydes as electrochemically regenerated NAD⁺ [28]. A primary benefit from employing FDH is gained from increased reactivity towards mesoxalic acid. In addition to increased rate of mesoxalate oxidation, the use of FDH enables collection of electrons from the CO₂ cleavage step(s) indirectly via TEMPO-catalyzed NAD⁺ regeneration.

The second expansion of the hybrid electrometabolic glycerol pathway demonstrates the possibility of utilizing a trihybrid catalytic cascade to efficiently collect electrons from each intermediate. In both of the two previous TEMPO/enzyme cascades, the overall catalytic rate was limited by the rate of CO₂ cleavage for either mesoxalate (OxO) or oxalate (FDH). Subsequent work showed that a TEMPO-modified redox polymer [TEMPO-modified linear poly(ethylenimine), TEMPO-LPEI] could catalyze electrochemical oxidation of steps 1–5 of the

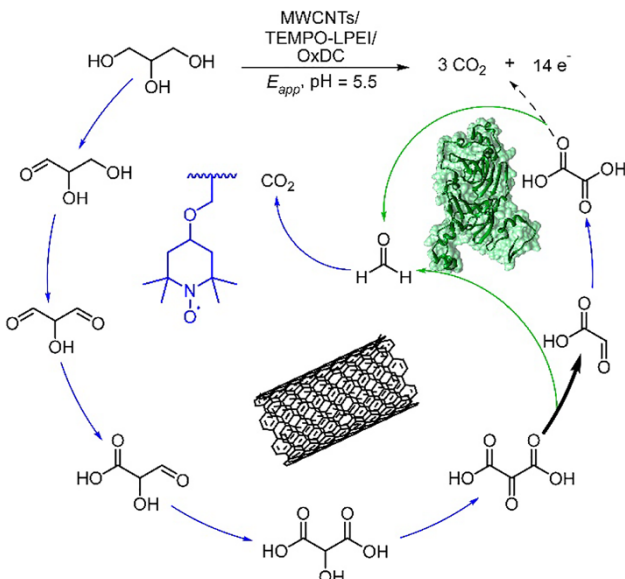


Fig. 4 Trihybrid electrometabolic glycerol pathway, employing a TEMPO-modified redox polymer to oxidize the steps highlighted in blue, MWCNTs to oxidize mesoxalate, and oxalate decarboxylase (OxDC) to hydrolytically cleave oxalate and mesoxalate into CO₂ and formate (highlighted by green arrows)

electrooxidative glycerol cascade (resulting in mesoxalic acid), while carboxylated multiwalled carbon nanotubes (MWCNT-COOH) were capable of electrooxidatively cleaving CO₂ from mesoxalate, and an oxalate decarboxylase enzyme was employed to hydrolytically cleave oxalate into CO₂ and formate (which was subsequently oxidized by TEMPO-LPEI) [29, 30]. The net result was a collection of 14 electrons per molecule of glycerol [30, 31] (Fig. 4).

4 Applications of Electroenzymatic Cascades

While the use of hybrid TEMPO/enzyme catalytic cascades has subsequently expanded to a variety of additional short-chain polyols, other hybrid catalytic cascades have employed combinations of immobilized redox enzymes with a variety of nanoparticles to enhance electrocatalytic rates and enable energy extraction from electrochemically inaccessible biofuels. Wang et al. used N-hydroxysuccinimide (NHS-) activated pyrene butyric acid to immobilize glucoamylase onto Au nanoparticle-decorated carbon nanofibers to hydrolyze starch to glucose and subsequently oxidize glucose to gluconolactone [32]. This enabled an array of multiple glucoamylase enzymes (which exhibits relatively sluggish kinetics) to be immobilized around relatively few Au nanoparticles on the carbon electrode surface.

In addition to energy conversion, the use of electrocatalytic cascades has been used extensively in the development of biosensors. Enzymatic and hybrid cascades have been employed to generate an electrochemical signal transduction pathway from electrochemically silent analytes. In an interesting demonstration of this approach, an electrometabolic cascade described recently by Kopiec et al. employs a bienzymatic system for the detection of phosphate [33]. In this biosensor, purine nucleoside phosphorylase (PNP) utilizes dissolved inorganic phosphate as an analyte to phosphorylate a sacrificial inosine molecule. Upon phosphorylation, inosine is cleaved into ribose-1-phosphate and hypoxanthine, which is subsequently oxidized twice by xanthine oxidase (XOx) to generate four electrons while producing uric acid. The generated uric acid is then directly oxidized at the electrode to generate a total of six electrons per molecule of inorganic phosphate (Fig. 5).

It should be noted that there are numerous reports of electrochemical biosensors employing a combination of glucose oxidase (which oxidizes glucose to gluconolactone and produces H₂O₂) with horseradish peroxidase (HRP) to reduce H₂O₂, where HRP is interfaced at an electrode via an electrochemical mediator. However, because the parent substrate (glucose) does not react further, these systems are not strictly considered cascades based on the criteria used herein. Therefore, the specifics of this literature will not be discussed here further. While the majority of examples to this point have focused on oxidative electrometabolic pathways, there has been a growing interest in hybrid catalytic motifs in the design of reductive electrometabolic pathways.

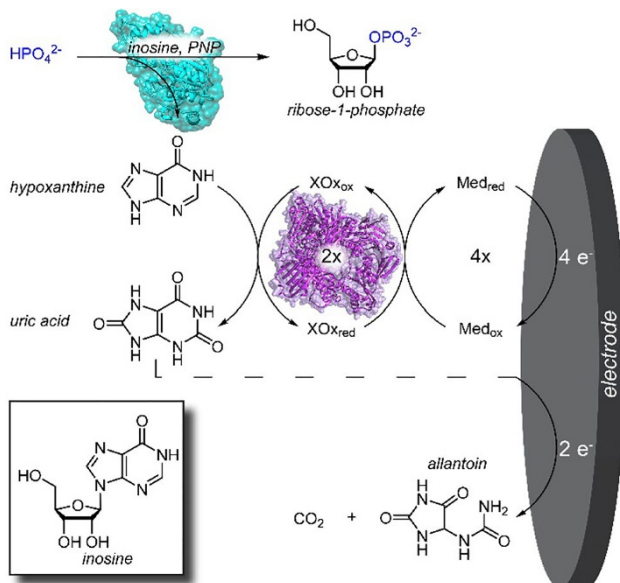


Fig. 5 Bioelectrocatalytic detection of inorganic phosphate using a sacrificial inosine molecule with purine nucleoside phosphorylase (PNP), electrochemically mediated xanthine oxidase (XOx), and direct electrochemical oxidation of uric acid to collect six electrons per molecule of phosphate analyte

5 Emergence of Reductive Electrometabolic Pathways for N_2 and CO_2 Reduction

As a primary biproduct of agricultural waste and a promoter of algal blooms, nitrate contamination in groundwater has led to rapidly growing environmental concerns regarding agricultural waste runoff. Consequently, there is increasing demand for techniques aimed at sustainable remediation of nitrate. To this end, Vincent and coworkers have designed a hybrid electrochemical cascade to reduce nitrate to ammonia [34]. Noble metal-catalyzed reduction of nitrate is slow under neutral aqueous conditions, while electroenzymatic reduction of nitrate to nitrite under the same conditions occurs rapidly, while the reverse is true for nitrite reduction to ammonia. Therefore, Duca et al. combined these two catalytic motifs to exploit the benefits of each to compensate for the drawbacks of the other. Nitrate reductase from *Escherichia (E.) coli* was combined with Pt nanoparticles on a carbon electrode to reduce nitrate to nitrite and nitrite to ammonia, respectively, in a sequential hybrid catalytic cascade [34]. This electrocatabolic nitrogen remediation pathway overcomes sluggish reduction rates exhibited by noble metals at pH 7, thereby eliminating one of the limiting factors in electrocatalytic denitrification. In addition to nitrate remediation, hybrid electrocatalytic cascades have been employed in strategies to address other environmental problems, such as CO_2 fixation.

The environmentally friendly reduction of CO_2 to into high-energy chemicals remains perhaps the greatest challenge facing scientists. A recent report by Park and

coworkers demonstrated the photoelectrochemical interpretation of a catalytic cascade originally reported by Obert and Bakul [35] employing a three-enzyme cascade including FDH, formaldehyde dehydrogenase (FaldDH), and ADH in the reverse directions from that described above to reduce CO₂ to formate, formaldehyde and then methanol [36]. Simultaneously, NADH was regenerated from NAD⁺ via a non-enzymatic cascade in which photoexcited electrons are transferred through a BiFeO₃ photocathode to a rhodium-based electrochemical mediator ([Cp*Rh(bpy)H₂O]⁺, Cp* = C₅Me₅, bpy = 2,2'-bipyridine). Coupled with a Co-P_i/α-Fe₂O₃ photoanode, this enzymatic cascade was able to reduce CO₂ to methanol in a divided photoelectrochemical cell under mild aqueous conditions (pH 7, 25 °C). This work illustrates the intricate level of complexity that can be achieved in designing hybrid electrometabolic pathways; however, expanding research of highly complex uncompartimentalized catalytic cascades requires strategies to mitigate diffusional and kinetic constraints.

6 Spatial Orientation and Substrate Channeling

As discussed above, the primary issues plaguing design of electrometabolic pathways arises from the multiplicity of intermediates and cofactors and their uncontrolled diffusion throughout the bulk media. As artificial pathways increase in complexity, there is an increasing probability that mismatched enzyme kinetics will lead to a buildup of intermediates. This reactivity bottleneck will in turn lead to product inhibition and ultimately result in sluggish cascade rates. Nature has evolved to overcome this problem through a combination of compartmentalization and spatial orientation of enzymes. A growing field of research has focused on fundamentally understanding the role that spatial organization plays in naturally occurring pathways and exploiting that knowledge in the design of artificial reaction cascades.

Enzymes that react sequentially can form transient non-covalent complexes, termed metabolons, that enhance metabolic flux by minimizing the distance required for a common reaction intermediate to diffuse from one enzyme to the next. Several groups have employed a strategy of co-immobilization of sequentially reacting enzymes onto a well-defined molecular scaffold to enable precise control over the ordering, ratio, and diffusional length scale between enzymes. Multiple synthetic and biologically engineered scaffolds have been employed, ranging from virus-based nanocages [37] to hydrophobized silica macropores [38] to DNA origami [39]. One scaffold that we will highlight here utilizes a series of selective binding proteins that natively exist to help form the cellulase complex (known as the cellulosome). These binding protein couples consist of two units, cohesins and dockerins, that exhibit a high binding specificity for one another; this specificity was exploited by Chen and coworkers (among others [40]) to spatially orient three sequential dehydrogenases (alcohol dehydrogenase, formaldehyde dehydrogenase, and formate dehydrogenase) to catalyze the oxidation of methanol to CO₂ [41]. Each enzyme was genetically engineered to contain a specific dockerin tag at the C-termini, that bind to the corresponding cohesin domain of a miniscuffoldin displayed on a yeast cell surface. The authors demonstrated that the scaffoldin-bound enzyme sequence exhibited a

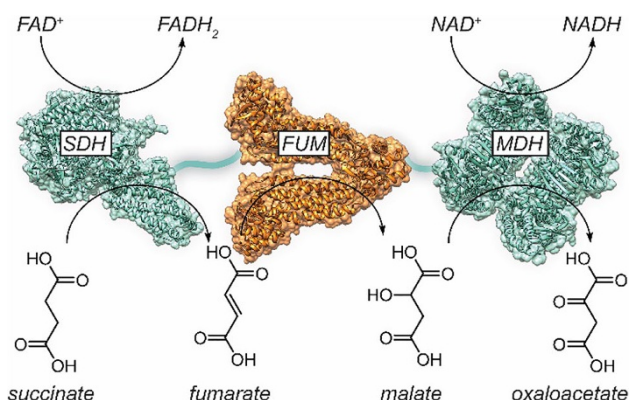


Fig. 6 An artificially cross-linked metabolon consisting of succinate dehydrogenase (SDH), fumarase (FUM), and malate dehydrogenase (MDH)

5.1x increase in overall cascade rate (as measured by NADH production) over the freely diffusing enzymes. In addition to artificial scaffolds, researchers have taken advantage of naturally occurring enzyme interactions to spatially orient sequential proteins relative to each other.

Moehlenbrock et al. demonstrated the adaptation of such naturally occurring interactions in the design of an electroenzymatic cascade based on a portion of the Kreb's cycle [42]. The sequential enzymes of the Kreb's cycle were covalently cross-linked within extracted mitochondria to ensure that the proteins were linked in a conformation that mimics their native metabolon complex (Fig. 6). The cross-linked metabolon complex was isolated from lysed mitochondria and immobilized onto an electrode.

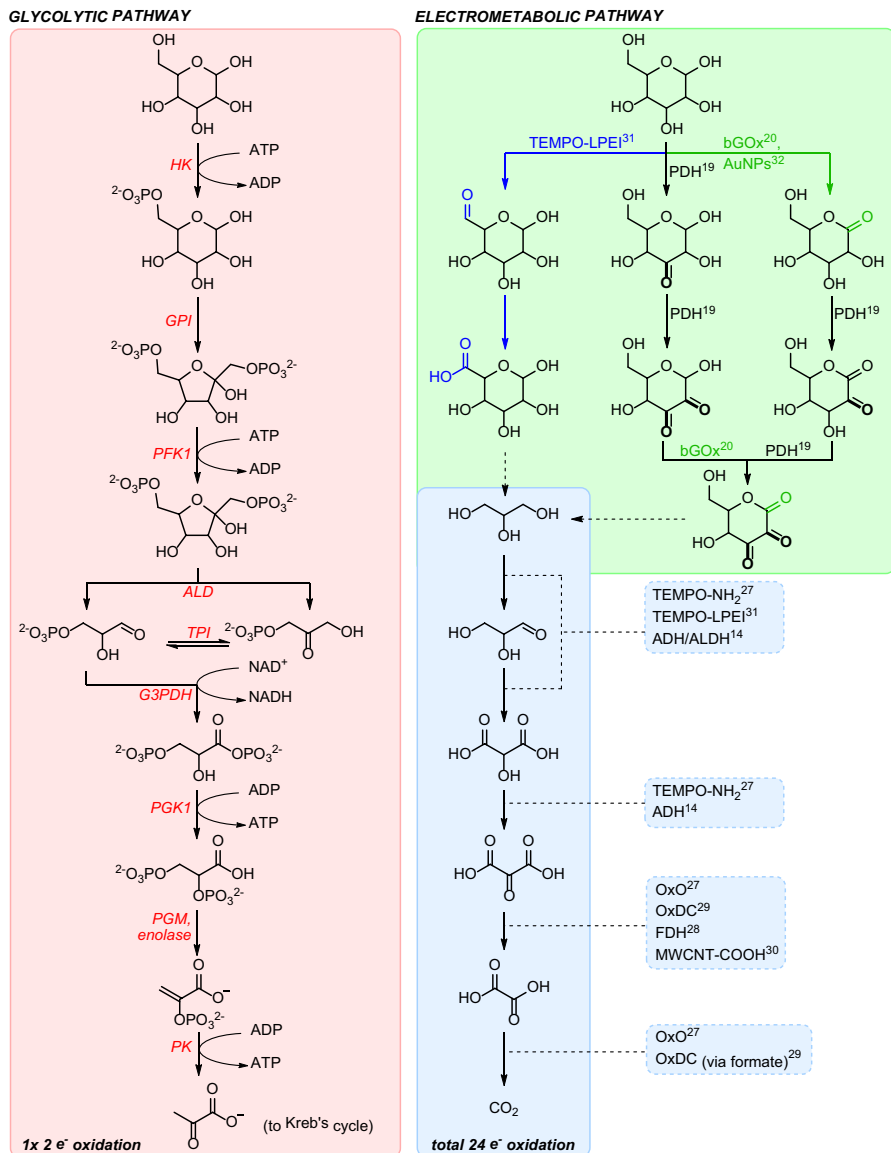


Fig. 7 Comparison between the native glycolytic pathway and a combination of electrometabolic pathways used to convert chemical energy (from glucose) into electrochemical energy

When cross-linked with dimethyl suberimidate, the isolated metabolon exhibited a 50% increase in catalytic current density over the free enzymes in solution.

As an extension of this work, Wu et al. were able to employ this same cross-linking strategy to isolate the eight enzyme components from the Kreb's cycle and identify interfacial amino acid residues between mitochondrial malate dehydrogenase, citrate synthase, and aconitase [43]. This led to the discovery of two electrostatic pathways

along the protein surfaces between the malate dehydrogenase-citrate synthase active sites and the citrate synthase-aconitase active sites [43]. These electrostatic surface pathways are oppositely charged to the shared reaction intermediate between adjacent enzymes and were proposed (and later experimentally confirmed [44]) as electrostatic channels to minimize intermediate diffusion into the bulk solution. This mechanism, termed electrostatic substrate channeling, has been the focus of growing interest as a design tool for controlling intermediate flux in artificial catalytic cascades [45]. While recent studies have suggested that electrostatic substrate channeling in enzymes occurs via discrete interactions between charged intermediates and oppositely charged solvent accessible amino acid residues [46–48], a precise understanding of this mechanism in artificial cascades is still being developed. Furthermore, continuing research is needed to define the role and limitations of substrate channeling as a design principle in artificial catalytic cascades.

7 Conclusion

In summary, electrochemical catalytic cascades can be used for complex fuel oxidation to yield high current and energy densities compared to individual components of the cascade. These cascades also benefit from substrate specificity and mild reaction conditions. As artificial electrometabolic pathways become more complex to facilitate multi-step oxidations, cascades become limited by diffusional and kinetic properties (Fig. 7). These limitations can be overcome by employing molecular architectures that enable precise spatial orientation of sequential catalysts, and continuing research may incorporate substrate channeling as a means of restricting diffusion of intermediates beyond simple proximity effects.

Acknowledgements The authors would like to thank the Army Research Office MURI award (W911NF-14-1-0263) for funding.

References

1. Sundaresan VB, Sarles SA, Leo DJ (2006) Stack of BioCells converting ATP to electrical power and possible applications. *MRS Proc.* <https://doi.org/10.1557/proc-0950-d01-03>
2. Qian H, Autzen Henriette E (2012) A little engine that could: ATP-powered electrical battery and heater inside cells. *Biophys J* 103(7):1409–1410. <https://doi.org/10.1016/j.bpj.2012.08.047>
3. Chen Y, Choi S, Thompson LT (2015) Low-temperature CO₂ hydrogenation to liquid products via a heterogeneous cascade catalytic system. *ACS Cat* 5(3):1717–1725. <https://doi.org/10.1021/cs501656x>
4. Macazo FC, Minteer SD (2017) Enzyme cascades in biofuel cells. *Curr Opin Electrochem* 5(1):114–120. <https://doi.org/10.1016/j.coelec.2017.07.010>
5. Szczupak A, Aizik D, Mora's S, Vazana Y, Barak Y, Bayer E, Alfonta L (2017) The electrosome: a surface-displayed enzymatic cascade in a biofuel cell's anode and a high-density surface-displayed biocathodic enzyme. *Nanomaterials* 7(7):153
6. Wu G, Gao Y, Zhao D, Ling P, Gao F (2017) Methanol/oxygen enzymatic biofuel cell using laccase and NAD⁺-dependent dehydrogenase cascades as biocatalysts on carbon nanodots

- electrodes. *ACS Appl Mater Interfaces* 9(46):40978–40986. <https://doi.org/10.1021/acsam.i.7b12295>
- 7. Franco JH, Minteer SD, de Andrade AR (2018) Product analysis of operating an ethanol/O₂ biofuel cell shows the synergy between enzymes within an enzymatic cascade. *J Electrochem Soc* 165(9):H575–H579. <https://doi.org/10.1149/2.0931809jes>
 - 8. Birmingham WR, Turner NJ (2018) A single enzyme oxidative “cascade” via a dual-functional galactose oxidase. *ACS Cat* 8(5):4025–4032. <https://doi.org/10.1021/acscatal.8b00043>
 - 9. Williams KR, Gregory DP (1963) Electrolytes for low-temperature fuel cells. *J Electrochem Soc* 110(3):209–213. <https://doi.org/10.1149/1.2425712>
 - 10. Du H, Zhao CX, Lin J, Guo J, Wang B, Hu Z, Shao Q, Pan D, Wujcik EK, Guo Z (2018) Carbon nanomaterials in direct liquid fuel cells. *Chem Rep* 22:22. <https://doi.org/10.1002/tcr.201800008>
 - 11. Ong BC, Kamarudin SK, Basri S (2017) Direct liquid fuel cells: a review. *Int J Hydrom Energy* 42(15):10142–10157. <https://doi.org/10.1016/j.ijhydene.2017.01.117>
 - 12. Li Y, Feng Y, Sun X, He Y (2017) A sodium-ion-conducting direct formate fuel cell: generating electricity and producing base. *Angewandte Chemie* 56(21):5734–5737. <https://doi.org/10.1002/anie.201701816>
 - 13. Wang R, Wu M, Haller S, Métivier P, Wang Y, Xia Y (2018) Hypophosphites as eco-compatible fuels for membrane-free direct liquid fuel cells. *Chem Eur J* 24(41):10310–10314. <https://doi.org/10.1002/chem.201801888>
 - 14. Palmore GTR, Bertschy H, Bergens SH, Whitesides GM (1998) A methanol/dioxygen biofuel cell that uses NAD⁺-dependent dehydrogenases as catalysts: application of an electro-enzymatic method to regenerate nicotinamide adenine dinucleotide at low overpotentials. *J Electroanal Chem* 443(1):155–161. [https://doi.org/10.1016/S0022-0728\(97\)00393-8](https://doi.org/10.1016/S0022-0728(97)00393-8)
 - 15. Sokic-Lazic D, Minteer SD (2009) Pyruvate/air enzymatic biofuel cell capable of complete oxidation. *Electrochim Solid State Lett* 12(9):F26–F28. <https://doi.org/10.1149/1.3170904>
 - 16. Zhu Z, Sun F, Zhang X, Zhang YHP (2012) Deep oxidation of glucose in enzymatic fuel cells through a synthetic enzymatic pathway containing a cascade of two thermostable dehydrogenases. *Biosens Bioelectron* 36(1):110–115. <https://doi.org/10.1016/j.bios.2012.04.001>
 - 17. Zhu Z, Kin Tam T, Sun F, You C, Percival Zhang YH (2014) A high-energy-density sugar biobattery based on a synthetic enzymatic pathway. *Nat Commun.* <https://doi.org/10.1038/ncomms4026>
 - 18. Zhu Z, Ma C, Percival Zhang YH (2018) Co-utilization of mixed sugars in an enzymatic fuel cell based on an *in vitro* enzymatic pathway. *Electrochim Acta* 263:184–191. <https://doi.org/10.1016/j.electacta.2017.11.083>
 - 19. Tasca F, Timur S, Ludwig R, Haltrich D, Volc J, Antiochia R, Gorton L (2007) Amperometric biosensors for detection of sugars based on the electrical wiring of different pyranose oxidases and pyranose dehydrogenases with osmium redox polymer on graphite electrodes. *Electroanalysis* 19(2–3):294–302. <https://doi.org/10.1002/elan.200603740>
 - 20. Habrioux A, Merle G, Servat K, Kokoh KB, Innocent C, Cretin M, Tingry S (2008) Concentric glucose/O₂ biofuel cell. *J Electroanal Chem* 622(1):97–102. <https://doi.org/10.1016/j.jelecchem.2008.05.011>
 - 21. Shao M, Nadeem Zafar M, Sygmund C, Guschin DA, Ludwig R, Peterbauer CK, Schuhmann W, Gorton L (2013) Mutual enhancement of the current density and the coulombic efficiency for a bio-anode by entrapping bi-enzymes with Os-complex modified electrodeposition paints. *Biosens Bioelectron* 40(1):308–314. <https://doi.org/10.1016/j.bios.2012.07.069>
 - 22. Holade Y, Yuan M, Milton RD, Hickey DP, Sugawara A, Peterbauer CK, Haltrich D, Minteer SD (2017) Rational combination of promiscuous enzymes yields a versatile enzymatic fuel cell with improved coulombic efficiency. *J Electrochem Soc* 164(3):H3073–H3082. <https://doi.org/10.1149/2.0111703jes>
 - 23. Beltrán-Prieto JC, Kolomazník K, Pechá J (2013) A review of catalytic systems for glycerol oxidation: alternatives for waste valorization. *Aust J Chem* 66(5):511–521. <https://doi.org/10.1071/CH12514>
 - 24. Sokic-Lazic D, Arechederra RL, Treu BL, Minteer SD (2010) Oxidation of biofuels: fuel diversity and effectiveness of fuel oxidation through multiple enzyme cascades. *Electroanalysis* 22(7–8):757–764. <https://doi.org/10.1002/elan.200980010>
 - 25. Arechederra RL, Minteer SD (2009) Complete oxidation of glycerol in an enzymatic biofuel cell. *Fuel Cells* 9(1):63–69. <https://doi.org/10.1002/fuce.200800029>
 - 26. Arechederra RL, Treu BL, Minteer SD (2007) Development of glycerol/O₂ biofuel cell. *J Power Sources* 173(1):156–161. <https://doi.org/10.1016/j.jpowsour.2007.08.012>

27. Hickey DP, McCamant MS, Giroud F, Sigman MS, Minteer SD (2014) Hybrid enzymatic and organic electrocatalytic cascade for the complete oxidation of glycerol. *J Am Chem Soc* 136(45):15917–15920. <https://doi.org/10.1021/ja5098379>
28. Abdellaoui S, Seow Chavez M, Matanovic I, Stephens AR, Atanassov P, Minteer SD (2017) Hybrid molecular/enzymatic catalytic cascade for complete electro-oxidation of glycerol using a promiscuous NAD-dependent formate dehydrogenase from *Candida boidinii*. *Chem Commun* 53(39):5368–5371. <https://doi.org/10.1039/c7cc01027c>
29. Abdellaoui S, Hickey DP, Stephens AR, Minteer SD (2015) Recombinant oxalate decarboxylase: enhancement of a hybrid catalytic cascade for the complete electro-oxidation of glycerol. *Chem Commun* 51(76):14330–14333. <https://doi.org/10.1039/c5cc06131h>
30. Macazo FC, Hickey DP, Abdellaoui S, Sigman MS, Minteer SD (2017) Polymer-immobilized, hybrid multi-catalyst architecture for enhanced electrochemical oxidation of glycerol. *Chem Commun* 53(74):10310–10313. <https://doi.org/10.1039/c7cc05724e>
31. Hickey DP, Milton RD, Chen D, Sigman MS, Minteer SD (2015) TEMPO-modified linear poly(ethylenimine) for immobilization-enhanced electrocatalytic oxidation of alcohols. *ACS Cat* 5(9):5519–5524. <https://doi.org/10.1021/acscatal.5b01668>
32. Wang Z, Xia L, Xia J, An Z, Gong S (2016) Direct energy harvesting from starch by hybrid enzymatic and non-enzymatic cascade bioanode. *RSC Adv* 6(31):26421–26424. <https://doi.org/10.1039/c6ra2059c>
33. Kopiec G, Starzec K, Kochana J, Kinnunen-Skidmore TP, Schuhmann W, Campbell WH, Ruff A, Plumeré N (2018) Bioelectrocatalytic and electrochemical cascade for phosphate sensing with up to 6 electrons per analyte molecule. *Biosens Bioelectron* 117:501–507. <https://doi.org/10.1016/j.bios.2018.06.047>
34. Duca M, Weeks JR, Fedor JG, Weiner JH, Vincent KA (2015) Combining noble metals and enzymes for relay cascade electrocatalysis of nitrate reduction to ammonia at neutral pH. *ChemElectroChem* 2(8):1086–1089. <https://doi.org/10.1002/celec.201500166>
35. Obert R, Dave BC (1999) Enzymatic conversion of carbon dioxide to methanol: enhanced methanol production in silica sol-gel matrices. *J Am Chem Soc* 121(51):12192–12193. <https://doi.org/10.1021/ja991899r>
36. Park DS, Abdelrahman OA, Vinter KP, Howe PM, Bond JQ, Reineke TM, Zhang K, Dauenhauer PJ (2018) Multifunctional cascade catalysis of itaconic acid hydrodeoxygénération to 3-methyl-tetrahydrofuran. *ACS Sustain Chem Eng* 6(7):9394–9402. <https://doi.org/10.1021/acssuschemeng.8b01743>
37. Brasch M, Putri RM, de Ruiter MV, Luque D, Koay MST, Castón JR, Cornelissen JJLM (2017) Assembling enzymatic cascade pathways inside virus-based nanocages using dual-tasking nucleic acid tags. *J Am Chem Soc* 139(4):1512–1519. <https://doi.org/10.1021/jacs.6b10948>
38. Parlett Christopher MA, Isaacs Mark A, Beaumont Simon K, Bingham Laura M, Hondow Nicole S, Wilson K, Lee Adam F (2015) Spatially orthogonal chemical functionalization of a hierarchical pore network for catalytic cascade reactions. *Nat Mater* 15:178. <https://doi.org/10.1038/nmat4478>
39. Maune HT, S-p Han, Barish RD, Bockrath M, Iii WAG, Rothemund PWK, Winfree E (2009) Self-assembly of carbon nanotubes into two-dimensional geometries using DNA origami templates. *Nat Nanotech* 5:61. <https://doi.org/10.1038/nnano.2009.311>
40. You C, Myung S, Zhang Y-HP (2012) Facilitated substrate channeling in a self-assembled trifunctional enzyme complex. *Angew Chem Int Ed* 51(35):8787–8790. <https://doi.org/10.1002/anie.201202441>
41. Liu F, Banta S, Chen W (2013) Functional assembly of a multi-enzyme methanol oxidation cascade on a surface-displayed trifunctional scaffold for enhanced NADH production. *Chem Commun* 49(36):3766–3768. <https://doi.org/10.1039/c3cc40454d>
42. Moehlenbrock MJ, Toby TK, Waheed A, Minteer SD (2010) Metabolon catalyzed pyruvate/air biofuel cell. *J Am Chem Soc* 132(18):6288–6289. <https://doi.org/10.1021/ja101326b>
43. Wu F, Minteer S (2015) Krebs cycle metabolon: structural evidence of substrate channeling revealed by cross-linking and mass spectrometry. *Angew Chem Int Ed* 54(6):1851–1854. <https://doi.org/10.1002/anie.201409336>
44. Wu F, Pelster LN, Minteer SD (2015) Krebs cycle metabolon formation: metabolite concentration gradient enhanced compartmentation of sequential enzymes. *Chem Commun* 51(7):1244–1247. <https://doi.org/10.1039/c4cc08702j>
45. Wheeldon I, Minteer SD, Banta S, Barton SC, Atanassov P, Sigman M (2016) Substrate channelling as an approach to cascade reactions. *Nat Chem* 8(4):299–309. <https://doi.org/10.1038/nchem.2459>

46. Liu Y, Hickey DP, Guo J-Y, Earl E, Abdellaoui S, Milton RD, Sigman MS, Minteer SD, Calabrese Barton S (2017) Substrate channeling in an artificial metabolon: a molecular dynamics blueprint for an experimental peptide bridge. *ACS Cat* 7(4):2486–2493. <https://doi.org/10.1021/acscatal.6b03440>
47. Earl E, Calabrese Barton S (2017) Simulation of intermediate transport in nanoscale scaffolds for multistep catalytic reactions. *PCCP* 19(23):15463–15470. <https://doi.org/10.1039/c7cp00239d>
48. Liu Y, Matanovic I, Hickey DP, Minteer SD, Atanassov P, Barton SC (2018) Cascade kinetics of an artificial metabolon by molecular dynamics and kinetic Monte Carlo. *ACS Cat* 8(8):7719–7726. <https://doi.org/10.1021/acscatal.8b01041>